

INFORMATION TO USERS

This manuscript has been reproduced from the microfilm master. UMI films the text directly from the original or copy submitted. Thus, some thesis and dissertation copies are in typewriter face, while others may be from any type of computer printer.

The quality of this reproduction is dependent upon the quality of the copy submitted. Broken or indistinct print, colored or poor quality illustrations and photographs, print bleedthrough, substandard margins, and improper alignment can adversely affect reproduction.

In the unlikely event that the author did not send UMI a complete manuscript and there are missing pages, these will be noted. Also, if unauthorized copyright material had to be removed, a note will indicate the deletion.

Oversize materials (e.g., maps, drawings, charts) are reproduced by sectioning the original, beginning at the upper left-hand corner and continuing from left to right in equal sections with small overlaps.

Photographs included in the original manuscript have been reproduced xerographically in this copy. Higher quality 6" x 9" black and white photographic prints are available for any photographs or illustrations appearing in this copy for an additional charge. Contact UMI directly to order.

ProQuest Information and Learning
300 North Zeeb Road, Ann Arbor, MI 48106-1346 USA
800-521-0600

UMI[®]

NOTE TO USERS

This reproduction is the best copy available.

UMI[®]

UNIVERSITY OF OKLAHOMA

GRADUATE COLLEGE

THE GEOCHEMICAL BUDGET OF BERYLLIUM IN SILICIC MELTS
& SUPERLIQUIDUS, SUBLIQUIDUS, AND STARTING STATE EFFECTS ON THE
KINETICS OF CRYSTALLIZATION IN HYDROUS HAPLOGRANITE MELTS

A Dissertation

SUBMITTED TO THE GRADUATE FACULTY

in partial fulfillment of the requirements for the

degree of

Doctor of Philosophy

(In Geology)

By

JOSEPH M. EVENSEN

Norman, Oklahoma

2001

UMI Number: 3014523

UMI[®]

UMI Microform 3014523

Copyright 2001 by Bell & Howell Information and Learning Company.

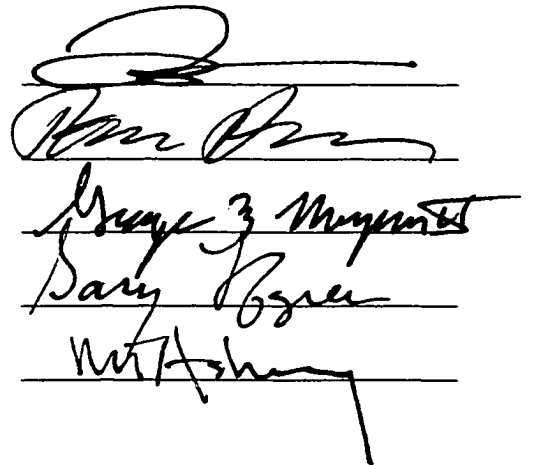
All rights reserved. This microform edition is protected against
unauthorized copying under Title 17, United States Code.

Bell & Howell Information and Learning Company
300 North Zeeb Road
P.O. Box 1346
Ann Arbor, MI 48106-1346

THE GEOCHEMICAL BUDGET OF BERYLLIUM IN SILICIC MELTS
& SUPERLIQUIDUS, SUBLIQUIDUS AND STARTING STATE EFFECTS ON
THE KINETICS OF CRYSTALLIZATION IN HYDROUS HAPLOGRANITE
MELTS

A Dissertation APPROVED FOR THE
SCHOOL OF GEOLOGY AND GEOPHYSICS

BY



The image shows four handwritten signatures, each written on a horizontal line. From top to bottom, the signatures are: a large, stylized signature; a signature that appears to be 'Dore Dore'; a signature that appears to be 'George J. Thompson'; and a signature that appears to be 'Dary Byrne'. Below these is a fourth signature that appears to be 'W. H. ...'.

© Copyright by JOSEPH M. EVENSEN 2001
All Rights Reserved.

ACKNOWLEDGEMENTS

Experimental and analytical work was supported by National Science Foundation EAR-9625517, 9618867, and 990165. The Electron Microprobe Laboratory was created by Department of Energy grant DE-FG22-87FE1146 with assistance from NSF GIF EAR-9404658 and support from the University of Oklahoma. Student research grants from the Society of Economic Geologists (SEG Foundation, 1998), the University of Oklahoma (OU Foundation, 2000), and the American Association of Petroleum Geologists (Grants-in-Aid, 2001) supported field research in New Mexico, Colorado, and Madagascar. Student travel grants for meeting attendance and presentation of papers from the Geological Society of America (1999), the University of Oklahoma (OU Graduate College, 1999, 2000), and Los Alamos National Laboratory (LANSCE, 2001) are gratefully acknowledged.

I thank my mentor, Dr. David London, for showing me the utility of experimentation as creative and powerful means for deciphering key geological processes. I thank David for our continual discussions—at the blackboard, computer and microprobe, in the field and laboratory, and at mineral shows and auctions—and for sharing his insight into crystalline and vitreous materials. I also thank David for sharing gourmet run products from his home kitchen laboratory on a regular basis, which allowed me to glean better experimental techniques, discuss pegmatitic inspirations and avoid starving during graduate study. Mostly, I want to thank David for his widespread support and outstanding advice.

I thank Dr. Thomas Dewers for being an enthusiastic source of ideas and for facilitating many critical components of my studies that relied heavily on his effort. I

want to thank Tom for encouraging the scientific process with open-mindedness. I would like to thank Dr. George Morgan for months of his effort toward chemical analyses and for showing me quantitative ways of elucidating geochemical process in experimental systems.

I thank Dr. Gary Lofgren (NASA Johnson Space Center) for his feedback and recommendations, and for facilitating potential applications of this work in the future. Gary's thoughtful comments greatly affected my conceptions of the crystallization process. I thank Dr. Michael Ashby for teaching an exceptional inorganic chemistry course, for stepping onto my committee at the last moment, and for helpful feedback on these studies. I thank Dr. Roger Frech for thoughtful questions on my written examinations—topics that I often consider and reconsider.

I appreciate continual discussions with Dr. Edward Grew (University of Maine) toward the crystal chemistry and petrochemistry of Be. I gratefully acknowledge Dr. Richard Hervig (Arizona State University) for helping with the analysis and interpretation of SIMS results and for sharing his insight into the geochemistry of Be. I owe a special thanks to Dr. Charles Gilbert for periodically getting me out to the spectacular granite occurrences of Oklahoma and for thoughtful discussions at the outcrop. I also thank Dr. Jon Price (Rensselaer Polytechnic Institute) for his friendship, for help with petrologic problems, and for guiding me through the Wichita Granite Province with a pegmatite focus. I thank Dr. John Kaszuba (Los Alamos National Laboratory) for his friendship and for his joint effort toward experiments using neutrons on Be-minerals. I also thank Dr. Antonio Acosta for numerous insightful discussions, particularly about magmatic cordierite. I appreciate effort by Drs. Skip Simmons

(University of New Orleans) and Federico Pezzotta (Museum of Natural History at Milan) toward a tour of the truly novel pegmatites in Madagascar. Helpful advice during my studies from Drs. Roger Slatt and Kevin Smart is also appreciated. Lastly, I thank Jeane Jerz (Virginia Tech) for her friendship and numerous, productive discussions about better approaches to science.

Several people are thanked for contributing so that my Be-cordierite working curve could be established: Dr. Thomas Armbruster (University of Bern) for donating Sponda cordierite, Dr. Edward Grew for donating Christmas Point surinamite, Dr. Joseph Peters (American Museum of Natural History) for donating Haddam cordierite, AMNH #39556, and Dr. Werner Schreyer (Ruhr-University at Bochum) for donating “BeMg-cordierite” experimental run products. I thank Dr. Carl Francis (Harvard Mineralogical Museum) for donating type bityite from LaCroix’s collection (Harvard #87680) toward the study of Be in pegmatitic micas. I also thank Dr. George Harlow (American Museum of Natural History) for contributing genthelvite from Mt. St. Hilaire (AMNH #39039) toward the successful analysis of Be analysis by microprobe.

I thank Roger Melick (USGS, Denver) and Dorinda Bair for their friendship, for several years of collecting pegmatite minerals in Colorado, and for outstanding discussions about the genesis of pegmatites. I thank Eric Fritz for his friendship, for effort toward maintenance in the Lab, and for time spent haggling at the Tucson Show and collecting at pegmatites in New Mexico.

Finally, I thank Sonja for sharing her dreams of grandeur and for her patience.

DEDICATION

This dissertation is dedicated to my lovely grandmother, Margaret.

TABLE OF CONTENTS

TITLE PAGE	i
SIGNATURE PAGE	ii
COPYRIGHT PAGE	iii
ACKNOWLEDGEMENTS	iv
DEDICATION PAGE	vii
TABLE OF CONTENTS	viii
LIST OF TABLES	x
LIST OF FIGURES	xiii
ABSTRACT	xvii
CHAPTER ONE	
OVERVIEW	1
CHAPTER TWO	
CRYSTAL CHEMISTRY AND PHASE RELATIONS OF CORDIERITE – BERYL SOLID SOLUTIONS IN GRANITIC SYSTEMS	10
CHAPTER THREE	
EXPERIMENTAL PARTITIONING OF BERYLLIUM AND OTHER TRACE ELEMENTS BETWEEN CORDIERITE AND SILICIC MELT, AND THE CHEMICAL SIGNATURE OF S-TYPE GRANITE	94
CHAPTER FOUR	
EXPERIMENTAL CALIBRATION OF THE BERYLLIUM CYCLE FROM MIGMATITE TO PEGMATITE	137

CHAPTER FIVE

KINETICS OF CRYSTALLIZATION IN UNDERCOOLED GRANITIC
MELTS (Ab-Or-Qtz-H₂O): SUPERLIQUIDUS, SUBLIQUIDUS AND
STARTING MATERIAL EFFECTS 212

LIST OF TABLES

TABLE 2-1	Ideal cation site occupancies and symmetry for cordierite to beryl structures	49
TABLE 2-2	Starting materials	50
TABLE 2-3	Starting mixtures	51
TABLE 2-4	Cordierite and glass chemical analyses	52
TABLE 2-5	Beryl analyses	55
TABLE 2-6	Convergence of calculated temperatures among alkalis, excess Si, Al, and Be using regressions of Figure 2-12	56
TABLE 2-7	Elemental partitioning data between beryllian cordierite and granitic melt	57
TABLE 2-8	Reported assemblages of Be-cordierite and other Be-minerals	58
TABLE 3-1	Starting materials	124
TABLE 3-2	Chemical analyses of cordierite – glass pairs	125
TABLE 3-3	Regressions of elemental partitioning between cordierite and granitic melt as a function of temperature	127
TABLE 3-4	Reported Be contents of granitic rocks and their association to cordierite-bearing source rocks	128
TABLE 3-5	Reported Be contents of migmatite systems	129
TABLE 3-6	Cordierite-bearing normative calculations of melt at 700°C	130
TABLE 4-1	Average beryllium contents of rock-forming minerals in	

silicic systems (granitoid rocks to pegmatites)	. . .	181
TABLE 4-2	Average beryllium contents of crustal rock systems . . .	182
TABLE 4-3	Starting materials	183
TABLE 4-4	Starting mixtures	184
TABLE 4-5a	K-alkali feldspar – glass compositional pairs . . .	185
TABLE 4-5b	K- and Na-alkali feldspar – glass compositional pairs . . .	186
TABLE 4-5c	Albite and andesine – glass compositional pairs . . .	187
TABLE 4-6	Quartz – glass compositional pairs	188
TABLE 4-7a	Dark mica – glass compositional pairs	189
TABLE 4-7b	White mica – glass compositional pairs	191
TABLE 4-8a	Experimentally calibrated partition coefficients of Be between rock-forming minerals and silicic melt and their T-dependence	193
TABLE 4-8b	Experimental mineral/mineral partition coefficients for Be in granitic melts	194
TABLE 4-9	Partition coefficients for Be from natural systems	195
TABLE 4-10	Reported Be contents of migmatite systems	197
TABLE 4-11	Reservoirs of Be in a schematic pegmatite dike	198
TABLE 4-12	Average Be content of granitic pegmatites	199
TABLE 4-13	Compositions of the beryllian wallrock alteration assemblage from the Harding Pegmatite, NM, USA	200
TABLE 4-14	Bulk distribution coefficients for Be	201
TABLE 5-1a	Melting experiments for determination of the freezing	

point of hydrous haplogranite at 200 MPa	249
TABLE 5-1b Composition of the synthetic haplogranite anhydrous starting glass and a representative hydrous run product	250
TABLE 5-1c Composition of haplogranite melt as a function of degree of water saturation	251
TABLE 5-1d Superliquidus melting experiments at 700° and 730°C	252
TABLE 5-2 Preliminary nucleation lag times	253
TABLE 5-3 Preliminary nucleation data for all crystalline phases	254
TABLE 5-4 Preliminary crystal growth rates of K-alkali feldspar	256
TABLE 5-5 Preliminary solidus crystal growth rates of K-alkali feldspar and graphic intergrowths	257
TABLE 5-6 A selected representation of preliminary crystal morphology measurements	258

LIST OF FIGURES

FIGURE 2-1	Working curve for SIMS analysis of Be	69
FIGURE 2-2	Backscattered electron micrographs: Experimental products	70
FIGURE 2-3	Backscattered electron micrographs: Cordierite – beryl assemblages and textures	71
FIGURE 2-4	Backscattered electron micrographs: Reaction relationships among beryl, phenakite, and seeded cordierite	72
FIGURE 2-5	Be contents of granitic melts at Be-cordierite \pm beryl saturation	73
FIGURE 2-6	Total tetrahedral versus total octahedral site occupancy in Be-cordierite formulae	74
FIGURE 2-7	Elemental constituents of cordierite as a function of temperature	75
FIGURE 2-8	Total occupancy at the tetrahedral sites for Be-cordierite	76
FIGURE 2-9	Be-coupled exchange mechanisms in cordierite with temperature	77
FIGURE 2-10	Beryllium substitution mechanisms in cordierite	78
FIGURE 2-11	Mean values of Be-coupled exchange components with temperature	79
FIGURE 2-12	Variations of cordierite channel-occupying constituents with temperature	80
FIGURE 2-13a	Elemental partitioning ratios between Be-cordierite and coexisting silicic melt from 675 to 850°C for cordierite-essential constituents	81
FIGURE 2-13b	Elemental partitioning ratios between Be-cordierite and coexisting silicic melt from 675 to 850°C for trace elements	82

FIGURE 2-14 Concentrations of element oxides between coexisting cordierite and granitic melt	83
FIGURE 2-15 Elemental constituents of beryl as a function of temperature .	84
FIGURE 2-16 Total tetrahedral versus total octahedral site occupancy in beryl formulae	85
FIGURE 2-17 Variations of the octahedral constituents of beryl with temperature	86
FIGURE 2-18 Variations of the tetrahedral constituents of beryl with temperature	87
FIGURE 2-19 Excess silicon vacancy exchange in beryl along the beryl – cordierite join	88
FIGURE 2-20 Variations of channel-occupying constituents of beryl with temperature	89
FIGURE 2-21 Miscibility relations between cordierite and beryl in granitic melts at 200 MPa as generalized by Be content	90
FIGURE 2-22 Miscibility relations between cordierite and beryl in granitic melts at 200 MPa as measured by the total chemical operator, $\text{Be}_3\text{SiAl}_2(\text{Mg,Fe})_2$	91
FIGURE 2-23 Cordierite – beryl compositions plotted by their normalized tetrahedral and octahedral pseudo-ternary constituents	92

FIGURE 2-24 Ternary projection normalized to cordierite – beryl formulae	93
FIGURE 3-1 Working curve for the analysis of Be by SIMS	133
FIGURE 3-2 Backscattered electron micrographs of experimental products and assemblages	134
FIGURE 3-3 Partitioning of Be between cordierite and melt at 200 MPa	135
FIGURE 3-4 Partitioning of Li, Rb, Cs, B, Ca, and Mn between cordierite and melt at 200 MPa	136
FIGURE 4-1 Working curve for the analysis of Be by SIMS	204
FIGURE 4-2 Backscattered electron micrographs of representative experimental products and assemblages	205
FIGURE 4-3 Distribution of Be within a granitic pegmatite showing characteristic events of beryl saturation	207
FIGURE 4-4 Schematic representation of the key stages of fractionation for the evolution of the Be budget in crustal magmas	208
FIGURE 4-5 Three geochemical pathways (a,b,c) for Be during the evolution of granitic magmas	209
FIGURE 5-1a Different starting conditions of the same material	263
FIGURE 5-1b Powdered X-ray diffraction spectra for crystalline products from starting powdered glass	264

FIGURE 5-2 Schematic run pathways for different experimental series as a function of time and temperature	265
FIGURE 5-3 Coverage of undercooling steps following a superheating of ~ 50°C ($T = 730^{\circ}\text{C}$) for 1 day	266
FIGURE 5-4 Number of observed crystals and nucleation centers as a function of time of the undercooling step after superheating at 730°C for 1 day	269
FIGURE 5-5 Examples of mineral growth sequences in run products	275
FIGURE 5-6 Mechanisms of crystallization in run products	278
FIGURE 5-7 Maximum crystal length (of Kfs) as a function of time of the undercooling step after superheating at 730°C for 1 day	281
FIGURE 5-8 Total percent crystallization of undercooled melts as a function of time	284
FIGURE 5-9 Sequences of growth of single and intergrown minerals in undercooled melts originating from (a) glass powder, (b) glass rod, and (c) crystalline materials	287
FIGURE 5-10a Vesicle populations in run products above and below T_G	289
FIGURE 5-10b Vesicle perimeter versus maximum vesicle diameter for vesicle populations above and below T_G	290
FIGURE 5-11 Evidence for the formation of boundary phases at crystallization fronts	291
FIGURE 5-12 Preliminary “fields” of crystal morphology in granitic melt	293

ABSTRACT

Experimental analysis at the P - T conditions of the shallow crust is used to evaluate (1) the beryllium budget of granitic melts and (2) the kinetics and mechanisms of crystallization in hydrous haplogranite melt. The first study utilizes mineral-melt partitioning behavior, relevant crystal-chemistry and stability relations, and reported compositions to assess Be geochemistry from low to high activities of Be in melt. The latter study examines the differences in solidification from melt as multivariable functions of starting state, superheating, undercooling, and time.

1. An investigation of cordierite – beryl equilibria in hydrous granitic melts using forward- and reversed-direction experiments from 675 to 900°C at 200 MPa ($P_{\text{H}_2\text{O}}$) has revealed the elucidate limits and mechanisms of solid solution among these phases. Beryllium-bearing cordierite (BeCrd) and beryl (Brl) coexist on a solvus that extends from ~ 675°C (the lowest temperature investigated) to beyond 900°C. BeO contents of cordierite (by SIMS) increase with T to reach 3.97 wt% at 850°C; this BeCrd has the empirical formula of $^{\text{ch}}(\text{Na,K,Ca})_{0.22}(\text{Mg,Fe,Mn})_{2.00}\text{Be}_{0.93}\text{Al}_{2.29}\text{Si}_{5.73}\text{O}_{18}\cdot 0.63\text{H}_2\text{O}$. FeMg-beryl contains a maximum of 0.43 ΣR^{2+} a.p.f.u. (atoms per formula unit), which partly correlates with increasing T . Solid solution between cordierite (Crd) and beryl is expressed in total by the site-independent component, $\text{Be}_3\text{SiAl}_2(\text{Mg,Fe})_{-2}$, which is a sum of 3 site-specific exchange mechanisms: $\text{Be}^{[4,\text{T1}]} \text{Si}^{[4,\text{T2}]} \text{Al}^{[4]}_{-2}$ (predominantly) and $\text{Be}^{[4,\text{T1}]} \text{Na}^{[\text{ch}]} \text{Al}^{[4,\text{T1}]}_{-1}$ (to a lesser degree), which vary inversely with T , plus the exchange in Brl, $\text{Al}^{[6]}(\text{Mg,Fe})^{[6]}_{-1} \text{Na}^{[\text{ch}]}_{-1}$, that increases with T . An additional exchange,

$\text{Si}^{[4]}\text{Be}^{[4]}_{-2}\square$, at the *Tl* site in beryl increases with *T* and may destabilize Brl. Cesium and Li become increasingly compatible in BeCrd (relative to Crd). In magmatic environments, cordierite will act as a crustal reservoir of the rarer elements Li, Be, Mn, and Cs.

In order to evaluate the trace element signature that cordierite imparts to silicic magmas, we have performed experiments on cordierite-bearing peraluminous granitic melts at 200 MPa ($P_{\text{H}_2\text{O}}$), and from 700 to 850°C in forward and reversed direction using metapelitic mineral mixtures. Most coefficients of elemental partitioning vary with *T*. Beryllium is strongly compatible, with $D_{\text{Be}}^{\text{Crd/melt}}$ values decreasing linearly from 202.0 to 6.7 as *T* rises from 700 to 850°C. Manganese is compatible ($D_{\text{Mn}}^{\text{Crd/melt}} = 7.67$ to 1.92 over the same range of *T*), and shows similar values to those reported for biotite in silicic melts. Incompatible components include Li, Rb, B, F and P, though Cs is nearly compatible in cordierite, especially at higher *T* ($D_{\text{Cs}}^{\text{Crd/melt}} = \sim 0.19$ to 0.60). Cordierite is likely to be the most effective crystalline reservoir of Cs in metapelites and their anatectic melts.

Natural data support the hypothesis that Crd, when present in granitic melts, sequesters Be, Cs and Mn. S-type granitic rocks containing Crd (typically in restite, though also in late facies) show diagnostically low Be contents (mean = 0.8 ppmw Be; average range = <1 to 1.20 ppmw), whereas Crd-absent granites (e.g., containing accessory garnet) exhibit distinctly higher Be contents (mean = 6 ppmw Be; range = 3 to 12 ppmw) that increases further in evolved apical facies (mean = 69 ppmw Be; average range = 11 to 145 ppmw) and commonly give rise to beryl-bearing pegmatites. Beryllium signatures can discriminate source environments of silicic magmas at a resolution equal

to the boundaries of the cordierite stability field—e.g., at the P - T - X conditions where cordierite gives rise to garnet + aluminosilicate. Cordierite-bearing granitic rocks contain low Cs contents (mean = 1.8 ppmw Cs) compared to the Cs-richer Crd-free equivalents (mean = 18 ppmw Cs); Mn contents also correlate with the presence (mean = 0.01 wt% MnO) or absence of Crd (mean = 0.09 wt% MnO). Depending on its contribution to anatexis, cordierite *sequesters* or rarely, *contributes* S-type chemical character to granitic rocks, giving rise to a distinctive Crd-associated subgroup of S-type elements—different from the signature of micas (high Li, F and to a lesser degree, Be and Mn). Whole rock analyses of granites along with a distinct absence of beryl in their associated pegmatites indicate that a sizable population of S-type granites contained cordierite in their restite. Calculated modal proportions of Crd may be used to distinguish restitic vs. magmatic histories. Routine analysis of Crd (and Be) may help quantitatively constrain sources and pathways during magmatic cycles of granite, because unlike micas, the Crd signature distinguishes sources of melting.

Partition coefficients ($D_{\text{Be}}^{\text{mineral/melt}}$) for beryllium between alkali feldspar, plagioclase, quartz, dark mica, and white mica and hydrous granitic melt were determined by experiments at 200 MPa H_2O as functions of temperature (650° to 900°C), activity of Be in melt (trace levels to beryl saturation), bulk composition, and thermal run direction. At trace levels, Be is compatible in plagioclase of An_{31} (1.84) and muscovite (1.35), but incompatible in biotite (0.39 to 0.54 from 650° to 800°C), alkali feldspar (0.38 to 0.19 from 680° to 850°C), quartz (0.24 at 800°C), and albite (0.10). The partition coefficients are different at saturation of the melt in beryl: plagioclase of An_{31} (0.89 at 700°C), muscovite (0.87 at 700°C), biotite (0.18 to 0.08 from 675° to 800°C), alkali

feldspar (0.18 to 0.14 from 680° to 700°C), quartz (0.17 to 0.08 from 750° to 800°C), and albite (0.37 at 750°C).

With other data sources, these new partition coefficients were utilized to model the distribution of Be between aluminous quartzofeldspathic source rocks and their anatectic melts, and to model the dispersion or concentration of Be in melt through igneous crystal fractionation of different magma types (e.g., S-type, I-type) up to beryl-saturated granitic pegmatites and their hydrothermal aureoles. Among the rock-forming minerals, cordierite, calcic oligoclase, and muscovite (in this order) control the fate of Be because of the compatibility of Be in these phases. In general, beryl-bearing pegmatites can arise only after extended crystal fractionation of large magma batches (to F, fraction of melt remaining, ≤ 0.05), and granitic magmas that originate from cordierite-bearing protoliths or that contain large modal quantities of calcic oligoclase will not achieve beryl saturation at any point in their evolution.

2. Unlike low-silica basic or alkaline magmas that closely track a condition of equilibrium between crystals and melt upon a liquidus line of descent, comparable crystal-melt reactions in silicic melts are highly susceptible to kinetic factors and do not track the equilibrium liquidus closely. We have experimentally assessed the kinetics of crystallization as a combined function of (1) starting state, (2) single step superheating, (3) single-step undercooling, and (4) time. Using a synthetic haplogranitic glass corresponding to the 200 MPa hydrous minimum melt composition prepared at 1800°C, 1 atm, three starting states of the glass were derived for starting materials of experiments: cylindrical rods, powder, and a finely crystalline variant created by devitrifying powder

(650°C for 4 days). The minimum melting temperature at 200 MPa (P_{H_2O}) is 683°C. For each starting state, crystallization was induced as a compound function of superheating T ($+\Delta T = T > T_{liquidus} = +50, +150^\circ\text{C}$) and duration (1, 7 days) and liquidus undercooling ($-\Delta T = T < T_{liquidus} = -10$ to -300°C), and duration (1 hour to 1 month). Rate and morphological data were obtained by image processing of backscattered electron micrographs. Results indicate that the mechanisms of crystallization vary as a composite function of (1) starting state of the medium and (2) superliquidus – subliquidus t - T pathways.

Nucleation lag times vary with starting state and increase with superheating T , but decrease with undercooling. For melts originating from glassy starting states, nucleation lag times fall between 3-7 days for $-\Delta T$ up to -150°C . No nucleation lag at low undercoolings for melts derived from crystalline material suggests that critical nuclei must persist beyond the 24 hour superheating step at 730°C ; with undercooling, however, nucleation lag times *increase*. Sidewall nucleation is dominant regardless of starting material; internal nucleation is more prevalent, though still rare, in melts of crystalline mixtures. In melts from both crystalline and glassy starting materials, Kfs crystallizes first followed by Qtz. As $-\Delta T$ increases, finely intergrown Afs (i.e., graphic feldspars) crystallizes prior to the appearance of monomineralic Qtz. With time, the general sequence of crystallization of $\text{Kfs} \rightarrow \text{Kfs} + \text{Qtz} \rightarrow \text{Kfs} + \text{Qtz} + \text{Ab} \rightarrow \text{Kfs} + \text{Ab} \rightarrow \text{Qtz}$ is observed, though several variations exist.

Mechanistically, growth fronts in melts from glassy starting states advance inward, parallel to sidewalls and with crystals oriented normal to edges of charges despite being hundreds of microns away. In melts of crystalline starting state, crystallization

proceeds inward from sidewalls as connective networks, following curved, bent and irregular routes. Preliminary rates show that nucleation varies \sim exponentially with $-\Delta T^*t$ for melts from glass, whereas scattered trends and overall lower rates of nucleation are observed for melts from the crystalline state. Compared to single crystals, growth rates increase, by an order of magnitude as each new phase joins the crystallizing intergrowth assemblage, which suggests a diffusion control in melt. Rapid growth rates occur for originally nuclei-free melts (surpassing others in $t^*\Delta T$), whereas solidification kinetics of nuclei-bearing melts show slower growth rates despite containing subcritical nuclei during the undercooling step. Nuclei-free and vesicle-free melts ultimately solidify more rapidly than nuclei- or vesicle-bearing melts.

Statistical image processing of thousands of crystals provided quantitative textural measures of run products. In melts containing residual subcritical nuclei, correlations of crystal geometries (via crystal area, perimeter, length, width, diameter aspect ratio, solidity, convexity and roundness) are seen with the magnitude of undercooling, the duration of undercooling, and the combination, $-\Delta T^*t$. Textures of granitic run products quantitatively reflect available nuclei in their melts and the magnitude of $-\Delta T$ and t steps. As such, these signatures identify superheating and undercooling histories.

Data from the run matrix suggest that undercooling primarily effects crystallization in this system. Regardless of starting medium, solidification appears to be most rapid at moderately high degrees of undercooling, from about $-\Delta T = -103$ to -150°C . With the increase of the combination of undercooling and duration (ΔT^*t), the intrinsic properties of high silica hydrous melt at 200 MPa become dominant.

The range of undercooling above appears to be most efficient at creating enrichments of crystal-incompatible components (water-rich, markedly sodic below T_G) at the crystallization front. Nucleation rates appear to increase as growth rates drop upon very high degrees of undercooling, below the glass transition temperature, where chabazite may join the assemblage as a boundary layer product.

The starting structural and nucleation state of the melt as assessed by variable superheating and variable starting material, give rise to secondary controls on crystallization. For undercooled silicic melts, the starting medium influences the rate and mechanisms of crystallization in three ways: (1), nucleation lag times are longest for the least physically disrupted nuclei-free melt (at the preconditioning step), (2), total solidification is fastest for the least physically disrupted nuclei-free melt (at the preconditioning step), and (3), the spatial advance of crystallization is different for melts that lacked critical nuclei upon undercooling (crystallization as 2-D fronts) versus those that contained silicate nuclei upon undercooling (crystallization as 3-D networks).

CHAPTER 1. OVERVIEW

The Geochemical Budget of Beryllium in Silicic Melts

Beryllium is a novel element in geologic systems for one reason above all others: it exhibits a “mixed” $1s^2 2s^2 - 1s^2 2s^1 2p^1$ electron configuration (e.g., Bader et al., 1967) that gives rise to appreciable covalent character (e.g., bonding with F, the most electronegative of elements, yields only 79% ionic character: Wuensch and Hörmann 1978). A small ionic radius ($0.27^{[41]}$ Å: Shannon 1976) and high field strength (charge density between that of Al and Si) make for a poor fit for beryllium in most rock-forming minerals. These characteristics make beryllium useful as a geochemical marker.

Applications of beryllium to petrologic systems have taken advantage of the fact that Be is strongly incompatible in most rock-forming minerals. Consequently, Be is unaffected by many solid-state changes with P and T (e.g., it acts as chemical reference for changes in subducting slabs: Ryan et al., 1996). Owing to a preference for the liquid state, it can also be an exceptional monitor of fluid-rock systems (e.g., Bebout et al., 1993; Domanik et al., 1993). Due to incompatibility, the portion of Be that resides in the mantle is miniscule. The global cycle of radiogenic (e.g., Morris, 1991) and stable Be entails the convergence of an atmospheric – terrestrial – marine geochemical cycle with that of mantle systems (e.g., Brenan et al., 1998) in subduction environments. From here, it begins a transfer from deep up to shallow levels of the crust via mafic volcanism (e.g., Ryan et al., 1996) and silicic magmatism (e.g., Beus, 1966). All notable beryllium on earth is enriched in the upper sialic continental crust. Despite widespread interest in Be, the geochemistry of Be in these silicic systems—including buffers and controls on its

total budget—have remained hypothetical and unconstrained. Arguably the most important part of the global cycle, the Be cycle of the crust, has been missing.

Through experimental calibration and comparative surveys of the Be signatures of natural systems, I have evaluated the Be Budget of the crust from trace quantities to ore grade. Beryllium is known to be enriched in pelitic sources that give rise to S-type granite magmas, but it is found as ore signature material originating from I- and A-type magmas bearing a mantle or previously depleted deep crustal component. Perhaps, this is best shown in Černý's classification (1991) of the ultimate products of felsic magmatism—pegmatites. In these final, small-volume deposits, Be is noticeably enriched in both LCT (key enrichments of Li-Cs-Ta) and NYF (same for Nb-Y-F) categories, meaning that it spans the magmatic spectrum of granite. In other words, it is relatively indifferent in chemical environments of the crust. The first question that must be addressed in order to construct the Be cycle of the crust, is "*Under what petrologic conditions does Be become reactive?*"

Perhaps the best approach of the compatibility of Be within common rock-forming minerals is the degree to which these structural geometries mimic those of Be-minerals. Over 90 minerals exist with essential structural Be. Among these, beryl ($\text{Be}_3\text{Al}_2\text{Si}_6\text{O}_{18}$) is by far the most common. In beryl, Be occupies the T1 or linking tetrahedral sites, forming skewed BeO_4 tetrahedra—a likely manifestation of the bonding asymmetry of Be. The similarities of tetrahedral sites within rock-forming minerals to the T1 site in beryl should reflect their capacity to house (and yield) Be.

The structural similarities between beryl and cordierite have long been recognized. What has been missing in the story are measurements of the Be contents of

natural cordierite. This problem has plagued Be geochemistry in general. Owing to difficulties of poor, soft X-ray yields by bulk whole rock X-Ray Fluorescence or spot Quantitative Electron Microprobe Analysis, Be has rarely been measured in past studies. Secondary Ion Mass Spectrometry (R.L. Hervig, 2001, in press), as well as other techniques today (e.g., LA-ICP-MS) circumvent this problem, but not withstanding difficulties of reference standard materials. A major part of this work has been in creating suitable standards and assessing their performance (see Methods, Chapter 4).

Chapter 2 is an investigation of how cordierite accommodates structural Be, from low to high concentrations. Specific crystal-chemical exchange mechanisms that allow for Be accommodation (at *Tl* sites) are elucidated. The total sum of exchange mechanisms gives rise to complete solid solution between cordierite and beryl in silicic melts—along a 2 crystalline phase solvus that closes near 900°C. Both high- and low-*T* applications to natural systems are explained. Importantly, these mechanisms allow for rare, though documented, “backdoor” enrichment mechanism for Be, by which Be is concentrated in Crd as restite during anatectic events. This mode is in contrast to normally very efficient fractionation that leads to (much more voluminous) enrichment of magmatic Be, and illustrates the dramatic effect that cordierite exerts on Be budgets.

Chapter 3 takes a look at similar effects of cordierite, though at very low concentrations of Be in melt. These compositions are most applicable for the more voluminous silicic magmas which contain only trace amounts of Be. Here, the partitioning capacity of cordierite to accommodate Be is second to none, and the resulting “Be Signatures” in whole-rock compositions are discussed for S-type granitic magmas (containing a meta-sedimentary component in their source). A strong natural correlation

was noted between cordierite-bearing and cordierite-absent granitic assemblages and their whole rock values of Be: 0.8 vs. 6 ppmw Be, respectively. Cordierite appears to have more of an effect on the Be budgets of crustal melts than any other crystalline phase. This calibration is then put to use for natural systems, relating chemical signatures to P-T limits.

A combination of Be, Cs and Mn absolute contents shows that the depth from which S-type magmas are derived can be estimated. Cordierite strongly sequesters these elements, and thus where these elemental contents are low, magmas experienced histories within the shallow cordierite stability field ($\sim < 300$ MPa and from 500 to 900°C). For granites in which these elemental contents are high, and contain obvious enrichments in the form of related mineralization, these melts originated from deeper environments—in the field of garnet + aluminosilicate (key breakdown products of the terminal cordierite reaction). Thus, specific (e.g., Portugal versus Spain) and regional (e.g., N. America) inferences can be made for constraint of the histories of S-type granite magmatism.

Chapter 4 looks in more detail at the bulk budget of Be in silicic magmas, using partitioning experiments between rock-forming minerals and melt as a guide. It is a summary in itself, which is concluded with the designation of 3 chemical pathways for Be that operate in the crust. These include cordierite-bearing, cordierite-free S-type, and I- and A-type pathways, in which the latter two have the potential to achieve ore-grade enrichment levels. The former pathway can deplete magmas to achieve ore grade levels in residual source material; such rocks are likely sources for low quantities of granulite facies beryllian metamorphic assemblages. Case examples are given from anatectic environments (Hercynian migmatites, Spain), to large volume magmatic environments

(various granites around the world), to evolved facies of granitic liquids (Morococala Volcanic Field, Bolivia; Mt. Antero Region, CO), to pegmatites (around the world), and finally, to hydrothermal alteration aureoles (Harding Pegmatite, NM; Honeycomb Hills, UT). The examples fit with the empirically derived Be cycle and provide insight into petrologic process at various stages along the way.

Kinetics of Crystallization in Hydrous Haplogranite Melt

Though Chapter 5 is short in comparison to Chapters 2 through 4, it represents more than half of the work involved in this dissertation. This section summarizes the current state of assessment of a large matrix of experimental runs that covers conditions pertinent to the crystallization of granitic melt. Three different starting media of the same material were used for isochemical experiments of variable time (1 hr. to 1 mo.), and combined superheating ($T >$ the saturation surfaces of the crystalline phases: quartz and alkali feldspar liquid) and undercooling ($T <$ those saturation surfaces). By choosing a starting composition at the 200 MPa hydrous haplogranite ternary minimum (Ab-Or-Qtz-H₂O), the functions of superheating (denoted by $+\Delta T$) and undercooling ($-\Delta T$) are in reference to that minimum melting point. Beyond the total number of experiments required to constrain the mechanisms (or lack of: i.e., including kinetic lags) and rates pertinent to the solidification of melt/glass, perhaps the greatest challenge lies in interpreting the results.

The first portion of the Chapter is dedicated to discussion of the approaches to data extraction from run products. This discussion includes the need for converging evidence, consistency of trends and (some) replication of the data in order for confident interpretations of crystallization processes to be reached.

Nucleation delays are noted for the melts from starting glass, but are negligible for crystalline mixtures. This suggests that critical nuclei persist beyond the preconditioning stage. For all systems, sidewall nucleation seems to be the rule. Both nucleation and growth rates, each measured in a few different ways (e.g., $\text{solidity} \cdot \text{area} / \text{time}$ for a “solidity growth rate”), vary with starting material. While the melts originating from glass rods are most sluggish to initiate crystallization, their rates ramp up with time so that these melts are first to completely solidify. A counter-intuitive observation of this nature suggests that available nuclei in undercooled melts may facilitate nucleation in the short term, but inhibit the mechanisms and kinetics of crystallization in the long term. It also suggests that despite no obvious correlation, the presence of vesicles may indeed exert a subtle effect on the kinetics of crystallization.

The role of two- and three-phase crystalline intergrowths is linked to achieving rapid crystallization. Growth rates of Kfs and those of graphically intergrown Kfs+Qtz and Kfs+Qtz+Ab are compared. The growth rates of multiphase intergrowths are found to be about an order of magnitude greater than those of individual crystals; rates increase as successive phases crystallize together. This seems to be the mechanism which leads to rapid solidification, for melts at low degrees of undercooling contain Kfs only and persist without significant growth for $t > 1$ mo. Maximum solidification rates are found at similar magnitudes of undercooling for melts of each starting material: -103 to -150°C. Within the maximum crystallization region of the $-\Delta T - t$ space mapped out by these experiments, evidence of excess-water (the only incompatible component in this system) boundary layers are found at the crystallization front – melt interface.

Nucleation and crystal growth rates increase with $-\Delta T$ and t , though it appears that rates slow at very large $-\Delta T$ conditions, significantly below the glass transition. Without a doubt, many processes relevant to crystallization kinetics occur as this boundary is crossed. Most of these questions remain unanswered at least for now.

Lastly, this chapter elucidates spatial signatures of crystals that correlate with different degrees of undercooling and duration. Clearly, there is a quantifiable component present in the crystalline products that reflects the histories of their melts. An attempt is made to relate preliminary “categories” of crystal populations back to morphological “fields” within $-\Delta T - t$ kinetic space. Oscillatory behavior of crystalline sequences is observed in many melts, and while generally following a pathway of



several other variations occur. This sequence may represent an oscillatory pathway between the two governing saturation surfaces—the metastable extensions of the quartz and feldspar liquid. A distinct population of zoned sequences of intergrowths occurs at conditions below the glass transition temperature.

The last chapter may end with more questions than which it begins. Consistency among the reduced dataset, however, allows for some fundamental conclusions to be drawn regarding critical aspects of experimental approaches and key factors that are likely to strongly affect crystallization in granitic magmas.

References Cited

- Bader, R.F., Keaven, I.T., and Cade, P.E. (1967) Molecular charge distributions and chemical binding. II. First-row diatomic hydrides, AH. *Journal of Chemical Physics* 47, 3381-3402.
- Bebout, G.E., Ryan, J.G., and Leeman, W.P. (1993) B-Be systematics in subduction-related metamorphic rocks: Characterization of the subducted component. *Geochimica et Cosmochimica Acta* 57, 2227-2237.
- Beus, A.A. (1966) *Geochemistry of Beryllium and Genetic Types of Beryllium Deposits*, 286 p. W.H. Freeman and Company, San Francisco.
- Černý, P. (1991) Rare-element granite pegmatites. Part I: anatomy and internal evolution of pegmatite deposits. *Geoscience Canada*, 18, 49-67.
- Domanik, K.J., Hervig, R.L., and Peacock, S.M. (1993) Beryllium and boron in subduction zone minerals: An ion microprobe study. *Geochimica et Cosmochimica Acta* 57, 4997-5010.
- Morris, J.D. (1991) Applications of cosmogenic ^{10}Be to problems in the earth sciences. *Annual Review of Earth and Planetary Sciences*, 19, 313-350.
- Ryan, J.G., Langmuir, C.H. (1988) Beryllium systematics in young volcanic rocks; implications for ^{10}Be . *Geochimica et Cosmochimica Acta* 52, 237-244.
- Ryan, J., Morris, J., Bebout, G., and Leeman, W. (1996) Describing chemical fluxes in subduction zones: Insights from "depth-profiling" studies of arc and forearc rocks. In: *Subduction: Top to Bottom* (Bebout, G.E., Scholl, D.W., Kirby, S.H., and Platt, J.P., eds.). American Geophysical Union, Monograph 96, 263-268.

Shannon, R.D. (1976) Revised effective ionic radii and systematic studies of interatomic distances in halides and chalcogenides. *Acta Crystallographica*, 32, 751-767.

Wuensch BJ, Hörmann PK (1978) Beryllium. In: Wedepohl KH (ed) *Handbook of Geochemistry*, vol II (1). Springer, Berlin Heidelberg New York, pp 4-A-1 to 4-O-1.

CHAPTER 2. CRYSTAL CHEMISTRY AND PHASE RELATIONS OF CORDIERITE – BERYL SOLID SOLUTIONS IN GRANITIC SYSTEMS

INTRODUCTION

This study is part of a growing application of the geochemistry of beryllium to petrological problems (e.g., Morris 1991; Ryan et al., 1996; Reviews in Mineralogy volume 43, in preparation). The work pertains to the portion of the geochemical cycle that transfers Be by way of silicic magmatism from midcrustal anatectic sources (metapelites and aluminous gneisses) to higher levels in the shallow continental crust as granites, pegmatites, and related rock types. The Be contents of beryl-saturated melts at evolved stages of this process were assessed by Evensen et al. (1999), and the partitioning of Be between early peraluminous partial melts and potential residual crystalline phases were described by Evensen and London (1999a,b). In those studies, cordierite (Crd) emerged as an important reservoir of Be. In this paper, we address the crystal chemistry and exchange mechanisms that accommodate Be in cordierite (as well as those that accommodate Fe and Mg in beryl), and the nature and extent of miscibility between cordierite and beryl. Cordierite-beryl-melt equilibria and phase compositions are also investigated at water-saturated conditions of 200 MPa ($P_{\text{H}_2\text{O}}$) at T in the range from 675–900°C.

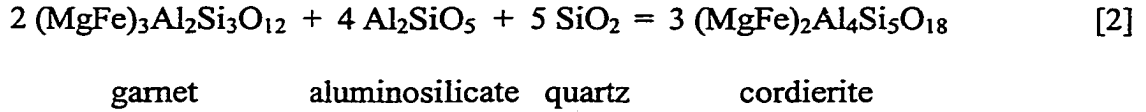
Background

Beryl (Brl, $\text{Be}_3\text{Al}_2\text{Si}_6\text{O}_{18}$), the most common but still volumetrically rare mineral with structural beryllium, largely occurs in evolved granitic pegmatites. Cordierite [Crd, $(\text{Mg,Fe})_2\text{Al}_4\text{Si}_5\text{O}_{18}$], including its Be-rich compositions, is a common rock-forming

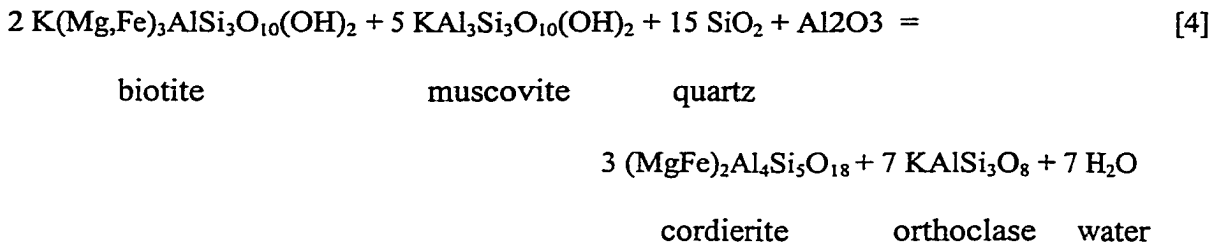
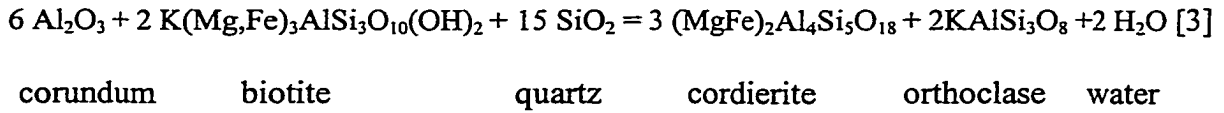
mineral in metapelites and aluminous gneisses formed at relatively low pressure (Mukhopadhyay and Holdaway 1994), and in peraluminous silicic magmas derived by anatexis of these protoliths. The hexagonal silicates beryl and indialite (the high temperature Crd polymorph, $\text{Mg}_2\text{Al}_4\text{Si}_5\text{O}_{18}$, which is isostructural with beryl: Miyashiro 1957) along with the orthorhombic cordierite ($\text{Mg}_2\text{Al}_4\text{Si}_5\text{O}_{18}$) – sekaninaite [$(\text{Mg,Fe})_2\text{Al}_4\text{Si}_5\text{O}_{18}$] series share resemblances to such a degree that miscibility among these phases has been hypothesized and tested experimentally (Povondra and Langer 1971, 1978, Hölscher and Schreyer 1989).

Solid solutions between cordierite and beryl occur in several crystallographic sites. These sites include linking tetrahedra, *T1* (Crd: Si, Al, Be; Brl: Be, rare Li), ring-forming tetrahedra, *T2* (Crd: Si, Al; Brl: Si), octahedra, *M* (Crd: Mg, Fe^{2+} ; Brl: Al, Mg, Fe^{2+} , Fe^{3+} , Sc), and channel voids (Crd: Na, K, Rb, Cs, H_2O , CO_2 , noble gases; Brl: Na, K, Rb, Cs, H_2O , OH, noble gases) (e.g., Damon and Kulp 1958; Gibbs 1966; Beltrame et al., 1976; Meagher and Gibbs 1977; Armbruster and Bloss 1982; Armbruster and Irouschek 1983; Aines and Rossman 1985; Gordillo et al., 1985; Predecki et al., 1987; Schreyer et al., 1990; Sherriff et al., 1991; Daniels 1992; Aurisicchio et al., 1994; Černý et al., 1997). Table 2-1 describes the site relations among Crd to Brl structures.

In cordierite, solid solution toward a hypothetical end-member $\text{NaMg}_2\text{BeAl}_3\text{Si}_5\text{O}_{18}$ goes as far as $\text{Na}_{0.65}\text{Mg}_2\text{Be}_{0.65}\text{Al}_{3.35}\text{Si}_5\text{O}_{18}$ at 700°C and 300 MPa (Povondra and Langer 1971, 1978). Beryllian cordierite containing up to 1 Be a.p.f.u. (i.e., $\text{Mg}_2\text{BeAl}_2\text{Si}_6\text{O}_{18}$), however, was synthesized in the Na-absent system (Hölscher and Schreyer 1989). Most natural Be-Crd tends to be sodic (with a maximum Be content found of 0.4 a.p.f.u.: Černý and Povondra 1966), which led to a proposed $\text{Be}^{[4]}\text{Na}^{[\text{ch}]}\text{Al}^{[4]}$.



These constituents produced melt with an ASI (Alumina Saturation Index \equiv mol $\text{Al}_2\text{O}_3 / (\text{Na}_2\text{O} + \text{K}_2\text{O} + \text{CaO} + \text{BaO} + \text{Li}_2\text{O} + \text{Rb}_2\text{O})$) of ~ 1.25 and enough ferromagnesian component (with dominant Mg) to provide cordierite stability (e.g., Clemmens and Wall 1988, Patiño Dulce 1992, Clarke 1995, Icenhower 1995). To a lesser degree, activated alumina + biotite, and white + dark mica were used as reactants for cordierite synthesis in melt, respectively:



Starting Materials. Seven different cordierite-forming mixtures were used.

Composite powders were formulated by combining mineral additives (Table 2-2) with either a large fraction of a pelite mineral mixture or a synthetic haplogranite glass with the composition of the metaluminous (ASI= 1.02) hydrous granite minimum at 200 MPa (Tuttle and Bowen 1958). For the mineral components, low-impurity regions of gem-quality crystals were selected for crushing. Crystal fragments were microscopically hand-sorted to remove impurities before grinding. Starting mixtures were ground in agate under ethanol to a mean grain size of 15 μm and dried in air at 140°C. Powdered

components were combined, ground together, and then dried (140°C). Finally, mixes were homogenized overnight in a tumbling mill. Proportions of ingredients are shown in Table 2-3.

The first mixture (SP-Crd1-Be) was the model Be-rich metapelite utilizing reactions [1] and [2]. The second mixture (SP-Bt1-Be) was a mica-rich variation of the former but without garnet—intended to barely reach cordierite saturation. The third mixture (SP-Bt2-Be) was similar to the second except that it contained activated, amorphous alumina (created by decomposing synthetic gibbsite in air at 400°C for 5 hours) to facilitate the cordierite-forming reaction, [3]. Mixture four (SP-Bt4-Be) utilized added cordierite to haplogranitic glass for back-reaction to new (Be-richer) cordierite. The fifth composition (SP-Mus2-Be) was potassic and less ferromagnesian than others, with its mode dominated by white mica (reaction [4]). Mixture six (SP-Crd2-Be) was a Be-richer variety of mixture 1, intended for evaluating bulk compositions intermediate between cordierite and beryl. Final charges further contained a slight excess of doubly distilled and deionized water needed to saturate a melt at 200 MPa and the *T* range investigated (~ 10 wt%). Each starting mixture successfully produced new cordierite (see Figure 2-2a).

Preparation of Charges. Gold capsules (3 x 20 mm) were cleaned by soaking overnight in bromopropane (25°C) then boiling for several hours in nitric acid. Afterwards, a few capsules still contained remnants of the extrusion lubricants used in the fabrication of the tubing, and these were removed with lint-free foam swabs.

Water was loaded into capsules first followed by powder mixes, with powder + water charges confined to a central 5 x 3 mm portion of the capsule, then sealed by DC-

plasma arc welding. Capsules were weighed before and after welding to check for leaks, and again after storage in a drying oven (140°C). The latter heating step allowed for homogenization of water contents throughout the powder prior to the experimental run.

Equipment. Experiments were pressurized cold in R-41® and NIMONIC-105® cold-seal reaction vessels using water plus a trace of Immunol® as the pressure medium. Pressure was set at 200 MPa and measured with a factory-calibrated Heise bourdon tube gauge. Fluctuations of < 3 MPa occurred over the course of experiments; total estimated accuracy was ± 10 MPa. Experiment durations varied from ~1 to 6 weeks.

Temperature was monitored by internal Chromel-Alumel thermocouples with estimated maximum error of ± 5°C. Experiments were quenched isobarically in compressed air jet (5 to 15°C/s). The fugacity of oxygen within capsules was regulated by diffusion of H₂ across the metal capsule; the f_{O_2} of the pressure medium at run conditions is estimated to be slightly below NNO (Huebner 1971). Following quench, capsules were weighed to check for leaks, punctured and the presence of free water was recorded. Punctured capsules were placed in a drying oven and, following dehydration, were reweighed to verify loss of free water and hydration of glass (melt). All capsules gain minor weight during experiments by diffusion of Ni-metal (from vessels and filler rods) into the precious metal capsules; none of the experimental products reported here, however, suffered contamination by Ni.

Run Pathways. Forward-direction experiments (prograde to run temperatures of 700 to 900°C, designated as “F” in Table 2-4) promoted simultaneous melting and new crystal growth. Reverse-direction experiments (designated as “R” in Table 4) were preconditioned by melting at 50° to 150°C above the final T of the experiment, quenched

isobarically to room temperature, and then run up to final temperatures in the range of 675 to 800°C. These reverse-direction experiments induced crystal growth from melts that were substantially supersaturated in the components of the crystalline phases at the final run *T*.

ANALYTICAL METHODS

Experimental products were initially inspected optically, and then using back-scattered electron imaging (BSEI) and energy-dispersive X-ray analysis (EDXA). Evidence for water saturation of melts included free water within capsules, no adherence of the charge to clean capsule walls, vapor dimples on glass surfaces, the presence of vapor deposits, and analytical totals for glass analyses by electron microprobe being < 100%.

Quantitative Electron Probe Microanalysis (QEPMA)

All major and minor element oxide constituents of cordierite and glass products, except Li, Be, B, Rb and Cs, were analyzed using wavelength-dispersive spectroscopy on a Cameca SX-50 electron microprobe at the University of Oklahoma. Zn and P were excluded from analyses of Crd because preliminary analyses showed their contents were equal to, or below, detection thresholds (≤ 0.05 or 0.02 wt% oxides, respectively). QEPMA utilized crystalline and glass standards with TAP, PET, LIF, and layered composite PC1 diffraction devices. Operating conditions for hydrous glass analyses included a two-beam condition (2 nA and 20 nA regulated current) with a 20 μm spot size, in which Na and Al were analyzed first to inhibit beam-induced migration effects (Morgan and London 1996). Analyses of minerals were conducted at 20 nA, 20 kV and a spot size of 3 to 5 μm . Counting times for all elements varied between 20 and 30 seconds.

Data were reduced using PAP (Pouchou and Pichoir 1985) matrix correction routines. Detection levels, taken at 3σ above mean background, were < 500 ppm for most elements. Based on similar experiments, Be is not lost to the capsule metal (Evensen and Meeker 1997).

Images were acquired using both backscattered and secondary electron signals as 1024×1024 pixelized data. Micrographs were processed (following Russ 1999) using either a low-pass or low-strength median filter (neighborhood ranking) for despeckling of noise. Images that contained minor periodic (instrumental) noise were corrected using Fourier transform processing techniques.

Secondary Ion Mass Spectrometry

Samples were analysed by SIMS using a Cameca Instruments IMS 3f at the Arizona State University at Tempe, AZ. A mass filtered $^{16}\text{O}^-$ primary beam was accelerated through a potential of 12.5 kV, with a beam current of 1.0 nA. The focused spot size varied from 15 to 5 μm . Targets were mapped in advance and verified by mass imaging using a combination of ^7Li , ^9Be , ^{23}Na , ^{26}Mg , ^{27}Al , ^{41}K , and ^{56}Fe before analysis.

Sputtered secondary ions were accelerated through a potential of 4.5 kV. The interference of $^{27}\text{Al}^{3+}$ (8.99384 amu) on ^9Be (9.01219 amu) is the most important concern in SIMS microanalysis of Be. However, the yield of ^9Be ions was so much greater than the $^{27}\text{Al}^{3+}$ species that the interference was negligible; no correction was made for the contribution of Al. This is in agreement with the observation by Grew et al. (1998) that Al^{3+} does not significantly affect analysis when Be contents are greater than ~ 30 ppm. Individual analyses consisted of collecting intensities on the following sequence of isotopes: ^{30}Si , ^7Li , ^9Be , ^{11}B , ^{85}Rb , ^{133}Cs , ^{30}Si . Integration times were sufficiently long to

achieve a counting statistical precision of at least 3%. The count rates were normalized to that for Si and then to the silica abundance in the sample (derived from QEPMA).

Calibration factors derived from the standards above allowed the normalized count rates to be converted to absolute concentrations. Total internal and external precision (ICP) of BeO analyses of crystals and glass was < 3.9% (relative to absolute concentrations).

The standard working curve for secondary ion mass spectrometry (SIMS) was calibrated for the analysis of Li, Be, B, Rb and Cs using glass standards. Three synthetic Be-rich granitic glasses (containing 0.57, 1.1, or 3.3 wt% BeO) that were previously characterized (homogeneous by aqua regia ICP-AES, QEPMA, and SIMS: Evensen 1997) were used as standards for the analysis of experimental glasses. The glasses contained appreciable B, Li, Rb, and Cs (at concentrations far above those estimated for each element in unknowns) and therefore served as standards for those elements as well. All trace elements were further calibrated against NIST 610 glass, containing nominally ~500 ppm of the elements above (Pearce et al., 1997). Data were acquired in two sessions, 9 months apart. Between these sessions, the working curves (Figure 1) and SIMS results were very reproducible (± 0.4 to 2.2 % relative).

RESULTS

Assemblages & Textures of Run Products

Forward-Direction Experiments. For initially cordierite-free compositions taken to 700°C, the assemblage beryllian cordierite + beryl + biotite + magnetite + plagioclase + quartz is stable with melt (Table 2-4a; Figure 2-2b). As temperature increases, plagioclase and quartz disappear from the liquidus surface leaving BeCr₂ +

beryl + biotite + magnetite stable in melt from 750° to 850°C (Figure 2-2c). Although starting mixtures were intended to buffer the melt activity of Be by beryl saturation, in the higher *T* experiments using SP-Crd1-Be beryllium became sufficiently compatible in Crd to leave the beryl saturation surface producing only BeCrd. In these runs, beryl disappears between 800° and 850°C (in forward and reversed runs). In more Be-rich bulk compositions (Table 2-4a), beryl remains part of the assemblage BeCrd + beryl + biotite + magnetite + melt from 800° to 900°C. Biotite is lost between 850° and 900°C.

Beryllian cordierite forms coarse (15 to 200 μm), prismatic blocky crystals (Figure 2-2); some crystals contain small (~1 to 10 μm) inclusions of magnetite or biotite. Quartz, when present, occurs poikilitically within Be-Crd hosts (Figure 2-2b) and as equant to subhedral crystals in glass. Plagioclase exhibits albitic cores surrounded by euhedral rims of sodic andesine. Andesine also exists as coarse, solid blocky crystals that are somewhat skeletal in form; these are interpreted to have formed late in the crystallization sequence. Biotite exhibits recrystallization of relict crystals (euhedral at the fine scale) plus new crystal growth (coarse euhedra: 5 to 30 μm). The oxide phase in all runs forms equant euhedra (~ 1 to 20 μm), and ranges in chemistry from magnetite to titanomagnetite (EDXA). Residual phenakite is present in some assemblages though completely armored by new BeCrd or beryl, suggesting that it acted as a nucleation substrate, and possibly a nutrient source, for the host crystal. At temperatures of 750°C or less, mixtures with added beryl contain sub- to anhedral relict crystals, indicating partial dissolution, with or without fine new euhedral beryl crystals. At higher temperatures, all residual beryl is completely armored by new beryl and cordierite growth.

Reverse-Direction Experiments. Unlike products of the forward path, reversals to 700°C (Table 2-4b and c; Figure 2-2d) lack plagioclase and quartz but otherwise contain the same crystalline assemblage. Euhedral crystal morphology and chemical relations of glass (Table 2-4b and c) to melting minima (haplogranite, $Ab_{39}Or_{27}Qtz_{34}$: Tuttle & Bowen 1958; metapelite, $Ab_{30}Or_{15}Mus_{20}Qtz_{35}$: Icenhower and London 1995) suggest that quartz and plagioclase are stable at 700°C. Destruction of their nuclei at superliquidus temperatures (e.g., Lofgren 1983, Marsh 1995) likely inhibited their nucleation upon reversals. Similarly, beryl was found in forward experiments to 750°C, though reversed runs at 750°C lack beryl but produced cordierite + biotite + magnetite from melt. The same assemblage is present at 800°C (Figure 2-2e). The reversal run to 675°C (BeP-51), which utilized a K- and Al-rich starting composition contains cordierite + beryl + orthoclase + muscovite + corundum + magnetite in glass (Figure 2-2f).

Reverse-direction products are texturally similar to forward-direction products for most shared phases. Muscovite nucleates abundantly as small, fibrous crystals (Figures 2-2a & 2-2f). K-rich alkali feldspar occurs as very coarse crystals (pheno- to megacrysts: 40 to 280 μm) that host muscovite and corundum inclusions. Corundum occurs in composite hexagonal aggregates, faceted in form (Figure 2-2f), and as individual prisms (~ 1 to 8 μm) in glass.

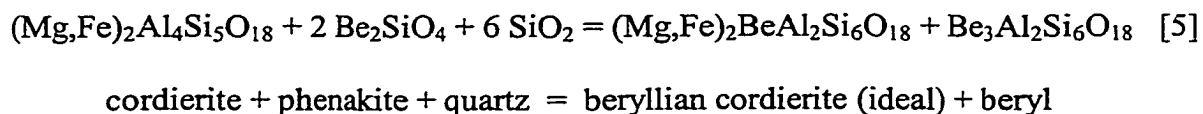
Unlike the coarse, consistently euhedral beryl of granitic experimental products from similar melts and conditions (cf. Evensen et al., 1999), beryl found in these experiments ranges from euhedral to faceted aggregates of fine-grained crystals (skeletal in macrocrystalline character). Thermal pathways within the stability field of beryl ($\leq 800^\circ\text{C}$) resulted in the growth of beryl with characteristic form. Run pathways that

thermally exceeded beryl stability and later returned to it, resulted in skeletal aggregates of beryl (Figure 2-3).

Cordierite – beryl aggregates nucleate on Be-cordierite and maintain topotaxial crystallographic relations of their host. Figure 2-3 shows that prismatic growth along [0001] continues through Crd-Brl contacts, as does growth along a-axes [1100](Figure 3). Topotaxial relations record the growth history and structural compatibility of (a) early, high-*T* Be-rich cordierite succeeded by later, beryl + cordierite with lower Be content (Figures 2-3b-d)

Figure 2-4 shows structural and chemical compatibility between cordierite and Be-minerals. Phenakite-bearing mixtures (Table 2-3) occasionally contained cores of relict phenakite in beryllian cordierite (Figure 2-4a). Experiment BeP-4 (Figure 2-4b) shows that seeded beryl (cf. “normal beryl”: Aurisicchio et al., 1988) in the starting mixture reacted to form Be-cordierite + FeMg-beryl (cf. “femag-beryl”: Schaller et al., 1962). Both products nucleate on the relict beryl substrate.

Cordierite-Bearing Experiments. In forward runs that contained cordierite in their starting mixtures (Figure 2-4c & d), relict cordierite is rimmed by overgrowths of new Be-cordierite (1 to 20 μm) or beryl (3 to 75 μm). Beryllian cordierite only nucleates on the cordierite substrate, while beryl additionally occurs as individual crystals in glass. In all cases, Crd is completely armored, showing it is a suitable substrate for BeCrd growth. Relict anhedral phenakite (5 to 75 μm) remains unarmored in melt, which suggests the overall reaction,



Relict cordierite shows embayed edges, indicative of dissolution, which are overprinted by thin overgrowths of Be-cordierite, suggesting the compositional stability of Be-Crd, instead of Crd, in the presence of beryl.

Compositions of Run Products

Melt chemistry. Even when only beryllian cordierite is stable without beryl (Table 2-4a and b), the BeO contents of melt are close to (slightly below) those of beryl saturation at similar ASI values of melt (Figure 2-5). Melt contents of BeO increase with T from 420 to 2620 ppm going from 675 to 850°C.

Be-Cordierite Chemistry. Beryllium contents of Crd increase linearly with increasing T from 1.01 to ~ 3.97 wt% BeO (Table 2-4a and b). These values are equivalent to, or greater than, those reported from natural assemblages (e.g., 0.4 to 2.0 wt% BeO: Gordillo et al., Armbruster and Irouschek 1982, Černý and Povondra 1966). At 850°C, BeO contents of 3.97 wt% are not far from the synthetic value of ~ 4.40 wt% (1.0 Be pfu by XRD: Hölscher and Schreyer 1989). With increasing T between 675 and 900°C, SiO₂ and MgO contents increase markedly (from 48.67 to 61.53 wt% and from 8.86 to ~11.00 wt%, respectively). Consequently, the Mg# [mol MgO/(MgO+FeO)] increases for Be-Crd (from 66.7 to ~85.0) over this range of T . Increases are observed for channel components K (from 0.29 to 1.05 wt% K₂O) and Cs (Table 2-4a and b) as well.

Concentrations of Al₂O₃ (from 30.23-16.59 wt%), FeO (7.22 to ~3.00 wt%), MnO (~ 0.79 to 0.21 wt%), Ca (0.47 to 0.08 wt% CaO) and Na (1.20 to 0.66 wt% Na₂O) increase with T over the interval of 675 to 850°C. Lithium decreases from 675 to 850°C (213 to 79 ppm Li₂O), whereas B and Rb contents remain approximately constant with

mean values of 5.2 ppm (B_2O_3) and ~ 38 ppm (Rb_2O). Ba and the halogens F and Cl seem to be negligible constituents in Crd, each near or below its detection limit by QEPMA. Zinc and P were also below detectable levels (see Analytical Methods).

Beryl Chemistry. Compositions of beryl that coexist with beryllian cordierite are reported in Table 2-5a. Going from 675° to 900°C, the main elemental variations away from stoichiometry include decreasing alumina (~17.26 to 15.85 wt%) decreasing Be contents (~12.02-10.69 wt% oxide by difference) and increasing silica (~66.56-68.11 wt%) and alkali contents. Among the alkalis, Na dominates from 675 to 750°C, Na and K contents are equivalent at 800°C, and K dominates at higher temperatures. Magnesium contents are either greater than, or roughly equivalent to iron contents.

DISCUSSION

Compositional Differences Between Cordierite and Be-Cordierite

Comparison of Be-Crd to Crd (Table 2-4c) utilized representative compositions from experiments containing no added Be-mineral (only trace quantities were liberated from starting white mica). Though the occupancy of the tetrahedral sites is predictably different, a similar variation in Mg# of both structures with T suggests that increasing Be contents does not appear to influence octahedral site-filling—in these products or in nature (Gordillo et al., 1985). Quantities of tetrahedral constituents typify Crd (Table 2-4c) and at the same time illustrate the extreme influence of Be on alumina and silica contents in Be-Crd. Channel Ca is equivalent in concentration between both structures, yet Li and Na contents of Be-Crd are about twice that seen in Crd grown from Be-poor conditions. Rubidium is greater in abundance in Be-Crd than in Crd by about a factor of

2.5. Potassium and Cs are notably greater in concentration in Be-Crd versus Crd. Channel water contents are similar.

Crystal Chemistry of Beryllian Cordierite

As temperature increases, the total tetrahedral and octahedral cations of cordierite maintain a sum of ~ 9.0 and ~ 2.0 , respectively (Table 2-4a and b). All the while, total channel alkali and H₂O contents decrease. These compositions are plotted in Figure 2-6, in which the sloped line marks ideal site-filling behavior. All cordierite compositions exhibit total occupancy, with most cation sums falling within propagated error.

The crystal chemistry of Be-cordierite is rather sensitive to temperature. Figure 2-7 illustrates appreciable changes as a function of temperature. In the *T1* and *T2* environments, Be and Si occupancy rises sharply with *T* while Al occupancy falls. In the channel environment, K contents increase regularly while Na and H₂O occupancy steadily decrease. Channel concentrations of Ca fall slightly with *T*. At the *M* site, Fe contents decrease in a concave pattern while Mg contents increase with a reciprocal convex trend, compensating for one another.

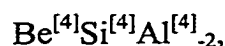
Tetrahedral Occupancy: The T-Dependent (Si,Na)Be = Al Exchange. When taken together, Be, Al and Si exhibit ideal tetrahedral occupancy (Figure 2-8). Yet Be accounts for Al deficiency (from 4.0 apfu) only in part: excess Si makes up the remainder. As *T* increases, cordierite formulae increase with BeSiAl₂ exchange.

Figure 2-9 illustrates that Be contents of Crd cannot be accounted for simply by the exchange operator, Be(Na,K)Al₁. Only cordierite from one experiment, BeP-41 (700°C, Table 3b), is adequately represented by this exchange (Al loss is accounted for solely by Be(Na,K)Al₁). All other cordierite products require a contribution by Si to

account for incorporated Be. This relationship is best illustrated by the sum of Al+Be+excess Si among cordierites grown (forward and reverse) over this range of temperature: their regression has no slope ($=10^{-5}T$) and an intercept at 4.0 apfu (Figure 2-9). Because the magnitude of excess Si to Na+K contents changes with T , the nature of Be exchange into Crd is an interplay of two mechanisms. The exchange lies between the binary exchanges,



and



which vary inversely with temperature (Figure 2-10). Alkali and silicon contributions are roughly equivalent between 750-800°C, but vary at higher and lower temperatures.

Figure 2-11 illustrates the T -dependent progression from (1) alkali -dominated to (2) mixed exchange then toward (3) silicon-dominated exchange for Be-cordierite. Natural compositions of cordierite fit among the high temperature (e.g., BeSi-Crd in granulites: Baba et al., 2000) and low temperature (e.g., BeNa-Crd in pegmatites) results of this study. Whereas the bulk beryllium-related chemistry of any cordierite is sufficiently represented using a combined term (i.e., $\text{Na}_x\text{Be}_{x+y}\text{Si}_y\text{Al}_{-(x+2y)}$: Baba et al., 2000), representation of exchange mechanisms may be separated because BeSiAl_2 and BeNaAl_1 operate independently.

Octahedral Occupancy. Lithium enters the Crd structure via

$\text{Na}^{[\text{ch}]}\text{Li}^{[6]}(\text{Mg,Fe})^{[6]}_{-1}$ in natural (Armbruster and Irouschek 1983, Gordillo et al., 1985, Černý et al., 1997) and experimental cordierite (Kirchner et al., 1984). The octahedral environment of Be-Crd, specifically Mg, Fe, and Mn contents, appears to be unaffected

by Be incorporation (see *M* site totals, Table 4). Beryllian cordierite, however, incorporates $\geq 50\%$ more Li than Be-poor cordierite, which grew from otherwise identical magmatic conditions. This raises the question, why?

Natural Li-rich cordierite occurs in either pegmatite, which likely crystallized at low-*T* following undercooling, or among low-*T* metamorphic regimes (e.g., peak temperatures of 600-650°C at 500-700 MPa: Armbruster and Irouschek 1984). A parallel observation is that alkali contents among cordierite (e.g., Mirward 1986; Kalt et al., 1998) and beryl (e.g., Černý and Turnock 1975) increase with decreasing *T* at the conditions which pegmatitic melts solidify (e.g., London 1992). Most Li-bearing Crd is thus, expectedly alkali-rich (e.g., Armbruster and Irouschek 1983; Gordillo et al., 1985; Černý et al., 1997). Because BeCrd in the current experiments contains about twice the contents of Na and K as the Be-poor Crd products, the presence of increased alkali content is likely to facilitate more Li incorporation than would otherwise exist—a function of Be exchange of the form NaLiR^{2+}_{-1} (Gordillo et al., 1985). This interpretation is supported by Černý et al. (1997), who were also unable to correlate Li with Be, though they noted that Be + Li contents correlated with Na concentrations.

Channel Occupancy. In the current experiments, water dominates channel occupancy but its abundance decreases with *T* (Figure 2-12a). Potassium contents increase with *T* (Figure 2-12b), whereas sodium contents decrease—a pattern similar to natural, K-rich, high-*T* cordierite (e.g., Schreyer et al., 1990). The alkalis Na, K, Rb, and Cs, however, also show increased abundances (2 to 5 times) going from Crd to BeCrd. Tetrahedral Be thus effects the channel geometry of Crd to better accommodate the alkalis. If Be distorts BeO_4 tetrahedra in beryllian cordierite as observed in beryl (e.g.,

Hawthorne and Černý 1977), then increasing the Be content (and field strength compared to Al) at $T1$ sites in Crd may effect the overall shape of the channels. Widening channel width in BeCrd likely facilitates an increase in the compatibility of Cs. Higher temperature crystallization favors higher contents of K, Rb, and Cs in Be-Crd (Table 2-4, see Figure 2-13b). Increasing temperature (e.g., Hochella and Brown 1986) and increasing contents of larger channel alkalis (e.g., Daniels 1992) have been shown to promote symmetry and Al/Si disorder, which occurs fully upon going from cordierite to indialite (e.g., Armbruster and Bloss 1981; Selregg and Bloss 1980). In addition, as K content increases in natural Crd, it exhibits lower distortion indices and more favorable kinetics toward a hexagonal geometry (Schreyer et al, 1990). Our Be-cordierite products trend toward $(\text{Mg,Fe})_2\text{BeAl}_2\text{Si}_6\text{O}_{18}$ as T increases, approaching the hexagonal Be-cordierite $\text{Mg}_2\text{BeAl}_2\text{Si}_6\text{O}_{18}$ (Hölscher and Schreyer 1989). Thus, Al/Si ought to exhibit notable disorder in this structure relative to cordierite.

Geothermometry. The concentrations of H_2O and Na in Crd channels have been used as geothermometers because of a recognized correlation with temperature (Mirwald 1986, Kalt et al., 1998). These may be applicable to Be-poor Crd, but clearly the chemistry of channel and tetrahedral sites becomes more complexly interrelated when Be is a significant component. With the compositional variations evident in these experiments, we have regressed each compositional variable (Na, K, Be, Al, and $\text{Si}_{\text{excess}}$) with respect to T , and have then calculated temperatures of crystallization for Be-Crd found in natural environments (Table 2-6). Temperatures calculated based on tetrahedral occupancy converge to a common T , whereas alkalis do not.

Elemental Partitioning Between Be-Cordierite and Melt

Partition coefficients of elements between Crd and melt ($D_x^{\text{mineral/melt}} = [X]_{\text{mineral}} / [X]_{\text{melt}}$; after Beatie et al., 1993) differ from those of Be-Crd and melt (Table 2-7, Figure 2-13), particularly in the case of Be ($D_{\text{Be}}^{\text{Crd/melt}} = \sim 200$ at 700°C: Evensen and London 1999b). A parallel study to this work at low concentrations of Be has been completed for cordierite (Evensen and London, in review, 2000) and suggests that for nearly all (low Be) crustal applications, partitioning ratios of cordierite should be taken from Evensen and London (1999a, 1999b).

Uptake of Li, Be, Mn and Cs by Cordierite. The significant trace elements that are hosted by Be-cordierite appear to be Li, Mn, and Cs, among which Li is the only completely incompatible component. Partitioning efficiency of each element can be assessed by Figure 2-14, which shows element contents of melt vs. coexisting cordierite; in all plots, temperature also increases from left to right for BeO, MnO and Cs₂O. Beryllia, Li₂O and Cs₂O trends covary in their contents in cordierite and melt. Contents of MnO in cordierite decrease with increasing MnO concentrations in melt, probably because of controls on the octahedral site with increasing T (Mg # increases with T) and prograde solubility in melt (similarly for Mg and Fe), leaving Mn far less compatible at 850 than 700°C. Multiple linear regressions on the Be, Cs, and Mn contents of cordierite, respectively, over T and melt concentration result in better fits (significantly increased r^2 values) than using linear regressions melt concentrations alone. Increasing or decreasing contents of these elements in the Be-cordierite structure are thus more dependent on temperature than on their abundance in melt (Figure 2-13b). Lithium contents of Be-cordierite, however, appear to be T -independent: increasing melt concentrations of Li₂O

coincide with increases in Li content in BeCr_d, but not all the data can be described in this manner (note the poor correlation, Figure 2-3b).

Other compatible elements. Manganese and Cs behave compatibly in beryllian cordierite (Figure 2-13a and b, Table 2-7), decreasing from $D \sim 10.67$ to 1.25 and increasing from $D = 0.64$ to 1.28, respectively, going from 675 to 850°C. Cesium becomes compatible in beryllian cordierite above 750°C. Compared to Cr_d, increases in D values for Mn and Cs reveal that these elements are more compatible in the BeCr_d structure than in Be-poor Cr_d. The slight decrease of D values for essential Be likely stems from the prograde solubility of Be-Cr_d (and Br_l).

Other incompatible elements. Boron is distributed similarly between melt and either Be-Cr_d or Cr_d (Figure 2-12, Table 2-4). Lithium shows roughly constant behavior over T ($D_{\text{Li}}^{\text{Cr}_d/\text{MELT}} = 0.40$). Calcium partitions into Be-Cr_d by a factor of two higher than Cr_d; rubidium partitioning mildly increases in Be-Cr_d.

Compositional Differences of Beryl in FeMg-Poor vs. -Rich Melts

Comparison of beryl compositions grown from haplogranite melts (Table 2-5b) versus those grown at the cordierite – beryl equilibrium in peraluminous granitic melts (Table 2-5a) indicate that simple differences distinguish the populations. Beyond the anticipated greater octahedral contents of R^{2+} in beryl grown from Mg- and Fe-rich liquids, tetrahedral differences also are seen. Compared to nominal beryl, FeMg-beryl in this study contains less Be, less Al, and more Si, each decreasing or increasing further with T .

Crystal Chemistry of (FeMg-) Beryl

Despite excess occupancy of octahedral components, recalculated formulas of all beryl products fall just short of ideal occupancy (Figure 2-16). This originates from low Be at the *T1* site, which decreases at twice the rate that excess Si increases in *T1*. Going from 675 to 900°C, Si, Fe, and K contents increase readily while Al contents fall (Table 2-5a). Figure 2-15 shows the variations of beryl constituents with temperature.

Octahedral Occupancy. Iron and magnesium contents reach a maximum sum of 0.43 R^{2+} in beryl formulae, occupying less than one quarter of the M site. This maximum is proximal to the upper range found in natural beryl ($\Sigma R^{2+} \sim 0.5$; obtained from Schaller et al., 1962, and the mean of the 4 upper values, 0.52, from Aurisicchio et al., 1988). Mean proportional octahedral occupancy is plotted in Figure 2-17 as a function of *T*. Mg and Fe contents of Brl show stay roughly constant with *T* (Figures 2-15 and 2-17; see Figure 2-24); although, correlations were found between Mg and Na, and Fe and K, suggesting coupled substitution (note graphical similarities in Figure 2-15). Two lines of evidence suggest R^{2+} valence in beryl. First, crystalline assemblages and the oxygen fugacities of melt at run conditions (\sim NNO, see Experimental Methods) indicate that Fe was predominantly restricted to the ferrous state. Second, high degrees of correlation among cation occupants were found between Mg and Na ($r = +0.980$) and Fe and Na ($r = +0.916$), as well as Mg and Al ($r = -0.878$) and Fe and Al ($r = -0.923$), and lastly Na and Al ($r = -0.878$). Together, these affinities point toward the octahedral exchange in beryl,



In this exchange, charge-balancing Na participates more often than K, and high contents of channel K typically are found with high contents of ferrous iron, i.e., by way of

KFeAl₁ (similar to Crd: cf. Geiger et al., 2000). Substitutions of this general form also occur in natural beryl (e.g., Aurisicchio et al., 1988).

Tetrahedral Occupancy. Total tetrahedral site filling is shown in Figure 2-18. Going from 700° to 900°C, three patterns are observed: (1) loss of Be, (2) a lesser increase in Si, and (3) a slight decline in excess Al^[6]. A high negative correlation coefficient (-0.845) suggests Si substitution involving Be; yet, neither Si nor Be seem to be correlated with Al content.

Excess Si (beyond 6.0 apfu in T2 sites) is interpreted to fill the T1 sites of Be, which requires facilitation by octahedral constituents. Excess occupancy in the octahedra likely contributes toward tetrahedral deficiencies, as seen in natural high-Crd (Schreyer et al., 1990). Despite the contribution from octahedral cations (particularly Fe²⁺, as in Crd: Geiger et al., 2000), deficiencies in the T1 site remain, varying from 0.03 to 0.27. Residual deficiencies are equivalent to the excess contents of Si (Figure 19), supporting the exchange



that produces a vacancy at T1 sites. This mechanism accounts for low total occupancy in T1 sites, and formula totals (Figure 16).

Bond angles in the beryl structure indicate a clear preference by Be for T1 over T2 geometries (e.g., Downs and Gibbs 1981). As octahedral Al³⁺ is replaced by larger Mg²⁺ or Fe²⁺ (each coupled with channel alkalis), the coordination octahedron must increase in size: approximately from 0.54 to 0.72 (Mg) or 0.78 Å (Fe) (Shannon and Prewitt 1969). Such a shift reduces the distortion in the BeO₄ group (Aurisicchio et al., 1988) thus widening the TOT bond, and thereby producing an unfavorable environment for Be

occupancy (e.g., Downs and Gibbs 1981) compared to Si. According to this exchange, the resulting larger TOT angles likely mandate a preference for Si coordination over Be, resulting in incomplete filling at the Be site—a new tetrahedral vector for beryl compositions.

Channel Occupancy. Potassium increases in content, regularly, from 700 to 900°C, following the pattern of channel occupancies of K (e.g., Schreyer et al., 1990) or even Cs (e.g., Daniels 1992) in high-Crd. Mean variations in alkali content with *T* are shown in Figure 20.

CONCLUSIONS

Solid Solution From Cordierite to Beryl

Written from cordierite, the total mass-balance exchange operator that links cordierite to beryl is



Here, the (site-independent) operation represents a combination of three site-specific exchanges that are evidenced by the chemistry of our run products. Namely, Be-Crd compositions show the extensive occurrence of



(from 0.25 to 1.0 Be apfu), more so than any other operator, going from 675 to 900°C.

Subtracting that operator from [6], it leaves the overall exchange $\text{Be}^{[4]}\text{Mg}^{[6]}_{-1}\text{Fe}^{[6]}_{-1}$, which is a sum of the site-specific exchanges



and



The first of these is observed to a small degree for cordierite; the second is observed at about twice that degree for beryl. Again, if the Al- and Na-facilitated exchanges operating in opposite directions are combined, the site-dependent constituents cancel to leave $\text{Be}^{[4]}(\text{Mg,Fe})^{[6]}_{-1}$, a site-independent representation of the theoretical crux of Crd – Brl chemical solid solution.

Five total operations among three site-specific exchange operators are required to chemically link Crd and Brl: 1 of $\text{Be}^{[4]}\text{Si}^{[4]}\text{Al}^{[4]}_{-2}$, 2 of $\text{Be}^{[4]}\text{Na}^{[\text{ch}]}\text{Al}^{[4]}_{-1}$, and 2 of $\text{Al}^{[6]}(\text{Mg,Fe})^{[6]}_{-1}\text{Na}^{[\text{ch}]}$. Of these, maxima of 1.0 BeSiAl_2 and ~ 0.25 BeNaAl_1 are seen occurring in Crd, with ~ 0.5 $\text{Al}(\text{Mg,Fe})_{-1}\text{Na}_1$ found in Brl. While maximum values of BeSiAl_2 (Crd) and $\text{Al}(\text{Mg,Fe})_{-1}\text{Na}_1$ (Brl) are seen at the highest T investigated, 850°C, the greatest extent of BeNaAl_1 exchange occurs at the lowest T studied, 675°C. Of five numerical operations needed for stoichiometric exchange, our findings indicate that about 2 occur going from 675-900°C at 200 MPa in granitic melts. However, our observation that the exchange,



increases with increasing T in beryl suggests that a limit of solution exists at some higher T . This is evidenced by the exchange leading Brl compositions off the cordierite – beryl join, acting to deteriorate, and ultimately alter the crystal structure.

Cordierite – Beryl Equilibrium Relations

In this study, the coexistence of beryl and beryllian cordierite in melt was observed between 675 to 900°C (along with $\text{Bt} + \text{Mt} \pm \text{Pl} \pm \text{Qtz} \pm \text{Mus} \pm \text{Or} \pm \text{Cor}$). Immiscibility between BeCrd and Brl is evidenced in the textures of reversed products

(Figures 2-2, 2-3, and 2-4), which show growth of a single phase followed at lower T by simultaneous growth of BeCrd and Brl. Continuous solid solution of dominantly BeSiAl_2 and minor BeNaAl_1 [with simultaneous contributions by $\text{Al}(\text{Mg,Fe}^{2+})_{-1}\text{Na}_{-1}$ in Brl] takes cordierite all the way to hexagonal $\text{Mg}_2\text{BeAl}_2\text{Si}_6\text{O}_{18}$.

The binary phase relations, projected from water saturation at 200 MPa indeed reveal a two crystalline phase solvus, in which BeCrd and Brl coexist with melt. Figure 21 casts the solution as an approximated function of Be content. Because some experimental products contained inadequate BeO in melt to remain on the BeCrd – Brl solvus, these contain BeCrd solid solution only (Table 2-4). Although projected BeO was found to be the single most useful indicator for Crd to Brl relations, and it generally depicts the shape of miscibility relations, it fails to represent the complete multicomponent exchange. Figure 22 reveals the complete equilibria between cordierite and beryl using the fictive component $\text{Be}_3\text{SiAl}_2\text{Mg}_{-1}\text{Fe}_{-1}$, which is comprised of two Be-coupled exchanges involving $T1$ and $T2$ sites ([7] and [8]), with NaAl-coupled exchange at the M site ([9]). Figure 23 plots tie lines between cordierite and beryl in their compositional space and shows the direction of their mutual chemical evolution upon cooling.

Of the limited studies of beryllian cordierite that document its natural assemblage, nearly all support the coexistence of beryllian cordierite with beryl in pegmatites (Table 8). Furthermore, previous studies have described heterogeneous nucleation relations between *primary* beryl and beryllian cordierite similar to relations found here (e.g., Gordillo et al., 1985; Jobin-Bevans and Černý 1998). Povondra and others (1978) described intergrowths of BeCrd + Brl in which the orientation of c axes were mutually

parallel—a texture reminiscent of the inherited crystal structures seen in this study. Though these authors described that beryl as the product of alteration, we suggest the possibility that the BeCrd + Brl pegmatitic assemblage is primary, originating from melt.

The Cordierite Reservoir of Li, Be, Mn and Cs

During anatexis, residual cordierite ought to sequester Be, Mn, and Cs, and to a lesser degree, Li from melt. If cordierite is stabilized in evolved magmas, it will act as a sink, tying up these elements. With increasing Be content in pegmatitic cordierite, increasing uptake of Mn, Cs and Li occurs from melt. Lithium contents are not directly sequestered, but coupled with alkali concentrations that are higher in Be-Crd over Crd.

Should cordierite-forming reactions occur during the lifetime of a granitic magma, melt contents of these constituents should fall appreciably. In contrast, if cordierite-melting or decomposition reactions occur, cordierite ought to contribute potentially high contents of Li, Be, Mn and Cs to melt. From anatectic source rock to the emplacement of pegmatites, the magmatic budgets of these elements may be affected greatly by the presence or absence of cordierite. In particular, cordierite is critical for bulk signatures of Be and Cs, as no other rock-forming mineral partitions these elements to this extent. At a lesser level, cordierite probably regulates mineral-melt budgets of Mn and Li, if their saturating phases (or micas in the case of Li) are absent. Altogether, the role of cordierite as a light and large-ion lithophile element sink in magmas becomes noteworthy for interpreting the signatures and geochemical budgets of mid- to shallow crustal aluminous rocks.

Petrogenesis of Beryllian Cordierite

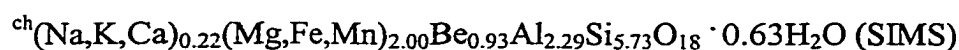
Although BeSiAl_2 is the primary vehicle for Crd – Brl solid solution, natural occurrences of NaBe-cordierite are far greater than BeSi-cordierite. This follows from the (undercooled) pegmatite environments in which NaBe-cordierite occurs; or alternately, from the difficulty of concentrating enough Be in melt to saturate in Be-Crd at the higher temperatures in which the Si-exchange dominates. Under our experimental conditions, melt contents of BeO must reach 2620 ppm BeO for Be-cordierite to crystallize at 850°C. If a melt contains fluxing components that structurally associate with aluminum in melt (e.g., P and F: Manning et al., 1980; Mysen and Virgo 1985; Gan and Hess 1989), then saturation requirements become greater for Be-cordierite according to the activity product,

$$\begin{array}{ccc} [a_{(\text{Mg})_2\text{BeAl}_2\text{Si}_6\text{O}_{18}}] & = & [a_{\text{MgO}}]^2 [a_{\text{BeO}}] [a_{\text{Al}_2\text{O}_3}] [a_{\text{SiO}_2}]^6 \\ \text{Be-cordierite} & & \text{melt} \end{array}$$

Relevant granitic compositions for Be-cordierite production are quartz-saturated or nearly so, relatively fixing the activity of silica. According to the relation above, as the activity of alumina increases, the beryllia requirements for saturation in Be-cordierite fall. Similar relationships were found for beryl (Evensen et al., 1999) where beryl crystallization was most readily achieved in low- T peraluminous haplogranite melt. Further, the T -dependent nature of the beryllian cordierite saturation surface indicates that although thorough fractionations are required for magmas at high T to achieve Be-Crd saturation (2620 ppm BeO at 850°C vs. 420 ppm at 675°C), liquidus (or solidus) undercooling allow for crystallization at low temperatures.

A trend of decreasing temperature is shown for experimental and reported Be-cordierite compositions (in Figure 2-24). Cooling relations are revealed using this plot because these components vary with T at their crystallographic sites. Beryl compositions trend directly away from the cordierite field with decreasing T . Cordierite compositions form a curving trend upon cooling, implying that populations of natural NaBe-cordierite arise from low- T parageneses—lower in T than the conditions of our investigations. Should further studies show that Be-cordierite chemistry behaves similarly at higher P , then geothermometry may help constrain the thermal history of applicable assemblages.

The most beryllian cordierite found in this study (at 850°C), has the formula



It is probable that about one stoichiometric BeSiAl_2 operation is the structural limit for cordierite, although the current experiments cannot confirm that hypothesis over a range of isobaric conditions. Hölscher and Schreyer (1989) showed that BeCrd forms upon isochemical breakdown of surinamite ($\text{Mg}_3\text{Al}_4\text{BeSi}_3\text{O}_{15}$). Figure 2-24 demonstrates that our data support similar reaction relationships, which may also include $\text{BeCrd} + \text{Brl}$ decomposition to assemblages also containing musgravite ($\text{Mg}_2\text{BeAl}_6\text{O}_{12}$; Schmetzer 1983) or taaffeite ($\text{Mg}_3\text{BeAl}_8\text{O}_{16}$) and Be-rich sapphirine (Grew 1998). Possible parageneses are suggested because taaffeite (or musgravite), Be- sapphirine, surinamite, and higher- T Be-cordierite occur along a line of roughly equivalent mole fraction Be.

From the deep to shallow crust, potential breakdown of surinamite and taaffeite (or musgravite) may back-react to form Be-cordierite. Restitic Be-cordierite could recrystallize to metamorphic surinamite, beryllian sapphirine, musgravite, etc. Parageneses among these phases, for which stabilities span from low to high P conditions

(e.g., BeCrd vs. surinamite), are far more common in metamorphic regimes from which such assemblages have been reported (e.g., Hölscher et al., 1986; Grew 1998; Woodford and Wilson 1976, Grew 1981, Franz and Morteani 1984, de Roever and Vrána 1985). A surinamite-bearing granulite assemblage recently was interpreted in a similar fashion by Baba and others (2000), who suggested that cordierite was a participant in both prograde and retrograde reaction of Be-minerals.

Experimental (Evensen et al., 1999), pegmatitic (e.g., Černý 1991), and post-eruptive devitrification (vapor-rich) occurrences of beryl (e.g., Christiansen et al., 1997, Della Ventura et al., 2000) point toward crystallization scenarios under rapidly cooling subsolidus conditions. Similarly, the crystallization of Be-Crd most likely occurs in evolved and substantially undercooled peraluminous granitic melts, probably with Mg-Fe infiltration from host rocks. Because beryl-bearing assemblages are common among pegmatite populations (e.g., Černý 1991) the Be contents of melt increase sufficiently during the late stages of evolution in many pegmatite magmas to achieve beryl-saturation. At some point, BeO quantities in these melts will surpass saturation requirements of Be-cordierite. Beyond this stage, so long as FeO and MgO contents remain adequate (e.g., and are not consumed by tourmaline: Wolf and London 1997), beryllian cordierite and beryl will crystallize as solvus pairs—their compositions reflecting the temperature of crystallization.

References Cited

- Aines, R.D. and Rossman, G.R. (1985) The high temperature behavior of trace hydrous components in silicate minerals. *American Mineralogist*, 70, 1169-1176.
- Armbruster, T. and Bloss, F.D. (1981) Mg-cordierites: Si/Al ordering, optical properties, and distortion. *Contributions to Mineralogy and Petrology*, 77, 332-336.
- Armbruster, T. and Irouschek, A. (1983) Cordierites from the Lepontine Alps: Na+Be→Al substitution, gas content, cell parameters, and optics. *Contributions to Mineralogy and Petrology*, 82, 389-396.
- Armbruster, T. and Bloss, F.D. (1982) Orientation and effects of channel H₂O and CO₂ in cordierites. *American Mineralogist*, 67, 284-291.
- Auricchio, C., Fioravanti, G., Grubessi, O., and Zanazzi, P.F. (1988) Reappraisal of the crystal chemistry of beryl. *American Mineralogist*, 73, 826-837.
- Auricchio, C., Grubessi, O., and Zecchini, P. (1994) Infrared spectroscopy and crystal chemistry of the beryl group. *Canadian Mineralogist*, 32, 55-68.
- Baba, S., Grew, E.S., Shearer, C.K., and Sheraton, J.W. (2000) Surinamite, a high-temperature metamorphic berylosilicate from Lewisian sapphirine-bearing kyanite- orthopyroxene-quartz-potassium feldspar gneiss at South Harris, N.W. Scotland. *American Mineralogist* 85, 1474-1484.
- Barton, M.D. (1986) Phase equilibria and thermodynamic properties of minerals in the BeO-Al₂O₃-SiO₂-H₂O (BASH) system , with petrologic applications. *American Mineralogist*, 71, 277-300.
- Beattie, P., Drake, M., Jones, J., Leeman, W., Longhi, J., McKay, G., Nielsen, R.,

- Herbert, P., Shaw, D., Takahashi, E., and Watson, B. (1993) Terminology for trace element partitioning. *Geochimica et Cosmochimica Acta*, 57, 1605-1606.
- Beltrame, R.J., Norman, D.I., Alexander, E.C., and Sawkins, F.J. (1976) Volatiles released by step-heating a cordierite to 1200°C. *Transactions of the American Geophysical Union*, 57, 352.
- Boberski, C., and Schreyer, W. (1990) Synthesis and water contents of Fe²⁺-bearing cordierites. *European Journal of Mineralogy*, 2, 565-584.
- Černý, P. (1991) Rare element granitic pegmatites. Part 1: anatomy and internal evolution of pegmatite deposits. *Geoscience Canada*, 18, 49-67.
- Černý, P. and Povondra, P. (1966) Beryllian cordierite from Vezna: (Na+K)+Be→Al. *Neues Jahrbuch für Mineralogie, Monatshefte* (1966), 36-44.
- Černý, P., and Turnock, C. (1975) Beryl from the granitic pegmatites at Greer Lake, southeastern Manitoba. *Canadian Mineralogist*, 13, 55-61.
- Černý, P., Chapman, R., Schreyer, W., Ottolini, L., Bottazzi, P., and McCammon, C.A. (1997) Lithium in sekaninaite from the type locality, Dolní Bory, Czech Republic. *Canadian Mineralogist*, 35, 167-173.
- Clarke, D.B. (1995) Cordierite in felsic igneous rocks: a synthesis. *Mineralogical Magazine*, 59, 311-325.
- Clemens, J.D., and Wall, V.J. (1988) Controls on the mineralogy of S-type volcanic and plutonic rocks. *Lithos*, 21, 53-66.
- Cohen, J.P., Ross, F.K., and Gibbs, G.V. (1977) An X-ray and neutron diffraction study of hydrous low cordierite. *American Mineralogist*, 62, 67-78.

- Damon, P.E., and Kulp, J.L. (1958) Excess helium and argon in beryl and other minerals. *American Mineralogist*, 43, 433-459.
- Daniels, P. (1992) Structural effects of the incorporation of large-radius alkalis in high cordierite. *American Mineralogist*, 77, 407-411.
- Della Ventura, G., Rossi, P., Parodi, G.C., Mottana, A., Raudsepp, M., and Prencipe, M. (2000) Stoppaniite, $(\text{Fe,Al,Mg})_4(\text{Be}_6\text{Si}_{12}\text{O}_{36}) \cdot (\text{H}_2\text{O})_2(\text{Na},\square)$ a new mineral of the beryl group from Latium (Italy). *European Journal of Mineralogy*, 12, 121-127.
- de Roever, E.W.F., and Vrána, S. (1985) Surinamite in pseudomorphs after cordierite in polymetamorphic granulites from Zambia. *American Mineralogist*, 70, 710-713.
- Downs, J.W., and Gibbs, G.V. (1981) The role of the BeOSi bond in the structures of beryllosilicate minerals. *American Mineralogist*, 66, 819-826.
- Evensen, J.M. (1997) Effects of beryllium on the liquidus phase relations of haplogranite. Colorado School of Mines, Golden, Colorado. MS Thesis, 92 p.
- Evensen, J.M., and Meeker, G.P. (1997) Feasibility of Be analysis for geologic materials using EPMA. *Microscopy Society of America, Proceedings: Microscopy and Microanalysis 1997*, 3 (2), 893-894.
- Evensen, J.M., & London, D. (1999a) Beryllium budgets in granitic magmas: Consequences of early cordierite for late beryl. *Canadian Mineralogist*, 37 (3), 821-823.
- Evensen, J.M., & London, D. (1999b) Beryllium reservoirs and sources for granitic melts: The significance of cordierite. *Geological Society of America, Abstracts with Programs*, 31 (7), A-305.
- Evensen, J.M., London, D., and Wendlandt, R.F. (1999) Solubility and stability of beryl

- in granitic melts. *American Mineralogist*, 84, 733-745.
- Ferraris, G., Prencipe, M., and Rossi, P. (1998) Stoppaniite, a new member of the beryl group: crystal structure and crystal-chemical implications. *European Journal of Mineralogy*, 10, 491-496.
- Franz, G., and Morteani, G. (1984) The formation of chrysoberyl in metamorphosed pegmatites. *Journal of Petrology*, 25, 27-52.
- Gan, H. and Hess, P.C. (1989) Phosphorus effects upon the structure of potassium aluminosilicate glass: inference from Raman and NMR. *Transactions of the American Geophysical Union (Eos)*, 70, 1375.
- Geiger, C.A., Armbruster, T., Khomenko, V., and Quartieri, S. (2000) Cordierite I: The coordination of Fe²⁺. *American Mineralogist*, 85, 1255-1264.
- Gibbs, G.V. (1966) The polymorphism of cordierite I: the crystal structure of low cordierite. *American Mineralogist*, 51, 1068-1087.
- Gordillo, C.E., Schreyer, W., Werding, G., and Abraham, K. (1985) Lithium in NaBe-cordierites from El Peñón, Sierra de Córdoba, Argentina. *Contributions to Mineralogy and Petrology*, 90, 93-101.
- Grew, E.S. (1981) Surinamite, taaffeite, and beryllian sapphirine from pegmatites in granulite-facies rocks of Casey Bay, Enderby Land, Antarctica. *American Mineralogist*, 66, 1022-1033.
- Grew, E.S. (1998) Boron and beryllium minerals in granulite-facies pegmatites and implications of beryllium pegmatites for the origin and evolution of the Archean Napier Complex of East Antarctica. *Mem. of Natl. Inst. Polar Res., Spec. Issue* 53, 74-92.

- Grew, E.S., Yates, M.G., Huijsmans, J.P., McGee, J.J., Shearer, C.K., Wiedenbeck, M., and Rouse, R. (1998) Werdingite, a borosilicate new to granitic pegmatites. *Canadian Mineralogist* 36, 399-414.
- Hawthorne, F.C. and Černý, P. (1977) The alkali-metal positions in Cs-Li beryl. *Canadian Mineralogist*, 15, 414-421.
- Henderson, W.A. (1975) The bertrandites of Connecticut. *Mineralogical Record* 6, 114-124.
- Hervig, R.L. (2001) Beryllium analyses by secondary ion mass spectrometry. In Grew, E.S. (ed.) *Beryllium: Mineralogy, Petrology and Geochemistry*. Mineralogical Society of America, *Reviews in Mineralogy* 43, in press.
- Hochella, M.F., and Brown, G.E. (1986) Structural mechanisms of anomalous thermal expansion of cordierite-beryl and other framework silicates. *Journal of the American Ceramic Society*, 69, 13-18.
- Hölscher, A. and Schreyer, W. (1989) A new synthetic hexagonal BeMg-cordierite, $\text{Mg}_2[\text{Al}_2\text{BeSi}_6\text{O}_{18}]$, and its relationship to Mg-cordierite. *European Journal of Mineralogy*, 1, 21-37.
- Hölscher, A., Schreyer, W., and Lattard, D. (1986) High-pressure, high-temperature stability of surinamite in the system $\text{MgO} - \text{BeO} - \text{Al}_2\text{O}_3 - \text{SiO}_2 - \text{H}_2\text{O}$. *Contributions to Mineralogy and Petrology* 92, 113-127.
- Huebner, J.S. (1971) Buffering techniques for hydrostatic systems at elevated pressures. In *Research Techniques for High Pressure and High Temperature* (G.C. Ulmer, ed.) Springer-Verlag, New York, 123-177.
- Icenhower, J.P. (1995) Experimental determination of element behavior in silicic systems

- during hydrous partial fusion. University of Oklahoma, Norman, Oklahoma. PhD dissertation. 227 p.
- Icenhower, J.P., and London, D. (1995) An experimental study of element partitioning among biotite, muscovite, and coexisting peraluminous silicic melt at 200 MPa (H₂O). *American Mineralogist*, 80, 1229-1251.
- Jacobson, M.I. (1993) Antero Aquamarines: Minerals from the Mount Antero – White Mountain region, Chaffee County, Colorado. L.R. Ream, Coeur d’Alene, Idaho, 126 p.
- Jobin-Bevans, S., and Černý, P. (1998) The beryllian cordierite + beryl + spessartine assemblage, and secondary beryl in altered cordierite, Greer Lake granitic pegmatites, Southeastern Manitoba. *Canadian Mineralogist*, 36, 447-462.
- Kalt, A., Altherr, R., and Ludwig, T. (1998) Contact metamorphism in pelitic rocks on the Island of Kos (Greece, eastern Aegean Sea): a test for the Na-in-cordierite thermometer. *Journal of Petrology*, 39, 663-688.
- Kirchner, D., Mirwald, P.W., and Schreyer, W. (1984) Experimenteller Li-Einbau in Mg-Cordierit. *Fortschritte der Mineralogie, Beiheft 62*, 119-120.
- Lofgren, G.E. (1983) Effect of heterogeneous nucleation on basaltic textures: A dynamic crystallization study. *Journal of Petrology*, 24, 229-255.
- Marsh, B.D. (1995) Solidification fronts and magmatic evolution. *Mineralogical Magazine*, 60, 5-40.
- Meagher, E.P., and Gibbs, G.V. (1977) The polymorphism of cordierite: II. The crystal structure of indialite. *Canadian Mineralogist*, 15, 43-49.
- Miyashiro, A. (1957) Cordierite-indialite relations. *American Journal of Science*, 255,

43-62.

- Mirwald, P.W. (1986) 1st Cordierite ein Geothermometer. *Fortschritte der Mineralogie*, 64, 119.
- Morgan, G.B., and London, D. (1996) Optimizing the electron microprobe of hydrous alkali aluminosilicate glasses. *American Mineralogist* 81, 1176-1185.
- Morgan, G.B., and London, D. (1999) Crystallization of the Little Three layered pegmatite-aplite dike, Ramona District, California. *Contributions to Mineralogy and Petrology*, 136, 310-330.
- Morris, J.D. (1991) Applications of cosmogenic ¹⁰Be to problems in the earth sciences. *Annual Review of Earth and Planetary Sciences*, 19, 313-350.
- Mysen, B. and Virgo, D. (1985) Structure and properties of fluorine-bearing aluminosilicate melts: the system Na₂O-Al₂O₃-SiO₂-F at 1 atm. *Contributions to Mineralogy and Petrology*, 91, 205-220.
- Newton, R.C. (1966) BeO in pegmatitic cordierite. *Mineralogical Magazine*, 35, 920-927.
- Patiño Douce, A.E. (1992) Calculated relationships between activity of alumina and phase assemblages of silica-saturated igneous rocks: Petrogenetic implications of magmatic cordierite, garnet and aluminosilicate. *Journal of Volcanology and Geothermal Research*, 52, 43-63.
- Pearce, N.J.G., Perkins, W.T., Westgate, J.A., Gorton, M.P., Jackson, S.E., Neal, C.R., and Chenery, S.P. (1997) A compilation of new and published major and trace element data for NIST SRM 610 and SRM 612 glass reference materials. *Geostandards Newsletter* 21, 115-144.
- Pouchou, J.L., and Pichoir, F. (1985) "PAP" (ϕ - ρ -Z) correction procedure improved

- quantitative microanalysis. In *Microbeam Analysis*, J.T. Armstrong, ed. 104-106. San Francisco Press.
- Povondra, P. and Čech, F. (1978) Sodium-beryllium-bearing cordierite from Haddam, Connecticut, U.S.A. *Neues Jahrbuch für Mineralogie, Monatshefte*, 5, 203-209.
- Povondra, P., Čech, F., and Burke, E.A.J. (1984) Sodium-beryllian cordierite from Gammelmorskärr, Kemiö Island, Finland, and its decomposition products. *Neues Jahrbuch für Mineralogie, Monatshefte* 3, 125-136.
- Povondra, P. and Langer, K. (1971) A note on the miscibility of magnesia-cordierite and beryl. *Mineralogical Magazine*, 38, 523-526.
- Povondra, P. and Langer, K. (1978) Synthesis and some properties of sodium-beryllium-bearing cordierite, $\text{Na}_x\text{Mg}_2(\text{Al}_{4-x}\text{Be}_x\text{Si}_5\text{O}_{18})$. *Neues Jahrbuch für Mineralogie, Abhandlungen*, 116, 1-19.
- Predecki, P., Haas, J., Faber, Jr., J., and Hitterman, R.L. (1987) Structural aspects of thermal expansion of hexagonal cordierite. *J. Am. Ceram. Soc.*, 70, 175-182.
- Russ, J.C. (1999) *The Image Processing Handbook*, 3rd Ed. CRC Press, Boca Raton, Florida. 771p.
- Ryan, J., Morris, J., Bebout, G., and Leeman, W. (1996) Describing chemical fluxes in subduction zones: Insights from “depth-profiling” studies of arc and forearc rocks. In *Subduction: Top to Bottom* (Bebout, G.E., Scholl, D.W., Kirby, S.H., and Platt, J.P., eds.). American Geophysical Union, Geophysical Monograph 96, 263-268.
- Schaller, W.T., Stevens, R.E., and Jahns, R.H. (1962) An unusual beryl from Arizona. *American Mineralogist*, 47, 672-699.

- Schmetzer, K. (1983) Crystal chemistry of natural Be-Mg-Al oxides: taaffeite, taprobanite, musgravite. *Neues Jahrbuch für Mineralogie, Abhandlungen*, 146, 15-28.
- Schreyer, W. (1964) Synthetische und natürliche Cordierite I. *Neues Jahrbuch für Mineralogie, Abhandlungen*, 102, 39-67.
- Schreyer, W., Gordillo, C.E., and Werding, G. (1979) A new sodium-beryllium cordierite from Soto, Argentina, and the relationship between distortion index, Be content, and state of hydration. *Contributions to Mineralogy and Petrology*, 70, 421-428.
- Schreyer, W., Maresch, W.V., Daniels, P., and Wolsdorff, P. (1990) Potassic cordierites: characteristic minerals for high-temperature, very low pressure environments. *Contributions to Mineralogy and Petrology*, 105, 162-172.
- Selkregg, K.R. and Bloss, F.D. (1980) Cordierites: compositional controls of Δ , cell parameters, and optical properties. *American Mineralogist*, 65, 522-533.
- Shannon, R.D., and Prewitt, C.T. (1969) Effective ionic radii in oxides and fluorides. *Acta Crystallographica*, 25, 925-946.
- Sherriff, B.L., Grundy, H.D., Hartman, J.S., Hawthorne, F.C., and Černý, P. (1991) The incorporation of alkalis in beryl: multi-nuclear MAS NMR and crystal-structure study. *Canadian Mineralogist*, 29, 271-285.
- Tuttle, O.F. and Bowen, N.L. (1958) Origin of granite in the light of experimental studies in the system $\text{NaAlSi}_3\text{O}_8$ - KAlSi_3O_8 - SiO_2 - H_2O . Geological Society of America, *Memoir* 74.
- Wolf, M.B. and London, D. (1997) Boron in granitic magmas: stability of tourmaline in

equilibrium with biotite and cordierite. *Contributions to Mineralogy and Petrology*, 130, 12-30.

Woodford, P.J., and Wilson, A.F. (1976) Sapphirine, hohbomite, kornepine, and surinamite from aluminous granulites, north-eastern Strangways Range, central Australia. *Neues Jahrbuch für Mineralogie, Monatshefte*, 1976 (1), 15-35.

Table 2-1. Ideal Cation Site Occupancies and Symmetry for Cordierite to Beryl Structures

Mineral	T1		T2		M	Symmetry	
cordierite	1 Si, 2 Al	ordered	4 Si, 2 Al	ordered	2 Mg	orthorhombic	<i>Cccm</i>
indialite	0.8 Si, 2.2 Al	disordered	4.2 Si, 1.8 Al	disordered	2 Mg	hexagonal	<i>P6/mcc</i>
"BeMg-Crd"	2 Al, 1 Be	intermediate	6 Si	disordered	2 Mg	hexagonal	<i>P6/mcc</i>
beryl	3 Be	disordered	6 Si	disordered	2 Al	hexagonal	<i>P6/mcc</i>
sekaninite	1 Si, 2 Al	ordered	4 Si, 2 Al	ordered	2 Fe	orthorhombic	<i>Cccm</i>
stoppanilite	3 Be	disordered	6 Si	disordered	2 Fe	hexagonal	<i>P6/mcc</i>

From Cohen et al., 1977; Meagher & Gibbs 1977; Selkregg & Bloss 1980; Hochella & Brown 1986; Holscher & Schreyer 1989; Boberski & Schreyer 1990; and Ferrais et al., 1998.

Table 2-2. STARTING MATERIALS

ADDED MINERALS & GLASS											
Mineral ^a	albite	orthoclase	quartz	muscovite ^b	biotite	beryl	cordierite	garnet Alm ₄₄ Pyp ₄₂ Gro ₁₃ Sps ₁		phenakite	haplogranite glass
No. of analyses	5	20	6	1-3	96	7	25	20	5	41	
oxide wt%											
SiO ₂	68.82 (0.16)	64.95 (0.36)	99.99 (0.03)	51.91 -	38.83 (0.29)	66.00 (0.20)	48.42 (0.25)	39.71 (0.26)	54.34 (0.32)	77.63 (0.59)	
TiO ₂	nd	nd	nd	0.22 -	2.05 (0.11)	0.06 (0.02)	0.01 (0.01)	0.04 (0.02)	0.00	0.01 (0.01)	
Al ₂ O ₃	19.76 (0.05)	18.76 (0.14)	nd	28.02 -	11.26 (0.12)	19.24 (0.10)	33.83 (0.13)	23.20 (0.16)	0.00	13.03 (0.16)	
Fe ₂ O ₃	-	-	-	3.53 -	-	-	-	-	-	-	
FeO	nd	nd	nd	0.82 ^c -	18.47 (0.25)	0.48 (0.13)	2.53 (0.07)	21.26 (0.14)	0.03 (0.02)	0.02 (0.01)	
MnO	nd	nd	nd	0.08 -	0.83 (0.04)	0.00	0.08 (0.02)	0.46 (0.02)	0.00	0.00	
ZnO	nd	nd	nd	nd	0.14 (0.04)	nd	nd	nd	nd	nd	
BeO ^d	nd	nd	nd	nd	nd	13.97 (0.05)	nd	nd	46.17 (0.99)	nd	
MgO	nd	nd	nd	1.00 -	14.08 (0.21)	0.00	12.62 (0.11)	11.46 (0.05)	0.00	0.01 (0.00)	
CaO	0.07 (0.01)	0.01 (0.02)	nd	0.30 -	0.00 (0.01)	0.00	0.02 (0.01)	5.07 (0.04)	0.00	0.01 (0.01)	
BaO	0.06 (0.05)	0.32 (0.04)	nd	0.09 ^e -	0.10 (0.02)	0.03 (0.03)	0.00	0.02 (0.02)	0.14 (0.01)	0.01 (0.01)	
Na ₂ O	11.59 (0.04)	1.21 (0.07)	nd	1.27 -	0.56 (0.14)	0.08 (0.01)	0.33 (0.02)	0.00	0.00	4.61 (0.11)	
K ₂ O	0.23 (0.02)	14.84 (0.07)	nd	8.90 -	9.01 (0.14)	0.03 (0.03)	0.06 (0.01)	0.00	0.00	4.79 (0.09)	
Rb ₂ O (ppm)	nd	nd	nd	895 ^e -	nd	151 ^g (5)	500 ^f	nd	nd	nd	
Cs ₂ O (ppm)	nd	nd	nd	23 ^e -	nd	2021 ^g (20)	1100 ^f	nd	nd	nd	
P ₂ O ₅	nd	nd	nd	nd	nd	nd	0.00	0.04 (0.01)	nd	0.01 (0.01)	
F	nd	nd	nd	nd	3.67 (0.14)	nd	0.02 (0.02)	0.02 (0.03)	nd	0.03 (0.03)	
Cl	nd	nd	nd	nd	0.05 (0.02)	nd	nd	0.01 (0.01)	nd	0.01 (0.01)	
H ₂ O	nd	nd	nd	nd	2.02 ^e (0.08)	nd	nd	nd	nd	nd	
LOI	-	-	-	3.87 -	-	-	-	-	-	-	
O=F					-1.54		-0.01	-0.01		-0.01	
O=Cl					-0.01		0.00			0.00	
Total	100.53 (0.18)	100.09 (0.40)	99.99 (0.03)	100.10 (0.16)	99.52 (0.53)	100.11 (0.26)	97.94 (0.31)	101.28 (0.35)	100.68 (1.04)	100.16 (0.63)	

^a albite, Copelinha, Minas Gerais, Brazil; orthoclase, St. Gotthard, Switzerland; quartz, ultrahigh purity, Feldspar Corp., Spruce Pine, NC, USA; muscovite, Spruce Pine, NC, USA; biotite, Ontario, Canada; garnet, Gore Mountain, NY, USA; phenakite, Espirito Santo, Minas Gerais, Brazil; beryl, Volodarsk, Ukraine; cordierite, Brazil; haplogranite glass, 200 MPa minimum anhydrous composition, Corning Glassworks, NY, USA.

^b Analysed at Activation Laboratories Ltd. (Lancaster, Ontario, Canada) by X-Ray fluorescence (fusion) unless otherwise specified.

^c Analysed by titration.

^d Analysed by secondary ion mass spectrometry.

^e Analysed by instrumental neutron activation analysis.

^f From Icenhower and London (1995).

All other values are from quantitative electron probe microanalysis (with total iron as FeO).

Numbers in parentheses represent 1 standard deviation of the mean.

Propagated precision is shown for total values; the italicized value represents estimated precision.

Table 2-3. STARTING MIXTURES

Mixture	Constituents (wt%)										
	albite	orthoclase	quartz	muscovite	biotite	garnet	Al ₂ O ₃	phenakite	beryl	cordierite	hapiogranite glass
SP-Crd1-Be	22.7	9.5	26.5	13.1	12.0	15.1		1.1			
SP-Bt1-Be	26.5	11.2	31.0	15.3	12.6				3.5		
SP-Bt2-Be	22.6	9.4	26.5	12.9	22.1		3.5		3.0		
SP-Bt4-Be								2.5		29.1	68.5
SP-Mus2-Be	21.8	9.2	25.6	37.8			2.7		2.9		
SP-Crd2-Be	20.0	8.4	23.4	11.5	8.7	6.3		0.8	20.9		
SP-Crd1-C	22.7	9.6	26.6	13.1	12.3	15.7					

The designation "-Be" refers to Be-rich mixtures; "-C" designates a Be-poor or control composition to which no Be-mineral was added. Analyses of these constituents are given in Table 1. Dehydrated reagent-grade gibbsite was used for a source of activated Al₂O₃.

Table 2-4. Cordierite & Glass Analyses

(a) Forward Experiments											
Run Mixture	BeP-53		BeP-54		BeP-55		BeP-65		BeP-120		BeP-121
Run Path/Duration (d)	700-F (27)		750-F (27)		800-F (14)		850-F (6)		850-F (6)		900-F (2)
Crystalline Products	Crd, Br, Bt, Mt, Qtz, Pl		Crd, Br, Bt, Mt		Crd, Br, Bt, Mt		Crd, Bt, Mt		Crd, Br, Bt, Mt		Crd, Br, Mt
Analysis of	cordierite glass		cordierite glass		cordierite glass		cordierite glass		cordierite glass		cordierite
No. analyses, OEPMA	21	11	8	11	8	11	12	10	18	12	12
No. analyses, SIMS	2	2	2	2	3	2	2	2	0	0	0
wt %	se	sd	se	sd	se	sd	se	sd	se	sd	se
SiO ₂	49.84 (0.15)	71.45 (0.56)	52.33 (0.70)	70.32 (0.41)	52.92 (0.62)	70.11 (0.48)	58.82 (0.88)	69.06 (0.41)	59.71 (0.25)	61.53 (0.27)	
TiO ₂	0.01 (0.00)	0.05 (0.02)	0.02 (0.01)	0.03 (0.02)	0.03 (0.01)	0.14 (0.02)	0.02 (0.02)	0.13 (0.02)	0.03 (0.01)	0.05 (0.01)	
B ₂ O ₃ (ppm) ¹	5 (1)	95 (2)	5 (1)	89 (3)	2 (0)	87 (1)	4 (1)	98 (3)	nd	nd	
Al ₂ O ₃	27.05 (0.12)	12.14 (0.13)	26.90 (0.70)	12.73 (0.14)	25.58 (0.46)	12.83 (0.12)	19.91 (0.72)	13.29 (0.18)	17.87 (0.30)	16.59 (0.14)	
FeO	7.22 (0.17)	0.57 (0.03)	3.51 (0.28)	0.57 (0.04)	3.12 (0.12)	0.82 (0.04)	2.38 (0.09)	1.12 (0.17)	2.75 (0.10)	3.51 (0.10)	
MnO	0.84 (0.02)	0.06 (0.01)	0.42 (0.03)	0.09 (0.02)	0.28 (0.03)	0.10 (0.02)	0.15 (0.02)	0.12 (0.01)	0.28 (0.01)	0.21 (0.01)	
MgO	8.86 (0.10)	0.15 (0.01)	11.22 (0.18)	0.23 (0.01)	11.92 (0.08)	0.39 (0.01)	12.33 (0.07)	0.72 (0.02)	11.87 (0.10)	10.72 (0.21)	
NiO	0	nd	0.01 (0.01)	nd	0.01 (0.01)	nd	0.00	nd	0.01 (0.00)	0.01 (0.01)	
ZnO	0.03 (0.00)	nd	nd	nd	nd	nd	nd	nd	nd	nd	
BeO ¹	2.507 (0.264)	0.100 (0.001)	2.397 (0.160)	0.152 (0.001)	3.079 (0.263)	0.202 (0.000)	3.988 (0.113)	0.282 (0.004)	nd	nd	
CaO	0.49 (0.03)	0.92 (0.08)	0.43 (0.03)	1.04 (0.10)	0.40 (0.02)	1.13 (0.18)	0.30 (0.01)	0.81 (0.11)	0.10 (0.01)	0.08 (0.01)	
BaO	nd	0.04 (0.03)	0.02 (0.01)	0.05 (0.03)	0.01 (0.01)	0.05 (0.03)	0.00	0.04 (0.03)	0.01 (0.01)	0.02 (0.02)	
Li ₂ O (ppm) ¹	213 (12)	436 (5)	210 (36)	405 (11)	158 (22)	447 (5)	79 (1)	342 (28)	nd	nd	
Na ₂ O	1.20 (0.02)	3.27 (0.15)	1.09 (0.07)	3.25 (0.12)	0.91 (0.07)	3.24 (0.09)	0.65 (0.02)	3.17 (0.06)	0.65 (0.02)	0.66 (0.03)	
K ₂ O	0.29 (0.04)	3.58 (0.15)	0.31 (0.04)	3.72 (0.12)	0.42 (0.04)	3.67 (0.10)	0.59 (0.04)	3.81 (0.10)	0.81 (0.05)	1.05 (0.06)	
Rb ₂ O (ppm) ¹	27 (3)	113 (3)	25 (0)	126 (12)	25 (1)	117 (3)	33 (1)	123 (2)	nd	nd	
Cs ₂ O (ppm) ¹	6 (2)	8 (1)	8 (0)	9 (3)	3 (0)	9 (1)	10 (0)	8 (1)	nd	nd	
P ₂ O ₅	nd	0.11 (0.07)	nd	0.09 (0.03)	nd	0.10 (0.03)	nd	0.07 (0.02)	nd	nd	
F	0.06 (0.03)	0.22 (0.07)	0.04 (0.03)	0.28 (0.07)	0.01 (0.01)	0.28 (0.05)	0.07 (0.03)	0.35 (0.05)	0.02 (0.02)	0.02 (0.02)	
Cl	nd	0.01 (0.01)	nd	0.01 (0.01)	nd	0.01 (0.01)	nd	0.01 (0.01)	nd	nd	
O=F	-0.02	-0.09	-0.12	-0.12	0.00	-0.12	-0.01	-0.15	-0.01	-0.01	
total	98.30 (0.19)	92.58 (0.64)	98.70 (0.18)	92.44 (0.47)	98.89 (0.48)	92.95 (0.59)	98.96 (0.27)	92.81 (0.38)	94.20 (0.21)	94.44 (0.15)	
H ₂ O by diff	1.70	7.42	1.30	7.58	1.31	7.05	1.02	7.39	5.80	5.56	
ASI		1.10 (0.03)		1.12 (0.03)		1.12 (0.03)		1.24 (0.04)			
Mg#	66.7 (0.7)		83.6 (0.4)		86.2 (0.4)		89.7 (0.3)		87.6 (0.3)	83.7 (0.3)	

cations/18 O						
Si	5.12 (0.02)		5.24 (0.08)		5.27 (0.07)	5.73 (0.08)
Al	3.27 (0.02)		3.17 (0.08)		3.00 (0.06)	2.29 (0.08)
Be	0.62 (0.04)		0.58 (0.02)		0.74 (0.03)	0.93 (0.01)
total T sites	9.01 (0.04)		8.99 (0.12)		9.01 (0.09)	8.95 (0.12)
Be by diff						1.08
Li	0.01 (0.00)		0.01 (0.00)		0.01 (0.00)	0.00 (0.00)
Mg	1.35 (0.02)		1.67 (0.03)		1.77 (0.01)	1.80 (0.01)
Fe ²⁺	0.62 (0.01)		0.29 (0.02)		0.28 (0.01)	0.19 (0.01)
Mn	0.06 (0.00)		0.04 (0.00)		0.02 (0.00)	0.01 (0.00)
total M site	2.04 (0.02)		2.01 (0.04)		2.06 (0.02)	2.00 (0.01)
total	11.05 (0.05)		11.00 (0.12)		11.07 (0.10)	10.95 (0.12)

channel occupants/18 O						
Ca	0.05 (0.00)		0.05 (0.00)		0.04 (0.00)	0.03 (0.00)
Na	0.24 (0.00)		0.21 (0.01)		0.18 (0.01)	0.12 (0.00)
K	0.04 (0.01)		0.04 (0.00)		0.05 (0.00)	0.07 (0.01)
H ₂ O	1.12		0.62		0.82	0.83
total	1.45 (0.01)		1.12 (0.01)		1.09 (0.01)	0.85 (0.01)

¹ Analysed by SIMS. Mineral abbreviations: Crd = cordierite, Br = beryl, Bt = biotite, Mus = muscovite, Mt = magnetite, Kfs = potassic feldspar, Pl = plagioclase, Qtz = quartz, Phn = phenakite. Abbreviations in parentheses indicate relict occurrence. Initial precision is reported in parentheses beside values using one standard deviation of the mean for glass and using standard error as a collective measure of individual crystal mean values. Total propagated precision is shown for analytical totals and mineral recalculations.

Table 2-4. Cordierite & Glass Analyses

(b) Reversed Experiments

Run	BeP-51			BeP-18			BeP-41		
Mixture	SP-Mus3-Be			SP-Crd1-Be			SP-BI2-Be		
Prec. Path/Duration (d)	730-F (21)			850-F (4)			750-F (21)		
Final Path/Duration (d)	875-R (36)			700-R (26)			700-R (26)		
Crystalline Products	Crd.(Br),Bl,Mt,Kfs,Mus,Cor			Crd,Br,Bl,Mt			Crd.(Br),Bl,Mt		
Analysis of	cordierite		glass	cordierite		glass	cordierite		glass
	cores	rims		cores	rims		cores	rims	
No. analyses, QEPMA	7	24	5	11	15	11	16	26	11
No. analyses, SIMS		2	2		1	2		2	

wt %	se	se	sd	se	se	sd	se	se	sd
SiO ₂	46.66 (0.27)	48.51 (0.18)	69.39 (0.77)	56.37 (0.72)	49.77 (0.29)	69.96 (0.88)	48.52 (0.26)	48.68 (0.30)	68.92 (0.49)
TiO ₂	0.01 (0.00)	0.01 (0.00)	0.04 (0.02)	0.02 (0.01)	0.02 (0.02)	0.06 (0.02)	0.02 (0.01)	0.02 (0.01)	0.08 (0.02)
B ₂ O ₃ (ppm) ¹	nd	8 (3)	174 (1)	nd	2	88 (2)	nd	5 (1)	98 (2)
Al ₂ O ₃	29.71 (0.24)	30.23 (0.22)	13.59 (0.24)	21.64 (0.48)	30.13 (0.29)	12.48 (0.20)	31.01 (0.13)	30.64 (0.10)	13.35 (0.07)
FeO	5.80 (0.08)	6.03 (0.08)	0.35 (0.03)	2.90 (0.09)	4.64 (0.07)	0.49 (0.04)	6.30 (0.04)	6.18 (0.02)	0.44 (0.03)
MnO	0.21 (0.03)	0.26 (0.02)	0.03 (0.01)	0.17 (0.03)	0.79 (0.02)	0.08 (0.02)	0.61 (0.03)	0.68 (0.07)	0.07 (0.02)
MgO	9.65 (0.12)	9.40 (0.09)	0.10 (0.01)	12.46 (0.09)	10.38 (0.11)	0.15 (0.01)	9.55 (0.03)	9.55 (0.01)	0.10 (0.01)
NiO	0.00	0.01 (0.00)	nd	0.01 (0.00)	0.01 (0.00)	nd	0.01 (0.01)	0.03 (0.01)	nd
BeO ¹	nd	1.126 (0.016)	0.042 (0.000)	nd	1.050	0.077 (0.001)	nd	1.010 (0.068)	0.051 (0.000)
CaO	0.06 (0.01)	0.07 (0.01)	0.30 (0.05)	0.30 (0.02)	0.56 (0.04)	0.67 (0.05)	0.02 (0.00)	0.03 (0.00)	0.16 (0.09)
BaO	nd	nd	0.03 (0.02)	0.01 (0.00)	0.01 (0.00)	0.05 (0.03)	0.01 (0.01)	0.01 (0.01)	0.05 (0.05)
Li ₂ O (ppm) ¹	nd	176 (25)	471 (1)	nd	170	384 (3)	nd	269 (24)	613 (2)
Na ₂ O	1.19 (0.05)	1.20 (0.03)	3.20 (0.14)	0.65 (0.03)	1.36 (0.02)	3.24 (0.11)	1.04 (0.06)	1.12 (0.05)	3.19 (0.07)
K ₂ O	0.29 (0.02)	0.28 (0.02)	4.50 (0.13)	0.50 (0.03)	0.34 (0.05)	3.43 (0.09)	0.22 (0.02)	0.26 (0.01)	4.60 (0.09)
Rb ₂ O (ppm) ¹	nd	51 (2)	279 (4)	nd	55	110 (2)	nd	28 (1)	153 (4)
Cs ₂ O (ppm) ¹	nd	20 (1)	32 (1)	nd	8	10 (1)	nd	17 (0)	35 (2)
P ₂ O ₅	nd	nd	0.09 (0.01)	nd	nd	0.04 (0.01)	nd	nd	0.08 (0.03)
F	0.03 (0.01)	0.01 (0.00)	0.13 (0.04)	0.04 (0.01)	0.04 (0.01)	0.23 (0.07)	0.01 (0.00)	0.02 (0.01)	0.50 (0.02)
Cl	nd	nd	0.01 (0.00)	nd	nd	0.01 (0.01)	nd	nd	0.01 (0.01)
O=F	-0.01		-0.08	-0.01	-0.02	-0.10	-0.01	-0.01	-0.21
total	95.62 (0.24)	97.14 (0.31)	91.74 (0.78)	95.26 (0.39)	99.08 (0.12)	91.07 (0.91)	97.31 (0.22)	98.22 (0.19)	91.37 (0.63)
H ₂ O by diff	4.38	2.86	8.28		0.62	8.93		1.78	8.63
ASI			1.28 (0.05)			1.16 (0.03)			1.25 (0.03)
Mg#	74.8 (0.2)	73.5 (0.4)		88.5 (0.4)	79.9 (0.2)		73.0 (0.3)	73.4 (0.3)	

cations/18O									
Si	5.05 (0.03)	5.02 (0.02)		5.84 (0.08)	5.04 (0.03)		5.04 (0.03)	5.00 (0.03)	
Al	3.63 (0.03)	3.69 (0.03)		2.64 (0.06)	3.60 (0.03)		3.80 (0.02)	3.71 (0.01)	
Be	nd	0.28 (0.00)		nd	0.26		nd	0.25 (0.02)	
total T sites		8.99 (0.04)			8.90 (0.05)			8.96 (0.04)	
Be by diff	0.31			0.34			0.08		
Li	(0.00)	0.01 (0.00)		(0.00)	0.01 (0.00)		(0.00)	0.01 (0.00)	
Mg	1.49 (0.02)	1.45 (0.02)		1.92 (0.02)	1.60 (0.02)		1.48 (0.01)	1.46 (0.00)	
Fe ²⁺	0.50 (0.01)	0.52 (0.01)		0.25 (0.01)	0.40 (0.01)		0.55 (0.00)	0.53 (0.00)	
Mn	0.02 (0.00)	0.02 (0.00)		0.01 (0.00)	0.07 (0.00)		0.05 (0.00)	0.08 (0.01)	
total M sites	2.01 (0.02)	2.00 (0.02)		2.19 (0.02)	2.08 (0.02)		2.08 (0.01)	2.06 (0.01)	
total	10.69 (0.05)	10.99 (0.04)		10.66 (0.10)	10.98 (0.05)		10.92 (0.04)	11.02 (0.04)	

channel occupants/18 O									
Ca	0.01 (0.00)	0.01 (0.00)		0.03 (0.00)	0.08 (0.00)		0.00 (0.00)	0.00 (0.00)	
Na	0.24 (0.01)	0.24 (0.01)		0.17 (0.01)	0.27 (0.00)		0.21 (0.01)	0.22 (0.01)	
K	0.04 (0.00)	0.04 (0.00)		0.07 (0.00)	0.04 (0.01)		0.03 (0.00)	0.03 (0.00)	
H ₂ O (from diff)		1.87			1.60			1.15	
total		2.16 (0.01)			2.17 (0.01)			1.40 (0.01)	

Table 2-4. Cordierite & Glass Analyses

(b) Reversed Experiments (continued)							(c) Representative Cordierite Grown from Be-Poor Melts	
Run	BeP-17			BeP-4			BeP-58	BeP-19
Mixture	SP-Crd1-Be			SP-B11-Be			SP-Crd1-C	SP-Crd1-C
Prec. Path/Duration (d)	850-F (4)			850-F (4)			850-F (4)	850-F (4)
Final Path/Duration (d)	750-R (26)			800-R (15)			700-R (28)	100-R (14)
Crystalline Products	Crd,Bt,Mt(Phn)			Crd,Bt,Mt			Crd,Bt,Mt	Crd,Bt,Mt
Analysis of	cordierite	cordierite	glass	cordierite	cordierite	glass	cordierite	cordierite
	cores	rims		cores	rims			
No. analyses, QEPMA	8	5	10	12	15	12	21	32
No. analyses, SIMS	1	1	2		2	3	3	6

wt %	se	se	sd	se	se	sd	sd	sd
SiO ₂	57.18 (0.31)	50.88 (0.10)	89.38 (1.17)	59.95 (0.39)	51.74 (0.33)	70.15 (0.61)	47.78 (1.14)	48.74 (0.90)
TiO ₂	0.02 (0.01)	0.01 (0.00)	0.04 (0.02)	0.02 (0.01)	0.02 (0.01)	0.11 (0.02)	0.02 (0.01)	0.02 (0.01)
B ₂ O ₃ (ppm) ¹	3	8	86 (0)	nd	8	89 (2)	12.72 (0.00)	5.37 (0.16)
Al ₂ O ₃	21.48 (0.43)	28.09 (0.33)	12.54 (0.44)	17.43 (0.34)	27.78 (0.24)	12.47 (0.15)	34.10 (0.62)	33.58 (0.73)
FeO	2.90 (0.05)	2.99 (0.04)	0.59 (0.04)	2.67 (0.05)	2.94 (0.04)	0.67 (0.05)	5.33 (0.67)	2.78 (0.11)
MnO	0.23 (0.02)	0.57 (0.03)	0.09 (0.01)	0.13 (0.01)	0.34 (0.01)	0.09 (0.01)	0.95 (0.06)	0.33 (0.02)
MgO	12.27 (0.10)	11.66 (0.08)	0.25 (0.01)	12.28 (0.05)	11.79 (0.03)	0.40 (0.01)	9.75 (0.43)	12.18 (0.27)
NiO	0	0.00	nd	0.01 (0.01)	0.05 (0.01)	nd	0.01 (0.01)	0.00 (0.01)
BeO ¹	3.725	2.098	0.145 (0.000)	nd	2.085	0.184 (0.002)	0.02 (0.00)	0.02 (0.00)
CaO	0.33 (0.02)	0.57 (0.02)	0.89 (0.05)	0.03 (0.00)	0.04 (0.00)	0.07 (0.03)	0.13 (0.05)	0.18 (0.05)
BaO	0.01 (0.01)	0.01 (0.01)	0.05 (0.03)	0.01 (0.01)	0.02 (0.01)	0.06 (0.04)	0.01 (0.01)	0.02 (0.02)
Li ₂ O (ppm) ¹	81	114	415 (19)	nd	204	398 (9)	152.40 (22.00)	79.93 (12.00)
Na ₂ O	0.80 (0.03)	1.30 (0.04)	3.31 (0.09)	0.75 (0.02)	1.18 (0.01)	3.46 (0.14)	0.51 (0.14)	0.36 (0.05)
K ₂ O	0.51 (0.05)	0.45 (0.05)	3.65 (0.07)	0.69 (0.02)	0.59 (0.01)	3.83 (0.10)	0.09 (0.03)	0.15 (0.08)
Rb ₂ O (ppm) ¹	34	42	118 (4)	nd	57	136 (2)	21.22 (2.19)	9.28 (0.05)
Cs ₂ O (ppm) ¹	10	12	10 (0)	nd	39	34 (1)	2.85 (0.00)	4.88 (0.00)
P ₂ O ₅	nd	nd	0.05 (0.02)	nd	nd	0.02 (0.02)	nd	nd
F	0.02 (0.01)	0.01 (0.01)	0.29 (0.09)	0.03 (0.01)	0.03 (0.01)	0.34 (0.08)	0.04 (0.04)	0.01 (0.02)
Cl	nd	nd	0.01 (0.01)	nd	nd	0.01 (0.01)	0.00	0.00
O=F	-0.01	0.00	-0.12	-0.01	-0.01	-0.14	-0.02	-0.01
total	99.46 (0.23)	98.64 (0.49)	91.14 (1.47)	93.97 (0.32)	98.60 (0.28)	91.70 (0.65)	98.68 (0.67)	98.35 (0.62)
H ₂ O by diff	0.54	1.36	8.66		1.40	8.30	1.32	1.65
ASI			1.13 (0.05)			1.24 (0.03)		
Mg#	88.3 (0.4)	87.4 (0.2)		89.1 (0.3)	87.7 (0.2)		73.48 (1.50)	87.42 (1.80)

cations/16O								
Si	5.60 (0.03)	5.11 (0.03)		8.25 (0.05)	5.19 (0.04)		4.87 (0.12)	4.92 (0.10)
Al	2.48 (0.05)	3.33 (0.04)		2.14 (0.04)	3.28 (0.03)		4.10 (0.08)	4.00 (0.07)
Be	0.88	0.51		nd	0.50		0.01 (0.00)	0.00
total T sites Be by diff	8.96 (0.06)	8.95 (0.05)		0.46	8.97 (0.05)		8.97 (0.20)	8.92 (0.18)
Li	0.00 (0.00)	0.00 (0.00)			0.01 (0.00)		0.01 (0.00)	0.00
Mg	1.79 (0.02)	1.75 (0.01)		1.91 (0.01)	1.78 (0.01)		1.49 (0.07)	1.83 (0.04)
Fe ²⁺	0.24 (0.00)	0.25 (0.00)		0.23 (0.00)	0.25 (0.00)		0.48 (0.06)	0.23 (0.01)
Mn	0.02 (0.00)	0.05 (0.00)		0.01 (0.00)	0.03 (0.00)		0.08 (0.00)	0.03 (0.00)
total M sites	2.05 (0.02)	2.05 (0.02)		2.15 (0.01)	2.04 (0.01)		2.03 (0.13)	2.09 (0.05)
total	11.01 (0.08)	11.00 (0.05)		10.54 (0.06)	11.01 (0.05)		11.00 (0.33)	11.01 (0.23)

channel occupants/16 O								
Ca	0.03 (0.00)	0.06 (0.00)		0.00 (0.00)	0.00 (0.00)		0.01 (0.00)	0.02 (0.01)
Na	0.15 (0.01)	0.25 (0.01)		0.15 (0.00)	0.23 (0.00)		0.11 (0.03)	0.07 (0.02)
K	0.08 (0.01)	0.06 (0.01)		0.09 (0.00)	0.08 (0.00)		0.02 (0.01)	0.02 (0.01)
H ₂ O (from diff)	0.33	0.86			0.99		0.85 (0.01)	0.83 (0.00)
total	0.57 (0.01)	1.23 (0.01)			1.30 (0.00)		0.98 (0.04)	0.93 (0.04)

Table 2-5. Beryl Analyses

(a) Beryl in Equilibrium with Be-Cordierite

Run	BeP-53	BeP-18	BeP-54	BeP-4	BeP-120	BeP-121
Mixture	SP-Crd1-Be	SP-Crd1-Be	SP-Crd1-Be	SP-Bt1-Be	SP-Crd2-Be	SP-Crd2-Be
Prec. Path/Duration (d)		850-F (4)		850-F (4)		
Final Path/Duration (d)	700-F (27)	700-R (28)	750-F (27)	800-R (16)	850-F (8)	900-F (2)
Crystalline Products	Crd,Bri,Bt,Mt, Qtz,Pl	Crd,Bri,Bt,Mt	Crd,Bri,Bt,Mt	Crd,Bri,Bt,Mt	Crd,Bri,Bt,Mt	Crd,Bri,Mt
No. analyses, QEPMA	8	5	8	7	11	12

wt %	se	se	se	se	se	se
SiO ₂	66.84 (0.63)	66.480 (0.69)	66.46 (0.34)	66.29 (0.21)	66.82 (0.22)	68.11 (0.26)
TiO ₂	0.03 (0.00)	0.010 (0.01)	0.01 (0.00)	0.02 (0.02)	0.02 (0.01)	0.04 (0.02)
Al ₂ O ₃	17.00 (0.32)	17.520 (0.18)	16.49 (0.23)	17.80 (0.05)	16.01 (0.13)	16.85 (0.16)
FeO	2.20 (0.24)	1.080 (0.07)	1.88 (0.09)	1.35 (0.01)	2.42 (0.07)	2.21 (0.11)
MnO	0.03 (0.01)	0.010 (0.00)	0.02 (0.01)	0.02 (0.00)	0.04 (0.01)	0.04 (0.02)
MgO	1.96 (0.14)	1.190 (0.15)	2.11 (0.17)	0.95 (0.31)	1.74 (0.14)	1.54 (0.12)
NiO	0.01 (0.01)	0.010 (0.00)	0.01 (0.00)	0.00	0.01 (0.01)	0.01 (0.01)
CaO	0.14 (0.03)	0.090 (0.02)	0.14 (0.03)	0.00	0.03 (0.01)	0.03 (0.02)
BaO	0.01 (0.00)	0.010 (0.01)	0.02 (0.01)	0.05 (0.05)	0.02 (0.02)	0.01 (0.01)
Na ₂ O	0.54 (0.07)	0.360 (0.02)	0.58 (0.03)	0.31 (0.11)	0.47 (0.03)	0.50 (0.03)
K ₂ O	0.31 (0.09)	0.290 (0.07)	0.53 (0.08)	0.41 (0.13)	0.82 (0.06)	0.82 (0.09)
F	0.04 (0.03)	0.040 (0.04)	0.01 (0.00)	0.02 (0.02)	0.02 (0.02)	0.07 (0.06)
Cl	0.00	nd	0.01 (0.00)	nd	0.00	0.01 (0.01)
O=F	-0.02 (0.01)	-0.020	0.00	-0.01	-0.01	-0.03
O=Cl	0.00				0.00	0.00
Total	88.88 (0.43)	87.080 (0.57)	88.25 (0.13)	89.21 (0.44)	88.41 (0.19)	89.31 (0.21)
Difference	11.12	12.920	11.75	10.79	11.59	10.69
Mg#	61.12 (7.68)	66.05 (9.21)	66.44 (6.45)	55.27 (0.41)	55.78 (4.75)	54.95 (5.18)

cations/18 O	se	se	se	se	se	se
Si	6.13 (0.08)	6.03 (0.06)	6.10 (0.03)	6.24 (0.02)	6.15 (0.02)	6.28 (0.03)
Be by DIFF	2.46	2.61	2.59	2.35	2.58	2.37
total T sites	8.59 (0.07)	8.65 (0.07)	8.69 (0.04)	8.59 (0.02)	8.71 (0.03)	8.65 (0.03)
Al	1.84 (0.03)	1.87 (0.02)	1.78 (0.02)	1.92 (0.01)	1.74 (0.01)	1.72 (0.02)
Mg	0.27 (0.02)	0.16 (0.02)	0.29 (0.02)	0.13 (0.04)	0.24 (0.02)	0.21 (0.02)
Fe2+	0.17 (0.02)	0.08 (0.00)	0.14 (0.01)	0.10 (0.00)	0.19 (0.01)	0.17 (0.01)
total M site	2.28 (0.04)	2.12 (0.03)	2.21 (0.04)	2.15 (0.04)	2.17 (0.02)	2.10 (0.03)
total	10.87 (0.07)	10.96 (0.07)	10.90 (0.05)	10.74 (0.05)	10.88 (0.03)	10.75 (0.04)

channel occupants/18 O	se	se	se	se	se	se
Ca	0.01 (0.00)	0.01 (0.00)	0.01 (0.00)	0.00	0.00	0.00
Na	0.10 (0.01)	0.06 (0.00)	0.10 (0.01)	0.05 (0.02)	0.08 (0.01)	0.09 (0.01)
K	0.04 (0.01)	0.03 (0.01)	0.06 (0.01)	0.05 (0.02)	0.10 (0.01)	0.11 (0.01)
H ₂ O	-	-	-	-	-	-
total	0.15 (0.02)	0.11 (0.01)	0.17 (0.01)	0.10 (0.02)	0.18 (0.01)	0.20 (0.01)

(b) Relict & Representative Beryl Grown from Haplogranite Melts

BeP-51	¹ Be-27	Be-10	Be-20
SP-Mus3-Be			
730-F (21)			850-F (6)
875-R (38)	700-F (35)	750-F (28)	750-R (28)
Crd,(Bri),Bt,Mt, Kfs,Mus,Cor			
10	12	12	12

se	sd	sd	sd
87.71 (0.18)	66.92 (0.29)	67.01 (0.39)	67.32 (0.39)
0.00	0.00	0.01 (0.01)	0.01 (0.01)
19.00 (0.04)	20.37 (0.12)	20.47 (0.22)	19.34 (0.16)
0.45 (0.03)	0.04 (0.01)	0.04 (0.01)	0.03 (0.01)
0.01 (0.00)	0.01 (0.00)	0.01 (0.00)	0.01 (0.00)
0.01 (0.01)	0.01 (0.01)	0.03 (0.01)	0.02 (0.01)
0.01 (0.00)	nd	nd	nd
0.01 (0.00)	0.01 (0.00)	0.01 (0.00)	0.01 (0.00)
0.01 (0.01)	nd	nd	nd
0.03 (0.00)	0.44 (0.09)	0.30 (0.03)	0.21 (0.03)
0.04 (0.01)	0.18 (0.03)	0.17 (0.02)	0.18 (0.04)
0.01 (0.01)	0.26 (0.03)	0.09 (0.02)	0.19 (0.02)
0.01 (0.00)	nd	nd	nd
0.00	-0.11	-0.04	-0.08
0.00			
87.29 (0.14)	88.13 (0.33)	88.10 (0.45)	87.24 (0.42)
12.71	11.87	11.90	12.76
-	-	-	-

se	sd	sd	sd
6.09 (0.02)	6.05 (0.02)	6.05 (0.03)	6.05 (0.03)
2.75	2.83	2.81	2.73
8.84 (0.02)	8.68 (0.02)	8.66 (0.03)	8.78 (0.03)
2.01 (0.01)	2.17 (0.01)	2.18 (0.01)	2.05 (0.01)
0.00	0.00	0.00	0.00
0.03 (0.00)	0.00	0.00	0.00
2.04 (0.01)	2.17 (0.01)	2.18 (0.01)	2.05 (0.01)
10.88 (0.02)	10.85 (0.03)	10.84 (0.04)	10.83 (0.03)

se	sd	sd	sd
0.00	0.00	0.00	0.00
0.01 (0.00)	0.08 (0.01)	0.05 (0.00)	0.04 (0.00)
0.00 (0.00)	0.02 (0.00)	0.02 (0.00)	0.02 (0.00)
-	-	-	-
0.01 (0.00)	0.10 (0.01)	0.07 (0.00)	0.06 (0.00)

¹ Experiments designated "Be-" represent beryl crystallized from water-saturated haplogranite melts (from Evensen 1997).

55

Table 2-6. Calculated temperature convergence among alkalis, excess Si, Al and Be using regressions of Figure 12

Reference	Partial BeCrd Compositions (apfu)					Calculated Temperatures					Mean Values	
	Na	K	(ex)Si	Al	Be	Na	K	(ex)Si	Al	Be	Na,K,Si,Al,Be	Si,Al,Be
												mean sd
1	0.38	0.04	-	3.73	0.27	483	703		678	684	578 (159)	681 (4)
1	0.40	-	5.06	3.62	0.27	451		706	695	684	634 (123)	695 (11)
1	0.42	-	-	3.69	0.30	418			684	692	598 (156)	688 (6)
1	0.35	-	-	3.75	0.23	531			675	672	626 (82)	673 (2)
1	0.35	-	5.07	3.65	0.23	531		709	690	672	651 (81)	690 (19)
2	0.30	0.09	5.02	3.60	0.41	609	895	695	698	720	674 (153)	704 (14)
3	0.32	-	-	3.76	0.21	580			673	666	639 (52)	669 (5)
3	0.25	-	-	3.85	0.16	693			658	649	667 (23)	653 (7)
3	0.23	-	-	3.91	0.15	725			649	645	673 (45)	647 (3)
3	0.25	-	-	3.81	0.17	693			665	652	670 (21)	659 (9)
3	0.27	-	5.06	3.74	0.17	661		706	676	652	674 (24)	678 (27)
4	0.27	-	-	3.76	0.52	661			673	748	694 (47)	710 (53)
4	0.33	-	-	3.77	-	564			671		617 (76)	671
5	0.25	0.00	-	3.76	0.23	688	549		673	673	672 (81)	673 (0)
6	0.28	0.07	-	4.03	-	649	807		629		659 (108)	629
6	0.17	0.04	-	4.05	-	817	703		625		759 (117)	625
6	0.30	0.00	-	3.74	0.36	619	549		676	707	643 (61)	692 (22)
7	0.40	0.07	-	3.52	0.44	451	828		710	728	586 (252)	719 (12)
8	0.17	-	-	3.88	0.13	822			653	637	704 (102)	645 (12)

1, Gordillo et al., 1985; 2, Povondra et al., 1984; 3, Armbruster and Irouschek 1983; 4, Selkregg and Bloss 1980;

5, Schreyer et al., 1979; 6, Povondra and Cech 1978; 7, Cerny and Povondra 1966; 8, Newton 1966.

Aluminum and Be T-values shown are means from 3 different statistical fits (linear, polynomial, & exponential or logarithmic). The first column of mean values utilizes all values; the second column reflects Si, Be and Al data only. Precision is reported in parantheses beside calculated values using 1 standard deviation of the mean.

Table 2-7. Elemental partitioning data between beryllian cordierite and granitic melt

Trace elements.	<i>T</i> -independent	<i>T</i> -dependent					linear fit	<i>r</i> ² value
		675 °C	700 °C	750 °C	800 °C	850 °C		
<i>D</i> _{Ca}	0.45 (0.06)							0.0371
<i>D</i> _{Mn}		8.67 (3.34)	10.09 (0.06)	5.50 (0.29)	3.24 (0.15)	1.25 (0.27)	$D_{Mn}^{Crd/MELT} = 47.87 - 0.06(T)$	0.8930
<i>D</i> _{Li}	0.40 (0.03)							0.1672
<i>D</i> _B	0.05 (0.01)							0.0127
<i>D</i> _{Rb}		0.18 (0.01)	0.30 (0.02)	0.28 (0.03)	0.32 (0.04)	0.27 (0.01)	$D_{Rb}^{Crd/MELT} = 0.09 + 2.52e^{-4}(T)$	0.0168
<i>D</i> _{Cs}		0.64 (0.03)	0.69 (0.19)	1.06 (0.08)	1.15 -	1.28 (0.17)	$D_{Cs}^{Crd/MELT} = -2.14 + 4.11e^{-3}(T)$	0.6648
Major elements.								
Be		26.59 (0.43)	19.50 (0.62)	15.11 (0.22)	13.99 (0.45)	15.14 (0.48)	$[Be]_{Crd/MELT} = 59.32 - 0.06(T)$	0.4292
Si		0.70 (0.01)	0.71 (0.00)	0.74 (0.00)	0.75 (0.00)	0.85 (0.02)	$[Si]_{Crd/MELT} = 0.21 + 7.11e^{-4}(T)$	0.8169
Al		2.22 (0.06)	2.31 (0.01)	2.18 (0.02)	2.08 (0.03)	1.50 (0.08)	$[Al]_{Crd/MELT} = 4.87 - 3.66e^{-3}(T)$	0.6780
Fe		17.23 (1.58)	12.06 (0.26)	5.62 (0.19)	4.09 (0.10)	2.13 (0.39)	$[Fe]_{Crd/MELT} = 68.84 - 0.08(T)$	0.8287
Mg		94.00 (9.65)	74.59 (2.07)	47.71 (0.38)	30.07 (0.17)	17.13 (0.52)	$[Mg]_{Crd/MELT} = 3.78e2 - 0.43(T)$	0.8546

Table 2-8. Reported assemblages of Be-cordierite and other Be-minerals

Be-Mineral Assemblage	Occurrence	Reference
Be-Crd + Btr	pegmatite	Henderson 1975, Povondra & Čech 1978
Be-Crd	wallrock alteration near pegmatite	Schreyer et al., 1979
Be-Crd	leucocratic gneiss proximal to Bt schist	Armbruster & Irouschek 1983
Be-Crd + Brl	pegmatite core margin	Povandra et al., 1984
Be-Crd + Brl	pegmatite-wallrock mixing region	Gordillo et al., 1985
Be-Crd + Brl	pegmatite to	Černý et al., 1995 (referring to Černý & Povondra 1966)
Be-Crd + Brl	pegmatite core margin	Jobin-Bevans & Černý 1998

Btr = bertrandite, which may become stable at the expense of beryl at lower *T* conditions (e.g., Barton 1986; Jacobson 1993).

Figure Captions

Figure 2-1. Calibrated working curve for the analysis of Be using Secondary Ion Mass Spectrometry. Ten data points are shown; most data plot on top of one another. Calibrations are shown for two analytical sessions, which took place 9 mo. apart but were highly reproducible. Standards consist of Be-doped synthetic rhyolitic glasses (Evensen 1997). Total propagated precision is shown with error bars.

Figure 2-2. Backscattered electron micrographs: Experimental products and assemblages. Image scale is shown in micrometers. Labeled phase abbreviations include: Crd=cordierite, Brl=beryl, Bt=biotite, Mus=muscovite, Mt=magnetite, Pl=plagioclase, Qtz=quartz, and gl=glass. Relict crystals are designated "(r)". (a) Secondary electron image showing cordierite growth, as typical coarse crystals, from a cordierite-free mixture using reactions [2] and [4]. Experiment BeP-51. (b) This image shows the stable assemblage Crd+Brl+Bt+Mt+Pl+Qtz+melt+vapor at 700°C. Experiment BeP-53. (c) The 750°C crystalline assemblage Crd+Brl+Bt+Mt+ melt is portrayed. Note that Brl nucleates on Crd. Experiment BeP-54. (d) The reversed assemblage at 700°C shows nucleation and growth relations among Crd and relict Brl. Experiment BeP-41. (e) Here, an 800°C reversal reveals 2 generations of Crd growth (at 850 vs. 800°C) that result in a Be-richer core relative to the crystal rim. The Be-Crd assemblage consumed the starting beryl at high T , so that the melt did not contain adequate Be contents to achieve Brl saturation at lower T . Experiment BeP-4. (f) A reversal to 675°C with the K-

and Al-rich starting mixture records abundant nucleation of Mus; Kfs is also part of the magmatic assemblage (not shown). Experiment BeP-52.

Figure 2-3. Backscattered electron micrographs: Cordierite – beryl assemblages and textures. (a) Nucleation of fine-scale “stag horn” beryl crystals on cordierite is shown. Prismatic growth of beryl extends outward along a-axes of the host Crd. Experiment BeP-43. (b) Inherited crystallographic relations are evidenced by continuous growth among [1], Be-rich Crd (I) grown at 850°C, followed by [2] simultaneous nucleation and growth at 700°C of a less Be-rich Crd (II) (along {1100}) and by beryl (along {1000}). Experiment BeP-18. (c) Two generations of growth with view parallel to a- and c-axes is shown. In this run, early Be-rich Crd I is rimmed by Crd II + beryl at lower T . At lower center of the image, stag horn beryl crystal growth is seen extending from {0001} of Be-cordierite, but only near the (faster-growing) corners of Crd I crystals. Cordierite II dominates growth in all other crystallographic dimensions. In the upper part of the image, Crd II nucleates and grows along {1100} while beryl, once again, dominates growth along the more efficient {1000} direction, despite less volumetric growth compared to Crd II. Experiment BeP-18. (d) Beryllian Crd and Brl relations in the same experiment in which beryl nucleation and growth at lower T is related to the higher T Be-Crd by simple twinning (along {1000}). New beryl growth also mimics that of the 850°C Be-rich Crd, showing faceted growth predominantly along corners; gaps in both Be-rich Crd and Brl are filled by (less dense) Crd II.

Figure 2-4. Backscattered electron micrographs: Reaction relationships among beryl – phenakite – and seeded cordierite. (a) Reversed experiment with new cordierite showing two generations of growth, one at 850°C, followed by rimming of Crd of lower Be content at 800°C. The center crystal hosts an anhedral phenakite inclusion near its core—suggesting nucleation by Crd—as well as growth inclusions of magnetite. Experiment BeP-16. (b) Forward-direction cordierite dissolution experiment at 800°C in which dissolving Crd reacted with phenakite to form overgrowths of new Be-rich Crd. Other products include new crystals of beryl. Following reaction [5], all Crd is armored by new Be-rich Crd. Experiment BeP-91. (c) Forward-direction cordierite dissolution experiment at 750°C that contained Phn in its starting mixture. Textural relations show that former Crd serves as a nucleation substrate for both new Be-Crd and Brl, which completely armor all relict Crd grains. Experiment BeP-90. (d) Reversed experiment containing beryl. Here, relict beryl that partly dissolved at 800°C served as a growth site for both Fe- and Mg-bearing new beryl and Be-rich cordierite, which armored it at 750°C. Experiment BeP-43.

Figure 2-5. Beryllium contents of granitic melt at beryllian cordierite \pm beryl saturation. Upward-pointing triangles indicate forward-direction experiments; downward-pointing triangles indicate reverse-direction experiments. Beryllian cordierite coexists with beryl in all melts except for the lower Be content reversals to 700, 750, and 800°C along with the 850°C data point. The dash curves delineate beryl-bearing granitic melts (from Evensen et al., 1999) for comparison. The beryl-bearing melt curves bracket, in values of ASI, the Be-cordierite-bearing melts.

Figure 2-6. Total tetrahedral versus total octahedral site occupancy among Be-cordierite formulae. Data cluster around the dashed line, which delineates ideal cation occupancy (sum of tetrahedral and octahedral cations = 11.0). Stoichiometric cordierite is shown by an open hexagon for comparison. Upward-pointing triangles indicate cordierite crystallized in forward-direction experiments; downward-pointing triangles indicate cordierite grown in reversed-direction. Total propagated error of recalculated mineral formula constituents is shown.

Figure 2-7. Elemental constituents of cordierite as a function of temperature. Analyses from 12 experiments are shown. Cordierite grown in the forward-direction is designated by upward-pointing triangles; downward-pointing triangles indicate reversed growth. The x-axis is equivalent in all plots; y-axes vary in scale. Linear regressions and their results are shown.

Figure 2-8. Total occupancy at the tetrahedral sites for Be-cordierite. The solid line represents a linear regression of experimental data (statistics are shown). The dashed line delineates ideal occupancy (sum of tetrahedral cations = 9.0). The direction of increasing temperature is shown. Gray circles indicate stoichiometric cordierite at left and $\text{Mg}_2\text{BeAl}_2\text{Si}_6\text{O}_{18}$ (Hölscher and Schreyer 1989) at right. Total propagated precision of mineral formulas is shown.

Figure 2-9. Be coupled-exchange mechanics in cordierite with temperature.

Aluminum loss is accounted for by Be + excess Si. Both Na + K and excess Si are needed to account for substituted Be in all cases except for one, in which Na + K account for all exchanged Be (points plot nearly on top of one another). The thick line depicts Na + K contents; its curvature results from increasing K content at higher temperatures, despite falling Na concentrations. Linear, 2nd or 3rd order polynomial regressions for each data set are shown at right.

Figure 2-10. Beryllium substitution mechanisms in cordierite. The exchange operators vary inversely with temperature. The $\text{Be}^{[4,T1]}\text{Si}^{[4,T2]}\text{Al}^{[4,T1,T2]}_{-2}$ exchange dominates at higher temperatures, and reaches a far greater magnitude (note the absolute scales) than seen by $\text{Be}^{[4,T1]}(\text{Na,K})^{[\text{chl}]} \text{Al}^{[4,T1]}_{-1}$. Linear regression of the data and its fit are shown.

Figure 2-11. Mean values of Be-exchange constituents with temperature (from Figure 9). Be incorporation into Al *T1* and *T2* sites of cordierite is compensated by additions of channel Na and K plus excess Si. Excess Si occupancy in *T2* sites increases rapidly with temperature. The Na- and K-coupled Be exchange operator decreases with *T*, yet absolute contents of K rise. Total column values decrease or rise due to alkali gain or loss of cordierite. Column widths reflect propagated total error of thermocouple read values ($\pm 7.2^\circ\text{C}$); propagated (vertical) precision for partial formula totals is ± 0.03 apfu.

Figure 2-12. Variations of cordierite channel-occupying constituents with *T*. Mean values are shown from 15 total experiments. (a) Total channel constituents. (b) Major

alkali constituents. Sodium contents decrease while potassium contents steadily rise to become equivalent at 900°C—a reflection of channel widening with *T*. Column widths reflect propagated total error of thermocouple read values ($\pm 7.5^\circ\text{C}$); propagated (vertical) precision for partial formulas in (b) is less than ± 0.01 apfu.

Figure 2-13a. Elemental partitioning ratios between Be-cordierite and coexisting silicic melt from 675-850°C for cordierite-essential constituents. Linear regressions are shown (values are in Table 7).

Figure 2-13b. Elemental partitioning ratios between Be-cordierite and coexisting silicic melt from 675-850°C for trace constituents. Highlighted titles indicate compatible behavior. Note vertical axis scale variation between plots as magnitude of *D* ratios changes; the horizontal scale for all plots is constant. The linear regression for the Cs plot does not include a 800°C outlier, though it is shown. Results of regressions are shown in Table 7. Ten experiments are shown. For data determined by SIMS but reported in single (Tables 2-3), estimated precision is depicted.

Figure 2-14. Concentrations of element oxides between coexisting cordierite and granitic melt. Temperature increases from left to right in each plot. Linear regressions and their statistics are shown. The regression for the Mn plot does not include a 675°C outlier, though it is shown.

Figure 2-15. Elemental constituents of beryl as a function of temperature. Mean analyses from 6 experiments are shown. The x-axis is equivalent in all plots; y-axes vary in scale. Linear regressions and their results are shown. Total propagated error is shown with error bars for all elements except Be, which is estimated by difference.

Figure 2-16. Total tetrahedral versus total octahedral site occupancy among beryl formulae. Data cluster below the dashed line, which delineates ideal cation occupancy (sum of tetrahedral and octahedral cations = 11.0). Stoichiometric beryl is shown by an open circle. The direction of increasing temperature is indicated. Total propagated error of recalculated mineral formula constituents is shown for octahedral cations; Be is estimated by difference..

Figure 2-17. Variations of beryl octahedral constituents with T . Iron contents increase slightly while Mg contents show more scatter as a function of temperature. Column widths reflect propagated total error of thermocouple read values ($\pm 7.2^\circ\text{C}$); propagated (vertical) precision for partial formulas is less than ± 0.04 apfu..

Figure 2-18. Variations of beryl tetrahedral constituents with T . Decreases are seen for Be and excess octahedral Al with increasing temperature. Silicon increases over this interval as it begins filling $T1$ sites. Column widths reflect propagated total error of thermocouple read values ($\pm 7.2^\circ\text{C}$); propagated (vertical) minimum precision for partial formulas is ± 0.05 apfu.

Figure 2-19. Excess silicon vacancy exchange in beryl along the cordierite – beryl join. The Be-loss exchange operator varies principally with temperature (shown). Excess Si plus the sum of excess octahedral constituents compensate for half the Be lost, which results in a vacancy-forming exchange in *T1* sites. The linear regression (values are shown) of this Si charge-balanced substitution shows an excellent agreement with ideality (dashed line). Total propagated precision for excess Si is less than the symbol size.

Figure 2-20. Variations of beryl channel-occupying constituents with *T*. Mean values are shown. Sodium contents slightly decrease while potassium contents steadily increase with temperature. Column widths reflect propagated total error of thermocouple read values ($\pm 7.2^\circ\text{C}$); propagated (vertical) precision for partial formulas is less than ± 0.02 apfu.

Figure 2-21. Cordierite – beryl miscibility relations in granitic melts at 200 MPa as depicted in general form by Be apfu. Complete solid solution occurs between Crd and BeCrd, but a magmatic solvus separates Be-Crd from beryl compositions. Stability fields in this space are indicated. Linear regression data for the Crd side of the solvus are shown. The regression for the beryl side poorly represented the data ($r^2 = 0.366$); its dashed trend shown in non-statistical. BeO contents of experimental beryls were estimated by difference.

Figure 2-22. Cordierite – beryl miscibility relations in granitic melts at 200 MPa as measured by the total chemical operator, $\text{Be}_3\text{SiAl}_2(\text{Mg,Fe})_2$. This plot better represents the solution relations of Crd and Brl by accounting for all components of the exchange. Magmatic stability fields of cordierite solid solution, beryl solid solution, and cordierite plus beryl are shown. All solid symbols represent cordierite – beryl pairs. A slightly curved 3rd order polynomial representation best fits the Crd side of the Crd + Brl (+ L) field; its results are shown. The steeply dipping trend of beryl data is best represented by a 2nd order polynomial fit, which is shown.

Figure 2-23. Cordierite – beryl compositions plotted by their normalized tetrahedral and octahedral pseudo-ternary constituents. Tie lines connecting coexisting cordierite solid solution and beryl solid solution compositions are shown. Going from 900 to 700°C, the data trend toward Crd (Al-Fe+Mg join) and beryl (Be-Al join), respectively. The arrow indicates the compositional evolution of cordierite – beryl pairs upon cooling.

Figure 2-24. Ternary projection normalized to cordierite – beryl formulae. Because *Mg#* and Be content change in Crd and Brl with *T*, this plot reveals compositional changes during cooling. The region between the sets of arrows reflects the miscibility gap between Crd and Brl at 900°C, 200 MPa. Arrows indicate cooling trends of mean Be-cordierite and beryl solid solution compositions, based upon 22 analyses, from 900 to 675°C. Be-cordierite compositions become less beryllian, less magnesian, and more ferrous (and more sodic) with decreasing temperature. The cooling trend extrapolates directly to most natural Be-Crd data; the dashed curve represents a further extension,

possibly at subsolidus conditions, toward rarer natural data. With decreasing temperature, beryl compositions become less magnesian and ferrous, trending directly away from Mg- and Fe-bearing compositions, in roughly equal proportion. Previous compositions of experimental Crd, which contain abundant Na contents, are shown. Natural Be-bearing cordierite and beryl group minerals are shown, as are ideal and natural compositions of chemically related Be-Mg-Fe-Al-Si minerals are also plotted (Taf = taaffeite; Sur = surinamite; Be-Spr = Be-rich sapphirine, Stp = stoppaniite), indicating their potential for reaction relationships involving Be-cordierite solid solutions. Be-Spr plots beside the 700°C Crd_{SS} point. Natural Be-cordierite compositions are from: Černý and Povondra 1966; Newton 1966; Povondra and Čech 1978, Schreyer et al., 1979; Povondra et al., 1984; and Gordillo et al., 1985. Natural beryl compositions are from: Sosedko 1957; Schaller et al., 1962; and Ferraris et al., 1998.

Figure 2-1.

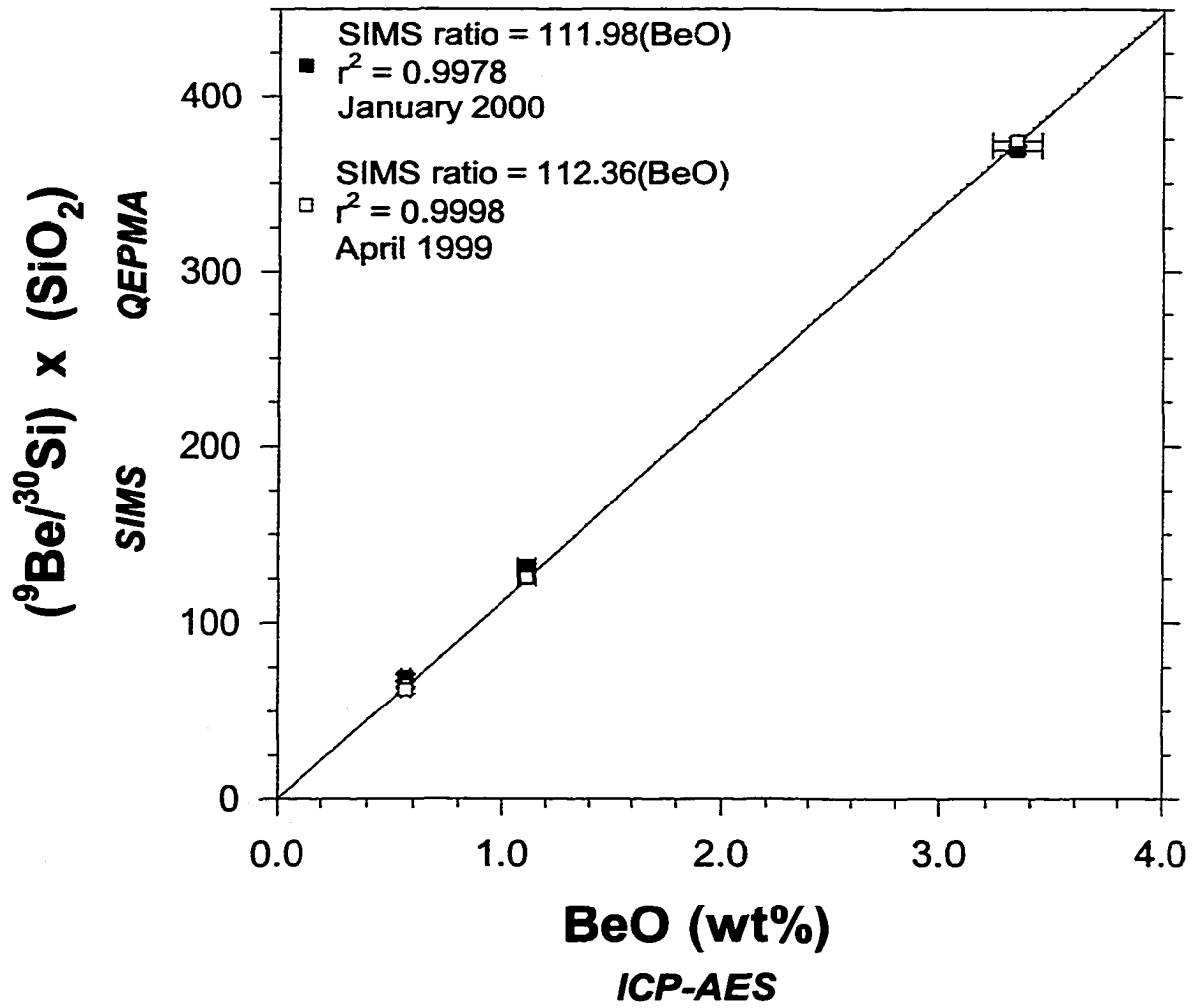


Figure 2-2.

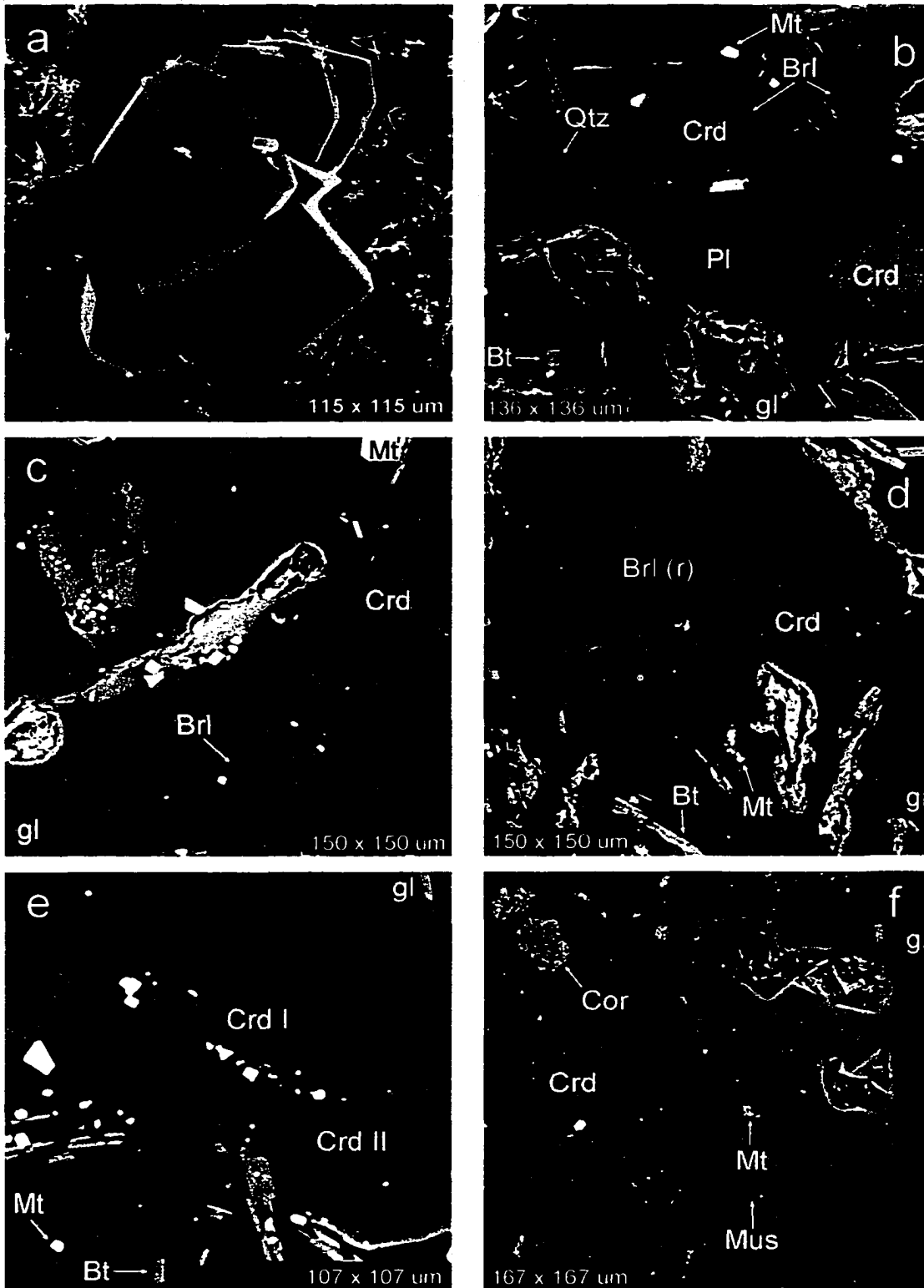


Figure 2-3.

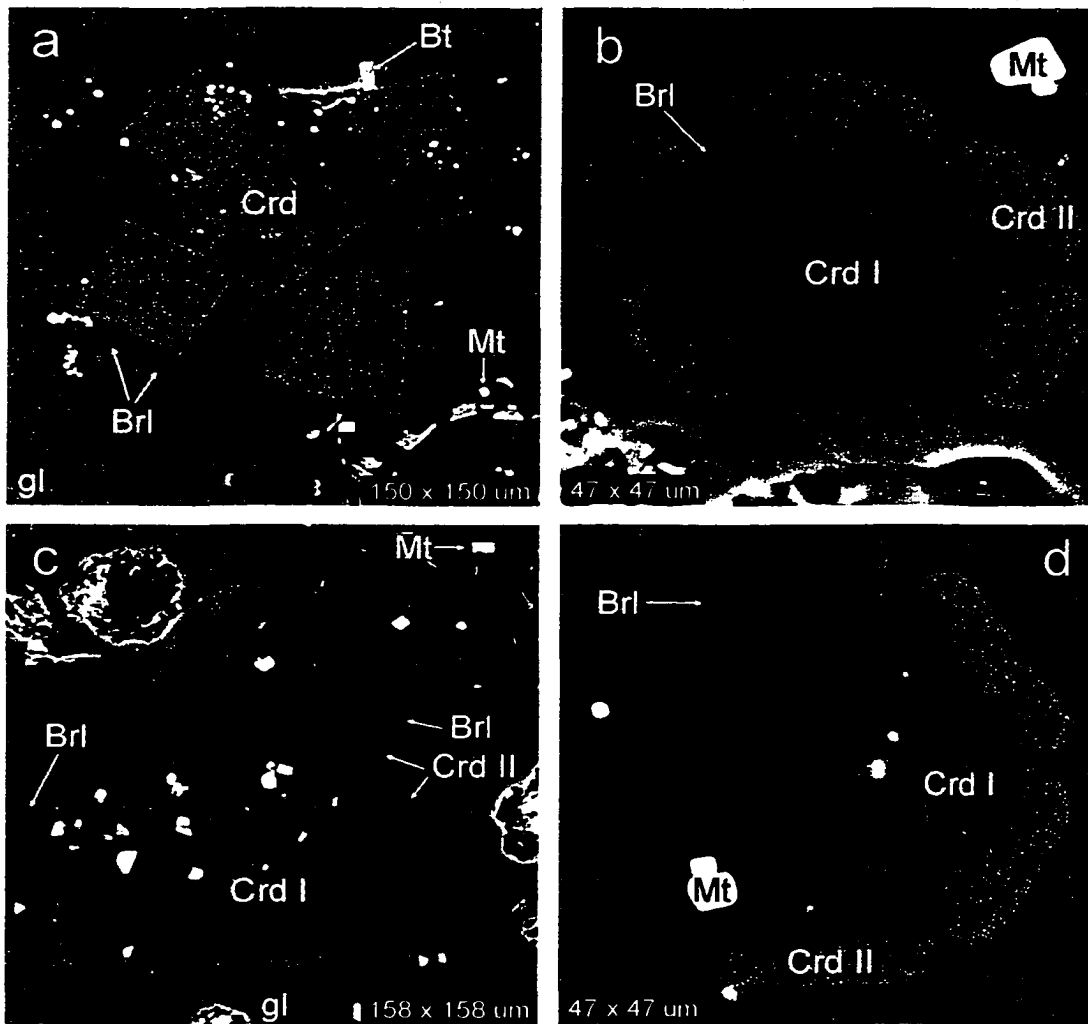


Figure 2-4.

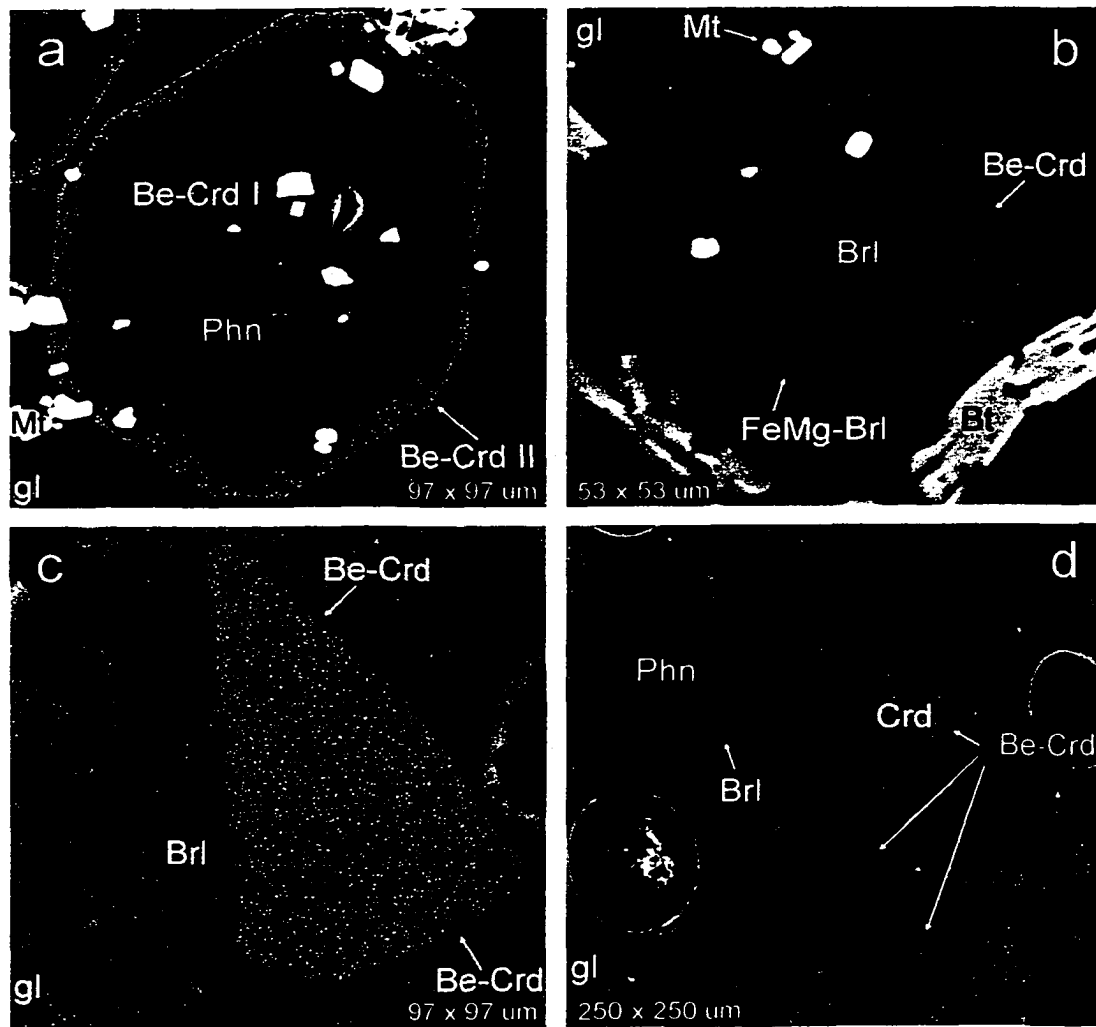


Figure 2-5.

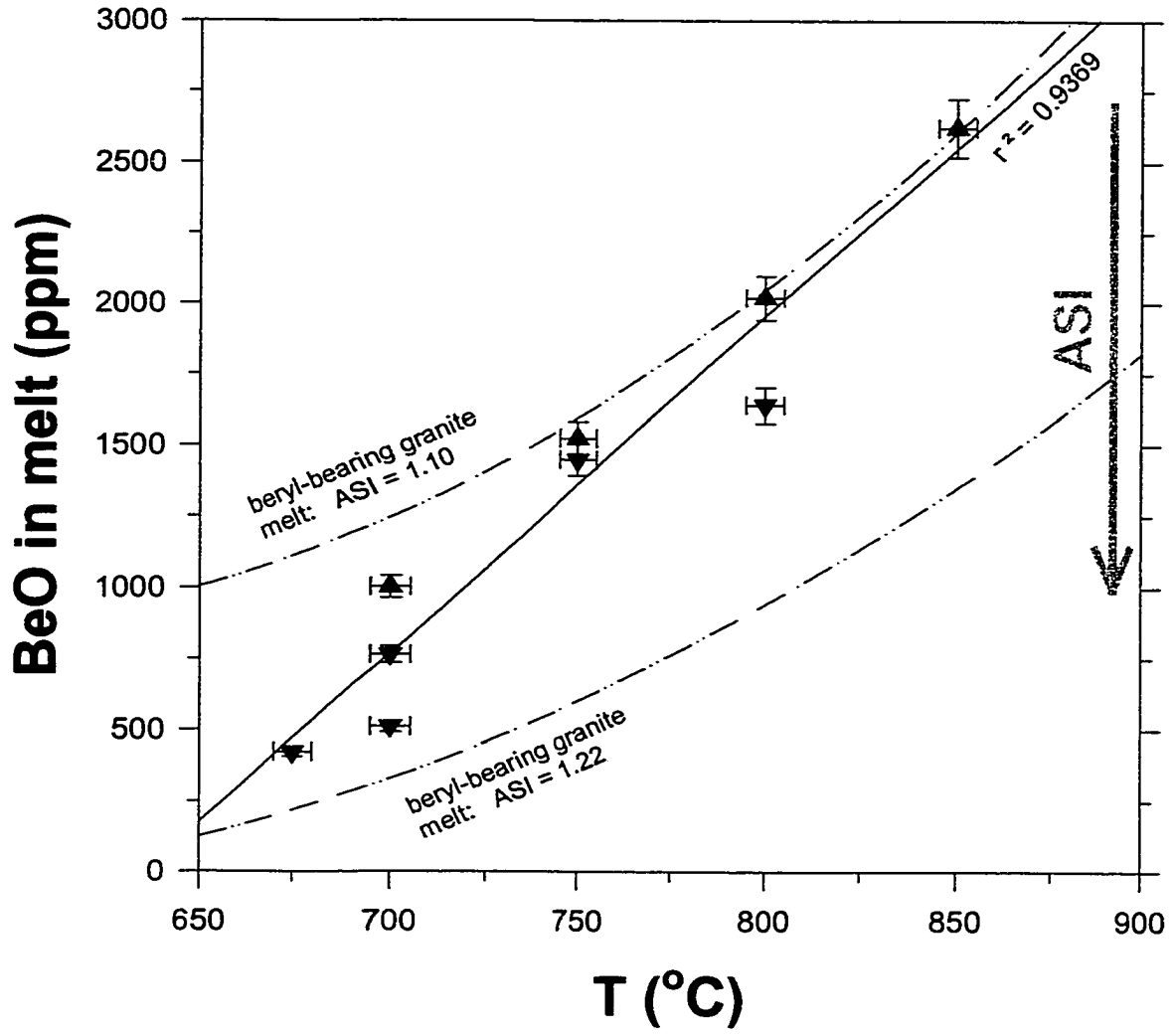


Figure 2-6.

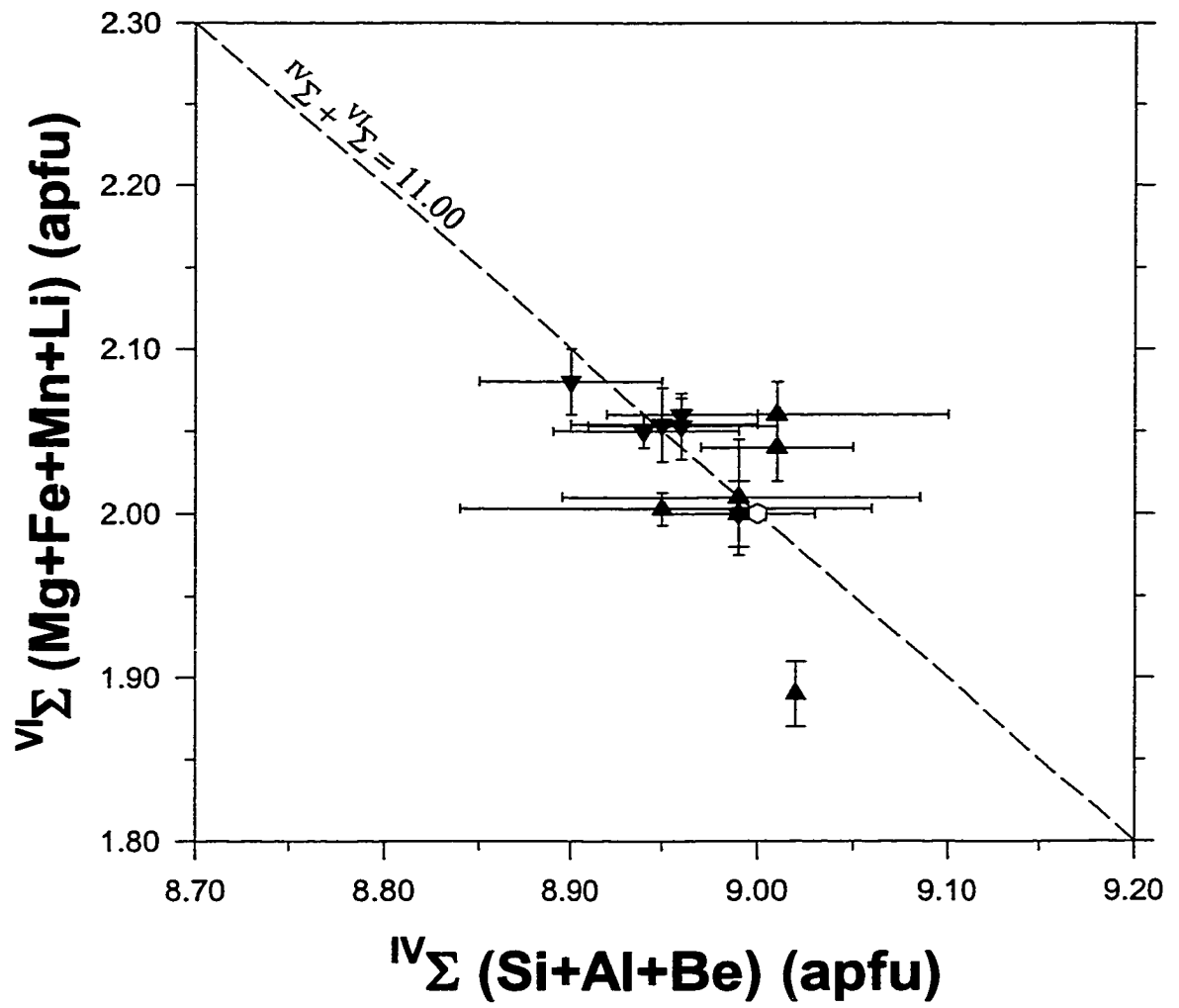


Figure 2-7.

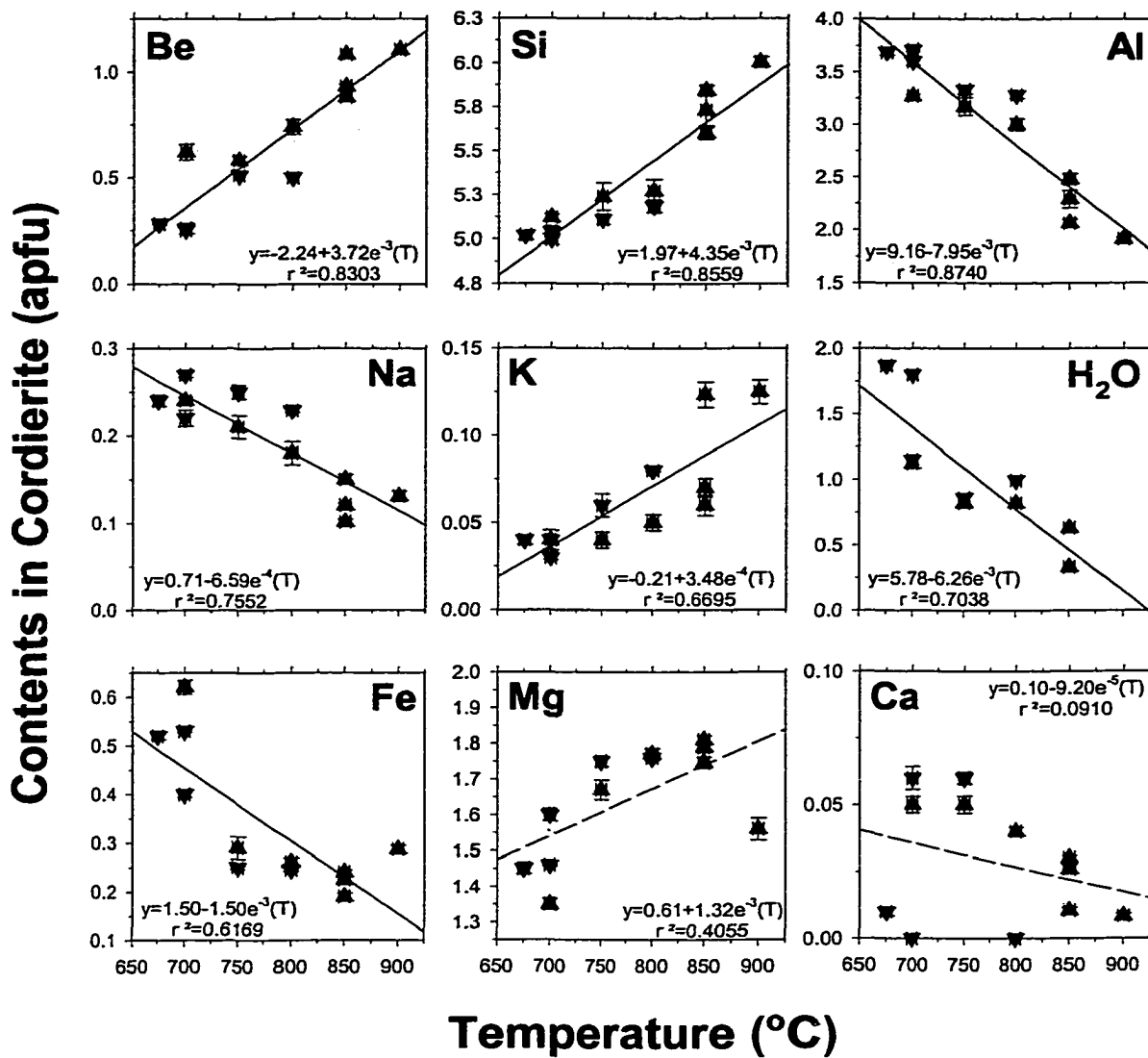


Figure 2-8.

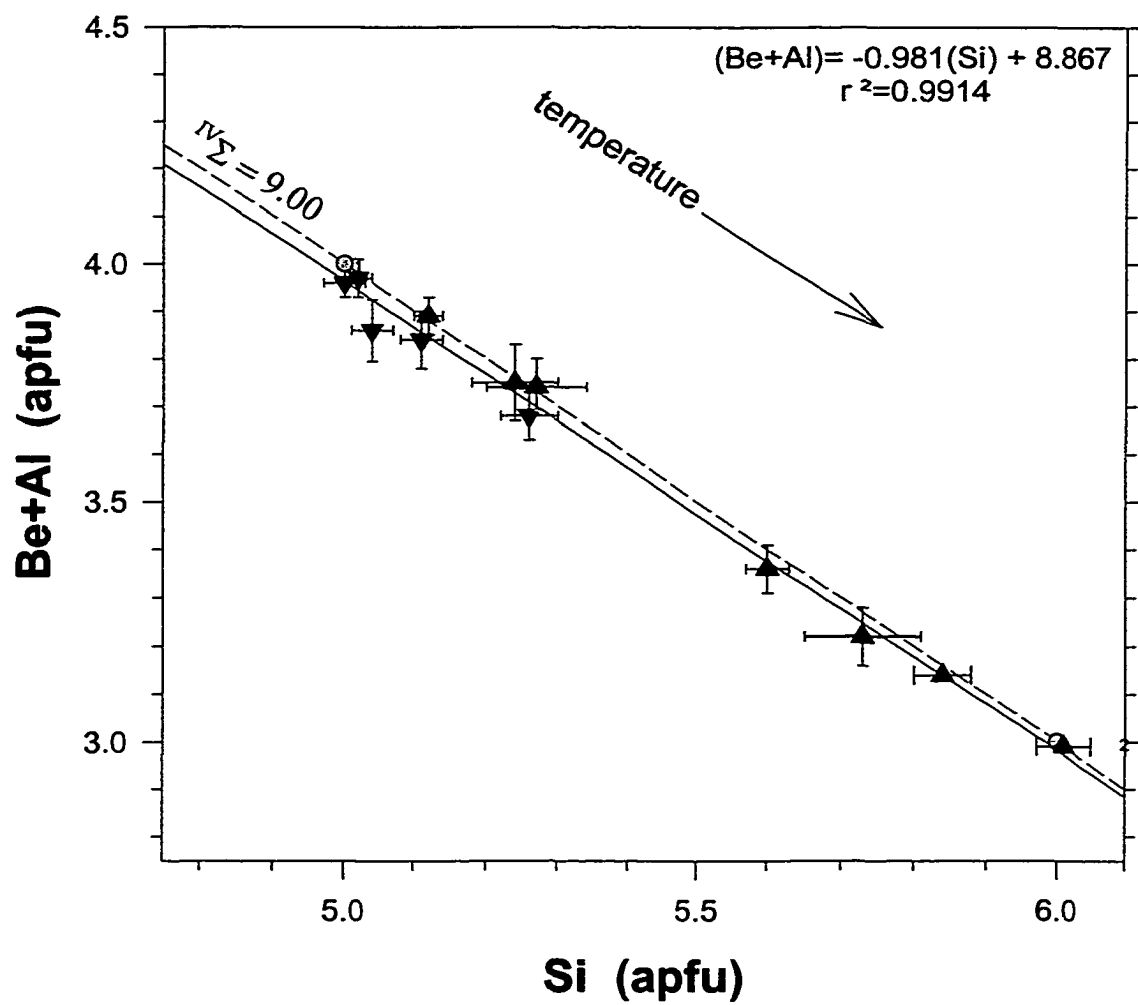


Figure 2-9.

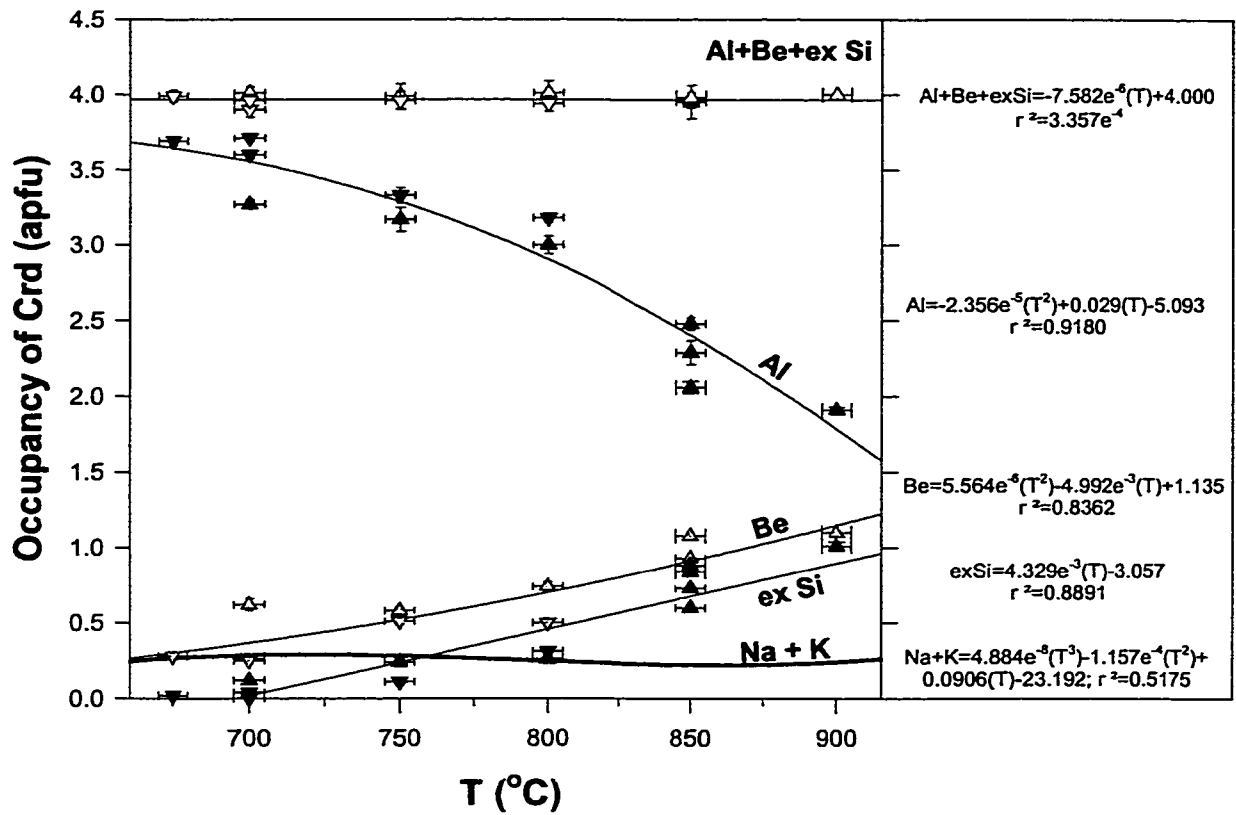


Figure 2-10.

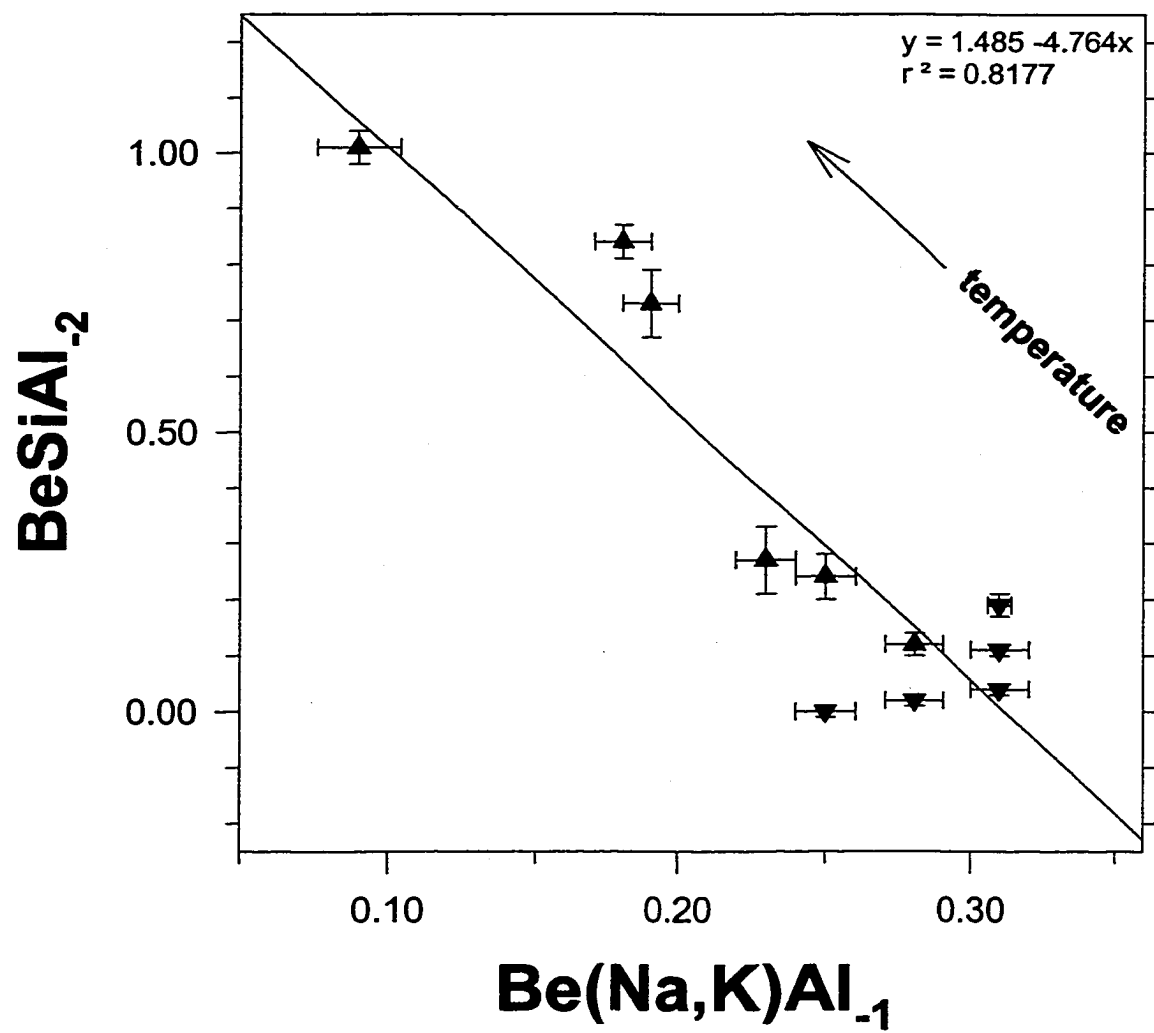


Figure 2-11.

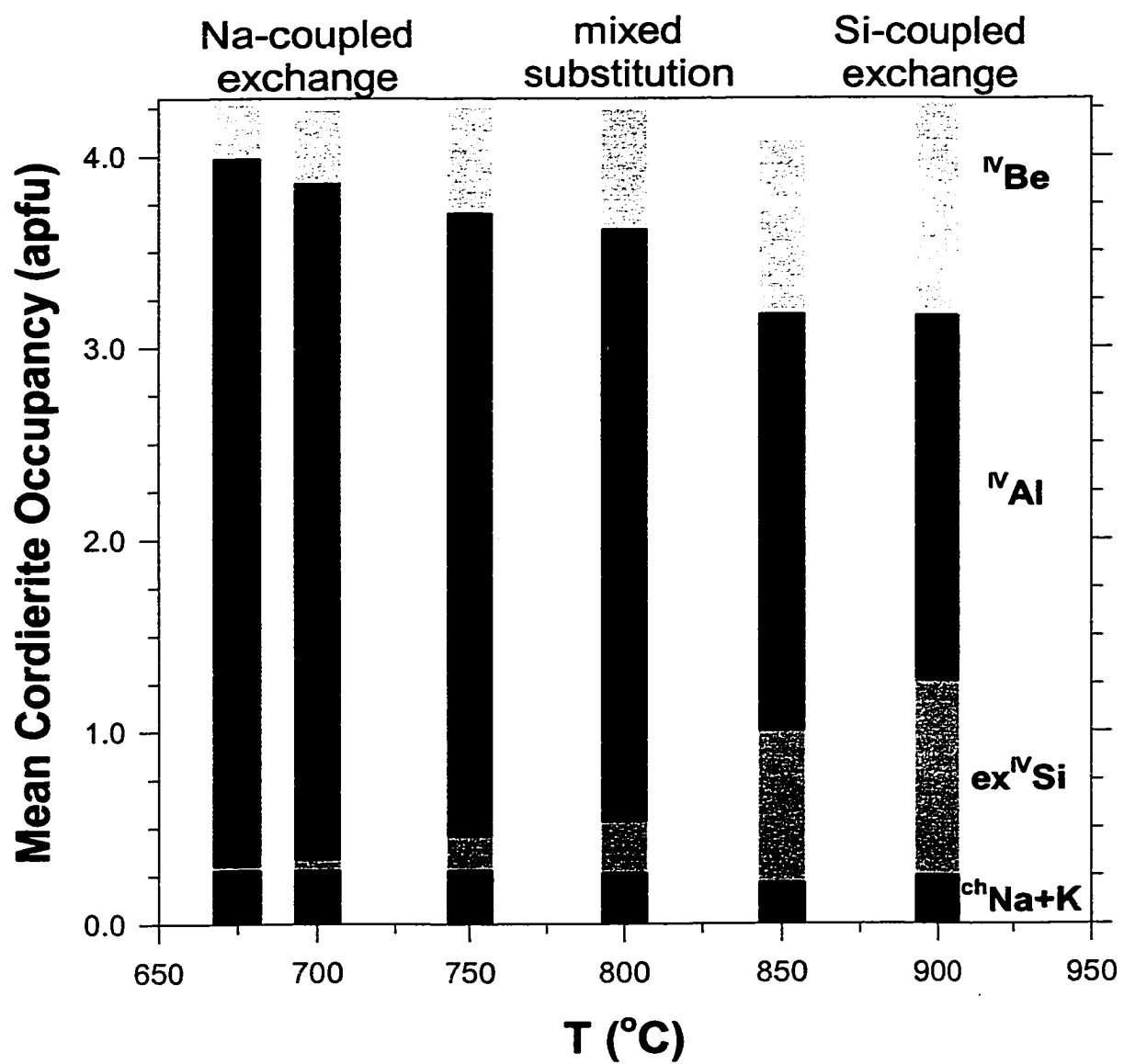


Figure 2-12.

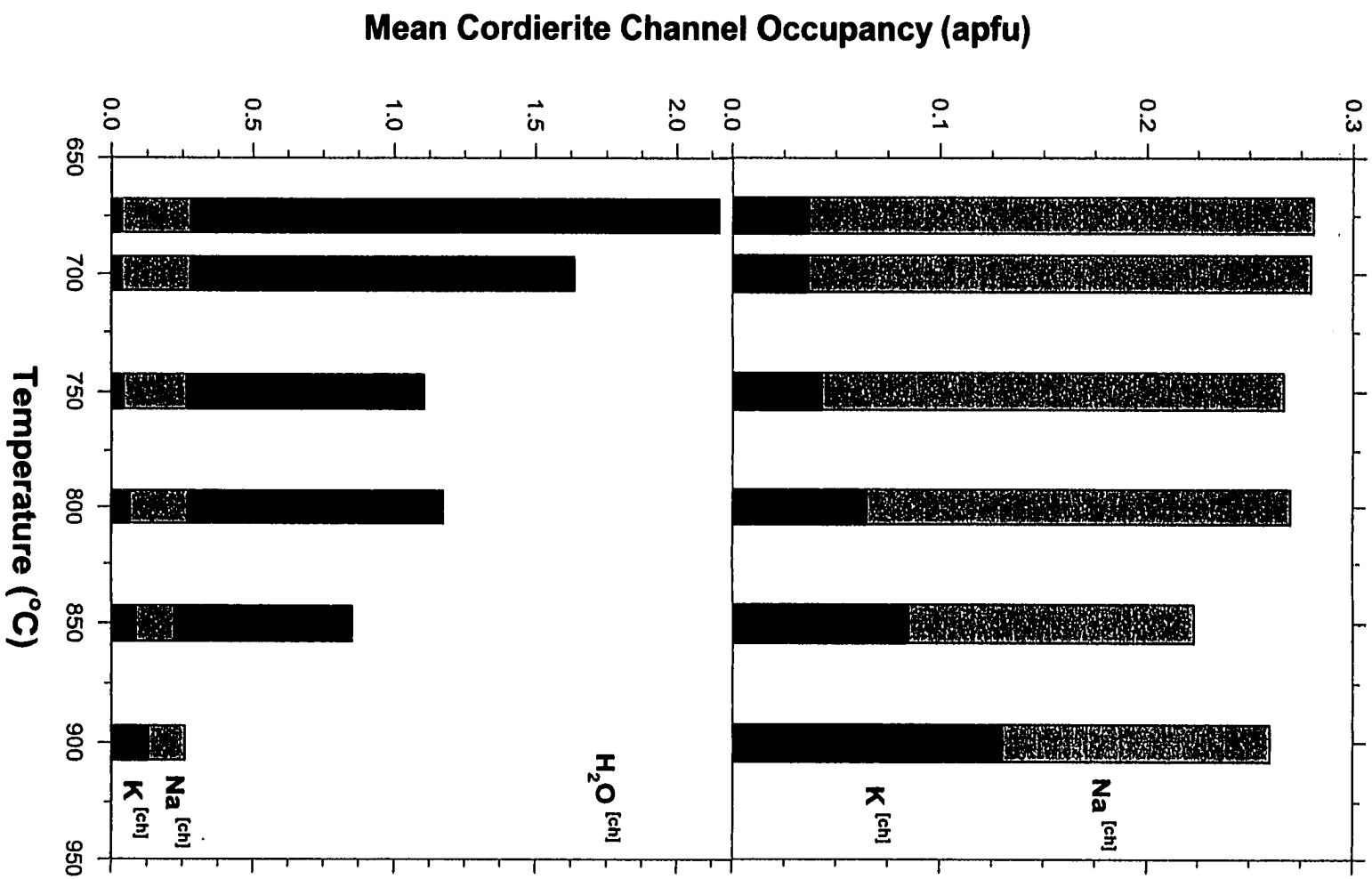


Figure 2-13a.

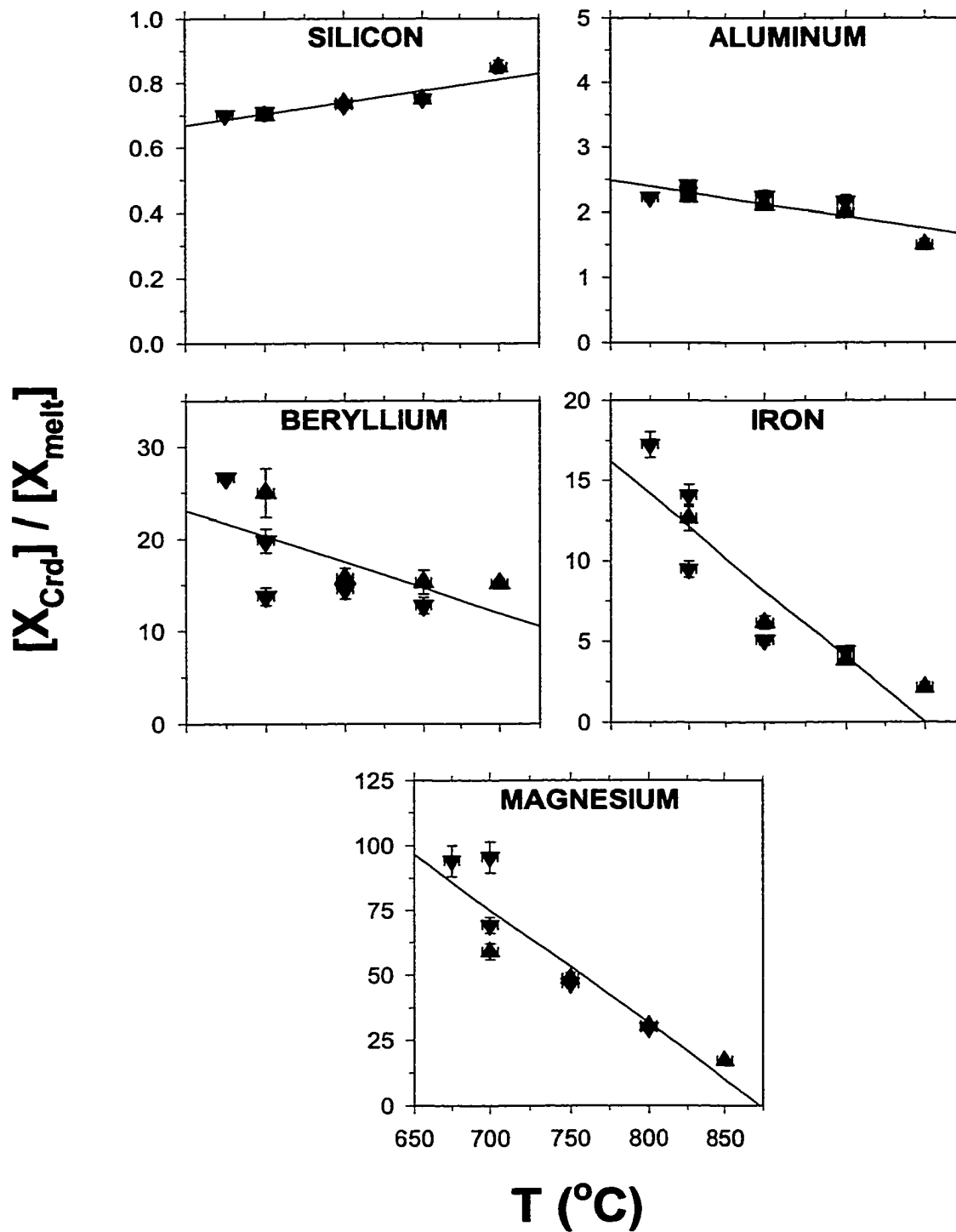


Figure 2-13b.

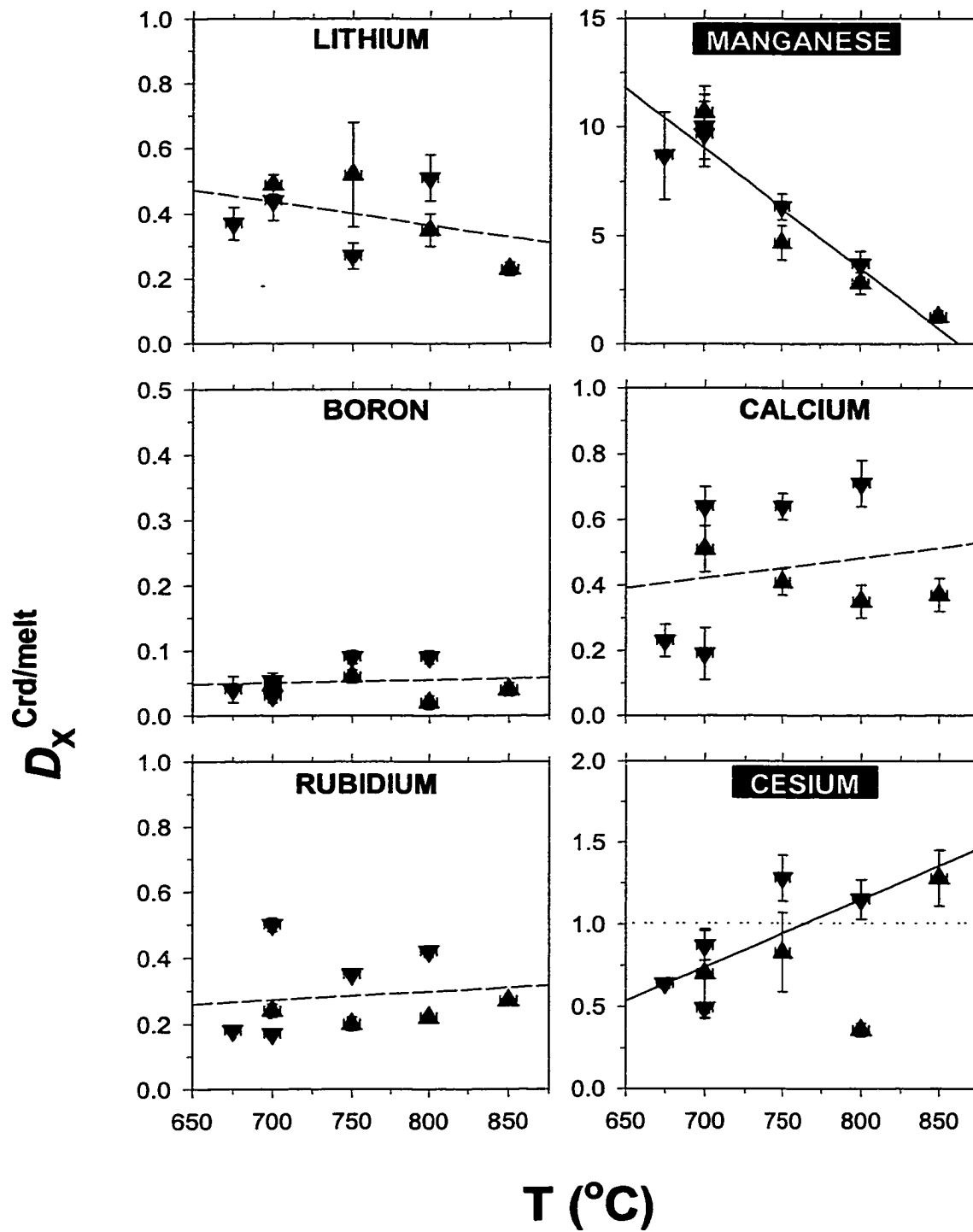


Figure 2-14.

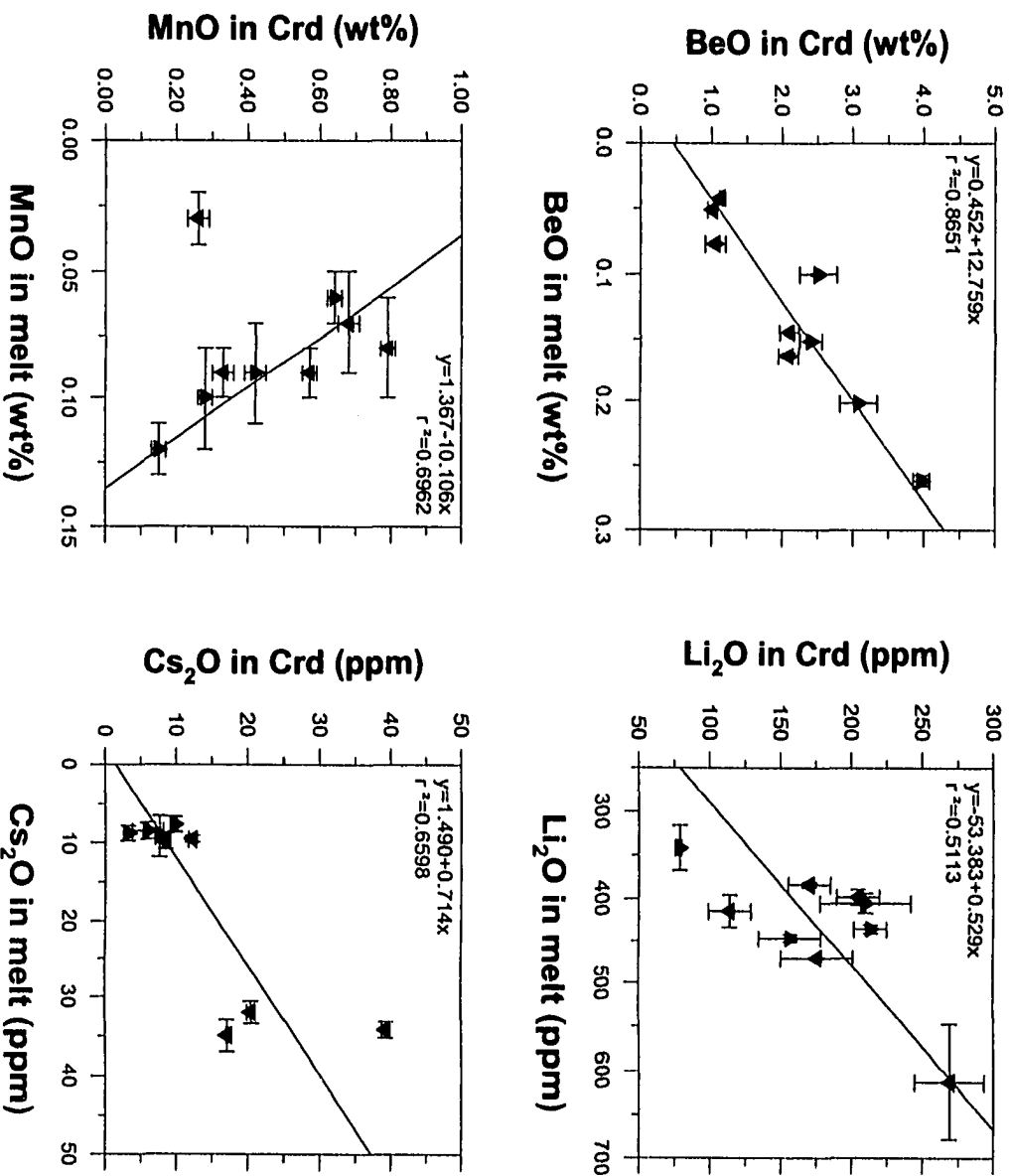


Figure 2-15.

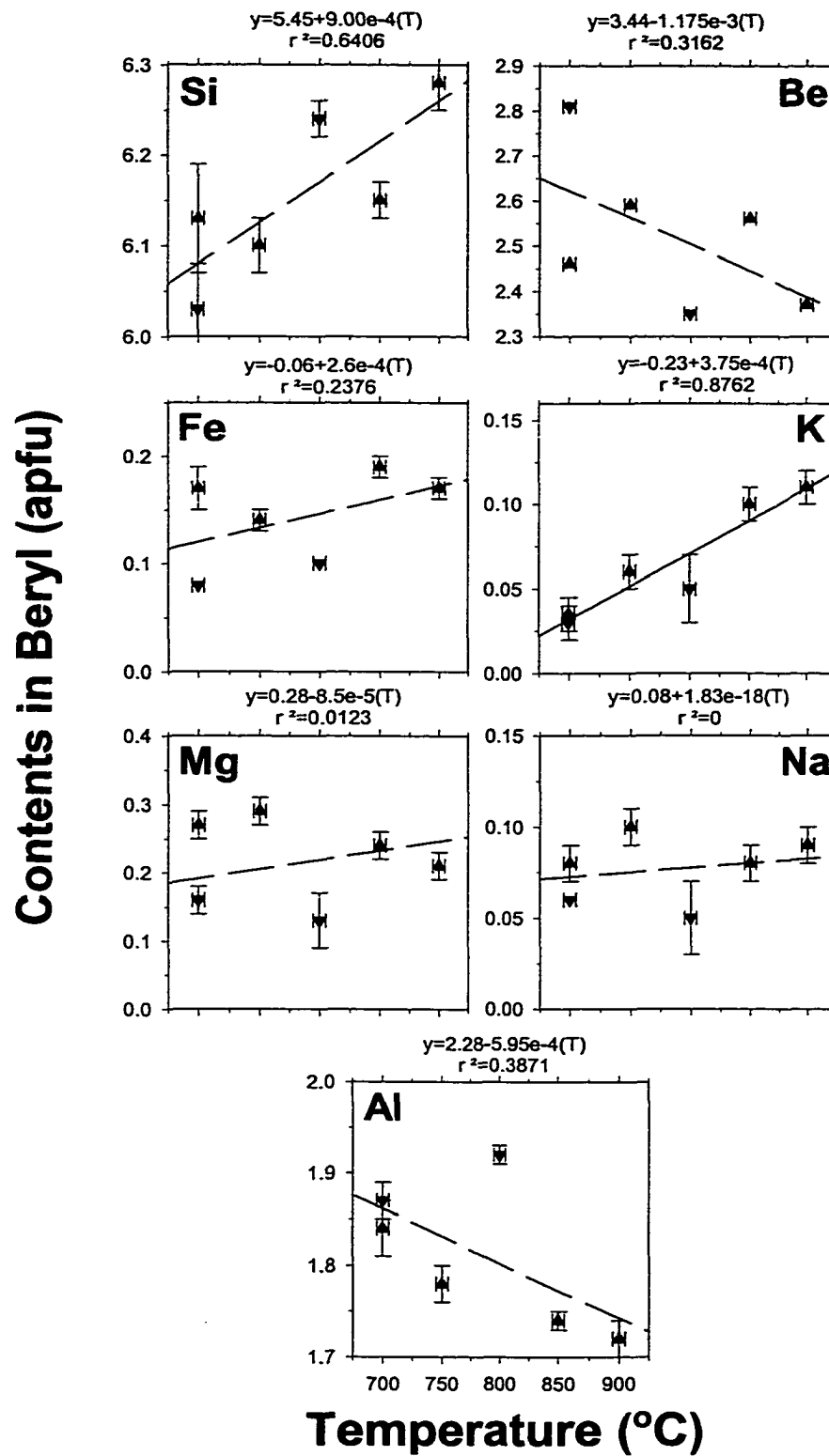


Figure 2-16.

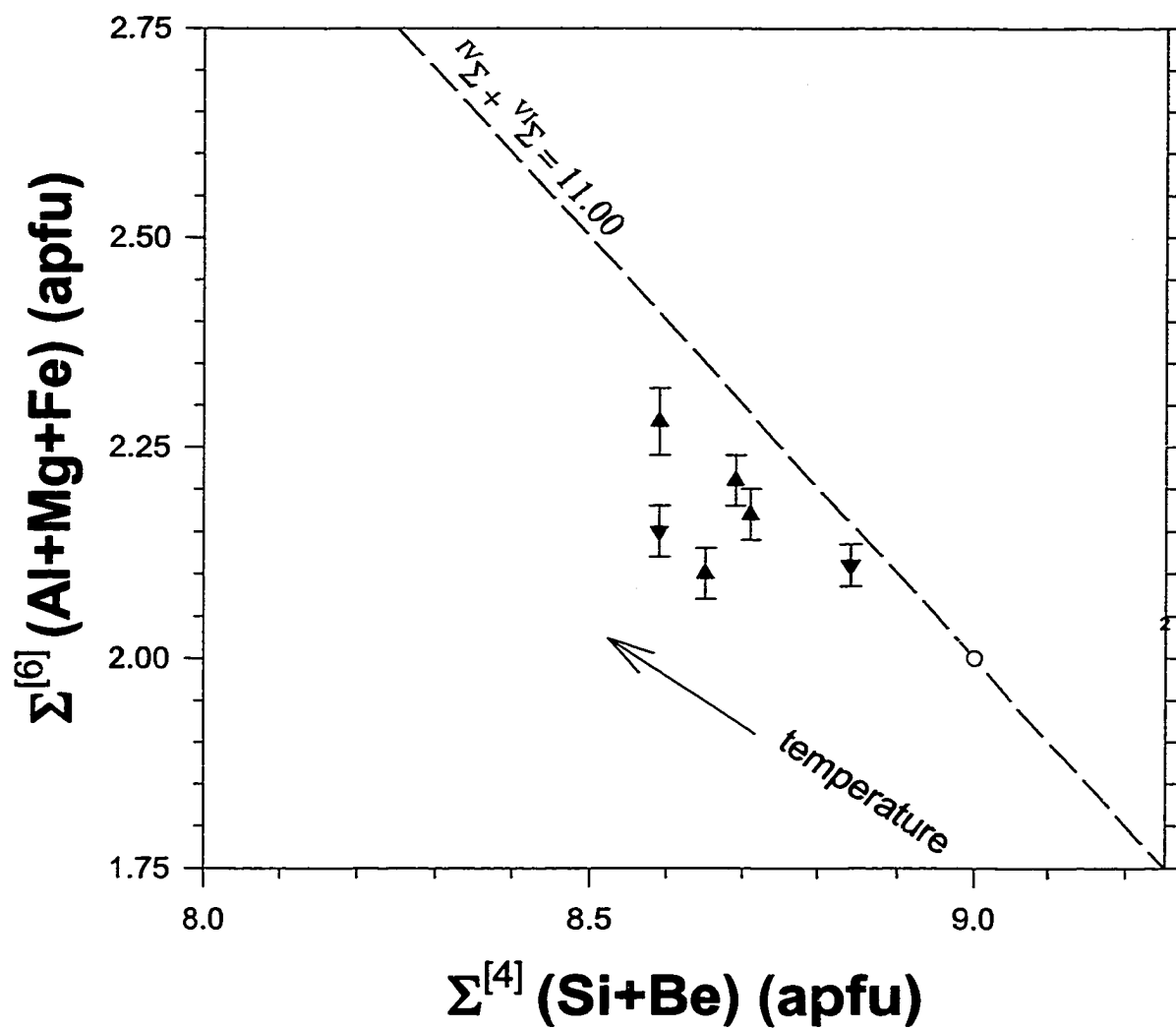


Figure 2-17.

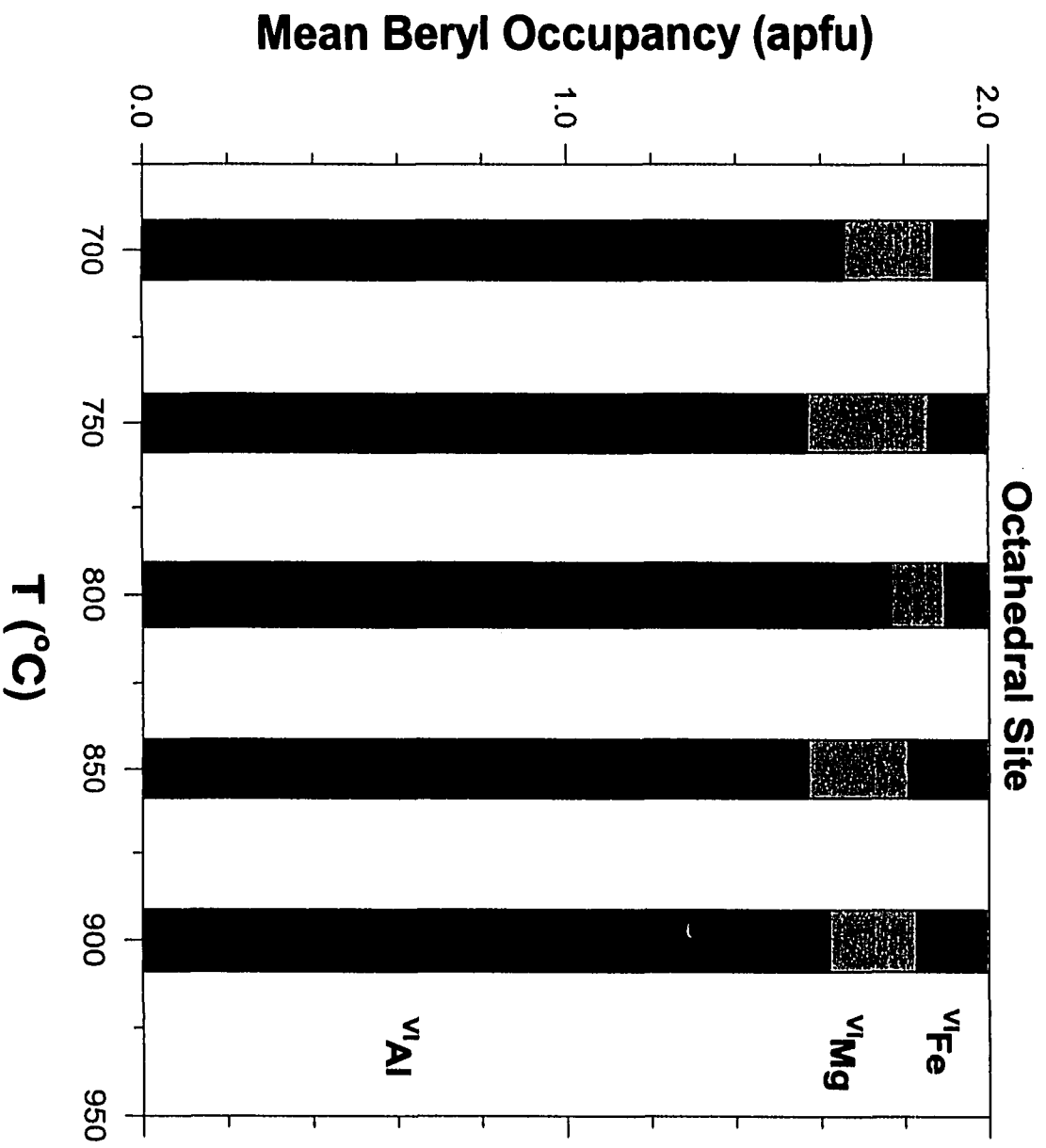


Figure 2-18.

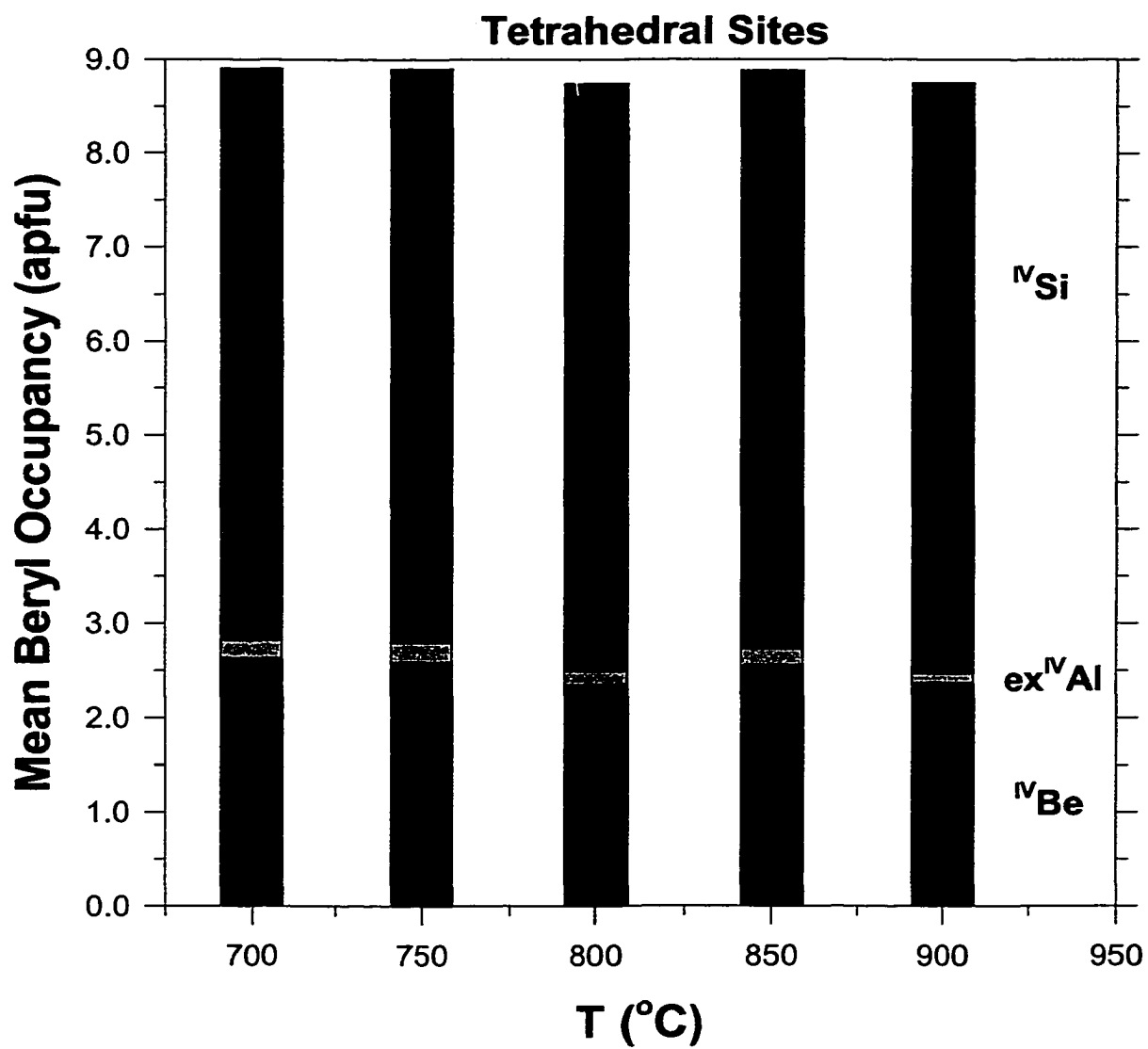


Figure 2-19.

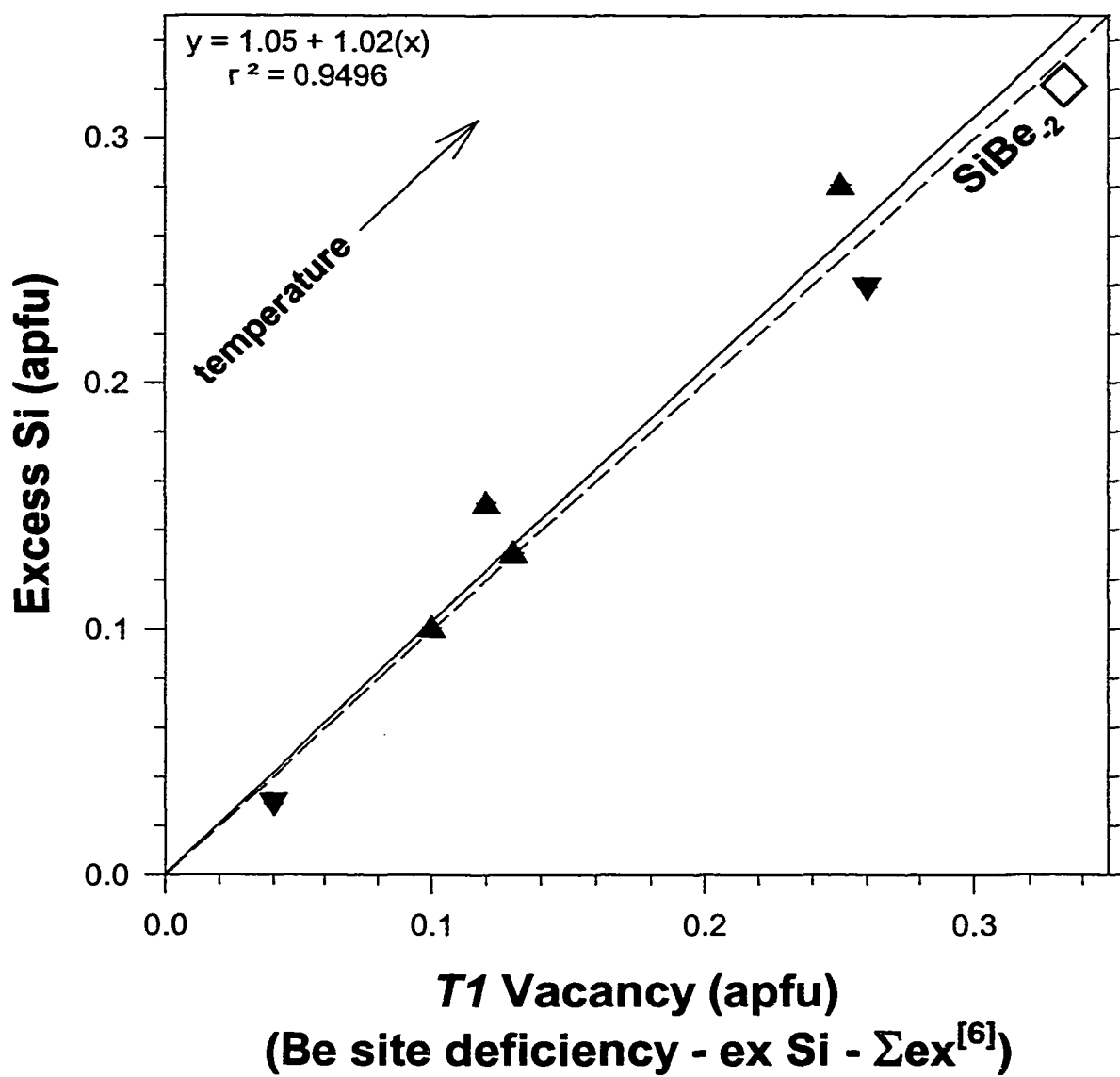


Figure 2-20.

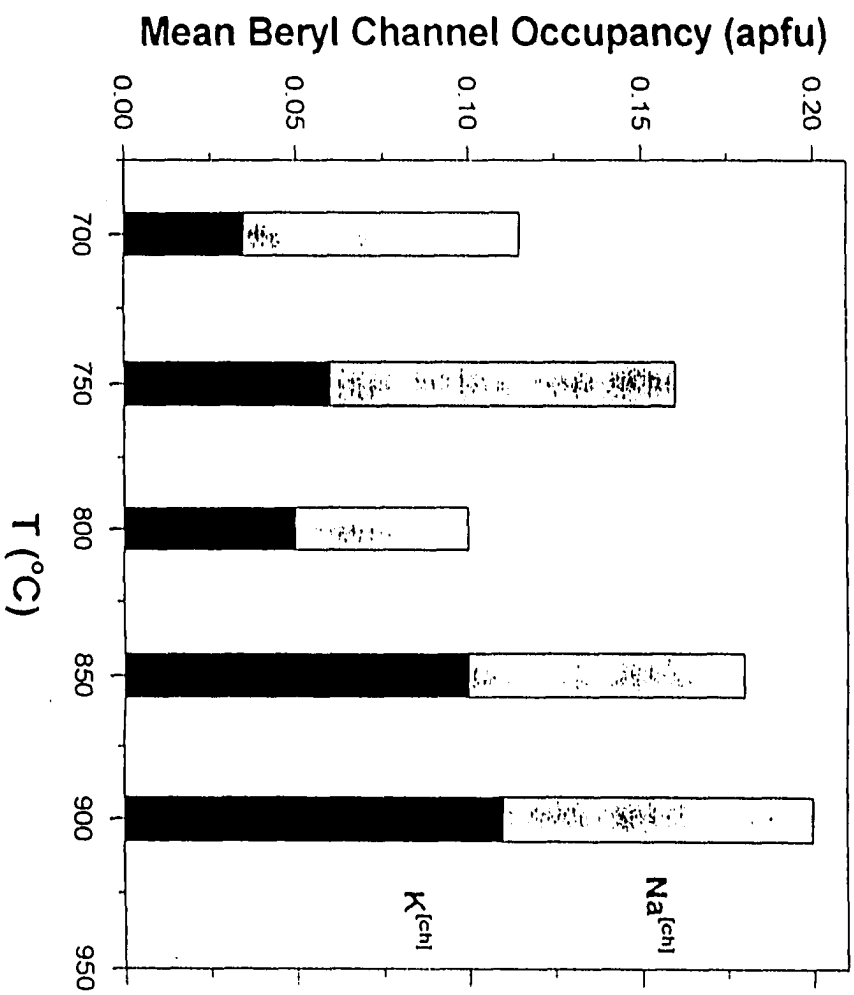


Figure 2-21.

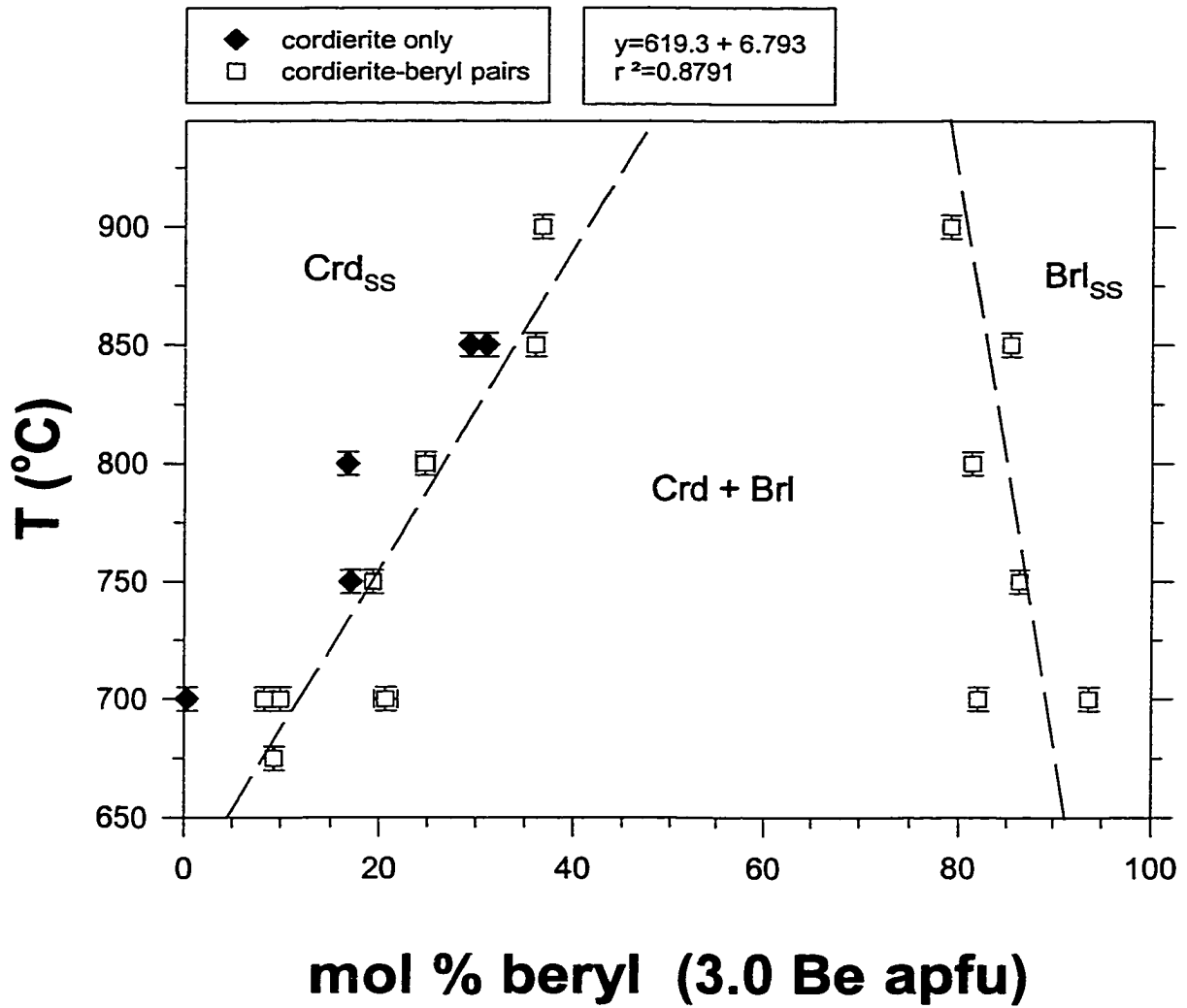


Figure 2-23.

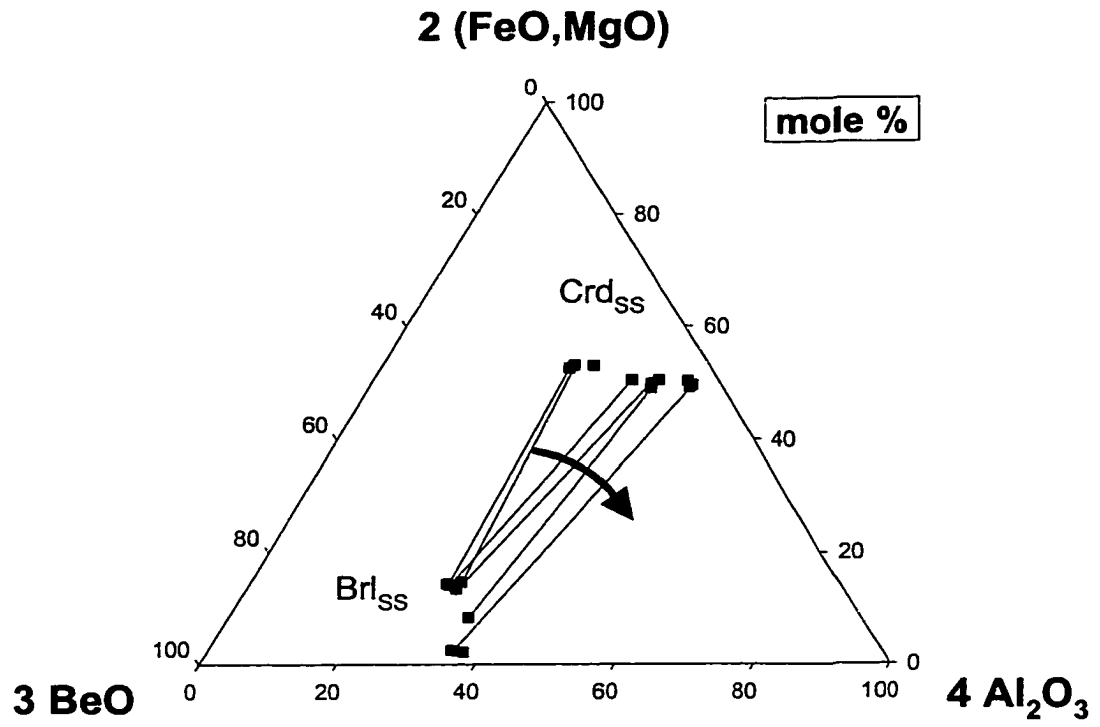
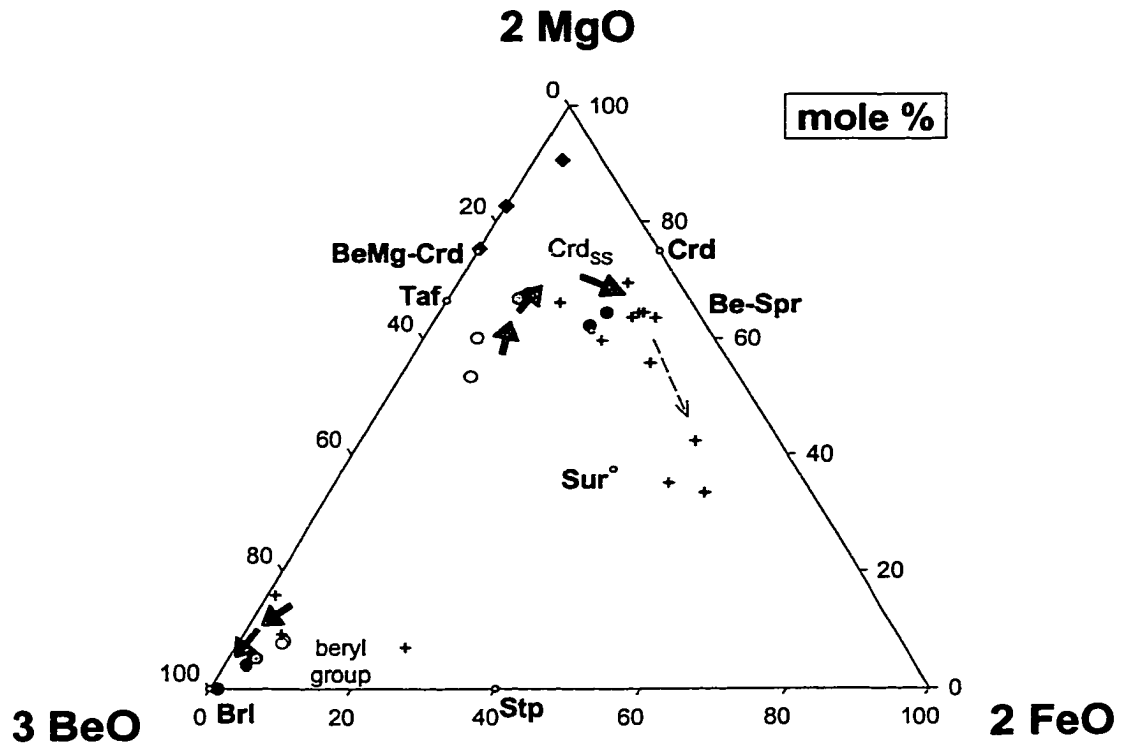


Figure 2-24.



CHAPTER 3. EXPERIMENTAL PARTITIONING OF BERYLLIUM AND OTHER TRACE ELEMENTS BETWEEN CORDIERITE AND SILICIC MELT, AND THE CHEMICAL SIGNATURE OF S-TYPE GRANITE

INTRODUCTION

Notwithstanding a well-defined association between parental magmas of S-type affinity and Be-enriched pegmatite products (LCT: Černý 1991), beryllium has not been assessed as a chemical discriminator among granitic rocks. Beryllium contents normally are very low (10^{-2} to 10^1 ppmw Be) in rock-forming minerals (e.g., Wuensch and Hörmann 1979). About 90 rare mineral species (E.S. Grew, pers. comm., 2000), the most common being beryl, contain Be as an essential structural component. Of the rock-forming minerals, appreciable contents of Be are found only in white mica and cordierite (e.g., Beus 1966; Černý and Povondra 1966; Wuensch and Hörmann 1978; Smeds 1992; Visser et al., 1994). Occurrences of Crd and white mica in S-type granitic rocks (Chappell and White 1974), along with their absence in I- and A-type assemblages logically suggest that Be may be a valuable indicator of granite petrogenesis.

The absence of chemical data for Be originates from the prevalence of laboratory analysis by electron microprobe or XRF. Beryllium normally is undetectable by these means (cf. Evensen and Meeker 1997). Analytical instrumentation (e.g., SIMS, LA-ICP-MS) has improved greatly in recent years and spot testing for Be at trace levels is now routine (e.g., R.L. Hervig 2001, Reviews in Mineralogy Vol. 43, in press). By far the majority of trace element studies on silicic rocks, however, continue to omit Be from the analytical suite.

S-type granitic rocks contain peraluminous assemblages composed largely of feldspars, quartz, and proportionally high contents of micas in addition to combinations of cordierite, garnet, aluminosilicate or orthopyroxene. The trace element signature of S-type granites (*sensu lato*, including leucogranite, pegmatites, and rhyolites) is typically manifested by higher contents of lithophile alkalis (Li, Rb, Cs), Be, B, P, distinct high-field strength elements (Nb, Ta, W, Sn), and rarely, U (e.g., London 1995). Many of the issues relevant to the petrology of S-type granite are focused on unraveling the signatures of trace elements to provide insight into partial melting (e.g., Bea 1996), resolving trace element discrepancies (e.g., Ugidos and Recio 1993), and placing constraints on anatexis to emplacement process (e.g., Cesare et al., 1997). Toward this end, Be signatures may be valuable.

Cordierite, $\text{Mg}_2\text{Al}_4\text{Si}_5\text{O}_{18} \cdot n\text{H}_2\text{O}$, has been recognized as both a magmatic source and sink for elements of S-type affinity—particularly Be (Evensen and London 1999) but also including Li, Cs, Mn, HREE and U (e.g., Bea et al., 1994b; Icenhower and London 1994; Icenhower 1995; Černý et al. 1997). Cordierite is found in metapelites and aluminous gneisses formed at relatively low pressure. The stability of Crd increases with Mg content up to its terminal reactions (mainly $\text{Crd} = \text{Gt} + \text{Als} + \text{Qtz} + \text{V}$) at pressures greater than ~ 500 to ~ 600 MPa at 650 to 900°C (e.g., Vielzeuf and Holloway 1988, Spear and Cheney 1989, Mukhopadhyay and Holdaway 1994). Cordierite, though believed to participate in melting reactions (e.g., Clemens and Wall 1988, Pereira and Bea 1994), commonly remains behind in restitic assemblages (e.g., Gordillo 1979; Ugidos 1988, 1990; Ugidos and Recio 1993; Bea et al. 1994b; Kamber et al., 1998; Kriegsman and Hensen 1998; Kalt et al., 1999). Peraluminous silicic magma derived by

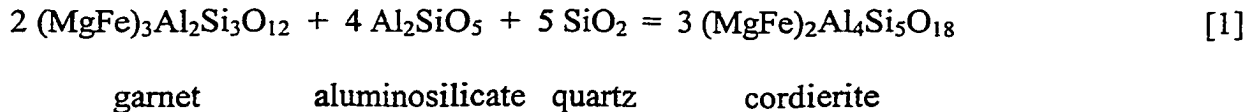
anatexis of mixed metapelitic-gneissic protoliths fractionates toward more peraluminous minimum melts (London 1995), and thus, cordierite also may occur within evolved granitic bodies—especially in apical plutons, leucogranite facies or pegmatite dikes. Many leucogranites that contain Crd, however, also contained Crd in their restite (e.g., Bea et al. 1994b). Commonly, Crd is present at the beginning of magmatic cycles, but not at the end. Instead the Crd component of melt is often manifested by saturation of late tourmaline (Wolf and London 1997). Nonetheless, the potential control by cordierite on the signatures of trace elements understandably stems from its occurrence: both as restite during anatexis and as a liquidus phase in evolved leucogranite.

Beryllium enters the cordierite structure via the exchanges $\text{Be}^{[4]}\text{Na}^{[\text{ch}]}\text{Al}^{[4]}_{-1}$ (low T) and $\text{Be}^{[4]}\text{Si}^{[4]}\text{Al}^{[4]}_{-2}$ (high T) that vary inversely with temperature (from $< 675^\circ$ to $> 900^\circ\text{C}$: see chapter 2). With an appreciation of these exchange mechanisms, this study addresses Be incorporation in Crd at lower concentrations in melt appropriate to natural S-type granite melts, and the absolute contents of minor and trace elements in Crd. Here we report mineral-melt partitioning behavior between cordierite and peraluminous granitic liquid at 200 MPa ($P_{\text{H}_2\text{O}}$), from 700° to 850°C , using both forward and reverse direction (prograde and retrograde) thermal experiments. Starting compositions reflect source rock assemblages containing garnet + biotite as dominant ferromagnesian silicates, yielding mildly to moderately peraluminous silicic melts. Beryllium was not added as a separate component, but only by way of trace quantities that exist in added natural white mica. Mineral/melt partitioning ratios are compared to existing data for S-type granites and migmatites.

EXPERIMENTAL METHODS

Starting Materials. A subset of the starting mixtures and cordierite-producing reactions used by Evensen and London (2001, in review) were utilized for Crd synthesis. Composite powders were formulated by combining mineral additives (Table 1) with a large fraction of a pelitic mineral mixture (designated “SPC”: Wolf and London 1997) to yield the weight fraction formulae $Ab_{22.7}Or_{9.6}Qtz_{26.6}Mus_{13.1}Bt_{12.3}Gt_{-15.7}$ and $Ab_{25.5}Or_{10.8}Qtz_{29.0}Mus_{14.8}Bt_{11.0}Gt_{-28.0}$, respectively. Mineral components were prepared from low-impurity regions of crushed gem-quality crystals. Crystal fragments were microscopically hand-sorted to remove impurities before grinding. Starting mixtures were ground in agate under ethanol to a mean grain size of 15 μm and dried in air at 140°C. Powdered components were combined, ground together, dried (140°C), and homogenized overnight in a tumbling mill.

At 200 MPa (P_{H_2O}) and in the presence of biotite, nucleation and growth of cordierite was achieved via the reaction:



in which aluminosilicate \pm quartz are components of melt. This approach yielded a melt with an ASI of ~ 1.25 (Alumina Saturation Index, $\equiv \text{mol Al}_2\text{O}_3 / \text{Na}_2\text{O} + \text{K}_2\text{O} + \text{CaO} + \text{BaO} + \text{Li}_2\text{O} + \text{Rb}_2\text{O}$) and typically Mg-rich cordierite (e.g., Clemens and Wall 1988, Patiño Douce 1992, Icenhower 1995; see Figure 3-2a).

Preparation of Charges. Gold capsules (3 x 20 mm) were cleaned by soaking overnight in bromopropane (25°C) then by boiling for several hours in nitric acid. Afterwards, a few capsules still contained remnants of the extrusion lubricants used in the

fabrication of the tubing, and these were removed with lint-free polyurethane foam swabs.

Charges contained a slight excess of doubly distilled deionized water (~ 10 wt% H₂O) needed to saturate a melt at 200 MPa over the T range investigated. Water followed by powder mixes were loaded in the central 5 x 3 mm portion of the capsules, which were sealed by DC-plasma arc welding. Capsules were weighed before after welding to check for leaks, and again after storage in a drying oven (140°C). The heating step further allowed for homogenization of water contents throughout the powder prior to the experimental run.

Equipment. Experiments were pressurized cold in R-41® and NIMONIC-105® cold-seal reaction vessels using water a plus trace Immunol® as the pressure medium. Pressure was measured with a factory-calibrated Heise bourdon tube gauge. Fluctuations of < 3 MPa occurred over the course of experiments, with a total estimated accuracy of \pm 10 MPa. Experiment durations varied from ~1 to 6 weeks. Temperature was monitored by internal Chromel-Alumel thermocouples with estimated maximum error of \pm 5°C. Experiments were quenched isobarically using compressed air jet (5 to 15°C/s). The fugacity of oxygen within capsules was regulated by diffusion of H₂ across the metal capsule; the f_{O_2} of the pressure medium is estimated to be slightly below NNO (Huebner 1971). Following quench, capsules were weighed to check for leaks, punctured and the presence of free water was recorded. Capsules were heated in a drying oven, and then reweighed to verify the proportion of water lost. All capsules gain minor weight during experiments by diffusion of Ni-metal (from vessels and filler rods) into the precious

metal capsule walls; none of the experimental products reported here—including biotite and cordierite—suffered contamination by Ni.

Run Pathways. Forward-direction experiments (prograde to run temperatures of 700 to 850°C, designated as “F” in Table 2) promoted concurrent melting and new crystal growth. Reverse-direction experiments (designated as “R” in Table 2) were preconditioned by melting at 50° to 150°C above the final *T* of the experiment, followed by isochoric quench to room temperature, then forward run up to final temperatures in the range of 700 to 800°C. These reverse-direction experiments induced crystal growth from melts that were substantially supersaturated in the components of the crystalline phases at the final run *T*.

ANALYTICAL METHODS

Quantitative Electron Probe Microanalysis (QEPMA)

All major and minor element oxide constituents of cordierite and glass products, except Li, Be, B, Rb and Cs, were analyzed using wavelength-dispersive spectroscopy on a Cameca SX-50 electron microprobe at the University of Oklahoma. Zinc and P were excluded from most analyses of Crd because analysis of the first experiments showed that their contents were at or below detection thresholds (≤ 0.05 or 0.02 wt% oxide, respectively). QEPMA utilized crystalline and glass standards with TAP, PET, LIF, and a layered composite (PC1) diffraction devices. Operating conditions for hydrous glass analyses used a two-beam condition (2 nA and 20 nA regulated current) with a 20 μm spot size, in which Na and Al were analyzed first (and concurrently) to inhibit beam-induced migration effects (Morgan and London 1996). Analyses of minerals were

conducted at 20 nA, 20 kV and a spot size of 3 to 5 μm . Counting times for all elements varied between 20 and 30 seconds. Data were reduced using PAP (Pouchou and Pichoir 1985) matrix correction routines. Detection levels, taken at 3σ above mean background, were < 500 ppm for most elements. Similar Be-rich experiments indicate that Be is not lost to the capsule metal (Evensen and Meeker 1997).

Images were acquired using both backscattered and secondary electron signals as 1024 X 1024 pixelized data. Micrographs were processed (following Russ 1999) using either a low-pass or median filter (low-strength neighborhood ranking) for despeckling of noise. Images that contained minor periodic (instrumental) noise were corrected using Fourier transform processing techniques.

Secondary Ion Mass Spectrometry

Samples were analysed by SIMS using a Cameca Instruments IMS 3f at Arizona State University at Tempe, AZ. A mass filtered $^{16}\text{O}^-$ primary beam was accelerated through a potential of 12.5 kV, with a beam current of 1.0 nA. The focused spot size varied from 15 to 5 μm . Targets were mapped in advance and verified by imaging a combination of ^7Li , ^9Be , ^{23}Na , ^{26}Mg , ^{27}Al , ^{41}K , and ^{56}Fe before analysis.

Sputtered secondary ions were accelerated through a potential of 4.5 kV. The interference of $^{27}\text{Al}^{3+}$ (8.99384 amu) on ^9Be (9.01219 amu) is the most important concern in SIMS microanalysis of Be. The yield of ^9Be is so much greater than the $^{27}\text{Al}^{3+}$ species when Be contents are high (e.g., Evensen and London 2001, in review) that interference is negligible and no correction is required. However, when Be contents are less than ~ 30 ppmw, it has been observed (Grew et al., 1998) that trivalent Al begins to affect the analysis. Thus, prior to each analysis, mass peak positions were distinguished from $^{27}\text{Al}^{3+}$

and manually adjusted to the ^9Be peak. The mass collecting position was also double-checked following glass analyses that exhibited low Be signals. Individual analyses consisted of collecting intensities on the following sequence of isotopes: ^{30}Si , ^7Li , ^9Be , ^{11}B , ^{85}Rb , ^{133}Cs , ^{30}Si . Integration times were sufficiently long to achieve a counting statistical precision of at least 3%. The count rates were normalized to that for Si and then to the silica abundance in the sample (derived from QEPMA). Calibration factors derived from the standards above allowed the normalized count rates to be converted to absolute concentrations. Total internal and external precision (ICP) of BeO analyses of crystals and glass was < 3.9%.

The standard working curves for secondary ion mass spectrometry (SIMS) were calibrated for the analysis of Li, Be, B, Rb and Cs using glass standards. Three synthetic Be-rich granitic glasses (containing 0.57, 1.11, or 3.33 wt% BeO) that were previously characterized (by aqua regia ICP-AES, QEPMA, and SIMS: Evensen 1997) were used as standards for the analysis of experimental products. The glasses contained appreciable B, Li, Rb, and Cs at concentrations far above those estimated for each element in unknowns and therefore served as standards for the suite of elements in question. All trace elements were further calibrated against NIST 610 glass, containing nominally ~500 ppmw of the elements above (Pearce et al., 1997). Data were acquired in three sessions over nearly a 2 year period. Between these sessions, the working curves (Figure 3-1) and SIMS results were very reproducible (± 0.4 to 2.2 %).

RESULTS

Experimental Products

Synthesis of cordierite using Crd-absent materials was successful for all starting mixtures (e.g., Figure 3-2a). Assemblages in forward-direction experiments (Table 3-2) contain cordierite + plagioclase + quartz + biotite + magnetite + melt (+vapor) at 700°C (Figure 3-2b). In the 700°C reversal, which was preconditioned at 850°C, plagioclase and quartz are absent (Figure 3-2c). We suggest that at the preconditioning temperature, critical plagioclase and quartz nuclei likely were destroyed (e.g., Lofgren 1983), thus inhibiting rapid nucleation at subliquidus temperatures. Plagioclase and quartz are lost by $T \geq 750^\circ\text{C}$, leaving cordierite + biotite + magnetite + melt stable from 750° to 850°C regardless of run direction (Figures 3-2c, d and e).

Cordierite forms blocky euhedral crystals (5 to 150 μm) in run products, sometimes containing minor inclusions of biotite or magnetite (Figure 3-2b to e). In reverse-direction experiments, the Mg:Fe ratio of cordierite tracks the temperature of growth (Table 3-2). Figures 3-2e and f show reverse-direction cordierite products in which the preconditioning step resulted in a more magnesian interior followed by an Fe-rich rim grown at lower T . Because of compositional zoning, crystal core and rim compositions were analysed; only rim data were used for calculations of mineral/melt equilibria. Plagioclase forms elongate and slightly skeletal crystals (20 to 80 μm) of albite-oligoclase, and these are typically overgrown by a thick rim (5 to 15 μm) of andesine also with skeletal morphology (Figure 2b). Andesine also is found as isolated crystals. Andesine occurs in run products in which the starting composition contained the higher grossular component (garnet-1 in Table 1), suggesting the reaction in melt:

grossular + aluminosilicate + quartz = anorthite

in which the grossular makes up only a small component of garnet, aluminosilicate is a component of melt, and the anorthite component gives rise to andesine. We interpret albite-oligoclase growth to be a product of early formed melt, whereas andesine crystallized later—commensurate with the complete dissolution of garnet. Such assemblages indicate the refractory nature of garnet relative to other crystalline phases.

Quartz mostly shows subhedral crystal morphology (3 to 30 μm), and often is poikilitically enclosed by cordierite. Biotite occurs as both elongated compound crystal aggregates and as isolated crystals ranging in length from 10 to 100 μm , though some crystals are only 1 μm thick. Large relict biotite crystals exhibit recrystallization to fine-grained biotite + magnetite. Magnetite forms equant crystals (1 to 50 μm).

Cordierite and Glass Chemistry

Cordierite. The chemistry and recalculated formulae of Crd are shown in Table 3-2. With increasing T from 700° to 850°C, contents of the tetrahedral components SiO_2 and Al_2O_3 remain roughly constant, whereas BeO values decrease from 291 to 61 ppmw. Over the same interval, octahedral Mg contents increase relative to Fe with increasing T , with $Mg\#$ [= 100*molar MgO/(MgO+FeO)] values increasing from 68.7 to ~ 85. Concomitantly, decreases are seen for the concentrations of other octahedral constituents Mn (~ 1.21 to ~ 0.50 wt% MnO) and Li (180 to 29 ppmw Li_2O). Concentrations of channel-occupying components vary over the same range of T . Sodium contents remain roughly constant whereas K values rise steadily with T (from ~ 0.06 to ~ 0.32 wt% K_2O). Calcium and H_2O values fall with T (from ~ 0.20 to ~ 0.05 wt% CaO and from 1.32 to ~ 0.73 wt% H_2O), though Rb and Cs contents increase (from 5 to 23 ppmw Rb_2O and from

2 to ~ 4 ppmw Cs₂O). Boron contents of cordierite are minor and show scatter (from 3 to 22 ppmw B₂O₃). Contents of Ti, Ni, Zn, Ba, P, F or Cl are at or below detection levels.

Mean values of recalculated cordierite formulae total 8.95 ± 0.01 and 10.99 ± 0.01 apfu (using standard error, se) for total tetrahedral and octahedral cations, respectively. These sums closely match the respective values of 9.0 and 11.0 of ideal cordierite. Total channel constituents (alkalis, Ca and water) decrease slightly from 700 to 850°C (from ~ 1.0 to ~ 0.75 apfu), but show scatter (se = ± 0.08) from steady increases in K contents but competing decreases in Na, Ca and H₂O contents.

Peraluminous granitic melts. Silicic glasses (Table 3-2) representing melts in equilibrium with cordierite contain normative components of corundum with a mean haplogranite normalization of Ab_{31.11}Or_{22.56}Qz_{42.40}Cor_{3.93}. Alumina contents of glass increase slightly from 700 to 850°C.

Elemental partitioning between cordierite and melt. Partitioning ratios are given in Table 3-2, following the notation of Beattie and others (1993; $D_X^{\text{min/melt}} = [X_{\text{mineral}}]/[X_{\text{melt}}]$). Of the nonessential elements in cordierite, the only ones that show compatible behavior are Be and Mn.

Figure 3-3 shows that Be strongly partitions into the cordierite structure over peraluminous silicic melt. As T rises from 700 to 850°C, $D_{\text{Be}}^{\text{Crd/melt}}$ values fall sharply from 202.00 to 6.70 along a linear trend. This points to the capacity of cordierite for sequestering available Be in silicic melts, demonstrating extraordinary efficiency at lower temperatures. Values of $D_{\text{Mn}}^{\text{Crd/melt}}$ (Figure 3-4) decrease linearly from 7.67 to 1.92 as T increases over the same range.

Of the partition coefficients for the incompatible minor and trace elements (Figure 4), Li decreases (from 0.44 to 0.12) as T rises from 700° to 850°C, whereas those for Rb and Cs decrease (from 0.05 to 0.20, and from 0.19 to ~ 0.60, respectively) over the same range of T . Values for B show a slight increase (from 0.03 to ~ 0.13) with increasing T , but both B and Ca D -values appear to be somewhat independent of T . Calcium partitioning exhibits a bimodal trend (D -ratios centered around 0.22 and 0.28), demonstrating a higher correlation with starting mixture than temperature. Table 3-3 displays regression data for minor and trace elements as a function of temperature. Of the elements that showed significant concentration in cordierite, only Ca and to a lesser extent B appear to be T -independent, as indicated by their low R^2 values.

DISCUSSION

Experimental Calibration of Cordierite-Associated Trace Elements in Silicic Melts

Beryllium. Going from the trace levels of BeO in melt (this study) up to concentrations of beryl saturation (Evensen et al., 1999), $D_{\text{Be}}^{\text{Crd/melt}}$ values shift from the range 202.0 - 6.7 (over 700° to 850°C) down to 26.6 -15.1 (675° to 850°C: Evensen and London, in review, 2001). This follows a structural change in cordierite, rather than owing to non-Henrian distribution behavior. Increasing structural disorder (up to hexagonal symmetry) is observed upon addition of significant Be contents to cordierite (e.g., Hölscher and Schreyer 1989) and this gives rise to at least nearly complete solid solution between cordierite and beryl in peraluminous granitic melts (at 200MPa: Evensen and London 2001, in review).

In both cordierite (e.g., Hölscher and Schreyer 1989) and beryl (e.g., Aurisicchio et al., 1998), Be resides in linking tetrahedral polyhedra, showing a clear bond angle preference that corresponds to linking versus ring-forming tetrahedral geometries (e.g., Downs and Gibbs 1981). This is seen in data from natural systems with moderate to very high contents of Be in cordierite (10s to 1000s of ppmw Be). Often, white mica is cited as the major source and control on Be contents of silicic rocks, originating from the relative high contents of Be in marine sediment (e.g., 2 ppmw: You et al., 1994) and pelite (e.g., 3 ppmw: Turekian and Wedepohl 1961). In mica, Be replaces tetrahedral Al, increasing tetrahedral ordering within the structure (e.g., Guggenheim 1984) and leading to Be-rich Ca-micas up to the bityite end-member. Polyhedral geometries of muscovite are likely to be somewhat less accommodating for Be²⁺, with natural Be contents commonly ranging up to the 10s of ppmw Be (only rarely reaching 100s of ppmw Be: e.g., Wuensch and Hörmann 1978; Černý and Burt 1984; Grew et al., 1986; Smeds 1992). Recent experimental studies of peraluminous granitic melts suggest that Be is slightly incompatible in white mica (London and Evensen 2001).

The reported contents of cordierite-bearing granites (Table 3-4) in conjunction with the above observations of white mica chemistry and crystallography suggest that cordierite, when stable, is far more effective than white mica at sequestering magmatic Be. The incorporation of Be into white mica becomes important only under conditions where cordierite is absent. As a result, the budget of Be in melt is most susceptible to rapid changes when an S-type magma reaches the boundaries of the cordierite stability field.

Manganese. This transition metal has a distorted octahedral radius, which inhibits direct substitutions into octahedral polyhedra that normally contain Fe^{2+} or Mg (e.g., Peacor and Wedepohl 1978; Burns et al., 1994). The proportion at which Mn is partitioned between peraluminous silicic melt and cordierite is nearly identical to the ratio between peraluminous silicic melt and biotite. The values of $D_{\text{Mn}}^{\text{Crd/melt}}$ fall from 7.67 to 1.92 as T increases from 700 to 850°C. Experimental values of $D_{\text{Mn}}^{\text{Bt/melt}}$ fall similarly from the range of 7.60 to 4.86 down to 3.78 to 3.50 as T increases from 650 to 750°C, respectively (Icenhower and London 1995). Because the slope of $D_{\text{Mn}}^{\text{Crd/melt}} - T$ nearly overlaps that of $D_{\text{Mn}}^{\text{Bt/melt}} - T$, cordierite and biotite ought to exert about the same degree of control on magmatic distribution of Mn. Therefore, when Crd is present, the uptake of Mn by crystalline silicates should occur at twice the magnitude.

Lithium. Lithium enters the cordierite structure by substitution for octahedral R^{2+} cations, e.g., via $\text{Na}^{[\text{ch}]}\text{Li}^{[6]}(\text{Mg,Fe})^{[6]}_{-1}$ (Armbruster and Irouschek 1983; Kirchner et al., 1984; Gordillo et al., 1985; Černý et al., 1997; Evensen and London 2001, in review). In the current experimental products, Li exhibits moderate to strong incompatibility in cordierite depending on the temperature of melt ($D_{\text{Li}}^{\text{Crd/melt}} = 0.44$ to 0.12 going from 700 to 850°C). Cordierite exerts no significant control on the Li contents of melt. Both white and dark micas, in which Li behaves compatibly, control the distribution of Li between minerals and melt (Icenhower and London 1995).

Cesium. Cordierite accommodates Cs at channels sites. Figure 3-4 shows that Cs contents increase regularly with T , a pattern recognized in other studies (Evans et al., 1980; Evensen and London 2001, in review). The structure of high-cordierite accommodates Cs by deformation of ring-forming tetrahedra in a manner that maintains

symmetry (Daniels 1992). In cordierite – beryl solid solutions at $\geq 800^\circ\text{C}$ and higher, the combination of increasing Al/Si disorder and effects of distorted BeO_4 linking tetrahedra widen channel sites to the extent that Cs becomes compatible over melt (Evensen and London 2001, in review).

At much higher melt contents of Cs_2O than evaluated by this study (~ 0.50 to 0.75 wt% versus \sim several ppmw Cs_2O), Icenhower (1995) reported a mean value for $D_{\text{Cs}}^{\text{Crd/melt}}$ of $0.72 (\pm 0.03)$ at 700°C . These data differ from the range of $D_{\text{Cs}}^{\text{Crd/melt}}$ ratios found here, which extend from ~ 0.19 to ~ 0.60 as T increases from 700 to 850°C , respectively. Thus, Cs incorporation into cordierite does not appear to follow Henry's Law. At the low Cs melt contents of most S-type magmas, Cs uptake by cordierite is most efficient at higher T though it is still noteworthy at 700°C .

Cordierite-Associated Trace Elements in Granitic Rocks

Cordierite-bearing granites. A survey of analyses that contained complete light element data (Table 3-4) illustrates that many S-type granites are distinguished by a paucity of Be in their whole rock values. Analyses from more than 13 cordierite-bearing granites yield a mean of $0.8 (\pm 0.03)$ ppmw Be. In addition, the Mn and Cs contents of the same granites are noticeably low, with mean values of 1.8 ppmw Cs (range = 1.54 to 2.1) and 0.01 wt% MnO (range = 0.00 to 0.03).

Cordierite-bearing granites also display a clear lack of beryl in their associated pegmatites (e.g., Barbey et al., 1999), regardless of whether they contain a homogeneous distribution of cordierite. This is manifested by either an association between Crd-free granite and beryl-bearing pegmatite fields, or an association between Crd-bearing granite

(containing negligible Be in whole rock values) and an absence of mineralized products (e.g., Breaks and Moore 1993).

Cordierite-absent granites. These rocks are distinctly Be-rich in their whole rock values. Analyses from more than 100 cordierite-bearing granites, excluding their very evolved facies (and mineralized products), yield a mean value of 6 (\pm 1.6) ppmw Be. It is evident from the range of values reported in Table 3-4 that many of these granites contain even higher Be contents. Table 3-4 also indicates a spatial correlation between these rocks, their beryl-bearing pegmatites and Be mineralization. About 115 analyses of the evolved facies of Crd-absent granites of S-type affinity yield a mean value of 69 (\pm 33) ppmw Be, once again, with a range of values that usually extends to much higher quantities. Converted to BeO, this value equals \sim 400 ppmw, which is near or beyond the melt saturation requirements for beryl in compositionally simple peraluminous haplogranitic melts at 700°C (Evensen et al., 1999). Evensen et al. (1999), however, noted that beryl saturation also is a function of the other fluxing melt species, with higher BeO contents required in B-, F-, and P-rich highly evolved melts. In summary, the database suggests that the Be contents of cordierite-free (mostly garnet-bearing) peraluminous granitic melts are 1, 2, and sometimes 3 orders of magnitude higher than those of cordierite-bearing peraluminous granites that contain Crd in their restite.

Migmatites. Some of the most thorough data for evaluating the effect of Crd on magmatic signatures is contained in the migmatite data of Bea et al. (1994b), a subset of which is summarized in Table 3-5. Here the Crd-bearing source rocks show intermediate concentrations of Be, Mn, and Cs between their derived melts (Crd-bearing leucosomes) and residual minerals (Crd-rich melanosomes). The restite shows an appreciable

enrichment of Be, Mn and Cs, whereas separated leucogranite dikes display marked depletions. These authors also estimated crystal/melt partition coefficients of migmatites using elemental contents of mesosome minerals versus the composition of genetically associated leucosomes. They noted favorable Be uptake by Crd at a magnitude lower than most other minerals, but within the range of $D_{\text{Be}}^{\text{Crd/melt}}$ values of our experiments (falling toward the higher T end, $\sim 800^\circ\text{C}$). They also reported that the $D_{\text{U}}^{\text{Crd/melt}}$ value (1.61) was the highest among any mineral, and their data suggest the same for Cs (despite a strongly compatible value, 31.5, where we found incompatibility). A similar argument was made for Li uptake by Crd; this is the only claim not supported by calibrations in this study and others (Icenhower and London 1995). Further evidence against cordierite as a chief carrier of Li is seen in lithophile element deposits. Li-rich systems, including albite-spodumene type and beryl type pegmatites of the LCT family (both believed to be derivatives of S-type magmas), may or may not contain appreciable Be (Černý 1991). In other words, there is no characteristic Be content of Li-enriched systems.

Regional trace element trends and pegmatite associations. Many S-type granitic rocks of Western Europe contain cordierite in their assemblage, and some are interpreted to have originated within the cordierite stability field (e.g., Bea et al., 1994a,b). These granite complexes or migmatite fields are conspicuously poor in Be except for their restitic counterparts (e.g., melanosomes with 3.51 – 8.10 ppmw Be, see Table 4) or cordierite-rich cockades (3.4 – 7.1 ppmw Be; Barbey et al., 1999). Using the partitioning data for Be, this trend logically suggests that the lack of Be in such granites is accounted for by the retention of Be in restitic Crd. This distribution falls in line with genetic models of high-grade metamorphic Be-rich assemblages in which cordierite

seems to have been an active participant in both prograde and retrograde pathways (e.g., Grew 1998; Baba et al., 2000). In these rocks, cordierite is also a probable contributor of Be, up to high levels—a signature that it probably acquired as restite, where it was able to deplete Be from large volumes of melt.

Of the few Be contents of granite reported, those of Portugal (Charoy and Noronha 1996, Ramirez and Grundvig 2000) are distinctly higher than nearby peraluminous granites of Spain (e.g., Bea et al., 1994b). Even in studies in which Be was not analysed, Cs and Mn contents of granites in central Portugal fall in line with (higher) Crd-absent values (e.g., Neiva et al., 1987). This discrepancy likely indicates petrogeneses at the shallow depths (low pressures) of cordierite stability for many granite provinces of Spain, and deeper sources for the granites of Portugal—in the field of garnet + aluminosilicate. Examinations of regional geology show that beryl-bearing pegmatites are common among S-type leucogranites in North America, suggesting greater depths of anatexis compared to Western Europe and Eastern Australia, where most granitic systems are Be-poor and notably beryl-absent.

Cordierite as a Normative Modal Component of Peraluminous Melt

Where Crd makes up a large portion of a natural mode (e.g., ~ 60 to 90 %: Gordillo 1979; Ugidos 1988, 1990; Kamber et al., 1998; Kalt et al., 1999), its restitic character is distinguished. In assemblages with minor amounts of cordierite, its restitic versus magmatic character may be subtle, if not indiscernible (e.g., Ugidos and Recio 1993). The normative cordierite component calculated from melt offers a means to constrain its modal abundance in granitic rocks, so that the volume fraction of Crd in a rock can be used to assess whether an assemblage represents a magmatic product or one

containing some component of restite. Because a normative calculation of this nature results in a non-unique solution, we have constrained the calculation by difference among other relevant crystalline phases in an iterative approach guided by natural assemblages. The calculations utilized the mean 700°C glass composition in Table 3-2, which represents the composition nearest to solidified rock in this study.

Normative Crd results of both Al- and Mg-limited approaches are displayed in Table 3-6. Normative cordierite (and that of Bt and Mus) arises from a combination of Hy, Cor and Mt components of the CIPW Normative. The products show that the normative component of cordierite in peraluminous granitic melt varies from 0 to a maximum of 4.0 % as Mus content varies inversely from about 5 to 0 %, respectively. When other peraluminous crystalline phases are present with Crd—a typical scenario for natural systems—a normative value of less than 4% Crd results. Many Crd-bearing granites are also Mus-poor, which corresponds to a value toward the higher end for Crd (~ 3 %); however, most Crd-bearing granites are also Bt-rich. Because the Mg component of the norm calculation is the major limiting component following Al, then a Bt-rich assemblage would yield a Crd normative component much closer to the lower end (~ 0%). Table 6 shows that with 5 norm % Bt, the Crd norm component falls to 0.25 % (with a leftover Cor component). In short, the most reasonable value is intermediate but variable between 0 to 4 norm % Crd. Thus, when Crd constitutes more than a few percent of a natural mode, the assemblage in question could not have originated strictly from melt. This restriction may help put the trace element character of Crd-bearing peraluminous granite in context. The small normative values also suggest that contrary to some written reactions and suggested roles for facilitating melt production (e.g., Clemens

and Wall 1988, Pereira and Bea 1994), the potential for cordierite to contribute significantly to anatexis is likely to be small.

PETROLOGIC SIGNIFICANCE

Cordierite and the S-type Granite Signature

White and Chappell (1974) and Zen (1987) have suggested using cordierite as an indicator of S-type granitic source terranes. The importance of cordierite for S-type silicic melts not only stems from phase equilibria (e.g., Green 1976, Vielzeuf and Holloway 1988, Patiño Douce 1992, Fitzsimons 1994) but also as noted here, in terms of a chemical contributor—a carrier of S-type elemental signatures.

The results of this study suggest that cordierite, more than any other participating mineral, controls the distribution of magmatic Be and Cs. Lithium budgets of melts are controlled by micas, whereas biotite and cordierite affect Mn distribution equally. This suggests that when cordierite is present, a 2-fold depletion of Mn contents from melt would be observed relative to cordierite-absent melts—a trend that ties the Mn budget back to cordierite. The ranges of mean values of Table 3-4 show clearly separate populations between Crd-bearing and Crd-free S-type granites. The only overlap (barely) is seen for MnO contents, which again reflects a cooperative control by Crd and Bt on its distribution.

The cordierite-associated S-type elemental signature involves the following elements, in decreasing order of the efficiency of accommodation by cordierite:

Be, Cs, Mn, Li

If cordierite is part of the restitic assemblage during anatexis, the derivative liquid will be depleted in this suite of elements. Magmas originating within the midcrustal (and deeper)

garnet + aluminosilicate stability field may achieve cordierite saturation after emplacement at shallow levels (e.g., Barbey et al., 1999). If Crd saturation is achieved during the late stages of crystallization of such liquids, it would likely deplete the remaining melt of Be and the other elements. The chemical signature of late Crd, however, may be one of distinctly lower contents in these elements (absolute values) compared to restitic Crd that may be appreciably enriched in Be, Cs and Mn.

On the other hand, as cordierite melts it may yield a Be-rich (or “Cordierite”) S-type signature to magma. Contributions of this type are typically found on smaller scales. Cordierite statistically accounts for sporadic Be contents (e.g., a mix of background and anomalously high values); for instance, values of Be that exhibit the most variability of any element have been documented where Crd-free peraluminous melts intrude Crd-bearing metamorphic rocks (Kretz et al., 1989). In environments of emplacement, wallrock interactions (and emplacement mechanisms) may leave local trace element fluctuations in the granite.

Lastly, if anatexis of a metasedimentary protolith occurs at pressures above the low pressure environment of cordierite, the suite of elements above will fractionate with that melt, their budgets being controlled mainly by white (Li, Be) and dark (Li, Mn, F) micas. Other essential contributors to the F, P, and B signatures in S-type systems are dark mica (Icenhower and London 1995, London 1995), apatite and other phosphates (Watson and Capiobianco 1981; Wolf and London 1994; London et al., 1999) and tourmaline (e.g., Wolf and London 1997), respectively. However, for a single mineral, the breadth of attributable elements for cordierite is considerable. Extensive surveys of

reported analyses in addition to distinct non-associations with beryl-bearing pegmatites indicate that a major population of granites contained cordierite as restite.

Clearly cordierite imparts or, more often, remove a distinct signature to S-type granitic melts. About an order of magnitude separates the whole rock contents of Be, Cs and Mn within Crd-bearing vs. Crd-free peraluminous granites. Routine analysis of Crd (and Be) may help to constrain sources and pathways during magmatic cycles of granite because unlike micas, the cordierite signature distinguishes the conditions of melting. Concentrations of Be, Cs and Mn in restitic vs. late-saturating Crd offer needed discriminators (e.g., Clemens 2001) for deciphering restitic versus magmatic mineralogy—an issue central to the interpretations of S-type granite (e.g., White et al., 1986a, 1986b; Ugidos and Recio 1993). This control on the magmatic budgets of the above elements at conditions of the cordierite stability field arises from the unique capacity of the cordierite crystal structure to accommodate a diverse range of ions, from those requiring the smallest (Be) to the largest (Cs, U) coordination polyhedra.

References Cited

- Armbruster T., Irouschek A (1983) Cordierites from the Lepontine Alps: Na+Be→Al substitution, gas content, cell parameters, and optics. *Contributions to Mineralogy and Petrology* 82, 389-396.
- Aurischio C, Fioravanti G, Grubessi O, Zanazzi PF (1988) Reappraisal of the crystal chemistry of beryl. *American Mineralogist* 73, 826-837.
- Bea F (1996) Controls on the trace element composition of crustal melts. *Trans Royal Society Edinburgh* 87: 33-41.
- Bea F, Pereira MD, Corretge LG, Fershtater GB (1994a) Differentiation of strongly peraluminous, perphosphorus granites: The Pedrobernardo pluton, central Spain. *Geochim Cosmochim Acta* 58: 2609-2627.
- Bea F, Pereira, MD, Stroh A (1994b) Mineral/leucosome trace-element partitioning in a peraluminous migmatite (a laser ablation-ICP-MS study). *Chem Geol* 117: 291-312.
- Breiter K, Sokolova M, Sokol A (1991) Geochemical specialization of the tin-bearing massifs of NW Bohemia. *Mineralium Deposita* 26: 298-306.
- Burns PC, MacDonald D.J., Hawthorne FC (1994) The crystal chemistry of manganese-bearing elbaite. *Can Mineral* 32: 31-41.
- Chappell BW, White AJR (1974) Two contrasting granite types. *Pac Geol* 8: 173-174.
- Charoy B, Noronha F (1996) Multistage growth of a rare-element, volatile-rich microgranite at Argemela (Portugal). *J Petrol* 37: 73-94.
- Černý P (1991) Fertile granites of Precambrian rare-element pegmatite fields: is

- geochemistry controlled by tectonic setting or source lithologies? *Precambrian Res* 51: 429-468.
- Černý P, Povondra P (1966) Beryllian cordierite from Vezna: $(Na+K)+Be \rightarrow Al$. *Neues Jahrb Mineral Monatshefte* (1966): 36-44.
- Černý P, Burt DM (1984) Paragenesis, crystallochemical characteristics, and geochemical evolution of micas in granite pegmatites. In: Bailey SW (ed) *Micas. Mineral Soc Am, Rev Mineral* 13: pp 257-298.
- Černý P, Chapman R, Schreyer W, Ottolini L, Bottazzi P, McCammon CA (1997) Lithium in sekaninaite from the type locality, Dolní Bory, Czech Republic. *Can Mineral* 35: 167-173.
- Cesare B, Salvioli Mariani E, Venturelli G (1997) Crustal anatexis and melt extraction during deformation in the restitic xenoliths at El Joyazo (SE Spain). *Mineral Mag* 61: 15-27.
- Clemens JD, Wall VJ (1988) Controls on the mineralogy of S-type volcanic and plutonic rocks. *Lithos* 21: 53-66.
- Clemens JD (2001) S-type granites – models and evidence. In: Chappell B, Fleming P (eds) *S-type granites and related rocks, abstracts*, Australian Geol Survey Org, Rec 2001/02, pp. 31-32.
- Daniels P (1992) Structural effects of the incorporation of large-radius alkalis in high cordierite. *Am Mineral* 77: 407-411.
- Downs JW, Gibbs GV (1981) The role of the BeOSi bond in the structures of beryllosilicate minerals. *Am Mineral* 66: 819-826.
- Evans DL, Fisher GR, Geiger JE, Martin FW (1980) Thermal expansions and chemical

- modifications of cordierite. *J Am Ceram Soc* 63: 629-634.
- Evensen JM, Meeker GP (1997) Feasibility of Be analysis for geologic materials using EPMA. *Microscopy Soc Am, Proc: Microscopy and Microanalysis 1997*, 3 (2): 893-894.
- Evensen JM, London D (1999) Beryllium reservoirs and sources for granitic melts: The significance of cordierite. *Geol Soc Am, Abstr Programs*, 31 (7): A-305.
- Evensen JM (1997) Effects of beryllium on the liquidus phase relations of haplogranite. MS Thesis, Colorado School of Mines, Golden, Colorado, 92 p.
- Evensen JM, London D, and Wendlandt RF (1999) Solubility and stability of beryl in granitic melts. *Am Mineral* 84: 733-745.
- Fitzsimons ICW (1994) Cordierite migmatites from East Antarctica; geochemical constraints on volatile distribution during crustal anatexis. *Mineral Mag* 58A: 274-275.
- Gordillo CE (1979) Observaciones sobre la petrología de las rocas cordieríticas de la Sierra de Córdoba. *Bol. Acad. Nac. Cienc. Córdoba Argentina* 53: 3-44.
- Gordillo CE, Schreyer W, Werding G, Abraham K (1985) Lithium in NaBe-cordierites from El Peñón, Sierra de Córdoba, Argentina. *Contrib Mineral Petrol* 90: 93-101.
- Green TH (1976) Experimental generation of cordierite- or garnet-bearing granitic liquids from a pelitic composition. *Geology* 4: 85-88.
- Grew ES, Hinthorne JR, Marquez N (1986) Li, Be, B, and Sr in margarite and paragonite from Antarctica. *Am Mineral* 71: 1129-1134.
- Grew ES, Yates MG, Huijsmans JP, McGee JJ, Shearer CK, Wiedenbeck M, Rouse R

- (1998) Werdingite, a borosilicate new to granitic pegmatites. *Can Mineral* 36: 399-414.
- Guggenheim, S. (1984) The brittle micas. In: Bailey SW (ed) *Micas*. Mineral Society Am, *Rev Mineral* 13: 257-298.
- Hölscher A, Schreyer W (1989) A new synthetic hexagonal BeMg-cordierite, $Mg_2[Al_2BeSi_6O_{18}]$, and its relationship to Mg-cordierite. *Eur J Mineral* 1: 21-37.
- Huebner, J.S. (1971) Buffering techniques for hydrostatic systems at elevated pressures. In: Ulmer GC (ed) *Research Techniques for High Pressure and High Temperature*. Springer-Verlag, New York, pp 123-177.
- Icenhower JP (1995) Experimental determination of element behavior in silicic systems during hydrous partial fusion. PhD Thesis, University of Oklahoma, Norman, Oklahoma, 227 p.
- Icenhower JP, London D, Layne GD (1994) Element partitioning among biotite, muscovite, garnet, cordierite, and peraluminous melt: Behavior of Li and Mn. *Geol Soc Am, Abstr Programs* 26 (7): 290.
- Icenhower JP, London D (1995) An experimental study of element partitioning among biotite, muscovite, and coexisting peraluminous silicic melt at 200 MPa (H_2O). *Am Mineral* 80: 1229-1251.
- Kamber BS, Frei R, Gibb AJ (1998) Pitfalls and new approaches in granulite chronometry: An example from Limpopo Belt, Zimbabwe. *Precam Res* 91: 269-285.
- Kalt A, Berger A, Blumel P (1999) Metamorphic evolution of cordierite-bearing

- migmatites from the Bayerische Wald (Variscan Belt, Germany). *J Petrol* 40: 601-627.
- Kennen P (2001) The S-type Leinster granite in SE Ireland. In: Chappell B, Fleming P (eds) S-type granites and related rocks, abstracts, Australian Geol Survey Org, Rec 2001/02, pp. 65-66.
- Kirchner D, Mirwald PW, Schreyer W (1984) Experimenteller Li-Einbau in Mg-Cordierit. *Fortschritte Mineral, Beiheft* 62: 119-120.
- Kretz R, Loop J, Hartree R (1989) Petrology and Li-Be-B geochemistry of muscovite-biotite granite and associated pegmatite near Yellowknife, Canada. *Contrib Mineral Petrol* 102: 174-190.
- Lofgren GE (1983) Effect of heterogeneous nucleation on basaltic textures: A dynamic crystallization study. *J Petrol* 24: 229-255.
- London D (1995) Geochemical features of peraluminous granites, pegmatites, and rhyolites as sources of lithophile metal deposits. In: Thompson JFH (ed) *Magmas, Fluids, and Ore Deposits, Mineral Assoc Can Short Course* 23: pp 175-202.
- London D, Wolf MB, Morgan GM, Gallegos Garrido M (1999) Experimental silicate-phosphate equilibria in peraluminous granitic magmas, with a case study of the Albuquerque Batholith at Tres Arroyos, Badajoz, Spain. *J Petrol* 40: 215-240.
- London D, Evensen JM (2001) The beryllium cycle from anatexis of metapelites to beryll-bearing pegmatites. 11th Annual V.M. Goldschmidt Conf, Hot Springs, VA, USA (submitted).
- Morgan GB, London D (1996) Optimizing the electron microprobe of hydrous alkali aluminosilicate glasses. *Am Mineral* 81: 1176-1185.

- Mukhopadhyay B, Holdaway MJ (1993) Cordierite-garnet-sillimanite-quartz equilibrium:
I. New experimental calibration in the system FeO-Al₂O₃-SiO₂-H₂O and certain
P-T-X_{H₂O} relations. *Contrib Mineral Petrol* 116: 462-472.
- Neiva ANR, Neiva JMC, Parry SJ (1987) Geochemistry of the granitic rocks and their
minerals from Serra da Estrela, central Portugal. *Geochim Cosmochim Acta* 51:
439-454.
- Norton JJ, Redden JA (1990) Relations of zoned pegmatites, granites, and metamorphic
rocks in the southern Black Hills, South Dakota. *Am Mineral* 75: 631-655.
- Pan Y, Brecks FW (1997) Rare-elements in fluoroapatite, Separation Lake Area, Ontario:
Evidence for S-Type granite – rare-element pegmatite linkage. *Can Mineral* 35:
659-671.
- Patiño Douce AE (1992) Calculated relationships between activity of alumina and phase
assemblages of silica-saturated igneous rocks: Petrogenetic implications of
magmatic cordierite, garnet and aluminosilicate. *J Vol Geotherm Res* 52: 43-63.
- Peacor DR, Wedepohl KH (1978) Manganese. In: Wedepohl KH (ed) *Handbook of
Geochemistry*, vol. II/3, Springer: pp 25-A-1 to 25-O-2.
- Pearce NJG, Perkins WT, Westgate JA, Gorton MP, Jackson SE, Neal CR, Chenery SP
(1997) A compilation of new and published major and trace element data for
NIST SRM 610 and SRM 612 glass reference materials. *Geostandards Newsletter*
21: 115-144.
- Pereira MD, Bea F (1994) Cordierite-producing reactions in the Peña Negra Complex,
Avila Batholith, Central Spain. *Can Mineral* 32: 763-780.
- Raimbault L, Cuney M, Azencott C, Duthou JL, Joron JL (1995) Geochemical evidence

- for a multistage magmatic genesis of Ta-Sn-Li mineralization in the granite at Beauvoir, French Massif Central. *Econ Geol Bull Soc Econ Geologists* 90: 548-576.
- Ramirez JA, Grundvig S (2000) Causes of geochemical diversity in peraluminous granitic plutons: the Jalmala pluton, Central-Iberian Zone (Spain and Portugal). *Lithos* 50: 171-190.
- Russ JC (1999) *The Image Processing Handbook*, 3rd Ed. CRC Press, Boca Raton, Florida. 771p.
- Smeds SA (1992) Trace element in potassium-feldspar and muscovite as a guide in the prospecting for lithium- and tin-bearing pegmatites in Sweden. *J Geochem Expl* 42: 351-369.
- Spear FS, Cheney JT (1989) A petrogenetic grid for pelitic schists in the system SiO_2 - Al_2O_3 - FeO - MgO - K_2O - H_2O . *Contrib Mineral Petrol* 101:149-164.
- Ugidos JM (1988) New aspects and considerations on the assimilation of cordierite-bearing rocks. *Rev. Soc. Geol. España* 1: 129-133.
- Ugidos JM (1990) Granites in the Central Iberian Massif as a paradigm of genetic processes of granitic rocks: I-types vs S-types. In: Dallmayer RD, Martínez García E (eds) *Pre-Mesozoic Geology of Iberia*, Springer: pp 189-206.
- Ugidos JM, Recio C (1993) Origin of cordierite-bearing granites by assimilation in the Central Iberian Massif (CIM), Spain. *Contrib Mineral Petrol* 103: 27-43.
- Vielzeuf D, Holloway JR (1988) Experimental determination of the fluid-absent melting relations in the pelitic system. *Contrib Mineral Petrol* 98: 257-276.
- Visser D, Kloprogge JT, Maijer C (1994) An infrared spectroscopic (IR) and light element (Li, Be, Na) study of cordierites from the Bamble Sector, South Norway. *Lithos* 32: 95-107.

- Watson EB, Capobianco CJ (1994) Phosphorus and the rare earth elements in felsic magmas: An assessment of the role of apatite. *Geochim Cosmochim Acta* 45: 2349-2359.
- White AJR, Clemens JD, Holloway JR, Silver LT, Chappell BW, Wall VJ (1986a) S-type granites and their probable absence in southwestern North America. *Geology* 14: 115-118.
- White AJR, Clemens JD, Holloway JR, Silver LT, Chappell BW, Wall VJ (1986b) Reply to C.F. Miller's Comment on S-type granites and their probable absence in southwestern North America. *Geology* 14: 805-806.
- Wolf MB, London D (1995) Incongruent dissolution of REE- and Sr-rich apatite in peraluminous granitic liquids: Differential apatite, monazite, and xenotime solubilities during anatexis. *Am Mineral* 80: 765-775.
- Wolf MB, London D (1997) Boron in granitic magmas: stability of tourmaline in equilibrium with biotite and cordierite. *Contrib Mineral Petrol* 130: 12-30.
- Wuensch BJ, Hörmann PK (1978) Beryllium. In: Wedepohl KH (ed) *Handbook of Geochemistry*, vol II (1). Springer, Berlin Heidelberg New York, pp 4-A-1 to 4-O-1.
- Zen E (1987) Wet and dry AFM assemblages of peraluminous granites and the usefulness of cordierite as the prime indicator of S-type granite. *Geol Soc Am, Abstr Programs* 19: 904.

Table 3-1. STARTING MATERIALS

ADDED MINERALS								
Mineral ^a	albite	orthoclase	quartz	muscovite ^b	biotite	garnet-1 Alm ₄₄ Pyp ₄₂ Gro ₁₃ Sps ₁	garnet-2 Alm ₄₆ Pyp ₄₄ Gro ₄ Sps ₆	
No. of analyses	5	20	6	1-3	96	20	20	
oxide wt%								
SiO ₂	68.82 (0.16)	64.95 (0.36)	99.99 (0.03)	51.91	-	38.83 (0.29)	39.71 (0.26)	39.53 (0.22)
TiO ₂	nd	nd	nd	0.22	-	2.05 (0.11)	0.04 (0.02)	0.01 (0.01)
Al ₂ O ₃	19.76 (0.05)	18.76 (0.14)	nd	28.02	-	11.26 (0.12)	23.20 (0.16)	23.14 (0.13)
Fe ₂ O ₃	-	-	-	3.53	-	-	-	-
FeO	nd	nd	nd	0.82 ^c	-	18.47 (0.25)	21.26 (0.14)	22.05 (0.17)
MnO	nd	nd	nd	0.08	-	0.83 (0.04)	0.46 (0.02)	3.11 (0.09)
ZnO	nd	nd	nd	nd	-	0.14 (0.04)	nd	nd
MgO	nd	nd	nd	1.00	-	14.08 (0.21)	11.46 (0.05)	11.89 (0.08)
CaO	0.07 (0.01)	0.01 (0.02)	nd	0.30	-	0.00 (0.01)	5.07 (0.04)	1.45 (0.02)
BaO	0.06 (0.05)	0.32 (0.04)	nd	0.09 ^d	-	0.10 (0.02)	0.02 (0.02)	0.02 (0.02)
Na ₂ O	11.59 (0.04)	1.21 (0.07)	nd	1.27	-	0.56 (0.14)	0.00	0.00
K ₂ O	0.23 (0.02)	14.84 (0.07)	nd	8.90	-	9.01 (0.14)	0.00	0.00
Rb ₂ O (ppmw)	nd	nd	nd	895 ^e	-	nd	nd	nd
Cs ₂ O (ppmw)	nd	nd	nd	23 ^e	-	nd	nd	nd
P ₂ O ₅	nd	nd	nd	nd	-	nd	0.04 (0.01)	0.07 (0.02)
F	nd	nd	nd	nd	-	3.67 (0.14)	0.02 (0.03)	0.01 (0.02)
Cl	nd	nd	nd	nd	-	0.05 (0.02)	0.01 (0.01)	0.00
H ₂ O	nd	nd	nd	nd	-	2.02 ^o (0.08)	nd	nd
LOI	-	-	-	3.87	-	-	-	-
O=F					-	-1.54	-0.01	0.00
O=Cl					-	-0.01	0.00	0.00
Total	100.53 (0.18)	100.09 (0.40)	99.99 (0.03)	100.10 (0.16)	99.52 (0.53)	101.28 (0.35)	101.28 (0.29)	

^a albite, Copelinha, Minas Geras, Brazil; orthoclase, St. Gotthard, Switzerland; quartz, ultrahigh purity, Feldspar Corp., Spruce Pine, NC, USA; muscovite, Spruce Pine, NC, USA; biotite, Ontario, Canada; garnet-1, Gore Mountain, NY, USA; garnet-2, laboratory standard.

^b Analysed at Activation Laboratories Ltd. (Lancaster, Ontario, Canada) by X-Ray fluorescence (fusion) unless otherwise specified.

^c Analysed by titration.

^d Analysed by instrumental neutron activation analysis.

All other values are from quantitative electron probe microanalysis (with total iron as FeO).

Numbers in parantheses represent 1 standard deviation of the mean.

Propagated precision is shown for total values; the italicized value represents estimated precision.

Table 3-2a. Cordierite - Glass Pairs from Forward Experiments

Run	BeP-56		BeP-60		BeP-57		BeP-58		BeP-68		BeP-105	
Mixture	SP-Crd-1		SP-Crd-1		SP-Crd-1		SP-Crd-1		SP-Crd-1		SP-Crd-2	
Prec. Path/Duration (d)												
Final Path/Duration (d)	700-F (26)		700-F (26)		750-F (26)		800-F (14)		800-F (17)		850-F (6)	
Crystalline Products	Crd,Bt,Mt,Qtz,Pl		Crd,Bt,Mt,Qtz,Pl		Crd,Bt,Mt		Crd,Bt,Mt		Crd,Bt,Mt		Crd,Bt,Mt	
Analysis of	Crd	glass	Crd	glass	Crd	glass	Crd	glass	Crd	glass	Crd	glass
No. analyses, QEPMA	7	11	20	10	10	11	10	11	18	10	10	12
No. analyses, SIMS	2	2	2	3	2	2	2	2	2	3	1	1
wt %	se	sd	se	sd	se	sd	se	sd	se	sd	se	sd
SiO ₂	48.47 (0.26)	70.95 (0.60)	48.42 (0.33)	70.83 (1.04)	48.25 (0.36)	70.57 (0.63)	48.25 (0.22)	70.01 (0.53)	48.27 (0.18)	70.79 (0.69)	49.14 (0.39)	69.23 (0.70)
TiO ₂	0.02 (0.01)	0.05 (0.01)	0.01 (0.01)	0.01 (0.01)	0.01 (0.01)	0.02 (0.01)	0.02 (0.01)	0.12 (0.02)	0.01 (0.01)	0.09 (0.02)	0.01 (0.01)	0.10 (0.02)
B ₂ O ₃ (ppmw) ¹	3 (0)	93 (2)	3 (1)	100 (1)	2 (0)	79 (0)	2 (0)	80 (0)	2 (0)	85 (1)	17 -	88 -
Al ₂ O ₃	34.66 (0.18)	12.80 (0.25)	33.78 (0.14)	12.12 (0.18)	34.73 (0.16)	12.85 (0.12)	33.93 (0.13)	13.12 (0.25)	34.28 (0.11)	13.10 (0.12)	33.65 (0.29)	13.44 (0.18)
FeO	8.79 (0.17)	0.82 (0.05)	3.13 (0.09)	0.38 (0.03)	2.77 (0.09)	0.58 (0.05)	2.94 (0.02)	0.81 (0.05)	3.77 (0.08)	0.99 (0.17)	3.59 (0.20)	1.32 (0.07)
MnO	0.69 (0.04)	0.09 (0.01)	0.78 (0.03)	0.10 (0.01)	0.47 (0.02)	0.10 (0.02)	0.33 (0.02)	0.11 (0.01)	0.37 (0.02)	0.12 (0.01)	0.50 (0.03)	0.26 (0.02)
MgO	9.24 (0.16)	0.21 (0.01)	10.94 (0.11)	0.15 (0.02)	11.98 (0.07)	0.27 (0.01)	12.05 (0.05)	0.52 (0.01)	11.42 (0.07)	0.47 (0.01)	11.26 (0.21)	0.84 (0.02)
NiO	0.00	nd	0.01 (0.01)	nd	0.00	nd	0.00	nd	0.01 (0.01)	nd	0.01 (0.01)	nd
ZnO	nd	nd	nd	nd	nd	nd	nd	nd	0.02 (0.02)	nd	0.02 (0.02)	nd
BeO (ppmw) ¹	290.60 (18.21)	1.45 (0.07)	121.20 (19.41)	0.60 (0.05)	191.20 (11.20)	1.15 (0.03)	157.10 (9.80)	5.00 (0.20)	173.40 (18.29)	4.40 (0.56)	61.00 -	9.10 -
CaO	0.20 (0.03)	0.85 (0.04)	0.17 (0.01)	0.61 (0.09)	0.17 (0.01)	1.07 (0.07)	0.16 (0.02)	1.06 (0.09)	0.18 (0.02)	0.92 (0.08)	0.05 (0.01)	0.28 (0.06)
BaO	0.01 (0.01)	0.06 (0.03)	0.02 (0.02)	nd	0.01 (0.01)	0.05 (0.02)	0.02 (0.02)	0.05 (0.03)	nd	0.04 (0.03)	nd	0.07 (0.05)
Li ₂ O (ppmw) ¹	180 (22)	452 (9)	181 (12)	409 (8)	137 (1)	399 (7)	92 (12)	434 (3)	98 (2)	369 (18)	29 -	255 -
Na ₂ O	0.48 (0.05)	3.21 (0.10)	0.52 (0.04)	3.04 (0.11)	0.41 (0.06)	3.27 (0.10)	0.38 (0.02)	3.14 (0.12)	0.38 (0.01)	3.32 (0.13)	0.49 (0.03)	3.35 (0.08)
K ₂ O	0.06 (0.01)	3.31 (0.10)	0.10 (0.02)	3.61 (0.10)	0.08 (0.01)	3.37 (0.08)	0.12 (0.01)	3.36 (0.15)	0.11 (0.02)	3.19 (0.06)	0.32 (0.05)	3.49 (0.08)
Rb ₂ O (ppmw) ¹	5 (2)	104 (3)	8 (1)	134 (5)	7 (0)	110 (1)	8 (0)	110 (1)	8 (0)	102 (4)	23 -	119 -
Cs ₂ O (ppmw) ¹	2 (0)	9 (0)	2 (0)	11 (2)	2 (1)	14 (3)	4 (0)	12 (2)	5 (1)	7 (0)	4 -	7 -
P ₂ O ₅	nd	0.12 (0.05)	nd	0.04 (0.03)	nd	0.11 (0.04)	nd	0.12 (0.03)	nd	0.06 (0.02)	nd	0.03 (0.03)
F	0.03 (0.03)	0.16 (0.04)	0.04 (0.04)	0.21 (0.05)	0.01 (0.01)	0.18 (0.07)	0.01 (0.01)	0.19 (0.07)	0.04 (0.03)	0.29 (0.09)	0.04 (0.04)	0.22 (0.07)
Cl	nd	0.01 (0.00)	0.00	0.00	nd	0.01 (0.01)	nd	0.01 (0.01)	0.00	0.01 (0.01)	nd	0.00
O=F	-0.01	-0.08	-0.02	-0.09	0.00	-0.08	-0.01	-0.08	-0.02	-0.12	-0.02	-0.09
O=Cl	0.00	0.00	0.00	0.00	0.00	0.00	0.00	0.00	0.00	0.00	0.00	0.00
total	98.69 (0.40)	92.43 (0.63)	97.91 (0.39)	91.03 (1.19)	98.92 (0.41)	92.39 (0.69)	98.22 (0.26)	92.58 (0.64)	98.85 (0.31)	93.31 (0.69)	99.05 (0.38)	92.57 (0.81)
H ₂ O by diff	1.31	7.57	2.09	8.97	1.08	7.61	1.78	7.42	1.15	6.69	0.95	7.43
ASI		1.21 (0.03)		1.20 (0.03)		1.16 (0.03)		1.21 (0.05)		1.23 (0.02)		1.36 (0.02)
Mg#	68.7 (1.7)		83.3 (2.4)		66.6 (2.8)		88.6 (0.8)		83.1 (1.8)		83.0 (4.6)	
D-B Crd/MELT	0.03 (0.00)		0.03 (0.01)		0.03 (0.00)		0.02 (0.00)		0.02 (0.00)		0.20	
D-Mn Crd/MELT	7.87 (0.96)		7.80 (0.82)		4.70 (0.86)		3.00 (0.33)		3.08 (0.31)		1.82 (0.19)	
D-Be Crd/MELT	200.41 (14.78)		202.00 (36.47)		166.26 (10.66)		31.42 (2.33)		39.41 (6.23)		6.70	
D-Ca Crd/MELT	0.24 (0.04)		0.28 (0.04)		0.16 (0.01)		0.15 (0.02)		0.20 (0.03)		0.18 (0.05)	
D-Li Crd/MELT	0.40 (0.05)		0.44 (0.03)		0.34 (0.01)		0.21 (0.03)		0.26 (0.01)		0.12	
D-Rb Crd/MELT	0.05 (0.02)		0.06 (0.01)		0.06 (0.00)		0.07 (0.00)		0.08 (0.00)		0.20	
D-Cs Crd/MELT	0.19 (0.00)		0.21 (0.04)		0.13 (0.08)		0.38 (0.08)		0.63 (0.14)		0.52	
structural cations/18O												
Si	4.77 (0.03)		4.92 (0.04)		4.85 (0.04)		4.88 (0.03)		4.87 (0.02)		4.94 (0.04)	
Al	4.20 (0.03)		4.05 (0.02)		4.11 (0.03)		4.04 (0.02)		4.07 (0.02)		3.99 (0.04)	
Be	0.01 (0.00)		0.00		0.00		0.00		0.00		0.00	
total T sites	8.98 (0.04)		8.97 (0.05)		8.96 (0.05)		8.92 (0.03)		8.94 (0.03)		8.93 (0.06)	
Li	0.01 (0.00)		0.01 (0.00)		0.01 (0.00)		0.00 (0.00)		0.00 (0.00)		0.00 (0.00)	
Mg	1.42 (0.03)		1.66 (0.02)		1.79 (0.01)		1.82 (0.01)		1.72 (0.01)		1.69 (0.03)	
Fe ²⁺	0.58 (0.01)		0.27 (0.01)		0.23 (0.01)		0.25 (0.00)		0.32 (0.01)		0.30 (0.02)	
Mn	0.06 (0.00)		0.07 (0.00)		0.04 (0.00)		0.03 (0.00)		0.03 (0.00)		0.04 (0.00)	
total M site	2.07 (0.03)		2.01 (0.02)		2.07 (0.02)		2.10 (0.01)		2.07 (0.01)		2.03 (0.04)	
total	11.05 (0.05)		10.98 (0.05)		11.03 (0.05)		11.02 (0.03)		11.01 (0.03)		10.96 (0.07)	
channel occupants/18 O												
Ca	0.02 (0.00)		0.02 (0.00)		0.02 (0.00)		0.02 (0.00)		0.02 (0.00)		0.01 (0.00)	
Na	0.10 (0.01)		0.10 (0.01)		0.08 (0.01)		0.07 (0.00)		0.07 (0.00)		0.10 (0.01)	
K	0.01 (0.00)		0.01 (0.00)		0.01 (0.00)		0.02 (0.00)		0.01 (0.00)		0.04 (0.01)	
H ₂ O	0.85 (0.00)		1.34 (0.01)		0.69 (0.00)		1.14 (0.00)		0.73 (0.00)		0.60 (0.00)	
total	0.98 (0.01)		1.47 (0.01)		0.80 (0.01)		1.25 (0.01)		0.83 (0.00)		0.75 (0.01)	

Table 3-2b. Cordierite - Glass Pairs from Reversed Experiments

Run	BeP-05			BeP-06			BeP-19			BeP-07		
Mixture	SP-Crd-2			SP-Crd-2			SP-Crd-1			SP-Crd-2		
Proc. Path/Duration (d)	850-F (6)			850-F (6)			850-F (6)			850-F (6)		
Final Path/Duration (d)	700-R (34)			750-R (21)			800-R (16)			800-R (14)		
Crystalline Products	Crd,Bt,Mt			Crd,Bt,Mt			Crd,Bt,Mt			Crd,Bt,Mt		
Analysis of	Crd	Crd	glass	Crd	Crd	glass	Crd	Crd	glass	Crd	Crd	glass
	cores	rims		cores	rims		cores	rims		cores	rims	
No. analyses, QEPMA	8	14	10	11	12	12	10	6	10	11	17	12
No. analyses, SIMS		1	2		2	5	1	1	2		1	3
wt %	se	se	sd	se	se	sd	se	se	sd	se	se	sd
SiO ₂	49.01 (0.23)	49.04 (0.11)	72.03 (0.52)	47.88 (0.41)	47.98 (0.32)	70.89 (0.77)	48.54 (0.28)	49.73 (0.19)	70.51 (0.38)	47.49 (0.41)	49.10 (0.32)	71.39 (0.63)
TiO ₂	0.01 (0.01)	0.01 (0.01)	0.03 (0.02)	0.01 (0.02)	0.01 (0.01)	0.05 (0.02)	0.02 (0.02)	0.02 (0.02)	0.08 (0.01)	0.02 (0.02)	0.01 (0.01)	0.10 (0.02)
B ₂ O ₃ (ppmw) ¹	nd	7 -	124 (3)	nd	3 (0)	83 (4)	8 -	13 -	133 (10)	nd	10 -	98 (4)
Al ₂ O ₃	33.21 (0.14)	33.54 (0.10)	12.05 (0.08)	33.79 (0.32)	33.18 (0.20)	12.24 (0.12)	33.83 (0.28)	32.88 (0.14)	12.97 (0.12)	34.39 (0.13)	34.18 (0.20)	12.85 (0.09)
FeO	4.78 (0.35)	3.88 (0.22)	0.39 (0.04)	5.72 (0.14)	8.03 (0.11)	0.78 (0.03)	2.88 (0.07)	2.46 (0.18)	0.75 (0.04)	5.02 (0.18)	2.88 (0.10)	0.61 (0.03)
MnO	0.98 (0.07)	1.21 (0.06)	0.18 (0.02)	0.83 (0.05)	1.06 (0.04)	0.20 (0.01)	0.27 (0.04)	0.34 (0.02)	0.10 (0.01)	0.70 (0.03)	0.72 (0.03)	0.20 (0.01)
MgO	9.73 (0.24)	10.25 (0.32)	0.17 (0.01)	9.41 (0.28)	8.45 (0.13)	0.21 (0.01)	12.74 (0.06)	12.38 (0.14)	0.45 (0.02)	10.28 (0.17)	11.58 (0.11)	0.38 (0.01)
NiO	0.01 (0.01)	0.01 (0.01)	nd	0.03 (0.01)	0.01 (0.01)	nd	0.01 (0.01)	0.01 (0.01)	nd	0.01 (0.00)	0.01 (0.01)	nd
ZnO	0.02 (0.02)	0.02 (0.02)	nd	0.01 (0.01)	0.01 (0.01)	nd	nd	nd	nd	0.02 (0.02)	0.02 (0.02)	nd
BeO (ppmw) ¹	nd	162.00 -	1.00 (0.18)	nd	195.80 (3.15)	1.40 (0.19)	16.00 -	201.00 -	6.55 (0.15)	nd	123.60 -	3.20 (0.29)
CaO	0.07 (0.02)	0.05 (0.01)	0.20 (0.05)	0.09 (0.02)	0.07 (0.02)	0.23 (0.06)	0.14 (0.02)	0.17 (0.02)	0.92 (0.06)	0.09 (0.06)	0.06 (0.02)	0.20 (0.05)
BeO	nd	nd	0.06 (0.03)	nd	nd	0.06 (0.04)	0.01 (0.01)	0.02 (0.02)	0.05 (0.03)	nd	nd	0.05 (0.03)
Li ₂ O (ppm) ¹	nd	125 -	383 (5)	nd	80 (7)	267 (18)	56 -	56 -	444 (8)	nd	80 -	257 (18)
Na ₂ O	0.58 (0.04)	0.54 (0.09)	3.68 (0.13)	0.65 (0.06)	0.59 (0.05)	3.62 (0.08)	0.37 (0.05)	0.33 (0.03)	3.21 (0.10)	0.54 (0.06)	0.48 (0.03)	3.44 (0.09)
K ₂ O	0.15 (0.02)	0.12 (0.02)	3.64 (0.10)	0.35 (0.03)	0.18 (0.01)	3.41 (0.10)	0.12 (0.03)	0.22 (0.03)	3.33 (0.06)	0.18 (0.04)	0.20 (0.03)	3.73 (0.10)
Rb ₂ O (ppmw) ¹	nd	9 -	102 (0)	nd	12 (1)	111 (4)	10 -	11 -	127 (1)	nd	10 -	128 (4)
Cs ₂ O (ppmw) ¹	nd	3 -	11 (1)	nd	4 (0)	11 (0)	3 -	6 -	15 (0)	nd	2 -	7 (0)
F ₂ O ₃	nd	nd	0.03 (0.02)	nd	nd	0.03 (0.02)	nd	nd	0.05 (0.02)	nd	nd	0.03 (0.02)
F	0.02 (0.02)	0.05 (0.05)	0.23 (0.06)	0.04 (0.04)	0.02 (0.02)	0.18 (0.05)	0.03 (0.03)	0.02 (0.03)	0.24 (0.09)	0.02 (0.03)	0.04 (0.04)	0.20 (0.05)
Cl	0.01 (0.01)	0	0.01 (0.00)	0	0	0.01 (0.01)	nd	nd	0.01 (0.00)	0	0.01 (0.01)	0.01 (0.00)
O=F	-0.01	-0.02	-0.10	-0.02	-0.01	-0.08	-0.01	-0.10	-0.10	-0.01	-0.02	-0.08
O=Cl			0.00	0	0	0.00			0.00	0	0.00	0.00
total	98.55 (0.38)	98.68 (0.43)	92.50 (0.87)	98.79 (0.61)	99.54 (0.42)	91.67 (0.84)	98.64 (0.40)	98.68 (0.33)	92.52 (0.44)	98.75 (0.50)	99.27 (0.41)	92.83 (0.66)
H ₂ O by diff	1.45	1.32	7.60		0.46	8.33	1.46	1.44	7.48	1.25	0.73	7.17
ASI			1.16 (0.03)			1.23 (0.03)			1.21 (0.02)			1.25 (0.03)
Mg#	75.0 (5.5)	78.2 (4.5)		71.9 (1.8)	82.3 (0.9)		88.5 (2.3)	88.7 (6.5)		78.2 (2.7)	85.1 (3.0)	
D-B Crd/MELT		0.06			0.04 (0.00)			0.10			0.10	
D-Mn Crd/MELT		7.58 (1.02)			5.30 (0.33)			3.40 (0.39)			3.80 (0.23)	
D-Be Crd/MELT		162.00			139.86 (18.92)			30.89			38.83	
D-Ca Crd/MELT		0.25 (0.08)			0.30 (0.12)			0.18 (0.02)			0.30 (0.13)	
D-Li Crd/MELT		0.33			0.30 (0.03)			0.13			0.31	
D-Rb Crd/MELT		0.09			0.11 (0.01)			0.09			0.13	
D-Cs Crd/MELT		0.28			0.35 (0.00)			0.39			0.34	
structural cations/18O												
Si	4.89 (0.03)	4.96 (0.02)		4.89 (0.05)	4.90 (0.04)		4.89 (0.03)	5.00 (0.03)		4.84 (0.05)	4.92 (0.04)	
Al	3.98 (0.02)	4.00 (0.02)		4.07 (0.05)	4.07 (0.03)		3.99 (0.03)	3.89 (0.02)		4.13 (0.03)	4.03 (0.03)	
Be		0.00			0.00		0.00	0.00			0.00	
total T sites	8.97 (0.04)	8.96 (0.03)		8.96 (0.07)	8.97 (0.05)		8.88 (0.05)	8.89 (0.03)		8.97 (0.06)	8.95 (0.05)	
Li		0.00			0.00		0.00	0.00			0.00	
Mg	1.48 (0.04)	1.55 (0.05)		1.43 (0.04)	1.44 (0.02)		1.91 (0.01)	1.85 (0.02)		1.58 (0.03)	1.73 (0.02)	
Fe ²⁺	0.41 (0.03)	0.33 (0.02)		0.49 (0.01)	0.47 (0.01)		0.23 (0.01)	0.21 (0.02)		0.43 (0.02)	0.24 (0.01)	
Mn	0.08 (0.01)	0.10 (0.00)		0.07 (0.00)	0.09 (0.00)		0.02 (0.00)	0.03 (0.00)		0.06 (0.00)	0.06 (0.00)	
total M site	1.97 (0.05)	1.98 (0.05)		1.99 (0.05)	2.00 (0.02)		2.16 (0.01)	2.09 (0.03)		2.05 (0.03)	2.03 (0.02)	
total	10.94 (0.00)	10.94 (0.06)		10.95 (0.08)	10.97 (0.05)		11.04 (0.05)	10.98 (0.04)		11.02 (0.06)	10.98 (0.05)	
channel occupants/18 O												
Ca	0.01 (0.00)	0.01 (0.00)		0.01 (0.00)	0.01 (0.00)		0.02 (0.00)	0.02 (0.00)		0.01 (0.01)	0.01 (0.00)	
Na	0.11 (0.01)	0.11 (0.02)		0.13 (0.01)	0.12 (0.01)		0.07 (0.01)	0.06 (0.01)		0.11 (0.01)	0.09 (0.01)	
K	0.02 (0.00)	0.02 (0.00)		0.05 (0.00)	0.02 (0.00)		0.02 (0.01)	0.03 (0.00)		0.02 (0.00)	0.03 (0.00)	
H ₂ O		0.84 (0.00)			0.70 (0.00)			0.91 (0.00)			0.48 (0.00)	
total	0.14 (0.01)	0.98 (0.02)		0.19 (0.01)	0.85 (0.01)		0.11 (0.01)	1.02 (0.01)		0.14 (0.01)	0.59 (0.01)	

Table 3-3. Regressions of elemental partitioning between cordierite and granitic melt as a function of temperature.

D Ratio	Linear Fit	R² value
<i>compatible</i>		
$D_{\text{Be}}^{\text{Crd / MELT}}$	$D = 1181.93 - 1.41(T)$	0.9087
$D_{\text{Mn}}^{\text{Crd / MELT}}$	$D = 35.46 - 0.04(T)$	0.9712
<i>incompatible</i>		
* $D_{\text{B}}^{\text{Crd / MELT}}$	$D = -0.42 + 6.38e^{-4}(T)$	0.3660
$D_{\text{Li}}^{\text{Crd / MELT}}$	$D = 1.61 - 1.733e^{-3}(T)$	0.7301
* $D_{\text{Ca}}^{\text{Crd / MELT}}$	$D = 0.60 - 4.88e^{-4}(T)$	0.2006
$D_{\text{Rb}}^{\text{Crd / MELT}}$	$D = -0.34 + 5.70e^{-4}(T)$	0.5015
$D_{\text{Cs}}^{\text{Crd / MELT}}$	$D = -1.28 + 2.12e^{-3}(T)$	0.5466

* *T*-independent

Table 3-4. Reported Be contents of granitic rocks and their association to cordierite-bearing source rocks

Granitic sample	Crd-bearing rock	Beryl-bearing pegmatites?	Be (ppmw)			Cs (ppmw)			MnO (wt%)			N	Granite Body	Location	Reference
			mean	se	range	mean	se	range	mean	se	range				
leucosome	restite, leucosome		1.20	0.10	0.37 - 2.04	1.54	0.06	0.93 - 2.01	0.02	0.00	0.01 - 0.02	6	Pena Negra Complex	Central Spain	Bea et al., 1994b
main granite	restite, leucosome, granite		0.4	-	-	-	-	-	0.00	-	-	1	Anragigues leucogranite	Massif Central, France	Barbey et al., 1999
main granite	restite, leucosome, granite		1.1	-	-	-	-	-	0.03	-	-	1	Le Roux granite	Massif Central, France	Barbey et al., 1999
main granite	granite		<1	-	-	2.1	0.21	1.7 - 2.8	0.01	0.00	0.00 - 0.01	5	Ghost Lake batholith	Ontario, Canada	Breaks and Moore 1993
upper granite	no Crd	Brl pegmatites	3	1	2 - 4	7.7	-	-	0.02	0.00	-	2	Ghost Lake batholith	Ontario, Canada	Breaks and Moore 1993
upper facies	no Crd		4.3	0.3	3.7 - 4.5	23.5	4.7	17.7 - 32.8	0.02	0.01	0.01 - 0.03	11	Pedroberardo pluton	Central Spain	Bea et al., 1994a
middle facies	no Crd		4.0	0.2	3.5 - 4.4	9.9	0.5	8.8 - 11.1	0.03	0.00	0.02 - 0.03	12	Pedroberardo pluton	Central Spain	Bea et al., 1994a
lower facies	no Crd		4.1	0.5	2.9 - 4.8	9.7	1.2	8.7 - 12.5	0.02	0.00	-	14	Pedroberardo pluton	Central Spain	Bea et al., 1994a
central granite	no Crd	Brl pegmatites	4.0	0.3	3.6 - 4.3	11.0	3.1	7.9 - 14	0.07	0.00	0.06 - 0.07	2	Port Mouton pluton	S. Nova Scotia, Canada	Currie et al., 1998
central granite	no Crd	Brl pegmatites	4.1	0.3	3.0 - 5.1	6.1	1.0	4.2 - 8.8	0.05	0.01	0.02 - 0.07	4	Shelburne pluton	S. Nova Scotia, Canada	Currie et al., 1998
granite facies	no Crd	Brl pegmatites	5	1	4 - 7	-	-	-	0.02	0.00	0.02 - 0.03	32	Sparrow granite	NWT, Canada	Kretz et al., 1989
central granite	no Crd		12	1	4 - 33	40	3	9.1 - 81.5	0.039	0.001	0.024 - 0.074	10	Tin-rich granites	NW Bohemia	Breiter et al., 1991
main granite	no Crd	Brl pegmatites	8	-	-	-	-	-	-	-	-		Harney Peak granite	South Dakota, USA	Norton and Redden 1990
upper facies	no Crd	Brl pegmatites	11.4	-	5.7 - 17	32	-	14 - 50	0.09	-	0.03 - 0.14		Elkhorn, Harney Peak granite	South Dakota, USA	Shearer et al., 1987
evolved facies	no Crd	Brl pegmatites	64.0	-	28.0 - 100	17	-	10 - 23	0.14	-	0.05 - 0.22		Sky Lode, Harney Peak granite	South Dakota, USA	Shearer et al., 1988
major facies	no Crd		6.1	0.3	3.6 - 8.0	23.5	1.1	11.1 - 45.2	0.61	0.03	0.19 - 0.99	10	Jalmala pluton	Central Spain	Ramirez and Grundvig 2000
evolved facies	no Crd		11.0	3.0	8.0 - 16.95	44.2	2.5	39.4 - 53.0	0.21	0.01	0.18 - 0.25	3	Jalmala pluton	Central Spain	Ramirez and Grundvig 2000
apical granite	no Crd	Brl pegmatites	11	2	9 - 12	14	2	12 - 15	0.05	0.00	0.05 - 0.06	3	Leinster granite	SE Ireland	Luecke 1981, Kennan 2001
evolved facies	no Crd	Brl pegmatites	11	5	6 - 25	47	33	13 - 145	0.06	0.01	0.06 - 0.10	4	Leinster granite	SE Ireland	Luecke 1981, Kennan 2001
evolved microgranite	no Crd	Accessory Brl	130	31	34 - 385	224	14	60 - 350	0.05	0.00	0.04 - 0.06	10	Argemela granite	Central Portugal	Charoy and Noronha 1996
evolved facies	no Crd	Be-phosphates	123	13.2	5.7 - 494	305	38.1	32.5 - 1471	0.044	0.003	0.014 - 0.108	95	Beauvolr granite	Massif Central, France	Raimbault et al., 1995
Average Be content of granite with early Crd			0.9	0.3	0.4 - 1.20	1.54	-	-	0.02	0.01	0.00 - 0.03				
Average Be content of granite with late Crd			0.7	0.2	<1 - 1.1	2.1	-	-	0.01	0.01	0.00 - 0.03				
Average Be content of Crd-bearing granite (at any stage)			0.8	0.2	<1 - 1.20	1.8	0.3	1.54 - 2.1	0.01	0.01	0.00 - 0.03				
Average Be content of Crd-free main granite			6	1.7	3 - 12	18	3.6	6.1 - 40	0.09	0.05	0.02 - 0.61				
Average Be content of granite with associated Brl pegmatites			14	8.4	3 - 64	15	4.7	6.1 - 32	0.06	0.02	0.02 - 0.14				
Average Be content of evolved granite facies			68	25.9	11 - 130	127	58	17 - 224	0.10	0.03	0.05 - 0.21				

Italicized entries represent median values.

Table 3-5. Reported Be contents of migmatite systems

*Pena Negra Complex, central Spain**(Bea et al., 1994b)*

Migmatite facies	Crd-bearing?	Be (ppmw)			Cs (ppmw)			MnO (wt%)			N
		mean	se	range	mean	se	range	mean	se	range	
mesosome	yes	2.34	0.65	1.13 - 4.75	5.69	0.35	4.89 - 6.58	0.07	0.01	0.05 - 0.11	5
melansome	yes	6.04	1.35	3.51 - 8.10	13.47	1.04	11.6 - 15.2	0.13	0.01	0.10 - 0.15	3
leucosome	yes	1.20	0.10	0.37 - 2.04	1.54	0.06	0.93 - 2.01	0.02	0.00	0.01 - 0.02	6

Table 3-6. Cordierite-Bearing Normative Calculations of Melt at 700°C

*Input Conditions for Iteration	Limiting Crd Component	Norm							
		Ab	Or	Qtz	Cor	Mus	Bt	Mt	Crd
0 % Cor, Bt, Mus	Al	17.5	13.7	64.6	0	0	0	0.3	4.0
5 % Bt	Mg	19.1	12.1	60.6	2.3	0	4.9	0.7	0.3
5 % Mus	Mg	17.5	9.9	65.0	1.0	4.8	0.6	0.2	1.0
8 % Mus	Mg	17.5	7.4	65.0	0	8.4	0.5	0.3	1.0
10 % Mus	Al	17.5	6.2	65.4	0	9.6	1.0	0.2	0.1

*Following the initial conditions, the remainder of the mode was calculated by allocating moles of Mg equally between Bt and Crd using the stoichiometry of their recalculated formulae (Table 2).

Figure Captions

Figure 3-1. Working curve for the analysis of beryllium by SIMS. A total of 33 data points are shown using standard glasses and natural beryllian cordierite, analysed between three different sessions. The linear fit verifies that no significant matrix effect is seen for Be between rhyolitic glass and cordierite. Glass standards were previously characterized by aqua regia ICP-AES and QEPMA (Evensen 1997); cordierite was previously verified by AA (“Sponda 454” of Armbruster and Irouschek 1983) and by QEPMA.

Figure 3-2. Backscattered electron micrographs of experimental products and assemblages. Image scale is shown in micrometers. Labeled phase abbreviations include: Crd=cordierite, Bt=biotite, Mt=magnetite, Pl=plagioclase, Qtz=quartz, and gl=glass. (a) Cordierite crystals showing successful synthesis via reaction [1]. Needle-like white mica and magnetite are also shown. (b) Forward Experiment BeP-56: This assemblage contains Qtz and Pl in addition to Crd+Bt (also in vapor cavities) +Mt+vapor +melt. (c) Reversed Experiment BeP-95: At temperatures $\geq 750^{\circ}\text{C}$, the crystalline assemblage yields Crd+Mt+Bt in melt. Both the Crd crystals and glass pools show typical targets amenable to analysis. (d) Forward Experiment BeP-58: A characteristic large Crd crystal is shown, stable with Mt, Bt (not pictured), vapor and melt. (e) Reversed Experiment BeP-62 (not analysed for Be): Early Mg-richer Crd cores ($Mg\# = 73.1$) grew during the preconditioning step at 800°C , whereas an Fe-richer rims and new Crd crystals ($Mg\# = 63.8$) formed at the 750°C lower T step. This pattern was commonly produced in reversed

runs. (e) Magnified image of a Crd crystal in the same experiment as (d) showing early magnesian high- T core (Crd I) and an intermediate Fe-Mg rim (Crd II) as a function of thermal pathway.

Figure 3-3. Partitioning of Be between cordierite and melt at 200 MPa. Ten data points are shown. Closed circles mark forward experiments; open circles designate reversed experiments. Error bars signify 1-sigma propagated precision.

Figure 3-4. Partitioning of Li, Rb, Cs, B, Ca, and Mn between cordierite and melt at 200 MPa. X-axes are constant, but note scale changes among Y axes. Of the elements shown, only Mn is compatible. D-ratios of Mn and Li steadily decrease with T , while those of Rb and Cs increase; partitioning ratios of B and Ca do not appear to vary significantly with temperature. Ten data points are displayed in each plot.

Figure 3-1.

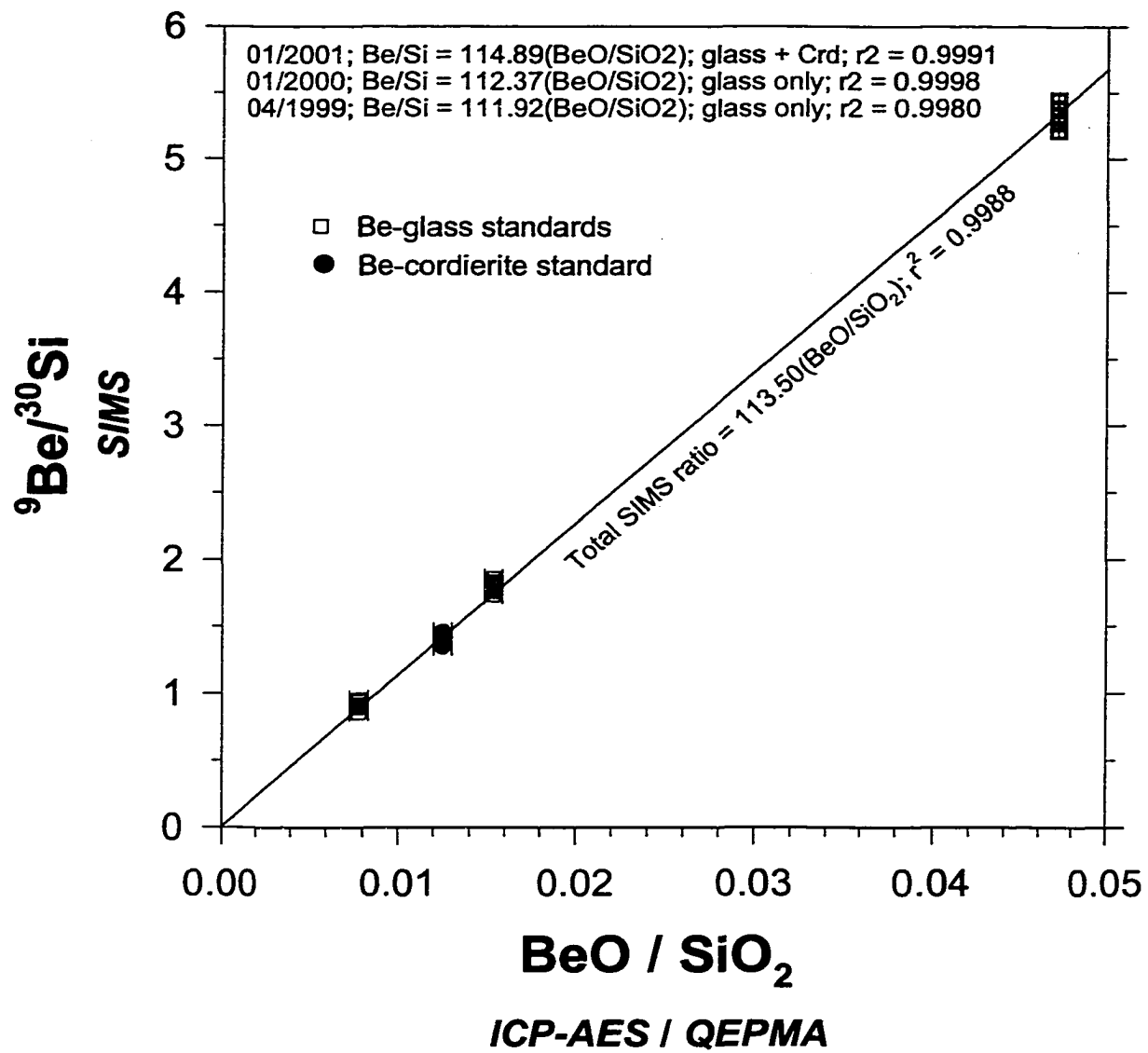


Figure 3-2.

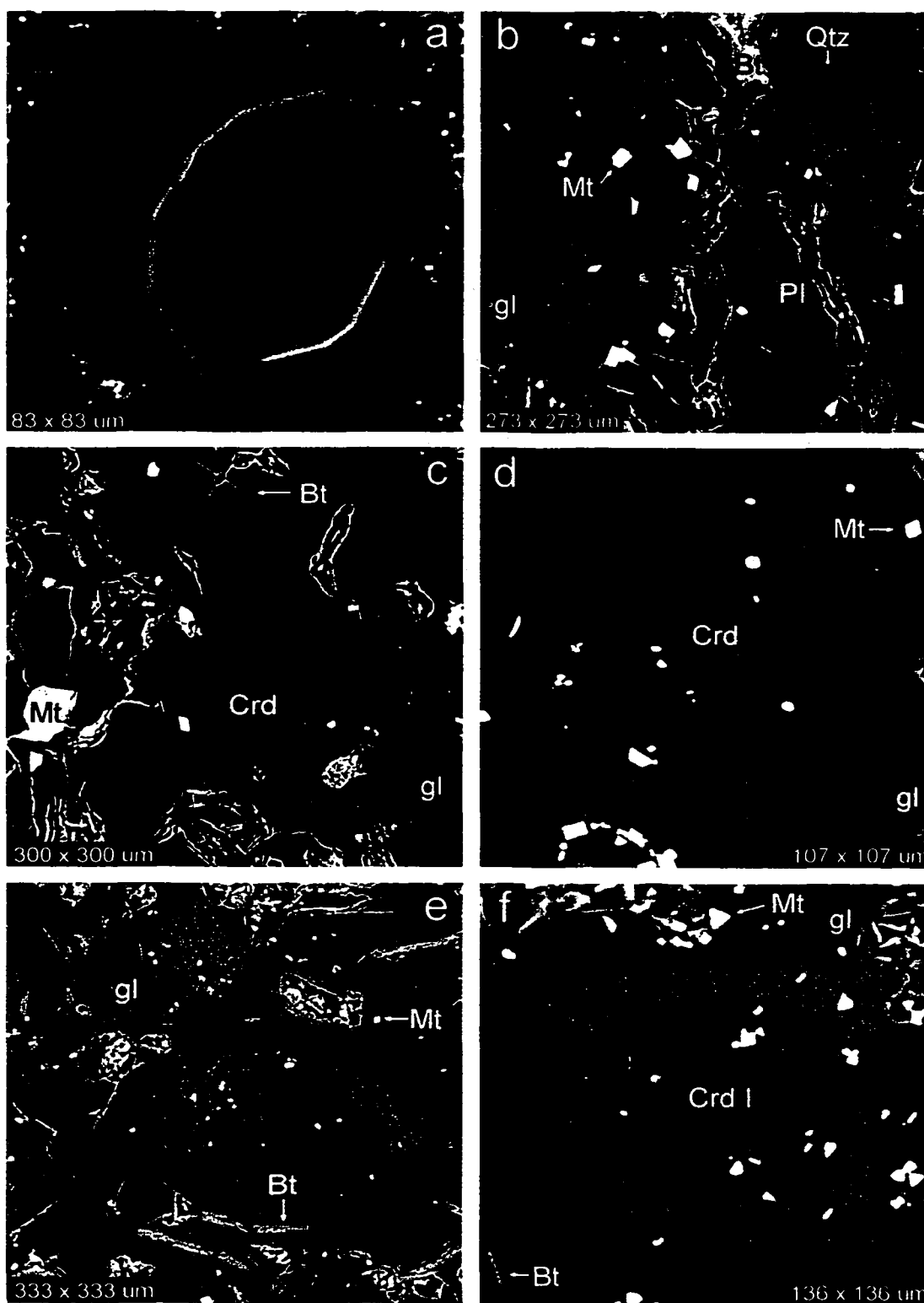


Figure 3-3.

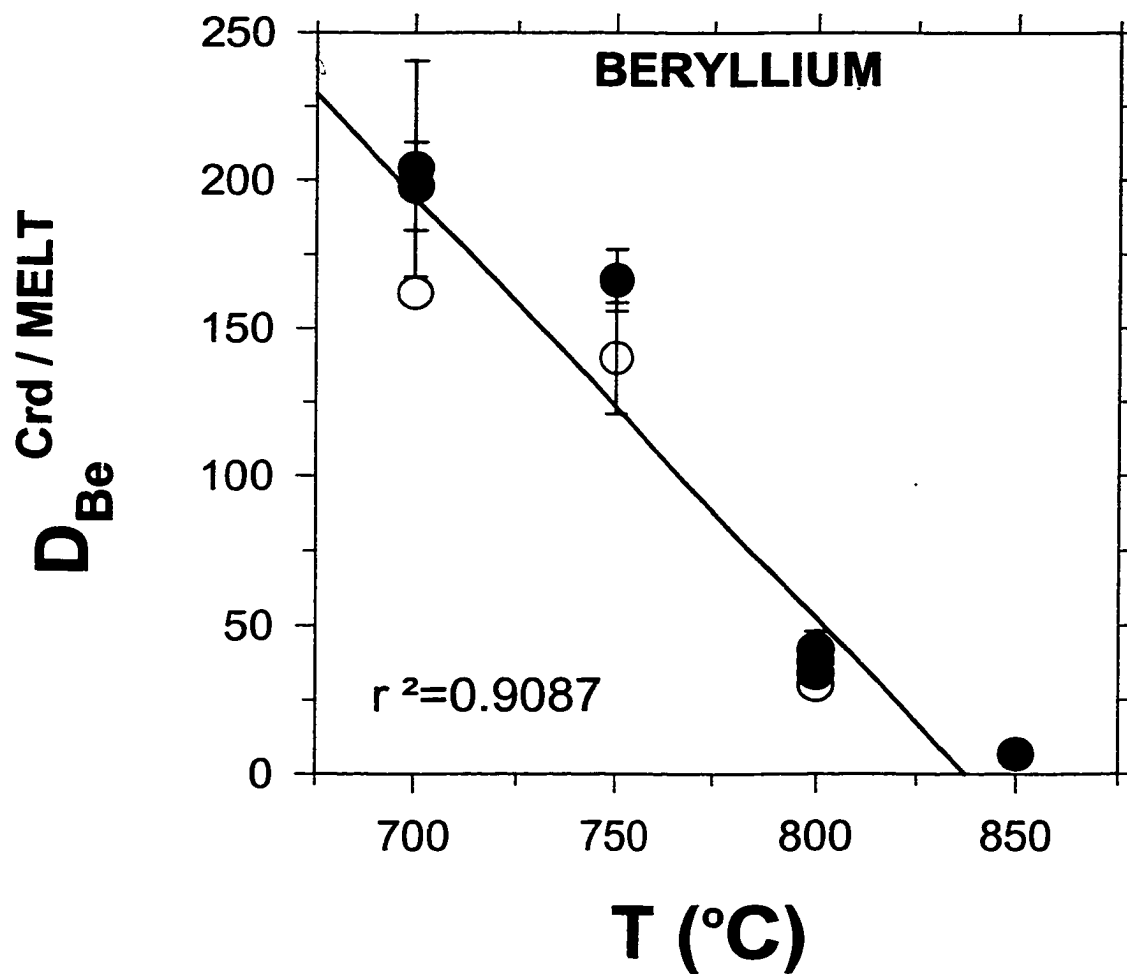
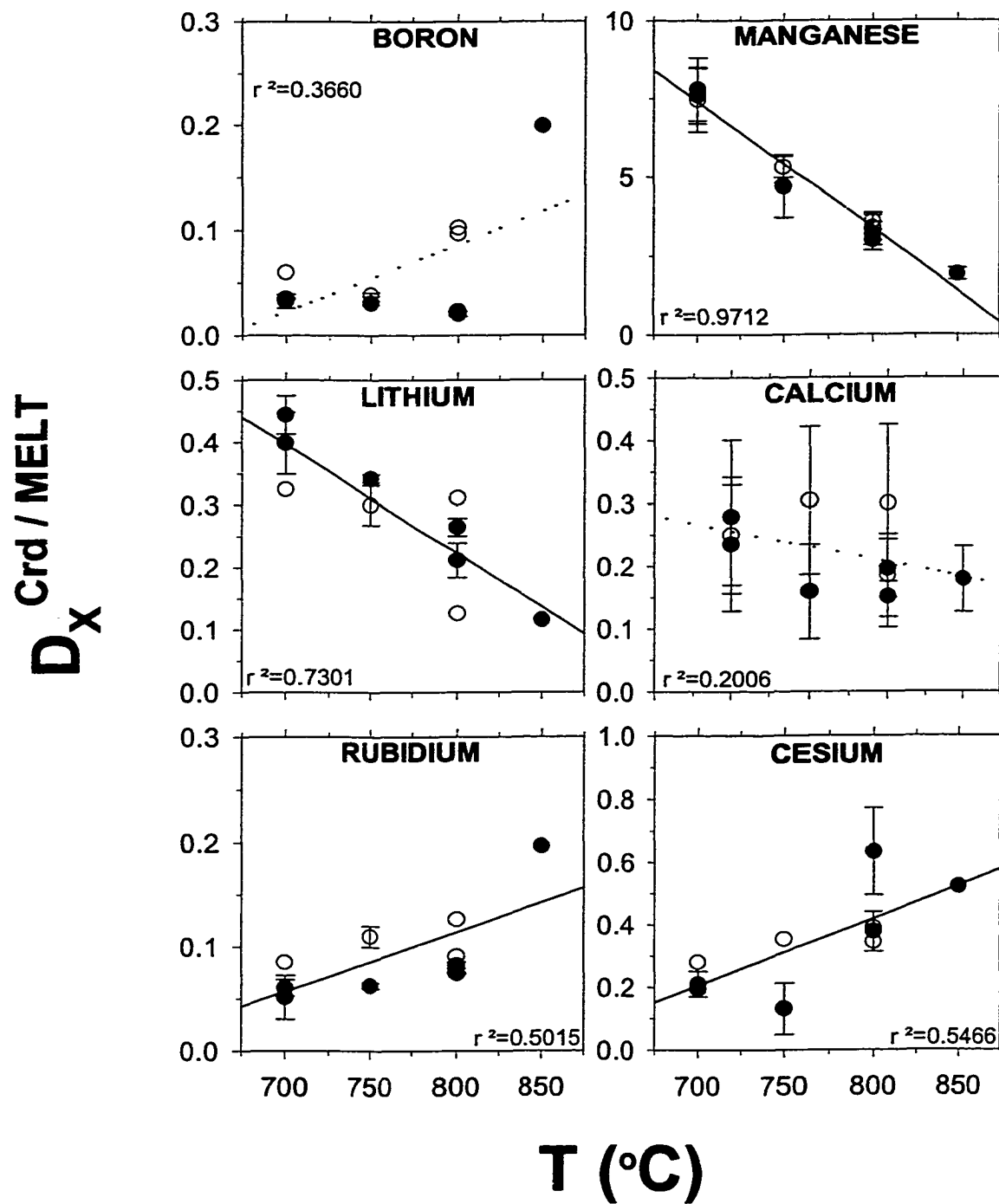


Figure 3-4.



CHAPTER 4. EXPERIMENTAL CALIBRATION OF THE BERYLLIUM CYCLE FROM MIGMATITE TO PEGMATITE

INTRODUCTION

Rock-forming minerals contain negligibly low contents of beryllium. The scarcity of Be (see Table 4-1) arises from a combination of crystal-chemical factors that include: 1) its small ionic radius ($0.27^{[4]}$ Å: Shannon, 1976), 2) mixed electron orbital configurations (e.g., Bader et al., 1967) that give rise to appreciable covalency, and 3) a charge density between that of Al and Si but a valence state (2+) that hinders direct substitution for these elements. Together, these characteristics make for a poor fit for Be in most structures. Numerous petrological applications have taken advantage of the fact that Be is strongly incompatible (and thus a reference for other chemical tracers: e.g., Ryan et al., 1996); but at the same time, its incompatibility raises the question, where does Be reside? Answering that question entails systematic study of the compatibility of Be in minerals, melts and fluids, in combination with a detailed survey of the natural abundances of Be.

Beryllium is dispersed over large-scale crustal (e.g., Wuensch & Hörmann 1978; Černý 1991b; Stix & Layne, 1996) and subduction environments (e.g., Ryan & Langmuir, 1988; Morris et al., 1990). At smaller scales in the continental crust, Be becomes mobile and shows transport (e.g., Bebout et al., 1993; Domanik et al., 1993; Webster et al., 1996) and enrichment by fractionation in silicic magmas (Beus, 1966). On earth, beryllium is most enriched in the felsic continental crust. Pathways that contribute

to the crustal cycle of Be (potential buffers, sinks and sources of Be) and control the systematics of such enrichment, however, remain unclear.

Where Does Beryllium Go?

Several mineralogical controls for Be have been suggested in the crustal environment. Beus (1966) noted the capacity of white mica to host Be. At the crustal scale, however, he predicted plagioclase to be the chief carrier of beryllium. Kosals and Mazurov (1968) found the whole-rock contents of Be to correlate with oligoclase (An_{25}) and biotite throughout a granitoid suite. But currently, it is widely held that white mica is the primary rock-forming mineral that houses Be (e.g., Bebout et al., 1993; Domanik et al., 1993; Grew 1998). It has recently been shown that the presence or absence of cordierite ($Mg_2Al_4Si_5O_{18}$, Crd) correlates with the whole-rock contents of Be in S-type granites worldwide (Evensen and London 2001a, in review)—a trend that matches experimental calibrations and ultimately stems from the complete solid solution between cordierite and beryl ($Be_3Al_2Si_6O_{18}$, Brl) in melt (Evensen and London 2001b, in review).

Following from laboratory synthesis (Toth et al., 1974), beryllium fluoride is commonly cited as a probable complex for transporting Be in melt, ultimately resulting in enrichment in evolved facies (e.g., Grew et al., 2000; Burt & Sheridan, 1987; Kosals et al., 1973; Kovalenko et al., 1977). Whereas the speciation of Be with F in hydrothermal systems has been documented on field, experimental and theoretical grounds (Wood 1992), direct evidence for magmatic complexation has never been reported (nor assessed by relevant experiment). Numerous studies on elemental affinities in granitic systems (e.g., Černý, 1991a; Lyakhovich, 1977; Webster and Duffield, 1991; Webster et al., 1996) report no correlation between Be and F in melt. Lines of evidence like these

suggest that complexation by F cannot be primarily responsible for the Be signatures in felsic rocks. Low preference for distribution of Be into vapor over melt (London et al., 1988; Webster et al., 1989) further suggest that crystal-melt equilibria is far more relevant to the geochemistry of beryllium.

Importance of the Crystal Chemistry of Be

Controls on the distribution of Be by rock-forming minerals have been debated, typically requiring empirical evidence to evaluate (e.g., in basic melts: Brenan et al., 1998a). The criterion of structural similarity between common minerals and those that contain essential Be offer a preview of the relative influences of crystallography on Be equilibria among fluid, mineral and vapor assemblages. Over 90 beryllium minerals are known. Among these, beryl is clearly the most common. In beryl, Be occupies linking tetrahedral sites (*TI*) to form skewed polyhedra (e.g., Aurisicchio et al., 1988) whose narrower TOT geometries favor Be occupancy (over that of Si: Downs and Gibbs 1981). The similarities of tetrahedral geometries within rock-forming minerals to the *TI* site in beryl should reflect their capacity to host (or yield) Be.

The majority of predictions toward crystalline controls on the chemical budget of Be have stemmed from its natural abundances in minerals and rock types as shown in Tables 4-1 and 4-2. Here, white mica, plagioclase and cordierite stand out as major carriers of Be. In previous considerations, cordierite has been notably absent from this list.

This Study

This study focuses on the budget of Be from the onset of crustal anatexis to the emplacement of evolved magmas at shallow levels, up to the point of beryl saturation in

granitic pegmatites and Be metasomatism in contact aureoles. Beryllium contents of melt needed to achieve beryl saturation (\pm phenakite, Be_2SiO_4 ; chrysoberyl, BeAl_2O_4) have already been reported (Evensen et al., 1999). These values provide model limits for the final stages of granite-pegmatite petrogenesis.

Here we follow the partitioning of Be between silicic melt and quartz, alkali and plagioclase feldspars, and dark and white micas at low (trace concentrations) and high activities of beryllium in melt (buffered by saturation in beryl, chrysoberyl, or phenakite). At 200 MPa H_2O and from 650° to 900°C, equilibrium is evaluated using forward and reverse-direction experiments (thermally prograde and retrograde, respectively). Together with reported data on cordierite, garnet, and whole-rock compositions of silicic systems, we track the accumulation of Be in melt by igneous crystal fractionation.

EXPERIMENTAL METHODS

Starting Materials. Powders were formulated by combining mineral components (Table 4-3) with either a base fraction of a pelite mineral mixture (“SP-”; Table 4-4), or a haplogranite mineral mixture (“HG-”; Table 4-4) or glass (synthesized by Corning to 1800°C at the 200 MPa minimum melt composition with an ASI = 1.02). Nine Be-poor and seven Be-rich starting mixtures (Table 4-4) containing mineral and synthetic components were used. Starting mixture abbreviations denote the base mineral mixtures (e.g., “SP-”), the major phase of interest (e.g., “Mus”), the variation on that mixture (as an integer, e.g., “Mus3”), and the low (“-C”) or high (“-Be”) beryllium content in the system, e.g., “SP-Mus3-Be”. In Be-poor mixtures, beryllium was not added explicitly, but by way of trace quantities in added white mica.

Regions of gem-quality crystals were selected for crushing. Crystal fragments were microscopically hand-sorted to remove impurities before grinding. Starting mixtures were ground in agate under ethanol to a mean grain size of 15 μm and dried in air at 140°C. Powdered components were combined, ground together, dried (140°C), and homogenized overnight in a tumbling mill.

Preparation of Charges. Gold capsules (3 x 20 mm) were cleaned by soaking overnight in bromopropane (25°C) then by boiling for several hours in nitric acid. Afterwards, a few capsules still contained remnants of the extrusion lubricants used in the fabrication of the tubing; these remnants were removed with polyurethane foam swabs.

Water, followed by powder mixes, were loaded into the central 5 x 3 mm portion of the capsules, and sealed by DC-plasma arc welding. All charges contained a slight excess of doubly distilled deionized water needed to slightly oversaturate a melt at 200 MPa and the T range investigated (~ 10 wt% H_2O). Capsules were weighed before and after welding, and again after storage in a drying oven (140°C) to check for leaks. The heating step further allowed for homogenization of water contents throughout the powder prior to the experimental run.

Equipment. Experiments were pressurized cold in R-41® and NIMONIC-105® cold-seal reaction vessels using water plus a trace of Immunol® as the pressure medium. Pressure was measured with a factory-calibrated Heise bourdon tube gauge; fluctuations of < 3 MPa occurred over the course of experiments, with a total estimated uncertainty of ± 10 MPa. Experiment durations varied from ~ 1 to 6 weeks. Temperature was monitored by internal Chromel-Alumel thermocouples with estimated maximum error of $\pm 5^\circ\text{C}$. Experiments were quenched isobarically using compressed air jet (5° to 15°C/s). The

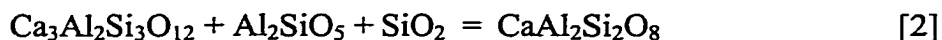
fugacity of oxygen within capsules was regulated by diffusion of H₂ across the metal capsule, and the f_{O_2} is estimated to be slightly below NNO (Huebner, 1971) at run conditions. Following quench, capsules were weighed to check for leaks, punctured and the presence of free water was recorded. Capsules were heated in a drying oven and reweighed to verify loss of free water (~ 25% of total added water). All capsules gain minor weight during experiments by diffusion of Ni-metal (from vessels and filler rods) into precious metal capsule walls; although, none of the experimental products reported here—including biotite—suffered detectable contamination by Ni.

Run Pathways and Experimental Strategy. Forward-direction experiments (prograde to run temperatures of 700° to 850°C, designated as “F” in Tables 4-5 to 4-7) promoted concurrent melting and new crystal growth. Reverse-direction experiments (designated as “R” in Table 4-5 to 4-7) were preconditioned by melting at 50° to 150°C above the final T of the experiment, followed by isobaric quench to room temperature, then forward run up to final temperatures in the range of 700° to 800°C. This pathway utilized glass to increase reaction rates upon the reversed step to avoid metastable persistence of granitic melt upon direct cooling. These reverse-direction experiments induced crystal growth from melts that were substantially supersaturated in the components of the crystalline phases at the final run T .

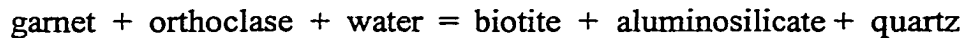
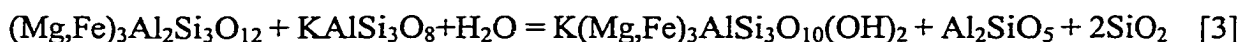
Variants of the first three mixtures (Table 4-4: HG-Or-, HG-Ab-, and HG-Qtz-) change in proportion of Qtz, Or, or Ab with temperature to be within the respective feldspar or quartz liquidus stability field at 200 MPa (Tuttle and Bowen, 1958). New quartz was crystallized in reversed experiments. Growth of K-rich alkali feldspar was achieved in reversed experiments and by the muscovite breakdown reaction,



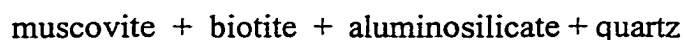
in forward experiments. Albite was precipitated in reversed experiments, whereas andesine was grown via the reaction of the grossular component of garnet in melt,



Dark mica was grown in reversed experiments and by the breakdown of garnet in melt with or without biotite seeds (added coarse biotite) in forward experiments,



and by decomposition of a ferroan component in the starting white mica (Mus-2; Table 4-4) into melt. White mica was grown in reversed experiments and by the decomposition of a garnet component in potassic, peraluminous melt with or without muscovite seeds,



In Be-rich experiments two reactions were utilized to buffer the activity of Be in melt. Saturation in beryl was achieved using the phenakite decomposition reaction,



In strongly peraluminous melts, saturation in chrysoberyl was achieved by reaction of beryl,



beryl + muscovite → chrysoberyl + K-feldspar + quartz (m) + water

Each starting mixture successfully produced the crystalline phase(s) of interest with crystals amenable to analysis (see Figure 4-2).

ANALYTICAL METHODS

Quantitative Electron Probe Microanalysis (QEPMA). All major and minor element oxide constituents of mineral and glass products, except H, Li, Be, B, Rb and Cs, were analyzed using wavelength-dispersive spectroscopy on a Cameca SX-50 electron microprobe at the University of Oklahoma. QEPMA utilized crystalline and glass standards with TAP, PET, LIF, and layered composite (PC1) diffraction devices. Operating conditions for hydrous glass analyses used a two-beam condition (2 nA and 20 nA regulated currents method) with a 20 μm spot size, in which Na and Al were analyzed first (and concurrently) to inhibit beam-induced migration effects (Morgan and London, 1996). Analyses of minerals were conducted at 20 nA, 20 kV and a spot size of 3 to 5 μm . Counting times for all elements varied between 20 and 30 seconds. Data were reduced using the PAP (Pouchou and Pichoir, 1985) matrix correction procedure. Detection levels, taken at 3σ above mean background, were < 500 ppmw for most elements. Analyses of similar Be-rich experiments indicate that Be is not lost to the capsule metal (Evensen and Meeker 1997).

Images were acquired using backscattered and secondary electron signals as 1024 X 1024 pixelized data. Micrographs were processed (following Russ, 1999) using low-pass or median filtering for reduction of noise.

Secondary Ion Mass Spectrometry (SIMS). Samples were analysed by SIMS using a Cameca Instruments IMS 3f at the Arizona State University at Tempe, AZ. An mass filtered $^{16}\text{O}^-$ primary beam was accelerated through a potential of 12.5 kV, with a beam current of 1.0 nA. The focused spot size varied from 15 to 5 μm . Targets were mapped in advance and verified by imaging a combination of ^7Li , ^9Be , ^{23}Na , ^{26}Mg , ^{27}Al , ^{41}K , and ^{56}Fe before analysis.

Sputtered secondary ions were accelerated through a potential of 4.5 kV. The interference of $^{27}\text{Al}^{3+}$ (8.99384 amu) on ^9Be (9.01219 amu) is the most important concern in SIMS microanalysis of Be (R. Hervig 2001, in press). The yield of ^9Be is substantially greater than the $^{27}\text{Al}^{3+}$ species when Be contents are high (e.g., Evensen and London 2001b, in review)—the interference becomes negligible and no correction is required. However, when Be contents are less than ~ 30 ppmw, it has been observed (Grew et al., 1998) that trivalent Al affects the analysis. Therefore, prior to and after each analysis, mass collecting position was distinguished from $^{27}\text{Al}^{3+}$ and aligned to the ^9Be peak. Individual analyses consisted of collecting intensities on the following sequence of isotopes: ^{30}Si , ^7Li , ^9Be , ^{11}B , ^{85}Rb , ^{133}Cs , ^{30}Si . Integration times were sufficiently long to achieve a counting statistical precision of at least 3%. The count rates were normalized to that for Si and then to the silica abundance in the sample (derived from QEPMA).

A standard working curve for SIMS was calibrated for the analysis of Li, Be, B, Rb and Cs using glass standards and one crystalline standard. Three synthetic granitic glasses doped with Be (0.57, 1.11, or 3.33 wt% BeO by aqua regia ICP-AES, QEPMA, and SIMS; Evensen, 1997) were used as standards for the analysis of experimental products. The glasses contained appreciable B, Li, Rb, and Cs (at concentrations far

above those estimated for each element in unknowns) and therefore served as standards for the suite of elements in question. All trace elements were further calibrated against the NIST 610 glass, containing nominally ~500 ppmw of the elements above (Pearce et al., 1997). Beryllian cordierite ("Sponda 454"; Armbruster and Irouschek, 1983) was used to assess the convergence of ^9Be yields between crystalline and vitreous materials. These tests showed similar results to previous studies (e.g., Ottolini et al., 1993) with marked convergence between crystalline and vitreous materials along the working curve. Calibration factors derived from the standards above allowed the normalized count rates to be converted to absolute concentrations. Total internal and external precision (ICP) of BeO analyses of crystals and glass was < 3.9%. Data were acquired in three sessions over a 2 year period. Between these sessions, the working calibration (Figure 4-1) and SIMS results were highly reproducible (± 0.4 to 2.2 %).

EXPERIMENTAL PARTITIONING RESULTS AND DISCUSSION

Potassic and Sodid Alkali Feldspars

Potassic alkali feldspar (Figure 4-2A-a,b) forms large euhedral and blocky crystals (relatively megacrystic) ranging in length from 25 to 325 μm , and occurring as either isolated crystals, glomerocrysts, or in crystal networks. In experiments that included added K-feldspar, crystalline fragments that did not melt completely at the preconditioning T are often preserved as cores that facilitated nucleation of overgrowths at the final T . Between the relict core (showing resorption textures) and thick new growth is occasionally a thin zone (2-7 μm) of a Ba-rich component (originating from added Kfs: Tables 4-3 and 4-4) that was stabilized at the preconditioning T . Small melt pools are

sometimes found within Afs as well as inclusions of Mus, Cor, Bt, Mag, Phn, Crd, or chrysoberyl (Cbr).

Sodic alkali feldspar (Figure 4-2A-c,d) forms euhedral and blocky crystals (10 to 60 μm in length) that rarely contain melt pools, but commonly contain inclusions of Phn. A very small fraction of crystals exhibit cores composed of a more albitic component that survived melting at the preconditioning step and, thus, served as nucleation sites for growth of Na-Afs.

Partitioning of Be. Partitioning coefficients (Table 4-5a,b) show scatter but average around 0.18 in Be-poor systems with no apparent correlation with T . D-values change from 0.18 to 0.14 with increasing T in systems saturated in a Be-mineral. Values of $D_{\text{Be}}^{\text{Na-Afs/melt}}$ taken from experiments at 700°C vary from 0.28 to 0.14 for Be-poor and Be-rich melts, respectively. Though similar in absolute value, Be appears to be slightly more compatible in sodic vs. potassic alkali feldspar. Unlike K-rich feldspar, sodic Afs shows a 2-fold decrease in Be compatibility upon beryl saturation.

Plagioclase Feldspars

Albite forms euhedral, blocky crystals, ranging from 10 to 525 μm in length, though most crystals are $\sim 30 \mu\text{m}$ long. Albite in Be-rich melts often contains inclusions of anhedral (partially resorbed) Phn. In experiments that contained grossular, andesine ($\sim \text{An}_{31}$; Table 4-5c) forms euhedral crystals with some skeletal character (Figure 4-2A-e,f). Crystals range from 10 to 125 μm in length. Some cores of relict albite exist from melting in forward experiments. These fragments are always completely armored by new andesine, which typically is free of inclusions.

Partitioning of Be. In reversed experiments at 750°C, values of $D_{\text{Be}}^{\text{Ab/melt}}$ range from 0.10 to 0.67 for Be-poor and phenakite-saturated melts, respectively (Table 4-5c). Partition coefficients for andesine at 700°C vary between an average of 1.84 ($se = \pm 0.05$) for Be-poor melts and 0.89 for beryl-saturated melts. Andesine is therefore the only feldspar in this study in which Be is compatible. This suggests that Ca facilitates the coordination environment that accommodates Be, supporting the exchange, $\text{CaBeNa}_{-1}\text{Al}_1$, in plagioclase.

Quartz

In the beryl-saturated experiments of Evensen et al. (1999), which were analysed here for partitioning relations, the crystalline assemblage consists of Qtz + Brl + Cbr. In the Be-poor systems utilized in this study, quartz forms nearly equant, euhedral, solid crystals that range from 2 to 50 μm in length. In these melts, quartz crystals occur in distinct networks that transect large areas of crystal-free melt. In beryl-saturated runs, quartz forms larger crystals (10 to 75 μm) of similar character that coexist with euhedral beryl and chrysoberyl (Figure 4-2B-a,b).

Partitioning of Be. In reversed experiments to 800°C in Be-poor melts, the partition coefficient is 0.24, whereas in beryl-saturated melts it varies from 0.17 to 0.07 from 750 to 800°C (Table 4-6). These values follow trends similar to other crystalline phases (decreasing with increasing T and with increasing activity of Be). Theoretically, Be should be accommodated by the structures of the silica polymorphs.

Dark Mica

Biotite occurs as both relict and new crystals clusters in most run products (Figure 4-2B-c,d). New biotite is characterized by euhedral, solid crystals ranging from 5 to 75

μm in length (commonly $\leq 10 \mu\text{m}$ wide). These crystals may contain inclusions of magnetite. New crystals are recognized by growth in [100] and by more magnesian compositions than the starting dark mica (cf. Tables 4-3 and 4-7). Relict dark mica is distinguished by coarse crystal size, conspicuous pitting, partly recrystallized crystal rims, and deformed crystal shapes.

Partitioning of Be. Partition coefficients between biotite and melts with trace contents of Be vary from 0.42 to 0.77 (mean = 0.50, se = ± 0.04) with no apparent correlation to T (650 to 800°C; Table 4-7a). In beryl-saturated melts, these ratios vary from 0.08 to 0.41 (mean = 0.22, se = ± 0.10) again, with no correlation to T (675 to 800°C).

White Mica

Muscovite occurs in crystal clusters comprised of numerous, small crystals—so numerous that finding Mus-free glass pools for analysis was at times difficult. Muscovite exhibits elongate, sometimes curved, solid crystals that are 1 to $\sim 60 \mu\text{m}$ long. Most crystals are $\ll 10 \mu\text{m}$ wide; although, there are notable exceptions (Figure 4-2B-e,f).

Partitioning of Be. Partition coefficients for Be between muscovite and melt (Table 4-7b) are 1.35 and 0.93 for Be-poor and beryl-saturated liquids, respectively.

Cordierite

Evensen and London (2001b, in review) show that Be is extremely compatible in cordierite grown from melts of synthetic metapelite composition that contain trace abundances of Be. Partition coefficients range from 202.0 to 6.70 as T increases from 700 to 850°C. As the activity of Be in melt increases, partition coefficients decrease from

26.59 to ~15.14 going from 675 to 850°C. However, in the latter case, Be represents a major structural component of cordierite (containing up to 4.4 wt% BeO).

Experimental and Natural Partition Coefficients

Mineral/Melt and Mineral/Mineral Partition Coefficients. The mineral/melt data of this study are summarized in Table 4-8 as a function of T . Mineral/mineral values obtained from the same experiments are compared with reported mineral/melt and mineral/mineral partitioning coefficients for natural systems in Table 4-9. Overall, the ratios from the majority of these systems closely match the experimental D_{Be} values, including those representing evolved, beryl-saturated liquids (Kovalenko et al., 1977). Deviations from the experimental calibration are seen in mineral/mineral values containing plutonic quartz. Because the compositions of coexisting minerals with quartz seem to otherwise converge with experimental partition coefficients, this disparity may possibly reflect some degree of recrystallization of plutonic quartz.

Vapor/melt Partition Coefficients and Vapor Transport. Relevant experimentation on F- and Cl-rich evolved silicic compositions (London et al., 1988; Webster et al., 1989) shows that vapor/melt partition coefficients for Be are generally ≤ 1 over a range of fluid compositions, salinities, temperatures, and pressures. Solubilities of Be complexes in equilibrium with Be-minerals are generally far lower (< 1 ppmw) in aqueous systems (Wood 1992) than in silicate melts, which are capable of dissolving hundreds to thousands of ppmw of Be (Evensen et al., 1999). In regard to the overall budget of Be, silicate melts appear to be more effective agents of transfer than are aqueous fluids. While hydrothermal fluid may still be important in the movement of Be through the crust (e.g., Tatsumi and Isoyama, 1988; Morris et al., 1990; Bebout et al.,

1993; Leeman, 1996; Brenan et al., 1998b) it appears that it is less effective than silicate melt on an equal-volume basis.

BERYLLIUM SYSTEMATICS IN NATURAL SYSTEMS

Natural Abundances in Rock-Forming Minerals

As a basis for understanding the behavior of beryllium in rock-forming minerals typically found in granites and their crustal source rocks, we begin by briefly reviewing the means by which Be is incorporated into the rock-forming minerals pertinent to this study, and we summarize the typical abundances of Be in these minerals.

Quartz

Beryllium-stuffed structures of the silica polymorphs are well known, particularly for cristobalite (e.g., Palmer, 1994), in which Na-Be coupling is frequently observed for the incorporation of Be.

Quartz in intrusive rocks shows a low mean content of 1.2 ppmw Be (Table 4-1). However, pervasive recrystallization of igneous quartz may be a common phenomenon (e.g., London 1985), so that the Be contents of quartz phenocrysts quenched in volcanic rocks might give the best indications of the concentrations of Be at magmatic conditions. Unfortunately, a database for Be contents in volcanic phenocrysts of quartz is non-existent and the disparity between experimental and plutonic quartz cannot be reconciled at the present time.

Plagioclase

The incorporation of Be in plagioclase is probably coupled with Ca, as the exchange operator $\text{CaBeNa}_1\text{Al}_1$. Robert et al. (1995) suggested a similar coupling of Ca

and Be for the Ca-Be white mica, bityite, and ~ 60% of all Be minerals also contain essential Ca.

Beus (1966) predicted that plagioclase is the chief carrier of beryllium in most crustal rocks. Kosals et al. (1973) found that the mean Be contents of plagioclase in granitic rocks, which varied from An₀ to An₅₀, peak at a maximum of ~ 11 ppmw in calcic oligoclase compositions (~ An₃₀). Beryllium decreases in abundance on both sides of ~ An₂₅, although albitic compositions contain more Be than very calcic compositions. Solodov (1959) noted that beryl-free portions of cleavandite-rich and aplitic units contain from ~ 2.0 to 4.5 times the Be content of albite in average beryl-bearing pegmatites.

Alkali feldspar

Beryllium likely substitutes into the feldspar structure at tetrahedral Al sites, maintaining charge balance by coupled substitution with alkaline earths: e.g., via CaBe^[4]Na₁Al₁^[4] in plagioclase (Kosals et al., 1973) and possibly BaBe^[4]K₁Al₁^[4] in alkali feldspars.

Table 4-1 shows that potassic feldspar typically contains 3.1 ppmw Be, and increases in Be content with fractionation to reach values of 7 ppmw Be in pegmatitic feldspar. Smeds (1992) found that among pegmatites, the most Be-rich K-feldspar (20 ppmw) was found in beryl-undersaturated rocks, while intermediate values (near 10 ppmw Be) were characteristic of beryl-bearing pegmatites.

Biotite

Divalent tetrahedral cations are known to enter the mica structure at Al^[4] sites by coupled incorporation of charge-balancing excess hydroxyl (Ginzburg, 1957). This

mechanism, documented in brittle micas, allows for the protonation of apical oxygen of BeO_4 tetrahedra to compensate underbonding at that site (Robert et al., 1995).

With a mean value of 5 ppmw Be in granitic rocks, biotite likely carries more Be than Kfs, less Be than white mica, and about an equivalent amount as sodic plagioclase (Table 4-1). This observation fits with measurements of whole-rock contents of Be in granitoid systems (Kosals and Mazurov, 1968): variations are attributed to the presence of biotite and plagioclase. Beryllium compositions of pegmatitic biotite have not been reported. If plagioclase more calcic than albite is absent, dark micas should be important reservoirs of Be.

Muscovite

In general, Be appears to be accommodated by white mica via $\text{CaLi}^{[6]}\text{Be}^{[4]}\text{Na}_{-1}\text{Si}^{[4]}_{-1}$ (Grew et al., 1986). Going from the brittle mica, margarite, the exchange operator $\text{Li}^{[6]}\text{Be}^{[4]}\text{Al}^{[4]}_{-1}$ leads to the beryllian end-member, bityite $[\text{CaLiAl}_3\text{BeSi}_2\text{O}_{10}(\text{OH})_2]$. However, another vector from margarite, $\text{HBe}^{[4]}\text{Al}^{[4]}_{-1}$, appears to also be important.

Next to cordierite (and for example, rarer amphiboles in some alkaline systems), white mica contains the highest Be contents among the rock-forming minerals. Mean contents are ~ 40 ppmw Be (Table 4-1), though the database is skewed toward pegmatite samples that contain abnormally high contents of Be. White mica in granitic rocks carries a representative mean content of ~ 25 ppmw Be. Muscovite displays higher Be contents in beryl-absent versus beryl-bearing pegmatites (e.g., Smeds 1992).

Cordierite

In cordierite, Be is accommodated in linking tetrahedral sites of Al by the alkali-coupled exchange, NaBeAl_1 (Černý and Povondra 1966) and by the excess silicon exchange, BeSiAl_2 (e.g., Hölscher and Schreyer 1989; Baba et al., 2000). These mechanisms vary inversely with temperature: NaBeAl_1 at $T < 750^\circ\text{C}$, and BeSiAl_2 at $T > 750^\circ\text{C}$ (Evensen and London 2001b, in review).

The database is sparse for Be contents of cordierite in silicic rocks, particularly for cordierite-bearing granites (Table 4-1). Available data, however, indicate that cordierite commonly contains more Be than most other rock-forming minerals. Cordierite from ordinary metamorphic rocks contains ~ 20 ppmw Be. Much higher Be contents have been reported from *cordieritites* (e.g., Gordillo, 1979; Schreyer et al., 1979), which probably represent restites from prior partial melting. Cordierite in S-type volcanics from the peraluminous Morococala volcanic suite, Bolivia, contains ~ 337 ppmw Be (G. Morgan and D. London, unpublished data). In pegmatites (and their equivalent in granulite facies assemblages: e.g., Baba et al., 2000; Grew et al., 2000), Be contents of cordierite reach weight percent levels. In some cases, pegmatitic Crd may have crystallized at conditions of beryl saturation (Evensen and London 2001b, in review).

A survey of S-type granite compositions (Evensen and London, 2001a, in review) shows two distinct populations by Be content: Crd-free granites enriched in Be (mean = 6 ppmw Be) and Crd-bearing granites depleted in Be (mean = 0.8 ppmw Be). The whole rock Be content of S-type granite appears to distinguish melts that originated from cordierite-bearing sources (with a depletion in Be) from those in deeper environments, in the stability field of aluminosilicate + garnet.

Influence of Rock-Forming Minerals on Be Systematics

Distribution coefficients indicate that the compatibility of Be (at normally trace levels) in crystalline phases decreases in the order:

cordierite » calcic oligoclase > white mica > dark mica > albite \cong alkali feldspar \cong quartz

Hence, the first three or four phases in this sequence control the distribution of Be between restite or crystalline magmatic phases, and melt. Among these minerals, Be is compatible in cordierite, calcic oligoclase, and white mica. The positioning of plagioclase in this sequence depends on its composition. From estimates, it appears that garnet resides approximately near albite in this sequence (Bea et al., 1994a).

When cordierite is present, it substantially reduces the Be contents of melt—a trend that is seen in whole-rock values. On the other hand, cordierite is the least abundant of these phases. Where cordierite is absent, micas and plagioclase monitor the contents of Be in melt.

The partitioning of Be between minerals and melt becomes non-Henrian in behavior as the melt composition approaches beryl saturation. For most minerals studied, partition coefficients at beryl saturation are far lower than at trace levels of Be, indicating that these rock-forming minerals (except cordierite) saturate in Be at values in the range of a few tens or hundreds of ppmw.

Mineralogical Controls during Anatexis

Metapelites at Shallow Crustal Levels: The Role of Cordierite

When present (e.g., Vielzeuf and Holloway, 1988, Mukhopadhyay and Holdaway, 1993) cordierite controls the Be contents of melts derived from metapelite sources at shallow depths. Cordierite becomes or remains a liquidus phase in many S-type granite

magmas (e.g., Ahmed-Said and Leake, 1990; Ugigios and Recio, 1993; Pereira and Bea, 1994; Bea et al., 1994b), and hence the crystallization of even small quantities of cordierite drives the Be content of melts down to values mostly near 1 ppmw.

Example 1: Hercynian Migmatites of Spain. Table 4-10 summarizes whole rock contents of Be in leucosomes, melanosomes, and mesosomes reported by Bea et al. (1994a). Though the starting mesosomes contain typical quantities of Be (2 ppmw), the melanosomes clearly show enrichment in cordierite-rich restite (6 ppmw Be) after melt has been extracted. This leaves the derivative partial melts, as represented by leucosomes, Be-poor (1 ppmw Be).

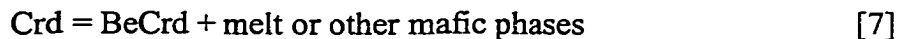
Example 2: Topaz Rhyolite at Honeycomb Hills, Utah, USA. This rhyolite was emplaced overlying metaluminous rhyolite and granite (Lindsey 1977). Here, the lack of compatibility of Be in minerals of the host rocks combined with a substantial source of enrichment allowed for Be contents in fluid to increase until reaching saturation by interaction with reactive siliceous wallrock, forming bertrandite [$\text{Be}_4\text{Si}_2\text{O}_7(\text{OH})_2$] (e.g., Wood 1992). Hydrothermally altered rhyolite in this area reaches exceedingly Be-rich levels as high as 267 ppmw (Congdon and Nash 1991). Because Be most frequently substitutes for tetrahedral Al in minerals, in the absence of aluminous host rock, enough Be may be enriched in hydrothermal solution to produce bertrandite or other Be-minerals at ore-grade levels.

Previously Depleted Metapelitic Sources: Cordieritites

At equilibrium with cordierite, hydrous granitic melt contains between 0 and 4 normative % cordierite component to temperatures of 850°C at 200 MPa (Evensen and

London, 2001a, in review). When the mode of Crd becomes greater than a few percent, it likely represents a component of restite.

Cordierite-rich restite, or *cordieritites* (up to 90% Crd in the mode), have been described in several studies (e.g., Gordillo, 1979; Ugidos, 1988; Ugidos and Recio, 1993) and some occurrences contain beryllian cordierite (Schreyer et al., 1979). Owing to the very high compatibility of Be in cordierite (far higher than for any other major or trace element: Evensen and London 2001a, in review), restitic cordierite should change composition continuously during advancing metamorphic reaction to conserve the most compatible elements. Refractory beryllian cordierite is thus formed by reaction with melt,



This depletion pathway, which is probably very common in shallow crustal migmatites, illustrates an important concept for the Be budget of melt: anatexis can separate a low-Be melt from a Be-enriched cordierite residuum, but the cordierite restite in turn represents a potential source of Be for the derivation of granulite-facies products (e.g., Grew, 1998; Baba et al., 2000; Grew et al., 2000).

Metapelites at Deeper Crustal Levels: The Roles of White Mica and Plagioclase

Terminal reactions of white mica ($\text{Mus} = \text{Kfs} + \text{Cor} + \text{H}_2\text{O}$; $\text{Mus} + \text{Qtz} = \text{Kfs} + \text{Als} + \text{H}_2\text{O}$) are likely to contribute substantial Be to melt, thereby raising Be contents early in the histories of S-type magmas from deeper sources. Because garnet/biotite + aluminosilicate (+ quartz) are stable instead of cordierite, the only notable sink for Be is calcic oligoclase, or biotite to a lesser degree. As long as melting takes place at pressures beyond the stability field of cordierite, then the anatexis of typical metapelites containing

white and dark micas, oligoclase-andesine, and garnet (in the place of cordierite) will normally produce melts with the highest initial Be content.

Other Quartzo-Feldspathic Sources: Roles of Plagioclase and Dark Mica

Melts from A-type or I-type sources commonly undergo fractional crystallization with plagioclase and biotite on the liquidus (e.g., Clemens et al., 1986), and these magmas lack (early) muscovite or cordierite. Thus, the accumulation of Be in melt depends primarily on the evolving composition of plagioclase, and on the modal amount of biotite crystallizing from the melt. Once the An content of plagioclase falls and restitic biotite is removed, the Be content of I- or A-type magmas can increase. Černý (1991a,b) has noted that granites with I- or A-type affinities can produce important Be deposits (beryl in the I-types, beryl or gadolinite in the A-types).

Controls During Fractionation

Crystallization of Plagioclase

Overall, plagioclase is the most common crystalline phase in which Be is compatible. Therefore it monitors the Be contents of voluminous granitic magmas until the anorthite component diminishes. From a combination of the compatible partition coefficient ($D_{\text{Be}}^{\text{An}31/\text{melt}} \sim 2$) and compositions reported by Kosals et al. (1973), it is clear that the compatibility of Be in plagioclase decreases significantly at compositions more sodic than middle oligoclase. Thus, the control by plagioclase on Be will decrease as saturation in albitic compositions is achieved. Once albite is stable, the Be contents of melt will no longer be moderated; Be should increase with fractionation until white mica crystallizes.

Crystallization of White Mica

Saturation in muscovite is normally achieved late among magmatic facies (e.g., Bea et al., 1994a). With moderate compatibility by Be in muscovite ($D_{\text{Be}}^{\text{Mus/melt}} = 1.35$), Be contents of melt are likely reduced to a slight degree in its presence. High contents of Be observed in white mica reflect formerly high contents of Be in melt. Though, muscovite clearly only monitors Be; continued fractionation of magma will result in even higher concentrations of Be.

Be Contents of Silicic Igneous Rocks Worldwide

Table 4-1 lists reported contents of Be in silicic rocks using 200 mean compositions of granites and porphyries and 1100 compositions of rhyolites for every continent with the exception of Antarctica. Among these, the contents of Be in ppmw vary around distinct values of: 1 in cordierite-bearing silicic rocks; 4 in the mean all silicic rocks; 6 in S-type silicic rocks without cordierite; and ≥ 15 , evolved facies of silicic melts. S-type magmas show an enrichment in relatively unfractionated melts (6 ppmw Be) and evolved melts (20 ppmw Be) that is slightly greater though roughly similar to those seen in A-type rocks (4 and 15 ppmw Be, respectively). I-type granitoids from convergent settings have lower Be contents (3 ppmw Be). Clearly, the most dramatic feature in this survey is the effect of cordierite on whole rock abundances of Be.

Beryl-Bearing Pegmatites

Beryl is the most common Be-saturating phase in pegmatitic liquids derived from parental magmas of all crustal signatures (S, I, A). Depending on the magnitude of cooling at which crystallization takes place, silicic melts may become saturated in beryl

with as little as ~ 70 ppmw Be (Evensen et al., 1999). Table 4-11 illustrates the distribution of Be in a schematic pegmatite dike of roughly mean Be content (140 ppmw) as it is subjected to differential degrees of cooling prior to crystallization. At 700°C, nearly all the Be in melt (96%) is housed by rock-forming minerals upon crystallization. These conditions correspond to muscovite class of granitic pegmatites (Černý 1991a) which are commonly barren and proximal to their parental granite. Upon cooling beryl saturation is rapidly reached, and this immediately results in abundant quantities of beryl for crystallization. Here, nearly 80 % of the total amount of Be is accounted for by beryl alone. This distribution nicely corresponds to the next distal class of pegmatites, the beryl-type, which contain abundant beryl (Trueman and Černý, 1982). At even cooler conditions corresponding to distal rare-element pegmatite formation, beryl houses the majority of available Be, with the remainder dispersed, mostly between muscovite and albite. In conclusion, temperature represents the largest control on the distribution of Be between rock-forming minerals and beryl and melt at the pegmatite stage.

Average Contents of Beryllium

Where the Be contents of pegmatites have been estimated, these range from ~ 35 to as much as ~ 575 ppmw Be (Table 4-12). Beryl is present in most of the pegmatites that contain greater than ~ 100 ppmw Be, and an average Be content for beryl-rich pegmatites lies near 230 ppmw Be (with considerable scatter; $sd = \pm 139$). Within a pegmatite, zonation in Be content often occurs as a primary function of two different episodes of beryl saturation as shown in Figure 4-3. The behavior stems from the saturation surfaces and differentiation mechanisms of pegmatite solidification (Evensen et al., 1999). Cooling results in early beryl at the margins of the pegmatite melt, and

progressive enrichment at the crystallization front during solidification (e.g., Morgan and London 1999) increases to achieved late beryl saturation in internal pegmatite zones. The latter type results in the common “beryl fringe” that occurs adjacent to a centralized quartz core.

Wallrock Alteration around Pegmatites

Because of the inward solidification process that gives rise to pegmatites, two types of wallrock alteration are commonly generated: (1) a localized bulk melt-wallrock interaction upon emplacement, and (2) typically far more significant alteration zones that mirror the internal abundances of chemically related mineralogy in the pegmatite (e.g., Morgan and London, 1987). While the former alteration style is volumetrically insignificant for most pegmatites, the latter category may result in “blowouts” that expel highly reactive fluids from pegmatites into wallrock. In this scenario, metasomatic mica generated in the wallrocks should at least partially consume Be carried by pegmatite-derived fluids. Cordierite could be an effective sink as well.

Example 1: the Harding Pegmatite, New Mexico, USA. Wallrock alteration around the large Li- and Be-rich Harding pegmatite generated assemblages containing tourmaline, holmquistite, and epidote in host amphibolites and spessartine, tourmaline, biotite, muscovite, and “beryllian margarite” in altered schists (London, 1986; Jahns and Ewing, 1977). The beryllian margarite contains 3.31 wt% BeO, while coexisting minerals contain from 0 to 10s ppmw Be (Table 4-13).

Example 2: Topaz Rhyolite at Honeycomb Hills, Utah, USA. This rhyolite was emplaced overlying metaluminous rhyolite and granite (Lindsey 1977). Here, the lack of compatibility of Be in minerals of the host rocks combined with a substantial source of

enrichment allowed for Be contents in fluid to increase until reaching saturation by interaction with reactive siliceous wallrock, forming bertrandite [$\text{Be}_4\text{Si}_2\text{O}_7(\text{OH})_2$] (e.g., Wood 1992). Hydrothermally altered rhyolite in this area reaches exceedingly Be-rich levels as high as 267 ppmw (Congdon and Nash 1991). Because Be most frequently substitutes for tetrahedral Al in minerals, in the absence of aluminous host rock, enough Be may be enriched in hydrothermal solution to produce bertrandite or other Be-minerals at ore-grade levels.

THE BERYLLIUM CYCLE IN FELSIC MAGMAS

Crystalline controls on Be geochemistry show that its magmatic cycle becomes a function of three different influences: (1), the abundance of quartz, alkali feldspars, and dark mica, which do little to moderate the Be content of granitic melts, (2), the *composition of plagioclase*, and specifically the presence of either calcic plagioclase or white mica or both, which constitute important sources or sinks for Be, and (3), the presence of cordierite, in which Be is so compatible that solid solutions exist all the way to beryl at high temperature.

In the presence of a crystallizing assemblage of quartz, alkali feldspars, albite and dark mica, Be behaves as an incompatible element and its abundance increases rapidly with crystal fractionation. Calcic oligoclase may drop bulk distribution coefficients for Be to near 1. The same is true for white mica (especially a combination of the two). Because muscovite typically constitutes a smaller modal fraction (~ 10%) than plagioclase and crystallization normally commences in late granite facies, the role of white mica in depleting Be contents of melt tends to be comparatively lesser than

plagioclase. Normally, cordierite behaves a refractory phase during the anatexis of metapelites, and hence it effectively sequesters Be from coexisting partial melts.

Using the experimental database, bulk distribution coefficients are calculated for a model metapelite and model haplogranite system in Table 4-14. These values are then used in the estimate of Be contents during magmatic evolution from metapelitic to depleted crustal sources, respectively.

Because metamorphic rocks usually arrive at anatectic conditions carrying from 0 to 5 ppmw Be (e.g., E. Grew, 2001, in press) in their whole rock values, the anatectic pathway for pelitic to quartzo-feldspathic rocks begins at an average value of 3 ppmw Be. In the absence of cordierite at higher pressures ($\sim \geq 500$ MPa: e.g., Vielzeuf and Holloway 1988, Mukhopadhyay and Holdaway 1993), garnet-bearing restitic assemblages will likely exert little influence on the Be contents of melt during anatexis. With a bulk distribution coefficient < 1 , early partial melts to become slightly enriched in Be as the early mica-rich assemblage begins melting. Thus leaves the a derived melt with 4 ppmw Be.

Raleigh fractional crystallization (RFC) calculations show that for a melt initially containing 4 ppmw Be, crystallization of 80% of the melt yields a concentration of ~ 15 to 18 ppmw Be in melt. This value is similar to the reported Be contents of small cupolas and dikes of evolved melt (e.g., Lueke, 1981; Kennen, 2001; Shearer et al., 1987; Breiter et al., 1991; see Table 4-2). When this smaller volume of melt has reached $\sim 80\%$ solidification, then the remaining liquid could possibly achieve beryl saturation assuming that it could be efficiently extracted to produce pegmatites. Figure 4-4 illustrates the 3-stage process. Kosals and Mazurov (1968) documented variations in Be content

throughout a vertical section of a stacked plutonic sequence (primitive to evolved facies to pegmatites) in Baykalia. They report mean values of 7 ppmw Be in main facies, 10 ppmw Be in a slightly enriched facies, and 21 ppmw Be in apical apophyses—values that closely parallel the model above.

Three Principle Pathways

S-Type Magmas with Cordierite

If cordierite is present, most of the available Be in the source will be retained in restite, leaving derivative melts highly depleted in Be. This pathway is shown in Figure 4-5a. Beginning with a whole-rock value of 3 ppmw Be, anatexis produces melt containing some ≤ 1 ppmw Be (Breaks and Moore, 1992; Bea et al., 1994a; Barbey et al., 1999; see Table 4-2). Be-enriched restite left at the source may later be modified by metamorphism to form higher-grade assemblages (e.g., surinamite, $\text{Mg}_3\text{Al}_4\text{BeSi}_3\text{O}_{15}$; taaffeite, $\text{Mg}_3\text{Al}_8\text{BeO}_{16}$; Be-rich sapphirine; Grew 1998) from reaction of beryllian cordierite. Cordierite is likely to persist as a liquidus phase, although, it may decline in abundance or go out as the muscovite or tourmaline consumes the negligible femic components of present in evolved, low-temperature melts. In evolved melt, the largest fraction of Be will be tied up white mica, and approximately 3 ppmw Be is likely to occur in melt (or whole-rocks). Pegmatites associated with the evolved melts likely contain ~ 25 ppmw Be in their bulk melts, and Be resides mainly in white micas and plagioclase. As noted above, these micas are likely to contain high contents of Be, higher than in micas of beryl-saturated pegmatites. Pegmatites derived from cordierite-bearing granites are not likely to contain Be minerals, nor will metasomatic aureoles contain elevated Be.

S-type Magmas with Garnet

Figure 4-5b begins from pelitic source rocks containing 3 ppmw Be. Anatexis results in about a two-fold enrichment of Be in melt (6 ppmw Be). Among restitic phases, plagioclase should house the greatest abundance of Be. Fractionation then progresses to evolved magmas forming apical plutons. These melts should contain substantial contents of Be. Commonly, 10s up to rarely 100s of ppmw Be are observed in whole-rock values of evolved S-type leucogranites (Charoy and Noronha, 1996; Ramirez and Grundvig, 2000; Shearer et al., 1987; Raimbault et al., 1995; Zraisky et al., 1997; see Table 4-2). As the Ca content of plagioclase falls with fractionation, white mica becomes the principal sink for Be.

Pegmatites derived from these apical stocks and plutons are predicted to contain ~ 70 ppmw Be in their melts, and thus will probably achieve beryl saturation upon undercooling (see Evensen et al., 1999). Pegmatitic melts may also reach saturation in chrysoberyl, Be-phosphates, beryllian cordierite, and other Be-minerals, and phenakite may result in pocket assemblages. Within a localized aureole (commonly, millimeter to decimeter in scale), metasomatic emerald and bityite or beryllian margarite may form in the wallrock alteration assemblage.

I- and A-type Magmas

Figure 4-5c shows the Be systematics using the model haplogranite bulk distribution coefficient relevant to I- and A-type petrogeneses. Sources for these melts likely begin with slightly lower or equivalent contents of Be in whole rocks (3 ppmw Be). Enrichment upon melting occurs, though to lesser a degree than in garnet-bearing metapelitic source rocks because of an absence of micas (mainly white mica) in these systems. Still, fractionation leading to the melt stage is likely to be significant with ~ 5

ppmw Be in melt. Here, oligoclase-andesine houses the greatest fraction of Be among the rock-forming minerals. In evolved melts, increasing sodic plagioclase and dark mica house the majority of Be in melts that show substantial enrichment of beryllium (~ 15 ppmw Be).

Pegmatites associated with these liquids probably contain adequate Be to reach beryl saturation. For instance, in Be-enriched apophyses of some of evolved A-type melts, saturation of beryl is achieved upon solidification of what is likely to be fractions of 1 % (rather than the model 20 %) of residual melt (e.g., “beryl clots” of Mt. Antero, Colorado, USA; see Jacobson 1993). Although such occurrences may have also been subject to significant cooling to reach beryl saturation (which is highly *T*-dependent: Evensen et al., 1999), these rocks support the idea that pegmatite-forming melts of this type are likely to be undersaturated (perhaps significantly) with respect to beryl upon emplacement. The styles of mineralization are thus different among these (NYF) pegmatites and those originating from S-type magmas. In summary, beryl may or may not crystallize in these pegmatites, along with several typical Be-minerals (e.g., gadolinite group, bazzite, behoite). Because the modal proportion of Be-minerals tends to be small in these systems, a significant reservoir of Be ends up in albite whether or not saturation in Be-minerals is reached. Significant Be may be available for late hydrothermal alteration, and if aluminous phases are absent in wallrock assemblages, these solutions may be quite rich in Be (~ 100 ppmw Be) with, for example, the capacity to precipitate bertrandite.

CONCLUSIONS

Beryllium partition coefficients can be used to determine the budget of Be at any stage in a magmatic cycle of the felsic crust, going from anatexis to late hydrothermal mineralization of pegmatites. Enrichment of Be will only be achieved in magmas that neither contained cordierite in their source rocks nor large modal proportions of calcic oligoclase as a liquidus phase. Where present, enrichment likely owes to either (1) a contribution of white mica at the source or (2) the absence of middle plagioclase \pm white mica throughout the crystallization interval so that Be fractionates in residual liquid. Extended fractionation beyond $\sim 95\%$ total solidification by at least a 3-step process is required to achieve beryl saturation in granite magmas.

References Cited

- Ahmed-Said, Y., and Leake, B.E. (1990) S-type granite formation in the Dalradian rocks of Connemara, W. Ireland. *Mineralogical Magazine* 54, 1-22.
- Armbruster, T. and Irouschek, A. (1983) Cordierites from the Lepontine Alps: Na+Be→Al substitution, gas content, cell parameters, and optics. *Contributions to Mineralogy and Petrology*, 82, 389-396.
- Auricchio, C., Fioravanti, G., Grubessi, O., & Zanazzi, P.F. (1988) Reappraisal of the crystal chemistry of beryl. *American Mineralogist*, 73, 826-837.
- Baba, S., Grew, E.S., Shearer, C.K., and Sheraton, J.W. (2000) Surinamite, a high-temperature metamorphic berylosilicate from Lewisian sapphirine-bearing kyanite- orthopyroxene-quartz-potassium feldspar gneiss at South Harris, N.W. Scotland. *American Mineralogist* 85, 1474-1484.
- Bader, R.F., Keaven, I.T., and Cade, P.E. (1967) Molecular charge distributions and chemical binding. II. First-row diatomic hydrides, AH. *Journal of Chemical Physics* 47, 3381-3402.
- Barbey, P., Marignac, C., Montel, J.M., Macaudiere, J., Gasquet, D., and Jabori, J. (1999) Cordierite growth textures and the conditions of genesis and emplacement of crustal granitic magmas; the Velay granite complex (Massif Central, France). *Journal of Petrology* 40, 1425-1441.
- Bea, F., Pereira, M.D., and Stroh, A. (1994a) Mineral/leucosome trace-element partitioning in a peraluminous migmatite (a laser ablation-ICP-MS study). *Chemical Geology* 117, 291-312.
- Bea, F., Pereira, M.D., Corretge, L.G., and Fershtater, G.B. (1994b) Differentiation of

- strongly peraluminous, perphosphorus granites: The Pedrobernardo pluton, central Spain. *Geochimica et Cosmochimica Acta* 58, 2609-2627.
- Bebout, G.E., Ryan, J.G., & Leeman, W.P. (1993) B-Be systematics in subduction-related metamorphic rocks: Characterization of the subducted component. *Geochimica et Cosmochimica Acta* 57, 2227-2237.
- Beus, A.A. (1966) *Geochemistry of Beryllium and Genetic Types of Beryllium Deposits*. W.H. Freeman and Company, San Francisco, 286 p.
- Breaks, F.W. and Moore, J.M. Jr. (1992) The Ghost Lake batholith, Superior Province of northwestern Ontario: a fertile S-type, peraluminous granite - rare-element pegmatite system. *Canadian Mineralogist*, 30, 835-875.
- Breiter, K., Sokolova, M., and Sokol, A. (1991) Geochemical specialization of the tin-bearing granitoid massifs of NW Bohemia. *Mineralium Deposita*, 26, 298-306.
- Brenan, J.M., Neroda, E., Lundstrom, C.C., Shaw, H.F., Ryerson, F.J., and Phinney, D.L. (1998a) Behavior of boron, beryllium, and lithium during melting and crystallization: Constraints from mineral-melt partitioning experiments. *Geochimica et Cosmochimica Acta* 62, 2129-2141.
- Brenan, J.M., Neroda, E., Lundstrom, C.C., Shaw, H.F., Ryerson, F.J., and Phinney, D.L. (1998b) Behaviour of boron, beryllium, and lithium during melting and crystallization: constraints from mineral-melt partitioning experiments. *Geochimica et Cosmochimica Acta*, 62, 2129-2141.
- Burt, D.M., & Sheridan, M.F. (1987) Types of mineralization related to fluorine-rich

- silicic lava flows. Geological Society of America Special Paper 212, 103-109.
- Černý, P. (1991a) Rare element granitic pegmatites. Part I: anatomy and internal evolution of pegmatite deposits. *Geoscience Canada* 18, 29-47.
- Černý, P. (1991b) Rare-element granitic pegmatites. Part II: Regional to global environments and petrogenesis. *Geoscience Canada* 18, 49-62.
- Černý, P., and Povondra, P. (1966) Beryllian cordierite from Vezna: $(\text{Na}+\text{K})+\text{Be}\rightarrow\text{Al}$. *Neues Jahr Mineral Monatshefte* (1966), 36-44.
- Černý, P., Chapman, R., Schreyer, W., Ottolini, L., Bottazzi, P., and McCammon, C.A. (1997) Lithium in sekaninaite from the type locality, Dolní Bory, Czech Republic. *Canadian Mineralogist*, 35, 167-173.
- Charoy, B. and Noronha, F. (1996) Multistage growth of a rare-element volatile-rich microgranite at Argemela (Portugal). *Journal of Petrology*, 37, 73-94.
- Clemens, J.D., Holloway, J.R., and White, A.J.R. (1986) Origin of A-type granite: Experimental constraints. *American Mineralogist* 71, 317-324.
- Congdon, R.D., & Nash, W.P. (1991) Eruptive pegmatite magma: rhyolite of the Honeycomb Hills, Utah. *American Mineralogist* 76, 1261-1278.
- Domanik, K.J., Hervig, R.L., & Peacock, S.M. (1993) Beryllium and boron in subduction zone minerals: An ion microprobe study. *Geochimica et Cosmochimica Acta* 57, 4997-5010.
- Downs, J.W., & Gibbs, G.V. (1981) The role of the BeOSi bond in the structures of beryllosilicate minerals. *American Mineralogist*, 66, 819-826.
- Evensen, J.M. (1997) *Effects of beryllium on the liquidus phase relations of haplogranite*. MS Thesis, Colorado School of Mines, Golden, Colorado, 92 p.

- Evensen, J.M., and Meeker, G.P. (1997) Feasibility of Be analysis for geologic materials using EPMA. *Microscopy Society of America, Proceedings: Microscopy and Microanalysis 1997*, 3 (2), 893-894.
- Evensen, J.M., and London, D. (2001a) Experimental partitioning of Be and other trace elements between cordierite and silicic melt, and the chemical signature of S-type granite. *Contributions to Mineralogy and Petrology*, in review.
- Evensen, J.M., and London, D. (2001b) Crystal chemistry and phase relations of cordierite – beryl solid solutions in granitic systems. *American Mineralogist*, in press.
- Evensen, J.M., London, D., and Wendlandt, R.F. (1999) Solubility and stability of beryl in granitic melts. *American Mineralogist* 84, 733-745.
- Ginzburg, A.I. (1957) Bityite – lithium-beryllium margarite. *Mineralogical Abstracts* 14, 136.
- Gordillo, C.E. (1979) Observaciones sobre la petrología de las rocas cordieríticas de la Sierra de Córdoba. *Bol. Acad. Nac. Cienc. Cordoba Argentina* 53, 3-44.
- Gordillo, C.E., Schreyer, W., Werding, G., and Abraham, K. (1985) Lithium in NaBe-cordierites from El Peñón, Sierra de Córdoba, Argentina. *Contributions to Mineralogy and Petrology* 90, 93-101.
- Gresens, R.L. (1966) Dimensional and compositional control of garnet growth by mineralogical environment. *American Mineralogist* 51, 524-528.
- Grew, E.S. (2001) Beryllium minerals and Be in rock-forming minerals in metamorphic

- environments. In Grew, E.S. (ed.) *Beryllium: Mineralogy, Petrology and Geochemistry*. Mineralogical Society of America, Reviews in Mineralogy, in press.
- Grew, E.S. (1998) Boron and beryllium minerals in granulite-facies pegmatites and implications of beryllium pegmatites for the origin and evolution of the Archean Napier Complex of East Antarctica. Mem. of Natl. Inst. Polar Res., Spec. Issue 53, 74-92.
- Grew, E.S., Hinthorne, J.R., and Marquez, N. (1986) Li, Be, B, and Sr in margarite and paragonite from Antarctica. *American Mineralogist* 71, 1129-1134.
- Grew, E.S., Yates, M.G., Huijsmans, J.P., McGee, J.J., Shearer, C.K., Wiedenbeck, M., and Rouse, R. (1998) Werdingite, a borosilicate new to granitic pegmatites. *Canadian Mineralogist* 36, 399-414.
- Grew, E.S., Yates, M.G., Barbier, J., Shearer, C.K., Sheraton, J.W., Shiraishi, K., and Motoyoshi, Y. (2000) Granulite-facies beryllium pegmatites in the Napier Complex in Khmara and Amundsen Bays, western Enderby Land, East Antarctica. *Polar Geoscience* 13, 1-40.
- Hervig, R.L. (2001) Beryllium analyses by secondary ion mass spectrometry. In Grew, E.S. (ed.) *Beryllium: Mineralogy, Petrology and Geochemistry*. Mineralogical Society of America, Reviews in Mineralogy, in press.
- Hölscher, A. and Schreyer, W. (1989) A new synthetic hexagonal BeMg-cordierite, $Mg_2(Al_2BeSi_6O_{18})$, and its relationship to Mg-cordierite. *European Journal of Mineralogy*, 1, 21-37.
- Huebner, J.S. (1971) Buffering techniques for hydrostatic systems at elevated pressures.

- In: *Research Techniques for High Pressure and High Temperature* (G.C. Ulmer, ed.) Springer-Verlag, New York, 123-177.
- Jacobson, M.I. (1993) *Antero Aquamarines: Minerals from the Mount Antero – White Mountain region, Chaffee County, Colorado*. L.R. Ream Publishing, 126 p.
- Jahns, R.H., and Ewing, R.C. (1977) The Harding Mine, Taos County, New Mexico. *Mineralogical Record* 8, 115-126.
- Kalt, A., Berger, A., and Blumel, P. (1999) Metamorphic evolution of cordierite-bearing migmatites from the Bayerische Wald (Variscan Belt, Germany). *J Petrol* 40: 601-627.
- Kennen, P. (2001) The S-type Leinster granite in SE Ireland. In: (Chappell, B., Fleming, P., eds.) *S-type granites and related rocks, abstracts*, Australian Geol Survey Org, Rec 2001/02, pp. 65-66.
- Kosals, Y.A., and Mazurov, M.P. (1968) Behavior of rare alkalis, boron, fluorine and beryllium during the emplacement of the Bitu-Dzhida granitic batholith, southwest Baykalia. *Geochemistry International* 1968, 1024-1034.
- Kosals, Y.A., Nedashkovskiy, P.G., Petrov, L.L., and Serykh, V.I. (1973) Beryllium distribution in granitoid plagioclase. *Geochemistry International* 10, 753-767
- Kovalenko, V.I., Antipin, V.S., and Petrov, L.L. (1977) Distribution coefficients of beryllium in ongonites and some notes on its behavior in the rare metal lithium-fluorine-granites. *Geochemistry International* 1977, 129-141.
- Kozlov, V.D. (1969) Use of concentrator minerals in evaluation of rarer-element accumulation in the differentiation products of granitoid intrusions. *Geochemistry International* 3, 309-321.

- Kretz, R., Loop, J., & Hartree, R. (1989) Petrology and Li-Be-B geochemistry of muscovite-biotite granite and associated pegmatite near Yellowknife, Canada. *Contributions to Mineralogy and Petrology* 102, 174-190.
- Leeman, W.P. (1996) Boron and other fluid-mobile elements in volcanic arc lavas; implications for subduction processes. In *Subduction top to bottom* (G.E. Bebout, D.W. Scholl, S.H. Kirby, and J.P. Platt, eds). *Geophysical Monograph* 96, 269-276.
- Lindsey, D.A. (1977) Epithermal beryllium deposits in water-laid tuff, western Utah. *Economic Geology and the Bulletin of the Society of Economic Geologists* 72, 219-232.
- London, D. (1985) Origin and significance of inclusions in quartz: A cautionary example from the Tanco Pegmatite, Manitoba. *Economic Geology* 80, 1988-1995.
- London, D. (1986) Holmquistite as a guide to pegmatite rare metal deposits. *Economic Geology* 81, 704-712.
- London, D., Hervig, R.L., and Morgan, G.B. (1988) Melt-vapor solubilities and elemental partitioning in peraluminous granite-pegmatite systems: experimental results with Macusani glass at 200 MPa. *Contributions to Mineralogy and Petrology* 99, 360-373.
- Luecke, W. (1981) Lithium pegmatites in the Leinster Granite (southeast Ireland). *Chemical Geology* 34, 195-233.
- Lyakhovick, V.V. (1977) Distribution of Li, Cs, Be and F in the vertical section of the Element'Dzhurtinsk Massif of porphyritic granites (Northern Caucasus). *Geochemistry International* 3, 360-372.

- Morgan, G.B., and London, D. (1987) Alteration of amphibolitic wallrocks around the Tanco rare-element pegmatite, Bernic Lake, Manitoba. *American Mineralogist* 72, 1097-1121.
- Morgan, G.B., and London, D. (1996) Optimizing the electron microprobe analysis of hydrous alkali aluminosilicate glasses. *American Mineralogist* 81, 1176-1185.
- Morgan, G.B., & London, D. (1999) Crystallization of the Little Three layered pegmatite-aplite dike, Ramona, California. *Contributions to Mineralogy and Petrology* 136, 310-330.
- Morgan, G.B., London, D., and Luedke, R.G. (1998) Petrochemistry of Late Miocene Peraluminous Silicic Volcanic Rocks from the Morococala Field, Bolivia. *Journal of Petrology* 39, 601-632.
- Morris, J.D., Leeman, W.P., & Tera, F. (1990) The subducted component in island arc lavas: constraints from Be isotopes and B-Be systematics. *Nature* 344, 31-36.
- Mukhopadhyay, B., and Holdaway, M.J. (1993) Cordierite-garnet-sillimanite-quartz equilibrium: I. New experimental calibration in the system FeO-Al₂O₃-SiO₂-H₂O and certain P-T-X_{H₂O} relations. *Contributions to Mineralogy and Petrology* 116, 462-472.
- Newton, R.C. (1966) BeO in pegmatitic cordierite. *Mineralogical Magazine*, 35, 920-927.
- Ottolini, L., Bottazzi, P., and Vannucci, R. (1993) Quantification of lithium, beryllium, and boron in silicates by secondary ion mass spectrometry using conventional energy filtering. *Analytical Chemistry* 65, 1960-1968.
- Palmer, D.C. (1994) Stuffed derivatives of the silica polymorphs. In *Silica: Physical*

- Behavior, Geochemistry and materials applications (Heaney, P.J., Prewitt, C.T., and Gibbs, G.V., eds.). Mineralogical Society of America, Reviews in Mineralogy 29, 83-122.
- Pereira, M.D., and Bea, F. (1994) Cordierite-producing reactions in the Peña Negra Complex, Avila Batholith, Central Spain. *Canadian Mineralogist* 32, 763-780.
- Pearce, N.J.G., Perkins, W.T., Westgate, J.A., Gorton, M.P., Jackson, S.E., Neal, C.R., and Cheney, S.P. (1997) A compilation of new and published major and trace element data for NIST SRM 610 and SRM 612 glass reference materials. *Geostandards Newsletter* 21, 115-144.
- Pouchou, J.L., and Pichoir, F. (1985) "PAP" (ϕ - ρ -Z) correction procedure improved quantitative microanalysis. In (J.T. Armstrong, ed.) *Microbeam Analysis*, San Francisco Press. 104-106.
- Povondra, P. and Čech, F. (1978) Sodium-beryllium-bearing cordierite from Haddam, Connecticut, U.S.A. *Neues Jahrbuch für Mineralogie, Monatshefte*, 5, 203-209.
- Povondra, P., Čech, F., and Burke, E.A.J. (1984) Sodian-beryllian cordierite from Gammelmorskärr, Kemiö Island, Finland, and its decomposition products. *Neues Jahrbuch für Mineralogie, Monatshefte* 3, 125-136.
- Raimbault, L., and Burnol, L. (1998) The Richemont rhyolite dyke, Massif Central, France: A subvolcanic equivalent of rare-metal granites. *Canadian Mineralogist* 36, 265-282.
- Raimbault, L., Cuney, M., Azencott, C., Duthou, J.L., and Joron, J.L. (1995)

- Geochemical evidence for a multistage magmatic genesis of Ta-Sn-Li mineralization in the granite at Beauvoir, French Massif Central. *Economic Geology Bulletin Society of Economic Geologists* 90, 548-576.
- Ramirez, J.A., and Grundvig, S. (2000) Causes of geochemical diversity in peraluminous granitic plutons: the Jalmala pluton, Central-Iberian Zone (Spain and Portugal). *Lithos* 50, 171-190.
- Robert, J.L., Hardy, M., and Sanz, J. (1995) Excess protons in synthetic micas with tetrahedrally coordinated divalent cations. *European Journal of Mineralogy* 7, 457-461.
- Russ, J.C. (1999) *The Image Processing Handbook*, 3rd Ed. CRC Press, Boca Raton, Florida. 771p.
- Ryan, J.G., & Langmuir, C.H. (1988) Beryllium systematics in young volcanic rocks: Implications for ¹⁰Be. *Geochimica et Cosmochimica Acta* 52, 237-244.
- Ryan, J., Morris, J., Bebout, G., and Leeman, W. (1996) Describing chemical fluxes in subduction zones: Insights from "depth-profiling" studies of arc and forearc rocks. In: Bebout, G.E., Scholl, D.W., Kirby, S.H., and Platt, J.P. (eds.) *Subduction: Top to Bottom*. American Geophysical Union, Geophysical Monograph 96, 263-268.
- Schreyer, W., Gordillo, C.E., and Werding, G. (1979) A new sodium-beryllium cordierite from Soto, Argentina, and the relationship between distortion index, Be content, and state of hydration. *Contributions to Mineralogy and Petrology*, 70, 421-428.
- Shannon, R.D. (1976) Revised effective ionic radii and systematic studies of interatomic distances in halides and chalcogenides. *Acta Crystallographica* A32, 925-946.

- Shearer, C.K., Papike, J.J., and Laul, J.C. (1987) Mineralogical and chemical evolution of a rare-element granite-pegmatite system; Harney Peak Granite, Black Hills, South Dakota. *Geochimica et Cosmochimica Acta* 51, 473-486.
- Smeds, S.A. (1992) Trace element in potassium-feldspar and muscovite as a guide in the prospecting for lithium- and tin-bearing pegmatites in Sweden. *Journal of Geochemical Exploration* 42, 351-369.
- Solodov, N.A. (1959) Certain regularities of distribution of rare elements in sharply zoned pegmatites (in Russian). *Geokhimiya* 4, 316-327.
- Stix, J., & Layne, G.D. (1996) Gas saturation and evolution of volatile and light lithophile elements in the Bandelier magma chamber between two caldera-forming eruptions. *Journal of Geophysical Research* 101 (B11), 25,181-25,196.
- Tatsumi, Y and Isoyama, H. (1988) Transportation of beryllium with H₂O at high pressures; implication for magma genesis in subduction zones. *Geophysical Research Letters*, 15, 180-183
- Toth, L.M., Bates, J.B., & Boyd, G.E. (1973) Raman spectra of Be₂F₇³⁻ and higher polymers of beryllium fluorides in the crystalline and molten state. *Journal of Physics and Chemistry*, 77, 216-221.
- Trueman, D.L., and Černý, P. (1982) Exploration for rare-element granitic pegmatites. In (P. Černý, ed.) *Granitic Pegmatites in Science and Industry*. Mineralogical Association of Canada Short Course Handbook 8, 463-493.
- Tuttle, O.F. and Bowen, N.L. (1958) Origin of granite in the light of experimental studies in the system NaAlSi₃O₈-KAlSi₃O₈-SiO₂-H₂O. *Geological Society of America, Memoir* 74.

- Ugidos, J.M. (1988) New aspects and considerations on the assimilation of cordierite-bearing rocks. *Rev. Soc. Geol. España* 1, 129-133.
- Ugidos, J.M., and Recio, C. (1993) Origin of cordierite-bearing granites by assimilation in the Central Iberian Massif (CIM), Spain. *Chemical Geology* 103, 27-43.
- Vielzeuf, D., and Holloway, J.R. (1988) Experimental determination of the fluid-absent melting relations in the pelitic system. *Contributions to Mineralogy and Petrology* 98, 257-276.
- Visser, D., Kloprogge, J.T., and Maijer, C. (1994) An infrared spectroscopic (IR) and light element (Li, Be, Na) study of cordierites from the Bamble Sector, South Norway. *Lithos* 32, 95-107.
- Webster, J.D., Burt, D.M., and Aguilon, A. (1996) Volatile and lithophile trace-element geochemistry of Mexican tin rhyolite magmas deduced from melt inclusions. *Geochimica et Cosmochimica Acta*, 60, 3267-3283.
- Webster, J.D. and Duffield, W.A. (1991) Extreme halogen enrichment in tin-rich magma of the Taylor Creek Rhyolite, New Mexico. *Economic Geology and the Bulletin of the Society of Economic Geologists*, 89, 840-850.
- Webster, J.D., Holloway, J.R., & Hervig R.L. (1989) Partitioning of lithophile trace elements between H₂O and H₂O + CO₂ fluids and topaz rhyolite melt. *Economic Geology and the Bulletin of the Society of Economic Geologists*, 84, 116-134.
- Wood, S.A. (1992) Theoretical prediction of speciation and solubility of beryllium in hydrothermal solution to 300°C at saturated vapor pressure: Application to bertrandite/phenakite deposits. *Ore Geology Reviews* 7, 249-278.
- Wuensch, B.J., & Hörmann, P.K. (1978) Beryllium. In: Wedepohl, K.H. (ed) *Handbook*

of Geochemistry, Vol. II (1). Springer, Berlin Heidelberg New York, pp 4-A-1 to 4-O-1.

Zaraisky, G.P., Seltmann, R., Shatov, V.V., Aksyuk, A.M., Shapovalov, Yu.B., and Chevychelov, V.Yu. (1997) Petrography and geochemistry of Li-F granites and pegmatite-aplite banded rocks from the Orlovka and Etyka tantalum deposits in Eastern Transbaikalia, Russia. In "Mineral Deposits: Research and Exploration. Where do they meet?" (H. Papunen ed.), Proceedings of the 4th Biennial Society for Geology Applied to Mineral Deposits Meeting, Turku, 11-23 August 1997. Rotterdam: Balkema, pp. 695-698.

Table 4-1. Average beryllium contents of rock-forming minerals in silicic systems (granitoid rocks to pegmatites)

Mineral	Mean Be (ppmw)	Range	N	Data Source
K-feldspar	3.1 (0.4)	0.85 to 10	>55	1,2,3
K-alkali feldspar (pegmatitic)	7 (6)	3 to 20	>15	1,4
Na-alkali feldspar	13 (4)	9 to 16	4	2,3
plagioclase	6.7 (1.2)	1.8 to 20	>30	1,2
albite	10.3 (1.6)	4 to 20	>13	1
albite (pegmatitic)	18.1 (2.8)	9 to 40	>10	1,2
oligoclase	10.7 (0.4)	<1 to 40	260	5
andesine	4.8 (1.1)	0.4 to 24	>40	5
quartz	1.2 (0.3)	0.1 to 7.2	>30	1
quartz (pegmatitic)	2.2 (0.0)	0.5 to 7.35	>25	1
muscovite	14 (1.9)	11 to 17	>5	2,3
muscovite (evolved magmatic)	39 (4.2)	31 to 50	>4	1
muscovite (pegmatitic)	36 (5.8)	12 to 120	106	1,2,4
lepidolite (pegmatitic)	63 (15.0)	48 to 78	>2	1
biotite	5.2 (0.8)	0.5 to 11.8		1,2,3
cordierite (migmatitic)	12.0 (4.31)	7.69 to 16.3	2	6
cordierite (restite)	7.3 -	-	1	6
cordierite (evolved magmatic)	7213 (1418)	110 to 10300	7	7,8
cordierite (pegmatitic)	4724 (1758)	10 to 17700	17	9-14
cordierite (metamorphic)	35 (9.4)	1 to 257	34	15,16
cordierite (metamorphic, leucocratic)	6775 (464.4)	6000 to 8100	4	17
garnet	11.5 (2.4)	6 to 20	>5	1
garnet (pegmatitic)	14.1 (4.3)	0.0 to 50.4	>12	1,18,19
hornblende	8.6 (1.4)	3.6 to 13.4		1
alkali amphibole	13.0 -	-	>>1	1
orthopyroxene				

Precision represents reported standard deviation or calculated standard error of the means.

Data sources include: 1, Wuensch and Homann 1974; 2, Kretz et al., 1989; 3, Luecke 1981; 4, Smeds 1992; 5, Kosals et al., 1973; 6, Bea et al., 1994a; 7, Schreyer et al., 1979; 8, Gordillo et al. 1985; 9, Cemy et al., 1997; 10, Cemy and Povondra 1966; 11, Povondra and Cech 1978; 12, Povondra et al., 1984; 13, Newton 1966; 14, Grew 2000; 15, Kalt et al., 1998; 16, Visser et al., 1994; 17, Armbruster and Irouschek 1983; 18, Gresens 1966; 19, this study.

Table 4-2. Average beryllium contents of crustal rock systems

Mineral	Mean Be (ppmw)	Range	N	Data Source
magmatic rocks				
gabbrodiorite	1 (1)			1
diorite	2 (0)	2 to 2.8	>5	1,2
granitic rocks	5 (0)	3 to 6.5	>75	2
<i>S-type granites</i>				
Crd-bearing	0.08 (0.2)	<1 to 1.20	13	4
Crd-absent	5.5 (1.7)	3 to 12	>110	1,3,4
with associated pegmatites	14.0 (8.4)	3 to 64	>50	4
evolved facies	68.0 (25.9)	11 to 130	>102	4
<i>S-type rhyolites</i>	14.1 (4.8)	4.3 to 37	42	4
<i>A-type granites</i>	6.0			4
<i>A-type rhyolites</i>	14-18 (7.5)	1.8 to 32	101	4
<i>I-type granodiorites</i>	2.9 (0.7)	0.4 to 12.2	>25	1,2
<i>I-type rhyolites</i>	2.6	1.3 to 5.5		4
metamorphic rocks				
pelitic schist	4 (0.9)		>10	2,5
quartzofeldspathic gneiss	3.6 (0.6)		>22	2,6
amphibolite	2.2 (0.6)		>3	2

Data sources:

- 1, Kozlov 1969
- 2, Wuensch and Hornmann 1974
- 3, Lyakhovich 1977
- 4, Evensen and London 2001b, in review, and references therein
- 5, Lueke 1981
- 6, Grew 2000

Table 4-3. STARTING MATERIALS

ADDED MINERALS & GLASS												
Mineral ^a	albite	adularia	orthoclase	quartz	muscovite-A ^b	muscovite-B	biotite	garnet		phenakite	beryl	haplogranite glass
Abbreviation	Ab	Or-A	Or-B	Qtz	Mus-A	Mus-B	Bt	Alm ₄₄ Pyp ₄₂ Gro ₁₃ Sps ₁	Gt	Phn	Brl	HG-glass
No. of analyses	5	20	166	6	1-3		96	20	5	7	41	
	sd	sd	se	sd		se	sd	sd	sd	sd	sd	sd
wt%												
SiO ₂	68.82 (0.16)	64.95 (0.36)	64.05 (0.04)	99.99 (0.03)	51.91 -	38.83 (0.29)	38.83 (0.29)	39.71 (0.26)	54.34 (0.32)	66.00 (0.20)	77.63 (0.59)	
TiO ₂	nd	nd	nd	nd	0.22 -	2.05 (0.11)	2.05 (0.11)	0.04 (0.02)	0.00	0.06 (0.02)	0.01 (0.01)	
Al ₂ O ₃	19.76 (0.05)	18.76 (0.14)	18.67 (0.02)	nd	28.02 -	11.26 (0.12)	11.26 (0.12)	23.20 (0.16)	0.00	19.24 (0.10)	13.03 (0.16)	
Fe ₂ O ₃	-	-	0.08 (0.00)	-	3.53 -	-	-	-	-	-	-	-
FeO	nd	nd	-	nd	0.82 ^c	18.47 (0.25)	18.47 (0.25)	21.26 (0.14)	0.03 (0.02)	0.48 (0.13)	0.02 (0.01)	
MnO	nd	nd	nd	nd	0.08 -	0.83 (0.04)	0.83 (0.04)	0.46 (0.02)	0.00	0.00	0.00	
ZnO	nd	nd	nd	nd	nd	0.14 (0.04)	0.14 (0.04)	nd	nd	nd	nd	
BeO ^d	nd	nd	nd	nd	nd	nd	nd	nd	46.17 (0.99)	13.97 (0.05)	nd	
MgO	nd	nd	nd	nd	1.00 -	14.08 (0.21)	14.08 (0.21)	11.46 (0.05)	0.00	0.00	0.01 (0.00)	
CaO	0.07 (0.01)	0.01 (0.02)	0.15 (0.00)	nd	0.30 -	0.00 (0.01)	0.00 (0.01)	5.07 (0.04)	0.00	0.00	0.01 (0.01)	
BaO	0.06 (0.05)	0.32 (0.04)	0.65 (0.01)	nd	0.09 ^e	0.10 (0.02)	0.10 (0.02)	0.02 (0.02)	0.14 (0.01)	0.03 (0.03)	0.01 (0.01)	
Na ₂ O	11.59 (0.04)	1.21 (0.07)	0.71 (0.01)	nd	1.27 -	0.56 (0.14)	0.56 (0.14)	0.00	0.00	0.08 (0.01)	4.61 (0.11)	
K ₂ O	0.23 (0.02)	14.84 (0.07)	15.41 (0.02)	nd	8.90 -	9.01 (0.14)	9.01 (0.14)	0.00	0.00	0.03 (0.03)	4.79 (0.09)	
Rb ₂ O (ppm)	nd	nd	nd	nd	895 ^a	nd	nd	nd	nd	151 ^a (5)	nd	
Cs ₂ O (ppm)	nd	nd	nd	nd	23 ^a	nd	nd	nd	nd	2021 ^a (20)	nd	
P ₂ O ₅	nd	nd	nd	nd	nd	nd	nd	0.04 (0.01)	nd	nd	0.01 (0.01)	
F	nd	nd	nd	nd	nd	3.67 (0.14)	3.67 (0.14)	0.02 (0.03)	nd	nd	0.03 (0.03)	
Cl	nd	nd	nd	nd	nd	0.05 (0.02)	0.05 (0.02)	0.01 (0.01)	nd	nd	0.01 (0.01)	
H ₂ O	nd	nd	nd	nd	nd	2.02 ^b (0.08)	2.02 ^b (0.08)	nd	nd	nd	nd	
LOI	-	-	-	-	3.87	-	-	-	-	-	-	-
O=F						-1.54	-1.54	-0.01				-0.01
O=Cl						-0.01	-0.01					0.00
Total	100.53 (0.18)	100.09 (0.40)	99.72 (0.12)	99.99 (0.03)	100.10 (0.16)	99.52 (0.53)	99.52 (0.53)	101.28 (0.35)	100.68 (1.04)	100.11 (0.26)	100.18 (0.63)	

^a albite, Copelinha, Minas Gerais, Brazil; adularia, St. Gothard, Switzerland; orthoclase, Betroka, Madagascar; quartz, ultrahigh purity, Feldspar Corp., Spruce Pine, NC, USA; muscovite-A, Spruce Pine, NC, USA; muscovite-B, Minas Gerais, Brazil; biotite, Ontario, Canada; garnet, Gore Mountain, NY, USA; phenakite, Espirito Santo, Minas Gerais, Brazil; beryl, Volodarsk, Ukraine; haplogranite glass, 200 MPa minimum anhydrous composition, Corning Glassworks, NY, USA.

^b Analysed at Activation Laboratories Ltd. (Lancaster, Ontario, Canada) by X-Ray fluorescence (fusion) unless otherwise specified.

^c Analysed by titration.

^d Analysed by secondary ion mass spectrometry.

^e Analysed by instrumental neutron activation analysis.

All other values are from quantitative electron probe microanalysis (with total iron as FeO, except for the orthoclase analysis). Numbers in parentheses either represent 1 standard deviation (sd) or the standard error (se) of the mean as shown in the header. Propagated precision is shown for total values; the italicized value represents estimated precision.

Table 4-4. STARTING MIXTURES

Mixture	Experiment Type	Constituents (wt%)											
		Ab	Or-A	Or-B	Qtz	Mus	Mus	Bt	Gt	Al ₂ O ₃	Phn	Brl	HG glass
HG-Or1-C	powder	24.3	23.5	21.5	23.6	7.1							
HG-Or2-C	powder	17.3	15.4	43.0	16.8	7.5							
HG-Or2-Be	powder	27.0	23.9	17.5	26.2						5.4		
HG-Ab1-C	powder	50.6	20.0		22.0	7.4							
HG-Ab2-C	powder	62.8	14.4		15.8	7.0							
HG-Ab1-Be	powder	53.8	19.9		21.8						4.5		
HG-Ab2-Be	powder	66.9	14.2		15.6						3.3		
HG-Qtz3-C	powder	23.3	20.6		49.4	6.7							
SP-Crd1-C	powder	22.7	9.6		26.6	13.1		12.3	15.7				
SP-Crd1-Be	powder	22.7	9.5		26.5	13.1		12.0	15.1		1.1		
SP-Bt2-C	coarse Bt	27.1	11.4		31.8	15.7		11.9		2.1			
SP-Bt2-Be	coarse Bt	22.6	9.4		26.5	12.9		22.1		3.5		3.0	
SP-Mus2-C	coarse Mus	26.7	11.2		31.2	15.4	12.5			3.0			
SP-Mus2-Be	coarse Mus	21.8	9.2		25.6	25.9	11.9			2.7		2.9	
SP-Mus3-C	coarse Mus						50.0						50.0
SP-Mus3-Be	"sandstone"					49.0					1.5		49.5

"SP-" and "HG-" in mineral abbreviations denote the base starting composition of "synthetic pelite" or haplogranite, respectively. The designation "-Be" marks Be-rich mixtures, whereas "-C" marks Be-poor (control) compositions in which no Be-mineral was added.

Experiment Type consisted of either 100% powdered constituents, powders + coarse mica (circular fragments, 2 mm in diameter), or "sandstone" textures comprised of 100% coarse sand-size grains (~ 1 mm in diameter).

Analyses of these constituents and definition of their abbreviations are given in Table 1. Dehydrated reagent-grade gibbsite was used for a source of activated Al₂O₃.

Table 4-5a. K-alkali feldspar – glass compositional pairs

Run	Low Be Contents									
	BeP-49		BeP-64		BeP-47		BeP-30		BeP-31	
Mixture	SP-Mus2-C		SP-Mus3-C		SP-Mus2-C		HG-Or-C		HG-Or-C	
Prec. Path/Duration (d)	730-F (21)		740-F (1)		730-F (21)		800-F (14)		850-F (5)	
Final Path/Duration (d)	675-R (36)		680-R (31)		700-R (28)		750-R (21)		800-R (15)	
Crystalline Products	Kfs,Mus,Als,Cor,Bt,Mt		Kfs,(Mus)		Kfs,Mus,Als,Cor,Bt,Mt		Kfs		Kfs	
Analysis of	K-Afs	glass	K-Afs	glass	K-Afs	glass	K-Afs	glass	K-Afs	glass
No. analyses, QEPMA	10	11	8	10	9	8	11	10	12	10
No. analyses, SIMS	1	1	1	2	1	1	1	5	1	1
Measure of precision		sd		sd		sd		sd		sd
wt %										
SiO ₂	64.24 (0.67)	69.45 (0.84)	64.63 (0.68)	72.23 (0.87)	63.29 (0.39)	69.12 (0.72)	64.95 (0.43)	70.21 (0.63)	64.83 (0.11)	68.83 (1.27)
TiO ₂	0.01 (0.01)	0.03 (0.01)	0.02 (0.01)	0.01 (0.01)	0.01 (0.01)	0.03 (0.01)	0.01 (0.00)	0.02 (0.02)	0.02 (0.01)	0.03 (0.02)
B ₂ O ₃ (ppm) ¹	19.50 -	203.12 -	28.20 -	74.89 (48.22)	6.89 -	184.24 -	13.66 -	47.99 (3.50)	18.07 -	55.79 -
Al ₂ O ₃	18.99 (0.37)	13.45 (0.39)	19.65 (0.27)	12.86 (0.39)	19.47 (0.48)	13.76 (0.30)	18.59 (0.29)	12.96 (0.32)	18.48 (0.09)	14.51 (0.27)
FeO	0.10 (0.02)	0.34 (0.03)	0.07 (0.02)	0.21 (0.02)	0.09 (0.02)	0.37 (0.02)	0.06 (0.01)	0.33 (0.02)	0.09 (0.01)	0.35 (0.02)
MnO	0.01 (0.01)	0.03 (0.01)	0.01 (0.00)	0.01 (0.01)	0.00 (0.01)	0.04 (0.01)	0.01 (0.00)	0.01 (0.01)	0.00 (0.00)	0.01 (0.01)
MgO	0.01 (0.00)	0.18 (0.01)	0.01 (0.00)	0.03 (0.01)	0.01 (0.00)	0.19 (0.01)	0.00 (0.00)	0.08 (0.01)	0.01 (0.00)	0.09 (0.01)
NiO	0.01 (0.00)	nd	0.00 (0.00)	nd	0.00 (0.00)	nd	0.01 (0.00)	nd	0.00 (0.00)	nd
ZnO	nd	nd	0.01 (0.00)	nd	nd	nd	nd	nd	nd	nd
BeO (ppm) ¹	1.22 -	17.14 -	1.73 -	4.55 (0.39)	0.24 -	13.76 -	1.35 -	5.27 (0.19)	1.00 -	5.18 -
CaO	0.02 (0.01)	0.36 (0.10)	0.03 (0.01)	0.02 (0.03)	0.02 (0.01)	0.24 (0.03)	0.01 (0.00)	0.15 (0.02)	0.03 (0.00)	0.28 (0.05)
BaO	0.49 (0.04)	0.01 (0.01)	nd	0.01 (0.01)	0.84 (0.18)	0.02 (0.02)	1.20 (0.02)	0.02 (0.02)	0.68 (0.05)	0.03 (0.04)
Li ₂ O (ppm) ¹	127.20 -	428.64 -	59.75 -	497.66 (32.24)	28.90 -	328.69 -	29.03 -	78.34 (4.87)	14.19 -	78.74 -
Na ₂ O	2.47 (0.08)	3.11 (0.13)	3.93 (0.11)	3.74 (0.18)	2.15 (0.07)	3.18 (0.11)	1.98 (0.02)	3.25 (0.14)	1.37 (0.01)	2.76 (0.09)
K ₂ O	12.70 (0.08)	4.82 (0.08)	10.79 (0.18)	4.00 (0.09)	13.01 (0.18)	5.18 (0.20)	13.31 (0.02)	5.79 (0.14)	14.11 (0.18)	7.12 (0.12)
Rb ₂ O (ppm) ¹	282.07 -	279.80 -	83.28 -	105.24 (3.29)	227.26 -	243.56 -	184.29 -	228.09 (5.78)	274.73 -	355.86 -
Cs ₂ O (ppm) ¹	3.26 -	9.86 -	1.48 -	3.73 (2.47)	1.59 -	9.04 -	3.30 -	8.91 (1.05)	0.65 -	9.36 -
P ₂ O ₅	nd	0.10 (0.03)	nd	0.04 (0.02)	nd	0.06 (0.04)	nd	0.08 (0.01)	nd	0.08 (0.04)
F	0.03 (0.03)	0.11 (0.04)	0.03 (0.01)	0.15 (0.07)	0.05 (0.04)	0.08 (0.07)	0.02 (0.02)	0.02 (0.02)	0.05 (0.02)	0.02 (0.03)
Cl	0.01 (0.00)	0.00 (0.00)	0.01 (0.00)	0.01 (0.01)	0.01 (0.01)	0.01 (0.01)	nd	0.01 (0.00)	nd	0.01 (0.00)
O=F	-0.01 (0.01)	-0.04 (0.02)	-0.01 (0.01)	-0.06 (0.03)	-0.02 (0.02)	-0.03 (0.03)	-0.01 (0.01)	-0.01 (0.01)	-0.02 (0.01)	-0.01 (0.01)
O=Cl	0.00 (0.00)	0.00 (0.00)	0.00 (0.00)	0.00 (0.00)	0.00 (0.00)	0.00 (0.00)	0.00 (0.00)	0.00 (0.00)	0.00 (0.00)	0.00 (0.00)
total	99.11 (0.35)	91.84 (0.68)	99.19 (0.84)	93.32 (0.68)	98.95 (0.64)	92.33 (0.51)	100.16 (0.64)	92.96 (0.81)	99.69 (0.84)	94.49 (1.44)
H ₂ O by diff		8.16		6.68		7.67		7.04		5.51
ASI		1.23 (0.02)		1.20 (0.03)		1.21 (0.03)		1.09 (0.03)		1.10 (0.03)
D-B Crd/MELT	0.10		0.38		0.04		0.28		0.32	
D-Mn Crd/MELT										
D-Be Crd/MELT	0.07		0.38		0.02		0.26		0.19	
D-Ca Crd/MELT	0.05 (0.02)				0.07 (0.04)		0.06 (0.02)		0.10 (0.02)	
D-Li Crd/MELT	0.30		0.12		0.08		0.38		0.18	
D-Rb Crd/MELT	0.94		0.79		0.93		0.82		0.77	
D-Cs Crd/MELT	0.33		0.40		0.18		0.37		0.07	
structural cations/18O										
Si	2.97 (0.03)		2.96 (0.04)		2.94 (0.03)		2.99 (0.03)		2.99 (0.02)	
Al	1.04 (0.02)		1.06 (0.02)		1.07 (0.03)		1.01 (0.02)		1.01 (0.01)	
Li	0.00		0.00		0.00		0.00		0.00	
Na	0.22 (0.01)		0.35 (0.01)		0.19 (0.01)		0.18 (0.00)		0.12 (0.00)	
K	0.75 (0.01)		0.63 (0.01)		0.77 (0.01)		0.78 (0.01)		0.83 (0.01)	
Rb	0.00		0.00		0.00		0.00		0.00	
Ca	0.00		0.00		0.00		0.00		0.00	
Ba	0.01 (0.00)		nd		0.02 (0.00)		0.02 (0.00)		0.01 (0.00)	
total	4.99 (0.04)		5.00 (0.04)		4.99 (0.04)		4.98 (0.03)		4.97 (0.02)	
mol% An	0.08 (0.00)		0.14 (0.00)		0.08 (0.00)		0.04 (0.00)		0.14 (0.00)	
mol% Ab	22.56 (0.93)		35.58 (1.37)		19.71 (0.81)		17.99 (0.49)		12.67 (0.34)	
mol% Or	76.37 (1.92)		64.25 (1.92)		78.58 (2.20)		79.71 (1.99)		85.84 (2.41)	
mol% Clsn	0.91 (0.08)		nd		1.56 (0.30)		2.21 (0.07)		1.28 (0.10)	

Table 4-5b. K- and Na-alkali feldspar-glass compositional pairs (continued)

Run	K-alkali feldspar, beryl-saturated				Na-alkali feldspar, Trace Be Content		Na-alkali feldspar, beryl-saturated	
	BeP-76		BeP-12		BeP-35		BeP-32	
Mixture	SP-Mus3-Be	direct	HG-Or-Be		HG-Ab-C		HG-Ab-Be	
Prec. Path/Duration (d)	740-F (1)	syn	800-F (6)		750-F (21)		750-F (21)	
Final Path/Duration (d)	680-R (31)		750-R (30)		700-R (28)		700-R (28)	
Crystalline Products	Kfs,Cor,Bi,Ml,(Mus),(Phn)		Kfs, (Phn)		Ab-Afs		Ab-Afs, (Phn)	
Analysis of	K-Afs glass		K-Afs glass		Na-Afs glass		Na-Afs glass	
No. analyses, QEPMA	11	10	19	12	13	10	17	10
No. analyses, SIMS	1	1	1	3	1	1	1	3
Measure of precision	se	sd	se	sd	se	sd	se	sd
wt %								
SiO ₂	64.57 (0.28)	70.89 (0.81)	62.40 (0.09)	68.90 (1.33)	67.64 (0.25)	70.76 (1.11)	67.01 (0.10)	72.10 (0.53)
TiO ₂	0.01 (0.00)	0.02 (0.02)	0.01 (0.00)	0.01 (0.01)	0.01 (0.01)	0.02 (0.01)	0.01 (0.01)	0.01 (0.01)
B ₂ O ₃ (ppm) ¹	619.36 -	78.15 -	8.10 -	24.93 (0.96)	18.912 -	54.752 -	2.705 -	46.00 (0.26)
Al ₂ O ₃	19.26 (0.09)	13.02 (0.25)	19.45 (0.06)	12.27 (0.35)	19.49 (0.16)	13.00 (0.32)	20.06 (0.23)	12.63 (0.33)
FeO	0.06 (0.01)	0.23 (0.02)	0.02 (0.00)	0.03 (0.01)	0.06 (0.01)	0.28 (0.03)	0.01 (0.00)	0.02 (0.01)
MnO	0.01 (0.00)	0.01 (0.01)	0.00	0.01 (0.01)	0.00	0.00	0.01 (0.00)	0.01 (0.01)
MgO	0.01 (0.00)	0.06 (0.01)	0.00	0.00	0.00	0.05 (0.01)	0.00	0.00
NiO	0.00	nd	0.00	nd	0.00	nd	0.01 (0.00)	nd
ZnO	0.01 (0.00)	nd	nd	nd	nd	nd	nd	nd
BeO (ppm) ¹	67.48 -	383.95 -	274.42 -	2002.86 (45.25)	5.971 -	21.358 -	190.113 -	#####
CaO	0.01 (0.00)	0.02 (0.03)	0.00	0.05 (0.02)	0.13 (0.01)	0.18 (0.03)	0.11 (0.01)	0.17 (0.05)
BaO	nd	0.01 (0.01)	3.33 (0.08)	0.15 (0.04)	0.24 (0.07)	0.00 (0.01)	0.33 (0.03)	0.02 (0.03)
Li ₂ O (ppm) ¹	45.77 -	727.38 -	2.07 -	12.98 (1.25)	41.930 -	#####	6.415 -	44.28 (0.05)
Na ₂ O	3.31 (0.05)	3.56 (0.11)	1.89 (0.01)	3.39 (0.10)	9.03 (0.11)	4.31 (0.06)	9.43 (0.10)	4.58 (0.14)
K ₂ O	11.83 (0.05)	4.25 (0.06)	12.55 (0.05)	5.72 (0.13)	3.37 (0.12)	3.77 (0.12)	2.24 (0.15)	3.62 (0.11)
Rb ₂ O (ppm) ¹	1197.39 -	213.78 -	117.94 -	162.34 (0.30)	42.969 -	#####	4.396 -	84.11 (2.29)
Cs ₂ O (ppm) ¹	24.51 -	8.06 -	2.91 -	11.68 (0.79)	7.505 -	10.296 -	3.340 -	35.45 (0.47)
P ₂ O ₅	nd	0.05 (0.03)	nd	0.02 (0.01)	nd	0.11 (0.03)	nd	0.09 (0.03)
F	0.05 (0.02)	0.18 (0.05)	0.02 (0.01)	0.05 (0.04)	0.03 (0.01)	0.05 (0.03)	0.04 (0.02)	0.01 (0.02)
Cl	0.00	0.00	nd	0.01 (0.00)	nd	0.01 (0.00)	nd	0.01 (0.01)
O=F	-0.02	-0.07	-0.01	-0.02	-0.01	-0.02	-0.02	-0.01
O=Cl	0.00	0.00	0.00	0.00	0.00	0.00	0.00	0.00
total	99.32 (0.26)	92.37 (0.58)	99.72 (0.20)	90.80 (1.66)	100.01 (0.80)	92.54 (1.25)	99.25 (0.64)	93.42 (0.73)
H ₂ O by diff		7.63		9.20		7.46		8.58
ASI		1.21 (0.03)		1.03 (0.03)		1.13 (0.03)		1.07 (0.04)
D-B Afs / MELT	7.92		0.32		0.35		0.06	
D-Mn Afs / MELT								
D-Be Afs / MELT	0.18		0.14		0.28		0.14	
D-Ca Afs / MELT	0.40 0.59				0.78 (0.14)		0.64 (0.19)	
D-Li Afs / MELT	0.06		0.18		0.33		0.14	
D-Rb Afs / MELT	5.60		0.73		0.37		0.05	
D-Cs Afs / MELT	3.04		0.25		0.73		0.09	
structural cations/18O								
Si	2.96 (0.02)		2.93 (0.01)		2.99 (0.02)		2.97 (0.02)	
Al	1.04 (0.01)		1.08 (0.00)		1.02 (0.01)		1.05 (0.01)	
Li	0.00		0.00		0.00		0.00	
Na	0.29 (0.00)		0.17 (0.00)		0.77 (0.01)		0.81 (0.01)	
K	0.69 (0.00)		0.75 (0.00)		0.19 (0.01)		0.13 (0.01)	
Rb	0.00		0.00		0.00		0.00	
Ca	0.00		0.00		0.01 (0.00)		0.01 (0.00)	
Ba	nd		0.06 (0.00)		0.00 (0.00)		0.01 (0.00)	
total	4.99 (0.02)		4.99 (0.01)		4.98 (0.03)		4.97 (0.03)	
mol% An	0.04 (0.00)		0.02 (0.00)		0.61 (0.01)		0.53 (0.01)	
mol% Ab	29.75 (0.25)		17.46 (0.08)		79.43 (1.08)		85.49 (1.36)	
mol% Or	69.85 (0.58)		78.27 (0.35)		19.52 (0.27)		13.38 (0.21)	
mol% Clsn	-		6.21 (0.15)		0.43 (0.13)		0.60 (0.06)	

Table 4-5c. Albite-glass and andesine-glass compositional pairs

Run	albite, Low Be Contents				albite, beryl-saturated				andesine, Low Be Contents				andesine, beryl-saturated			
	BeP-36		glass		BeP-33		glass		BeP-56		glass		BeP-60		glass	
Mixture	HG-Ab-C				HG-Ab-Be				SP-Crd1-C				SP-Crd1-C			
Prec. Path/Duration (d)	800-F (13)				800-F (13)				700-F (27)				700-F (27)			
Final Path/Duration (d)	750-R (21)				750-R (21)				Crd,Pl,Mt,Bt,Qtz				Crd,Qtz,Pl,Bt,Mt			
Crystalline Products	Ab				Ab, (Phn)				Crd,Pl,Mt,Bt,Qtz				Crd,Qtz,Pl,Bt,Mt			
Composition of	Ab	glass			Ab	glass			An32	glass	An31	glass	An31	glass		
No. analyses, QEPMA	14	10			10	10			9	11	19	10	9	11		
No. analyses, SIMS	2	1			1	3			2	2	3	3	2	2		
Measure of precision	sd	sd			se	sd			se	sd	se	sd	se	sd		
wt %																
SiO ₂	67.12 (0.40)	65.87 (0.89)			67.70 (0.20)	67.07 (1.07)			59.11 (0.32)	70.95 (0.60)	61.13 (0.66)	70.83 (1.04)	61.60 (0.40)	71.45 (0.56)		
TiO ₂	0.01 (0.01)	0.02 (0.02)			0.01 (0.00)	0.00 (0.01)			0.01 (0.01)	0.05 (0.01)	0.01 (0.01)	0.01 (0.01)	0.01 (0.01)	0.05 (0.02)		
B ₂ O ₃ (ppm) ¹	1.559 (0.26)	77.001 -			45.530 -	43.54 -			78.99 (1.48)	92.68 (2.42)	14.32 (0.70)	99.83 (0.77)	92.16 (2.64)	95.32 (0.58)		
Al ₂ O ₃	19.95 (0.27)	15.26 (0.44)			20.18 (0.13)	14.59 (0.32)			24.99 (0.10)	12.80 (0.25)	24.38 (0.49)	12.12 (0.18)	24.45 (0.14)	12.14 (0.13)		
FeO	0.08 (0.01)	0.25 (0.02)			0.01 (0.00)	0.03 (0.01)			0.20 (0.02)	0.62 (0.05)	0.21 (0.02)	0.36 (0.03)	0.29 (0.03)	0.57 (0.03)		
MnO	0.00	0.01 (0.01)			0.01 (0.00)	0.01 (0.01)			0.02 (0.01)	0.09 (0.01)	0.03 (0.01)	0.10 (0.01)	0.01 (0.01)	0.06 (0.01)		
MgO	0.00	0.05 (0.00)			0.00	0.00			0.00	0.21 (0.01)	0.02 (0.01)	0.15 (0.02)	0.00	0.15 (0.01)		
NiO	0.01 (0.00)	nd			0.01 (0.00)	nd			0.01 (0.01)	nd	0.00	nd	0.00	nd		
BeO (ppm) ¹	1.108 (0.01)	10.939 -			1249.08 -	##### -			2.45 (0.67)	1.45 (0.07)	1.19 (0.29)	0.60 (0.05)	889.28 (2.97)	##### (11.10)		
CaO	0.30 (0.03)	0.15 (0.02)			0.18 (0.02)	0.10 (0.03)			6.30 (0.10)	0.85 (0.04)	6.26 (0.23)	0.61 (0.09)	6.04 (0.06)	0.62 (0.08)		
BaO	0.30 (0.05)	0.04 (0.03)			0.14 (0.03)	0.04 (0.03)			0.01 (0.01)	0.06 (0.03)	0.03 (0.02)	nd	0.03 (0.04)	0.04 (0.03)		
Li ₂ O (ppm) ¹	12.315 (0.31)	##### -			40.090 -	42.10 -			379.30 (1.14)	451.82 (9.00)	116.08 (4.70)	408.56 (8.00)	331.84 (#####)	435.90 (1.31)		
Na ₂ O	10.50 (0.10)	6.37 (0.13)			10.83 (0.04)	6.63 (0.18)			7.35 (0.08)	3.21 (0.10)	7.49 (0.20)	3.04 (0.11)	7.55 (0.02)	3.27 (0.15)		
K ₂ O	1.11 (0.07)	2.97 (0.06)			0.73 (0.04)	2.39 (0.07)			0.35 (0.02)	3.31 (0.10)	0.53 (0.07)	3.61 (0.10)	0.48 (0.04)	3.68 (0.16)		
Rb ₂ O (ppm) ¹	2.924 (0.01)	80.920 -			41.130 -	49.76 -			90.31 (1.13)	104.33 (3.01)	7.66 (0.01)	134.08 (5.00)	96.00 (2.20)	114.46 (0.89)		
Cs ₂ O (ppm) ¹	0.000 -	17.456 -			19.100 -	27.69 -			7.91 (2.47)	8.75 (0.00)	1.88 -	10.60 (2.00)	10.89 (0.59)	8.43 (0.39)		
P ₂ O ₅	nd	0.10 (0.02)			nd	0.12 (0.08)			nd	0.12 (0.05)	nd	0.04 (0.03)	nd	0.11 (0.07)		
F	0.02 (0.01)	0.02 (0.02)			0.02 (0.01)	0.05 (0.04)			0.02 (0.02)	0.18 (0.04)	0.02 (0.01)	0.21 (0.05)	0.00	0.22 (0.07)		
Cl	nd	0.01 (0.01)			nd	0.01 (0.00)			nd	0.01 (0.00)	0.00	0.00	nd	0.01 (0.01)		
O=F	-0.01	-0.01			-0.01	-0.02			-0.01	-0.08	-0.01	-0.09	0.00	-0.09		
O=Cl	-0.002	0.00				0.00			0.00	0.00	0.00	0.00				
total	99.37 (0.57)	91.13 (1.29)			99.74 (0.64)	91.37 (1.26)			98.42 (0.34)	92.45 (0.83)	100.12 (0.40)	91.06 (1.19)	100.62 (0.59)	92.65 (0.64)		
H ₂ O by diff		8.87				8.63				7.65		8.94		7.35		
ASI		1.09 (0.03)				1.07 (0.04)				1.21 (0.03)		1.19 (0.03)		1.10 (0.03)		
D-B Ab / MELT	0.02				1.05				0.85 (0.03)		0.14 (0.01)		0.97			
D-Mn Ab / MELT	-				-				0.26 (0.09)		0.35 (0.08)		0.21 (0.14)			
D-Be Ab / MELT	0.10				0.37				1.69 (0.47)		1.99 (0.51)		0.89			
D-Ca Ab / MELT	2.00 (0.37)				1.80 (0.58)				7.41 (0.37)		10.26 (1.56)		6.57 (0.57)			
D-Li Ab / MELT	0.11				0.95				0.84 (0.02)		0.28 (0.01)		0.76			
D-Rb Ab / MELT	0.04				0.83				0.87 (0.03)		0.06 (0.00)		0.84			
D-Cs Ab / MELT	0.00				0.69				0.90 (0.28)		0.18		1.29			
structural cations/18O																
Si	2.97 (0.02)				2.71 (0.02)				2.67 (0.02)		2.72 (0.03)		2.72 (0.02)			
Al	1.04 (0.02)				0.95 (0.01)				1.33 (0.01)		1.28 (0.03)		1.27 (0.01)			
Li	0.00				0.00				0.01		0.00		0.01			
Na	0.90 (0.01)				0.83 (0.01)				0.64 (0.01)		0.65 (0.02)		0.65 (0.00)			
K	0.08 (0.00)				0.04 (0.00)				0.02 (0.00)		0.03 (0.00)		0.03 (0.00)			
Rb	0.00				0.00				0.00		0.00		0.00			
Ca	0.01 (0.00)				0.01 (0.00)				0.31 (0.01)		0.30 (0.01)		0.29 (0.00)			
Ba	0.01 (0.00)				0.00				0.00 (0.00)		0.00 (0.00)		0.00 (0.00)			
total	4.99 (0.03)				4.54 (0.02)				4.98 (0.02)		4.97 (0.04)		4.96 (0.03)			
mol% An	1.43 (0.03)				0.89 (0.01)				31.47 (0.29)		30.59 (0.77)		29.77 (0.39)			
mol% Ab	91.69 (2.27)				94.59 (1.18)				66.40 (0.61)		66.25 (1.66)		67.36 (0.88)			
mol% Or	6.35 (0.11)				4.27 (0.05)				2.09 (0.02)		3.11 (0.08)		2.79 (0.04)			
mol% Clsn	0.52 (0.10)				0.25 (0.00)				0.02 (0.01)		0.05 (0.03)		0.06 (0.06)			

Table 4-6. Quartz-glass pairs

Run	Low Be Contents		High Be Contents (beryl-saturated)			
	BeP-40		Be-71 ^a		Be-75 ^a	
Mixture	HG-Qtz-C					
Prec. Path/Duration (d)	850-F (6)		800-F (6)		850-F (21)	
Final Path/Duration (d)	800-R (14)		750-R (30)		800-R (36)	
Crystalline Products	Qtz		Qtz, Brl, Cbr		Qtz, Brl, Cbr	
Analysis of	Qtz	glass	Qtz	glass ^b	Qtz	glass ^b
No. analyses, QEPMA	10	10	11	12	10	12
No. analyses, SIMS	1	1	2	3	1	2
Measure of precision		se sd	se sd	se sd	se sd	se sd
wt %						
SiO ₂	98.80 (0.34)	77.68 (0.78)	99.31 (0.38)	74.73 (0.43)	99.51 (0.23)	75.86 (0.42)
TiO ₂	0.01 (0.00)	0.02 (0.02)	0.00 (0.00)	nd	0.01 (0.00)	nd
B ₂ O ₃ (ppm) ¹	6.31 -	23.35 -	4.73 -	nd	2.13 -	nd
Al ₂ O ₃	0.08 (0.01)	9.66 (0.24)	0.16 (0.01)	11.69 (0.18)	0.07 (0.03)	10.81 (0.10)
FeO	0.01 (0.01)	0.26 (0.01)	0.00	nd	0.00	nd
MnO	0.01 (0.00)	0.01 (0.01)	0.00	nd	0.00	nd
MgO	0.00	0.06 (0.01)	0.00	nd	0.00	nd
NiO	0.01 (0.00)	nd (0.04)	0.00	nd	0.01 (0.00)	nd
ZnO	0.02 (0.02)	nd	nd	nd	nd	nd
BeO (ppm) ¹	0.96 -	3.95 -	78.90 -	452 (13)	70.59 -	982 (6)
CaO	0.01 (0.00)	0.17 (0.04)	0.00	0.03 (0.01)	0.00	0.02 (0.02)
BaO	0.01 (0.00)	0.06 (0.04)	0.01 (0.01)	nd	0.02 (0.01)	nd
Li ₂ O (ppm) ¹	6.16 -	67.74 -	0.77 -	nd	1.83 -	nd
Na ₂ O	0.01 (0.00)	2.76 (0.11)	0.01 (0.01)	3.16 (0.12)	0.02 (0.01)	2.78 (0.07)
K ₂ O	0.01 (0.00)	3.68 (0.11)	0.01 (0.00)	3.56 (0.12)	0.01 (0.00)	3.11 (0.08)
Rb ₂ O (ppm) ¹	17.39 -	72.22 -	1.72 -	nd	3.93 -	nd
Cs ₂ O (ppm) ¹	0.66 -	7.06 -	1.90 -	nd	3.63 -	nd
P ₂ O ₅	nd	0.10 (0.04)	nd	nd	nd	nd
F	0.05 (0.02)	0.06 (0.04)	0.07 (0.05)	nd	0.03 (0.01)	nd
Cl	0.00	0.01 (0.00)	0.00	nd	0.01 (0.00)	nd
O=F	-0.02	-0.03	-0.03		-0.01	
O=Cl	0.00	0.00	0.00		0.00	
total	99.00 (0.30)	94.51 (0.58)	99.57 (0.37)	93.19 (1.66)	99.67 (0.21)	92.67 (0.68)
H ₂ O by diff		5.49		6.81		7.33
ASI		1.09 (0.03)		1.28 (0.03)		1.35 (0.02)
D-B Qtz / MELT	0.27					
D-Mn Qtz / MELT	0.85 (1.12)					
D-Be Qtz / MELT	0.24		0.17		0.07	
D-Ca Qtz / MELT	0.04 (0.02)					
D-Li Qtz / MELT	0.09					
D-Rb Qtz / MELT	0.24					
D-Cs Qtz / MELT	0.09					

^a from Evensen et al., 1999^b major element glass chemistry taken from Evensen et al., 1999

Table 4-7a. Dark mica-glass pairs

Run Mixture Prec. Path/Duration (d) Final Path/Duration (d) Crystalline Products	Low Be Contents													
	BeP-60 SP-Crd-1		Run 6+6*				BeP-58 SP-Crd-1		Run 5+15*		BeP-47 SP-Mus2-C 730-F (22) 700-R (29)		BeP-20 SP-Crd1-C 850-F (8) 700-R (28)	
	700-F (26) Crd,Bt,Mt,Qtz,Pl		700-F		800-F (14) Crd,Bt,Mt		750-F (21) 850-R (36)		Kfs,Cor,Mus,Als,Bt,Mt		700-R (28)		Crd,Bt,Mt	
Analysis of	Bt	glass	Bt	glass	Bt	glass	Bt	glass	Bt	glass	Bt	glass	Bt	glass
No. analyses, OEPMA	8	10	8	7	19	11	11	20	8	8	9	8	9	8
No. analyses, SIMS	2	3	2	2	1	2	2	2	2	1	1	2	1	2
Measure of precision	se	sd	se	sd	se	sd	se	sd	se	sd	se	sd	se	sd
wt %														
SiO ₂	40.42 (1.56)	70.83 (1.04)	35.5 (1.50)	62.00 (1.33)	62.40 (0.09)	70.01 (0.53)	62.64 (0.35)	63.94 (0.20)	41.12 (2.81)	69.12 (0.72)	63.03 (0.36)	70.82 (0.83)	63.03 (0.36)	70.82 (0.83)
TiO ₂	2.01 (0.16)	0.01 (0.01)	1.9 (0.10)	0.01 (0.01)	0.01 (0.00)	0.12 (0.02)	0.02 (8.12)	0.09 (0.01)	0.51 (0.05)	0.03 (0.01)	0.01 (0.00)	0.04 (0.01)	0.01 (0.00)	0.04 (0.01)
B ₂ O ₃ (ppm) ¹	41.798 (6.86)	99.83 (0.77)	110.3 (6.37)	231.08 (1.00)	3.70 -	79.54 (0.32)	131.80 (5.70)	298.25 (7.26)	60.86 (10.08)	164.24 -	54.49 -	123.80 (1.93)	54.49 -	123.80 (1.93)
Al ₂ O ₃	12.09 (0.37)	12.12 (0.18)	22.5 (0.55)	18.00 (0.35)	19.45 (0.06)	13.12 (0.25)	18.77 (0.27)	15.84 (0)	20.89 (0.49)	13.76 (0.30)	18.47 (0.11)	12.47 (0.18)	18.47 (0.11)	12.47 (0.18)
FeO	13.47 (1.98)	(0.03)	15.7 (0.74)	0.88 (0.01)	0.02 (0.00)	0.81 (0.05)	0.12 (0.00)	0.74 (0.06)	9.48 (0.70)	0.37 (0.02)	0.09 (0.01)	0.87 (0.13)	0.09 (0.01)	0.87 (0.13)
MnO	0.55 (0.13)	0.10 (0.01)	0.3 (0.02)	0.01 (0.01)	0.00 (0.00)	0.11 (0.01)	0.01 (0.00)	0.07 (0.00)	0.09 (0.01)	0.04 (0.01)	0.00 (0.00)	0.09 (0.01)	0.00 (0.00)	0.09 (0.01)
MgO	16.40 (1.20)	0.15 (0.02)	6.7 (0.41)	0.00 (0.00)	0.00 (0.00)	0.52 (0.01)	0.01 (0.00)	0.18 (0.02)	12.47 (1.00)	0.19 (0.01)	0.01 (0.00)	0.22 (0.01)	0.01 (0.00)	0.22 (0.01)
NiO	0.01 (0.02)	nd	0.6 (0.12)	nd	0.00 (0.00)	nd	0.01 (0.00)	0.04 (0.03)	0.47 (0.06)	nd	0.01 (0.00)	nd	0.01 (0.00)	nd
ZnO	0.020 (0.02)	nd	nd	nd	nd	nd	nd	nd	0.01 (0.01)	nd	nd	nd	nd	nd
BeO (ppm) ¹	0.279 (0.02)	0.60 (0.05)	22.5 (0.86)	53.41 (2.20)	2.33 -	5.00 (0.20)	28.73 (1.05)	68.70 (0.250)	6.82 (0.20)	13.76 -	2.62 -	3390 (0.136)	6.82 (0.20)	13.76 -
CaO	0.03 (0.02)	0.61 (0.09)	0.0 (0.04)	0.05 (0.02)	0.00 (0.00)	1.06 (0.09)	0.02 (0.00)	0.63 (0.01)	0.02 (0.01)	0.24 (0.03)	0.02 (0.00)	0.66 (0.05)	0.02 (0.00)	0.66 (0.05)
BaO	0.10 (0.04)	nd	3.3 (0.33)	0.27 (0.04)	3.33 (0.08)	0.05 (0.03)	0.52 (0.01)	0.27 (0.03)	0.25 (0.03)	0.02 (0.02)	0.94 (0.10)	0.05 (0.05)	0.25 (0.03)	0.02 (0.02)
Li ₂ O (ppm) ¹	188.189 (3.26)	408.56 (8.03)	3153.3 (139)	4720.40 (158.02)	72.35 -	434.39 (3.23)	5088.59 (10.03)	7182.40 (31)	194.05 (8.12)	328.59 -	121.84 -	383.37 (2.02)	194.05 (8.12)	328.59 -
Na ₂ O	0.27 (0.03)	3.04 (0.11)	0.4 (0.04)	2.20 (0.10)	1.89 (0.01)	3.14 (0.12)	2.30 (0.04)	1.95 (0.02)	0.51 (0.11)	3.18 (0.11)	2.18 (0.05)	3.30 (0.09)	0.51 (0.11)	3.18 (0.11)
K ₂ O	9.07 (0.26)	3.61 (0.10)	7.8 (0.31)	3.30 (0.13)	12.55 (0.05)	3.36 (0.15)	12.91 (0.08)	3.28 (0.040)	7.95 (0.39)	5.18 (0.20)	12.09 (0.10)	2.77 (0.06)	7.95 (0.39)	5.18 (0.20)
Rb ₂ O (ppm) ¹	331.569 (4.55)	134.08 (4.80)	3214.1 (498)	3120.81 (10.02)	358.58 -	109.89 (0.55)	2608.85 (459.98)	4166.39 (12.06)	293.59 (14.6)	243.56 -	378.29 -	101.95 (0.00)	293.59 (14.6)	243.56 -
Ca ₂ O (ppm) ¹	10.803 (2.80)	10.80 (2.12)	2309.4 (61)	4032.61 (100.88)	4.06 -	11.82 (2.00)	4420.28 (161.09)	7777.36 (184)	5.40 (0.83)	9.04 -	48.23 -	10.70 (1.31)	5.40 (0.83)	9.04 -
P ₂ O ₅	nd	0.04 (0.03)	nd	0.02 (0.01)	nd	0.12 (0.03)	nd	0.06 (0.04)	nd	0.06 (0.04)	nd	0.04 (0.02)	nd	0.06 (0.04)
F	2.83 (0.28)	0.21 (0.05)	2.7 (0.12)	0.05 (0.04)	0.02 (0.01)	0.19 (0.07)	0.04 (0.02)	1.74 (0.04)	0.88 (0.10)	0.08 (0.07)	0.05 (0.03)	0.18 (0.07)	0.88 (0.10)	0.08 (0.07)
Cl	0.05 (0.01)	0.00	0.0 (0.00)	0.01 (0.00)	nd	0.01 (0.01)	nd	nd	0.01 (0.00)	0.01 (0.01)	nd	0.01 (0.01)	0.01 (0.00)	0.01 (0.01)
O=F	-1.19 (0.12)	-0.09	-1.1 (0.05)	-0.02 (0.02)	-0.01	-0.08	-0.02 (0.01)	-0.04	-0.37 (0.04)	-0.03 (0.03)	-0.02 (0.01)	-0.07 (0.03)	-0.37 (0.04)	-0.03 (0.03)
O=Cl	-0.01 (0.00)	0.00	0.0 (0.00)	0.00 (0.00)	0.00	0.00	0.00	0.00	0.00 (0.00)	0.00 (0.00)	0.00 (0.00)	0.00 (0.00)	0.00 (0.00)	0.00 (0.00)
total	96.171 (0.37)	90.605 (1.19)	97.1 (0.960)	85.99 (1.66)	99.72 (0.20)	92.58 (0.64)	98.46 (0.60)	90.85 (1)	94.34 (0.78)	92.33 (0.51)	97.81 (0.64)	91.605 (1)	94.34 (0.78)	92.33 (0.51)
H ₂ O by diff	3.829	9.30	2.9	1.76 (0.03)	0.28	7.42	1.54	9.15	5.88	7.67	2.19	8.395	5.88	7.67
ASI	67.8 (1.2)	1.19 (0.03)	42.7 (2.2)	1.76 (0.03)	20.5 (0.8)	1.21 (0.05)	74.8 (0.5)	1.45 (0.02)	89.9 (1.4)	1.21 (0.03)	13.6 (0.8)	1.21 (0.02)	89.9 (1.4)	1.21 (0.03)
Mg#	0.42 (0.07)		0.48 (0.04)		0.05		0.44 (0.02)		0.37		0.44		0.44 (0.02)	
D-Bt Bt / MELT	3.84 (0.97)		78.30 (75.78)		0.01 (0.00)		0.04 (0.01)		0.47 (0.13)		0.01 (0.01)		0.47 (0.13)	
D-Mn Bt / MELT	0.47 (0.05)		0.42 (0.02)		0.47		0.42 (0.02)		0.80		0.67		0.42 (0.02)	
D-Ca Bt / MELT	0.04 (0.04)		0.45 (0.78)		0.00 (0.00)		0.02 (0.00)		0.10 (0.05)		0.02 (0.00)		0.02 (0.00)	
D-Li Bt / MELT	0.46 (0.01)		0.87 (0.04)		0.17		0.71 (0.00)		0.59		0.32		0.71 (0.00)	
D-Rb Bt / MELT	2.47 (0.09)		1.03 (0.16)		3.27		0.63 (0.11)		1.21		3.69		0.63 (0.11)	
D-Cs Bt / MELT	1.02 (0.32)		0.57 (0.02)		0.34		0.57 (0.02)		0.60		4.51		0.57 (0.02)	
structural cations / 12 O														
Si	2.84 (0.11)		2.81 (0.12)		2.73 (0.01)		2.99 (0.02)		2.91 (0.19)		2.60 (0.02)		2.91 (0.19)	
Ti	0.11 (0.01)		0.11 (0.01)		0.10 (0.02)		0.06 (40.64)		0.03 (0.00)		0.07 (0.02)		0.03 (0.00)	
Al	1.00 (0.03)		1.06 (0.03)		1.17 (0.00)		0.92 (0.01)		1.06 (0.03)		1.23 (0.01)		1.06 (0.03)	
^{IV} total	3.94 (0.11)		4.00 (0.13)		4.00 (0.02)		3.99 (40.64)		4.00 (0.19)		4.00 (0.03)		4.00 (0.19)	
Al	0.00		0.00		0.14		0.12		0.68 (0.01)		0.03		0.68 (0.01)	
Fe	0.78 (0.12)		1.04 (0.05)		0.72 (0.08)		0.57 (0.02)		0.56 (0.04)		0.48 (0.03)		0.57 (0.02)	
Mn	0.03 (0.01)		0.02 (0.00)		0.02 (0.00)		0.02 (0.01)		0.01 (0.00)		0.02 (0.01)		0.02 (0.01)	
Mg	1.72 (0.13)		0.79 (0.05)		1.48 (0.14)		1.74 (0.24)		1.32 (0.11)		1.83 (0.19)		1.74 (0.24)	
Li	0.01		0.10		0.02		0.01		0.01		0.01		0.01	
^{IV} total	2.55 (0.17)		1.95 (0.07)		2.38 (0.15)		2.46 (0.24)		2.57 (0.11)		2.36 (0.19)		2.46 (0.24)	
Ba	0.00 (0.00)		0.10 (0.01)		0.01 (0.00)		0.00 (0.00)		0.01 (0.00)		0.01 (0.00)		0.01 (0.00)	
Na	0.04 (0.00)		0.06 (0.01)		0.07 (0.00)		0.06 (0.00)		0.07 (0.01)		0.09 (0.00)		0.06 (0.00)	
K	0.81 (0.02)		0.79 (0.03)		0.80 (0.00)		0.67 (0.01)		0.72 (0.04)		0.76 (0.01)		0.67 (0.01)	
Rb	0.00		0.02		0.00		0.00		0.00		0.00		0.00	
Cs	0.00		0.01		0.00		0.00		0.00		0.00		0.00	
^{IV} total	0.85 (0.02)		0.97 (0.03)		0.87 (0.00)		0.74 (0.01)		0.80 (0.04)		0.86 (0.01)		0.74 (0.01)	
total cations	0.85 (0.21)		6.92 (0.15)		7.26 (0.15)		7.18 (40.65)		7.36 (0.22)		7.22 (0.20)		7.18 (40.65)	
F	0.83 (0.08)		0.669 (0.31)		0.67 (2.76)		0.57 (3.58)		0.20 (0.85)		0.79 (5.10)		0.57 (3.58)	

* from Icenhaver and London 1995

Table 4-7a (continued). Dark mica-glass pairs

Run	Low Be Contents					High Be Contents (beryl saturated)					
	BeP-45		BeP-46			BeP-41		BeP-54		BeP-43	
Mixture	SP-Bi2-C		SP-Bi2-C			SP-Bi2-Be		SP-Crd1-Be		SP-Bi2-Be	
Proc. Path/Duration (d)	800-F (15)		850-F (8)			750-F (21)		750-F (27)		850-F (8)	
Final Path/Duration (d)	750-R (23)		800-R (14)			700-R (28)				800-R (14)	
Crystalline Products	Crd,Bi,Mt		Bi,Mt			Crd,Bi,Bt,Mt		Crd,Bi,Bt,Mt		Crd,Bi,Bt,Mt	
Analysis of	Bi	glass	Bi	glass	Bi	glass	Bi	glass	Bi	glass	
No. analyses, OEPMA	10	10	12	10	14	11	19	12	19	10	
No. analyses, SIMS	1	1	1	1	1	2	1	2	1	1	
Measure of precision	se	sd	se	sd	se	sd	se	sd	se	sd	
wt %											
SiO ₂	40.14 (0.85)	70.58 (0.65)	45.79 (1.89)	69.54 (0.80)	38.99 (0.52)	68.92 (0.49)	43.93 (1.87)	70.32 (0.41)	40.87 (0.91)	70.04 (0.33)	
TiO ₂	1.64 (0.09)	0.07 (0.02)	1.29 (0.06)	0.17 (0.03)	1.98 (0.04)	0.08 (0.02)	1.57 (0.19)	0.03 (0.02)	1.48 (0.05)	0.16 (0.03)	
B ₂ O ₃ (ppm) ¹	84.44 -	149.42 -	74.26 -	99.21 -	213.05 -	98.05 (1.77)	70.97 -	88.55 (3.00)	138.24 -	131.70 -	
Al ₂ O ₃	16.15 (0.88)	13.82 (0.20)	15.91 (0.46)	13.78 (0.21)	15.89 (1.32)	13.35 (0.07)	12.97 (0.83)	12.73 (0.14)	16.18 (0.13)	13.99 (0.24)	
FeO	8.73 (0.26)	0.57 (0.04)	8.89 (0.50)	0.79 (0.04)	12.26 (0.82)	0.44 (0.03)	10.03 (1.96)	0.57 (0.04)	8.58 (0.35)	0.78 (0.04)	
MnO	0.29 (0.01)	0.15 (0.01)	0.27 (0.01)	0.17 (0.02)	0.36 (0.02)	0.07 (0.02)	0.30 (0.03)	0.09 (0.02)	0.28 (0.01)	0.13 (0.01)	
MgO	17.87 (0.23)	0.35 (0.01)	15.93 (0.71)	0.42 (0.01)	14.19 (0.69)	0.10 (0.01)	17.19 (1.10)	0.23 (0.01)	18.51 (0.38)	0.33 (0.01)	
NiO	0.09 (0.02)	nd	0.10 (0.02)	nd	0.27 (0.24)	nd	0.01 (0.00)	nd	0.20 (0.06)	nd	
ZnO	nd	nd	nd	nd	nd	nd	nd	nd	nd	nd	
BeO (ppm) ¹	4.67 -	12.10 -	7.14 -	12.77 -	90.03 -	511.10 (2.87)	821.17 -	1523.02 (9.80)	147.33 -	1890.58 -	
CaO	0.00 (0.00)	0.19 (0.03)	0.02 (0.00)	0.20 (0.07)	0.01 (0.00)	0.18 (0.09)	0.14 (0.06)	1.04 (0.10)	0.00 (0.00)	0.24 (0.08)	
BaO	0.24 (0.04)	0.02 (0.02)	0.26 (0.04)	0.04 (0.02)	0.33 (0.06)	0.05 (0.05)	0.11 (0.03)	0.05 (0.03)	0.40 (0.03)	0.06 (0.04)	
Li ₂ O (ppm) ¹	371.56 -	628.79 -	520.34 -	856.42 -	628.06 -	613.05 (22.39)	233.12 -	405.33 (11.41)	458.89 -	802.09 -	
Na ₂ O	0.59 (0.04)	3.29 (0.18)	0.74 (0.03)	3.31 (0.12)	0.49 (0.09)	3.19 (0.07)	0.47 (0.08)	3.25 (0.12)	0.68 (0.02)	3.24 (0.14)	
K ₂ O	8.92 (0.11)	4.14 (0.11)	7.83 (0.23)	4.31 (0.11)	8.92 (0.20)	4.60 (0.09)	7.73 (0.71)	3.72 (0.12)	9.02 (0.06)	4.80 (0.14)	
Rb ₂ O (ppm) ¹	188.73 -	182.88 -	189.76 -	151.00 -	418.13 -	153.21 (3.55)	159.48 -	125.65 (12.22)	441.67 -	185.89 -	
Cs ₂ O (ppm) ¹	8.08 -	12.88 -	13.74 -	8.65 -	41.26 -	34.99 (2.00)	14.13 -	9.17 (2.62)	59.49 -	38.42 -	
P ₂ O ₅	nd	0.09 (0.02)	nd	0.10 (0.04)	nd	0.06 (0.03)	nd	0.09 (0.03)	nd	0.08 (0.02)	
F	3.44 (0.17)	0.47 (0.07)	3.25 (0.13)	0.54 (0.05)	3.05 (0.20)	0.50 (0.02)	2.65 (0.23)	0.28 (0.07)	3.79 (0.18)	0.86 (0.05)	
Cl	nd	0.01 (0.01)	nd	0.02 (0.01)	nd	0.01 (0.01)	0.03 (0.01)	0.01 (0.01)	nd	0.01 (0.01)	
O=F	-1.45 (0.07)	-0.20 (0.03)	-1.37 (0.06)	-0.23 (0.02)	-1.28 (0.08)	-0.21	-1.12	-0.12	-1.59 (0.16)	-0.28 (0.02)	
O=Cl	0.00 (0.00)	0.00 (0.00)	0.00 (0.00)	0.00 (0.00)	0.00	0.00	-0.01	0.00	0.00 (0.00)	0.00 (0.00)	
total	96.72 (0.18)	93.64 (0.81)	96.99 (0.37)	93.25 (0.85)	95.59 (0.34)	91.46 (0.63)	96.14 (0.69)	92.51 (0.47)	96.33 (0.28)	94.56 (0.53)	
H ₂ O by diff	3.28		3.01		4.41	8.54	3.86	7.49	1.67		
ASI		1.32 (0.03)		1.28 (0.04)		1.24 (0.03)		1.12 (0.03)		1.24 (0.04)	
Mg#	77.9 (0.6)		79.9 (0.7)		66.7 (0.5)		74.8 (14.8)		78.8 (0.6)		
D-B Bi / MELT	0.43		0.75		2.17		0.80		1.05		
D-Mn Bi / MELT	1.91 (0.13)		1.59 (0.21)		5.14 (1.49)		3.36 (0.84)		2.12 (0.23)		
D-Be Bi / MELT	0.39		0.56		0.18		0.41		0.06		
D-Ca Bi / MELT	0.01 (0.01)		0.10 (0.04)		0.05 (0.03)		0.14 (0.06)		0.02 (0.01)		
D-Li Bi / MELT	0.59		0.61		1.02		0.58		0.57		
D-Rb Bi / MELT	0.92		1.26		2.73		1.27		2.38		
D-Cs Bi / MELT	0.63		1.59		1.16		1.54		1.55		
structural cations / 12 O											
Si	2.71 (0.06)		3.00 (0.11)		2.73 (0.04)		2.99 (0.13)		2.69 (0.06)		
Ti	0.06 (0.00)		0.06 (0.00)		0.10 (0.00)		0.08 (0.01)		0.07 (0.00)		
Al	1.21 (0.07)		0.93 (0.02)		1.17 (0.06)		0.92 (0.05)		1.23 (0.01)		
Be	0.00		0.00		0.00		0.01		0.00		
¹¹ B total	4.00 (0.09)		4.00 (0.11)		4.00 (0.10)		4.00 (0.14)		4.00 (0.06)		
Al	0.08 (0.00)		0.30 (0.00)		0.14 (0.01)		0.12 (0.01)		0.03 (0.00)		
Fe	0.48 (0.01)		0.38 (0.03)		0.72 (0.04)		0.57 (0.11)		0.48 (0.02)		
Mn	0.02 (0.00)		0.02 (0.00)		0.02 (0.00)		0.02 (0.00)		0.02 (0.00)		
Mg	1.80 (0.02)		1.56 (0.07)		1.48 (0.07)		1.74 (0.11)		1.83 (0.04)		
Li	0.01		0.01		0.02		0.01		0.01		
¹⁰ B total	2.40 (0.03)		2.26 (0.08)		2.38 (0.08)		2.46 (0.16)		2.36 (0.04)		
Ba	0.01 (0.00)		0.01 (0.00)		0.01 (0.00)		0.00 (0.00)		0.01 (0.00)		
Na	0.08 (0.01)		0.09 (0.00)		0.07 (0.01)		0.06 (0.01)		0.09 (0.00)		
K	0.77 (0.01)		0.66 (0.02)		0.80 (0.02)		0.67 (0.06)		0.78 (0.01)		
Rb	0.00		0.00		0.00		0.00		0.00		
¹⁷ O total	0.85 (0.01)		0.76 (0.02)		0.87 (0.02)		0.74 (0.06)		0.86 (0.01)		
total cations	7.25 (0.10)		7.02 (0.14)		7.26 (0.13)		7.19 (0.22)		7.22 (0.06)		
F	0.74 (0.04)		0.87 (0.03)		0.67 (0.04)		0.57 (0.05)		0.79 (0.03)		

Table 4-7b. White mica-glass pairs

Run	Low Be Contents				High Be Contents (Brl-saturated)			
	BeP-47				BeP-52			
Mixture	SP-Mus2-C				SP-Mus2-Be			
Prec. Path/Duration (d)	730-F (21)				750-F (21)			
Final Path/Duration (d)	700-R (31)				700-R (28)			
Crystalline Products	Kfs,Mus				Kfs,Mus,Als,Cor,Bt,Mt			
Analysis of	Mus		glass		Mus		glass	
		sd		sd		se		sd
No. analyses, QEPMA	8		10		9		8	
No. analyses, SIMS	1		3		1		1	
wt %								
SiO ₂	64.63 (1.35)		72.23 (0.87)		63.03 (0.36)		69.12 (0.72)	
TiO ₂	0.02 (0.01)		0.01 (0.01)		0.01 (0.00)		0.03 (0.01)	
B ₂ O ₃ (ppm) ¹	533.07 -		171.63 -		204.71 -		250.40 -	
Al ₂ O ₃	19.65 (1)		12.86 (0)		18.47 (0)		13.76 (0)	
FeO	0.07 (0.05)		0.21 (0.02)		0.09 (0.01)		0.37 (0.02)	
MnO	0.01 (0.01)		0.01 (0.01)		0.00 (0.00)		0.04 (0.01)	
MgO	0.01 (0.01)		0.03 (0.01)		0.01 (0.00)		0.19 (0.01)	
NiO	0.00 (0.00)		nd		0.01 (0.00)		nd	
ZnO	0.01 (0.01)		nd		nd		nd	
BeO (ppm) ¹	19.43 -		14.38 -		755.02 -		869.44 -	
CaO	0.03 (0.03)		0.02 (0.03)		0.02 (0.00)		0.24 (0.03)	
BaO	nd		0.01 (0.01)		0.94 (0.10)		0.02 (0.02)	
Li ₂ O (ppm) ¹	444.98 -		341.29 -		385.18 -		353.75 -	
Na ₂ O	3.93 (0.230)		3.74 (0.18)		2.16 (0.051)		3.18 (0.11)	
K ₂ O	10.79 (0.35)		4.00 (0.090)		12.98 (0.10)		5.18 (0.202)	
Rb ₂ O (ppm) ¹	224.95 -		254.51 -		316.84 -		359.96 -	
Cs ₂ O (ppm) ¹	7.45 -		9.45 -		35.20 -		42.70 -	
P ₂ O ₅	nd		0.04 (0.02)		nd		0.06 (0.04)	
F	0.03 (0.03)		0.15 (0.07)		0.05 (0.03)		0.08 (0.07)	
Cl	0.01 (0)		0.01 (0)		nd		0.01 (0)	
O=F	-0.01 (0.01)		-0.06 (0.03)		-0.02 (0)		-0.03 (0.03)	
O=Cl	0.00 (0.00)		0.00 (0.00)				0.00 (0.00)	
total	99.30 (0.18)		93.33 (1)		97.92 (0.18)		92.44 (1)	
H ₂ O by diff	0.70				2.08			
ASI			1.21 (0.03)				1.21 (0.03)	
D-B Crd/MELT	3.11				0.82			
D-Mn Crd/MELT								
D-Be Crd/MELT	1.35				0.87			
D-Ca Crd/MELT					0.09 (0.01)			
D-Li Crd/MELT	1.30				1.09			
D-Rb Crd/MELT	0.88				0.88			

D-Cs Crd/MELT	0.79	0.82
structural cations / 12 O		
Si	4.06 (0.09)	4.08 (0.02)
B	0.01	0.00
Be	0.00	0.01
^[4] total	4.06 (0.09)	4.08 (0.02)
Al	1.45 (0.04)	1.41 (0.01)
Fe	0.00	0.01
Li	0.01	0.01
^[6] total	1.46 (0.04)	1.42 (0.01)
Na	0.45 (0.03)	0.27 (0.01)
K	0.87 (0.03)	1.07 (0.01)
Rb	0.00	0.00
Cs	0.00	0.00
^[12] total	1.32 (0.04)	1.34 (0.01)
total cations	6.83 (0.10)	6.85 (0.03)
F	0.01 (0.00)	0.01 (0.01)
mol% Mus	64.36 (4.32)	79.79 (5.35)
mol% Pa	35.64 (2.39)	20.21 (1.35)

Table 4-8a. Experimentally calibrated partition coefficients of Be between rock-forming minerals and silicic melt and their T-dependence.

Mineral	trace Be contents						
	T (°C)						
	650	675	680	700	750	800	850
K-rich alkali feldspar		0.07 -	0.38 -	0.02 -	0.26 -	0.19 -	0.19 -
Na-rich alkali feldspar				0.28 -			
albite					0.10 -		
oligoclase-andesine				1.84 (0.05)			
quartz						0.24 -	
dark mica	0.42 (0.02)			0.54 (0.08)	0.39 -	0.52 (0.02)	
white mica				1.35 -			
cordierite ¹				201.21 (0.28)	153.06 (4.67)	35.04 (2.31)	6.70 -
	beryl saturation						
K-rich alkali feldspar			0.18 -	0.14 -			
Na-rich alkali feldspar				0.14 -			
albite					0.37 -		
oligoclase-andesine				0.89 -			
quartz					0.17 -	0.07 -	
dark mica		0.18 -			0.41 -	0.08 -	
white mica				0.87 -			
cordierite ¹	26.59 (0.43)	19.50 (0.62)		15.11 (0.22)	13.99 (0.45)	15.14 (0.48)	

Table 4-8b. Experimental mineral/mineral partitioning coefficients for

Be in granitic melts

D x/x	T (°C)	<i>trace Be</i>	<i>beryl-saturated</i>			
		700	675	700	750	800
Mus/Kfs		80.96				
Bt/Kfs		29.98				
An ₃₂ /Bt		4.27		15.18		
Mus/Bt		2.70				
Crd/Bt	17.77 - 196.9			255.2	38.59	67.42
Crd/Kfs			767.0			
Crd/An ₃₂		118.6		28.19		

Table 4-9. Partition coefficients for Be from natural systems

Phases	Source	D[Be] Avg (s.d.)	Reference
phenocryst/groundmass of ongonite, Mongolia			Kovalenko et al. (1977)
K-feldspar/groundmass		0.53(0.19)	
albite/groundmass		1.56(1.46)	
Li-"mica"/groundmass		6.11(2.76)	
K-feldspar/albite		0.34	
Li-"mica"/K-feldspar		11.53	
Li-"mica"/albite		3.92	
restite/leucosome Pena Negra, Spain			Bea et al. (1994)
K-feldspar/leucosome		3.05(0.3)	
plagioclase/leucosome		3.13(0.4)	
biotite/leucosome		15.5(0.9)	
garnet/leucosome		3.23(0.25)	
cordierite/leucosome		29.1(2.1)	
quartz monzonite			Beus (1966)
K-feldspar/plagioclase		0.25	
K-feldspar/quartz		2.86	
K-feldspar/biotite		2.00	
biotite/quartz		1.43	
biotite/plagioclase		0.13	
coarse-grained biotite granite			Beus (1966)
K-feldspar/plagioclase		2.5	
K-feldspar/quartz		25	
K-feldspar/biotite		0.5	
biotite/quartz		50	
biotite/plagioclase		5	
muscovite granite			Beus (1966)
muscovite/plagioclase		5	
muscovite/quartz		250	
plagioclase/quartz		50	
coarse-grained "albitized" granite			Beus (1966)
muscovite/feldspar		2.45	

muscovite/quartz	49	
feldspar/quartz	20	
coarse-grained "greisenized"		Beus (1966)
 muscovite granite		
muscovite/feldspar	2	
muscovite/quartz	31	
feldspar/quartz	16	
evolved rhyolitic dike		Raimbault and Burnol (1998)
muscovite/groundmass	0.24	
evolved rhyolitic series		G.Morgan and D.London,
muscovite/biotite	2.10	unpublished data (2001)
cordierite/biotite	200.1 - 514.4	
andalusite/biotite	0.08	

Table 4-10. Reported Be contents of migmatite systems

Pena Negra Complex, central Spain
Data from Bea et al. (1994b)

Migmatite facies	Crd-bearing?	Be (ppmw)			N
		mean	se	range	
mesosome	yes	2.34	0.65	1.13 - 4.75	5
melansome	yes	6.04	1.35	3.51 - 8.10	3
leucosome	yes	1.20	0.10	0.37 - 2.04	6

Table 4-11. Beryllium reservoirs in a schematic pegmatite dike

Temperature	700	600	500	400
Be content of melt (ppmw)	140	60	50	40
Mineral and Mode				
K-feldspar (20%)	27	10	8	6
plagioclase (40%)	258(An ₃₁)	14(An ₁)	12	9
quartz (30%)	34	7	6	5
muscovite (10%)	189	52	44	34
Total Be in RFM:	137	25	12	8
Be in beryl (% total Be)	1%	75%	76%	80%

Pegmatite Class: muscovite beryl rare-element



Table 4-12. Average BeO content of granitic pegmatites

Location	Pegmatite Type (where known)	average Be ppmw	Source
Tanco Manitoba, Canada	complex Li petalite	163	Stilling (1998)
Sparrow Pluton Yellowknife, NWT, Canada	beryl	260	Kretz et al. (1989)
Helen Beryl Black Hills, SD USA	beryl	92	Staatz et al. (1963)
Tin Mountain Black Hills, SD USA	complex Li spodumene	223	Staatz et al. (1963)
Souchon Kamativi mine, Zimbabwe	complex Li lepidolite	202	Gallagher (1975) Rijks and van der Veen (1972)
Augustus near Salisbury, Zimbabwe	complex Li lepidolite	202	Gallagher (1975) Ackerman et al. (1968)
Mistress near Salisbury, Zimbabwe	complex Li lepidolite	432	Gallagher (1975) Ackerman et al. (1968)
Benson 1 Mtoko district, Zimbabwe	complex Li lepidolite	577	Gallagher (1975) Ackerman et al. (1968)
Benson 4 Mtoko district, Zimbabwe	complex Li lepidolite	76	Gallagher (1975) Ackerman et al. (1968)
Benson 2 Mtoko district, Zimbabwe	complex Li lepidolite	36	Gallagher (1975) Ackerman et al. (1968)
Al Hayat Bikita district, Zimbabwe	complex Li spodumene	126	Gallagher (1975) Ackerman et al. (1968)
Bikita Main Bikita district, Zimbabwe	complex Li petalite	180	Gallagher (1975) Ackerman et al. (1968)
Gobi Field East Gobi, Mongolia	complex Li lepidolite	155	Rossovskiy and Matrosov (1974)
Beryl Rose Darwin district, Zimbabwe		151	Gallagher (1975)

Table 4-13. Compositions of the beryllian wallrock alteration assemblage from the Harding Pegmatite, NM, USA

Analysis of	"Be-margarite"	biotite	tourmaline	spessartine
No. crystals analysed	5	4	2	2
No. analyses, QEPMA	11	11	10	11
No. analyses, SIMS	2	2	2	2
wt %	sd	sd	sd	sd
SiO ₂	31.14 (0.15)	42.23 #####	35.81 (0.23)	36.13 (0.04)
TiO ₂	0.08 (0.02)	0.74 #####	0.49 (0.05)	0.04 (0.02)
B ₂ O ₃ (ppm) ^{SIMS}	434 (24)	18 (3)	91260 (24)	7 (4)
Al ₂ O ₃	44.87 (0.49)	18.58 #####	32.23 (0.23)	20.95 (0.04)
FeO	0.16 (0.02)	11.04 #####	9.17 (0.15)	8.22 (0.19)
MnO	0.02 (0.01)	0.44 #####	0.20 (0.04)	32.13 (0.19)
MgO	0.03 (0.00)	9.40 #####	5.62 (0.36)	0.13 (0.01)
NiO	0.01 (0.01)	0.01 #####	0.01 (0.01)	0.01 (0.01)
BeO^{SIMS} (^a = ppmw Be)	3.3072 (0.0482)	^a16.8 (0.3)	^a11.3 (0.6)	^a0.0
CaO	12.76 (0.17)	0.00	1.42 (0.18)	2.20 (0.29)
BaO	0.01 (0.01)	0.05 #####	0.03 (0.03)	0.01 (0.01)
Li ₂ O ^{SIMS} (^a = ppmw)	1.2293 #####	1.99 #####	^a 473.6 #####	^a 39.6 (19.4)
Na ₂ O	0.77 (0.10)	0.18 #####	1.95 (0.05)	0.00
K ₂ O	0.00	9.17 #####	0.03 (0.01)	0.00
Rb ₂ O (ppm) ^{SIMS}	2 (0)	8474 (278)	6 (1)	19 (2)
Cs ₂ O (ppm) ^{SIMS}	3 (0)	2549 (148)	nd	nd
F	1.60 (0.08)	4.72 #####	0.96 (0.07)	0.15 (0.07)
Cl	0.00	0.00	0.00	0.00
O=F	-0.67	-1.99	-0.40	-0.06
total without H ₂ O	95.36 (0.69)	97.67 (0.77)	96.69 (0.50)	99.92 (0.38)
H ₂ O by SIMS	4.76 (0.25)	3.48 (0.37)	3.70 (0.10)	0.40 (0.04)
H ₂ O by diff	4.64	2.33	3.31	0.08
total by SIMS	100.12 (0.73)	101.15 (0.85)	100.39 (0.51)	100.32 (0.38)

Table 4-14. Bulk distribution coefficients for Be

Phase	$K_{Be}^{mineral/melt}$	Normative wt fraction	Proportionate $K_{Be}^{mineral/melt}$
haplogranite minimum at 200 MPa H₂O			
Qtz	0.24	0.34	0.08
Pl	0.19	0.38	0.07
Kf	0.15	0.28	0.04
$K_{Be}^{eutectic\ assemblage}$			0.20
muscovite-saturated granite minimum at 200 MPa H₂O			
Qtz	0.0012	0.33	0.00
Pl	0.14	0.37	0.05
Kf	0.03	0.10	0.00
Ms	1.35	0.20	0.27
$K_{Be}^{eutectic\ assemblage}$			0.33

Figure Captions

Figure 4-1. Working curve for the analysis of Be by SIMS. Analytical techniques are indicated with labels of axes. Nearly 30 data points are shown (most plot on top of each other) from 3 SIMS sessions over a 2 year period. Propagated internal and external precision is shown with error bars.

Figure 4-2. Backscattered electron micrographs of representative experimental products and assemblages. Image scale is shown in micrometers. Phase abbreviations include: Kfs=K-feldspar, K-Afs=potassic alkali feldspar, Mus=muscovite, Phn=phenakite, Ab=albite, Crd=cordierite, Bt=biotite, Mt=magnetite, Pl=plagioclase, Qtz=quartz, Brl=beryl, Cbr=chrysoberyl, and gl=glass. [A] (a) Reversed Experiment BeP-64: K-feldspar crystals grown by reaction [1] from relict Mus in granitic melt that contained trace contents of Be. (b) Reversed Experiment BeP-12: K-rich alkali feldspar grown at 750 °C from granitic melt saturated in phenakite. (c) Reversed Experiment BeP-35: Na-rich alkali feldspar grown at 750 °C in Be-poor granitic melt. (d) Reversed Experiment BeP-32: Na-rich alkali feldspar grown at 750 °C in granitic melt saturated in phenakite. (e) Forward Experiment BeP-56: Andesine (Pl) grown by the decomposition of starting grossular in granitic melt containing trace contents of Be. It occurs with the crystalline assemblage Crd + Bt + Mt + Qtz. (f) Forward Experiment BeP-53: Andesine grown in a similar assemblage in Be-rich granitic melt, with beryl as a liquidus phase. Beryl shows new growth at low T with residual cores from the preconditioning T . [B] (a) Reversed Experiment BeP-40: New quartz grown at 800 °C in granitic melt with trace contents of

Be. (b) Reversed Experiment Be-75: New quartz grown under beryl-saturated conditions at 800 °C. The assemblage contains Qtz + Brl + Cbr in hydrous granitic melt. (c) Reversed Experiment BeP-20: New biotite grown at 700 °C by reaction [3] in Be-poor granitic melt. (d) Reversed Experiment BeP-41: Biotite grown at 700 °C in equilibrium with beryl. The assemblage contains Crd + Bt + Mt + Brl in granitic melt. (e) Reversed Experiment BeP-47: Coarse muscovite intergrowths with biotite in silicic melt containing Kfs + Mus + Als + Cor + Bt + Mt. Numerous, small crystals of new muscovite are present at lower left. (f) Reversed Experiment BeP-52: Abundant muscovite crystals grown in melt saturated with beryl and chrysoberyl; otherwise this charge contains a similar assemblage as (e).

Figure 4-3. Distribution of Be within a granitic pegmatite showing characteristic crystallization events of beryl. Modified from Solodov (1959).

Figure 4-4. Schematic representation of the key stages of fractionation for the evolution of the Be budget in crustal magmas.

Figure 4-5. Three geochemical pathways (a,b,c) for Be during the evolution of granitic magmas. The magmatic budget of Be, the crystalline controls on Be contents of melt, and the common products in solidified rock are given for successive stages.

Figure 4-1.

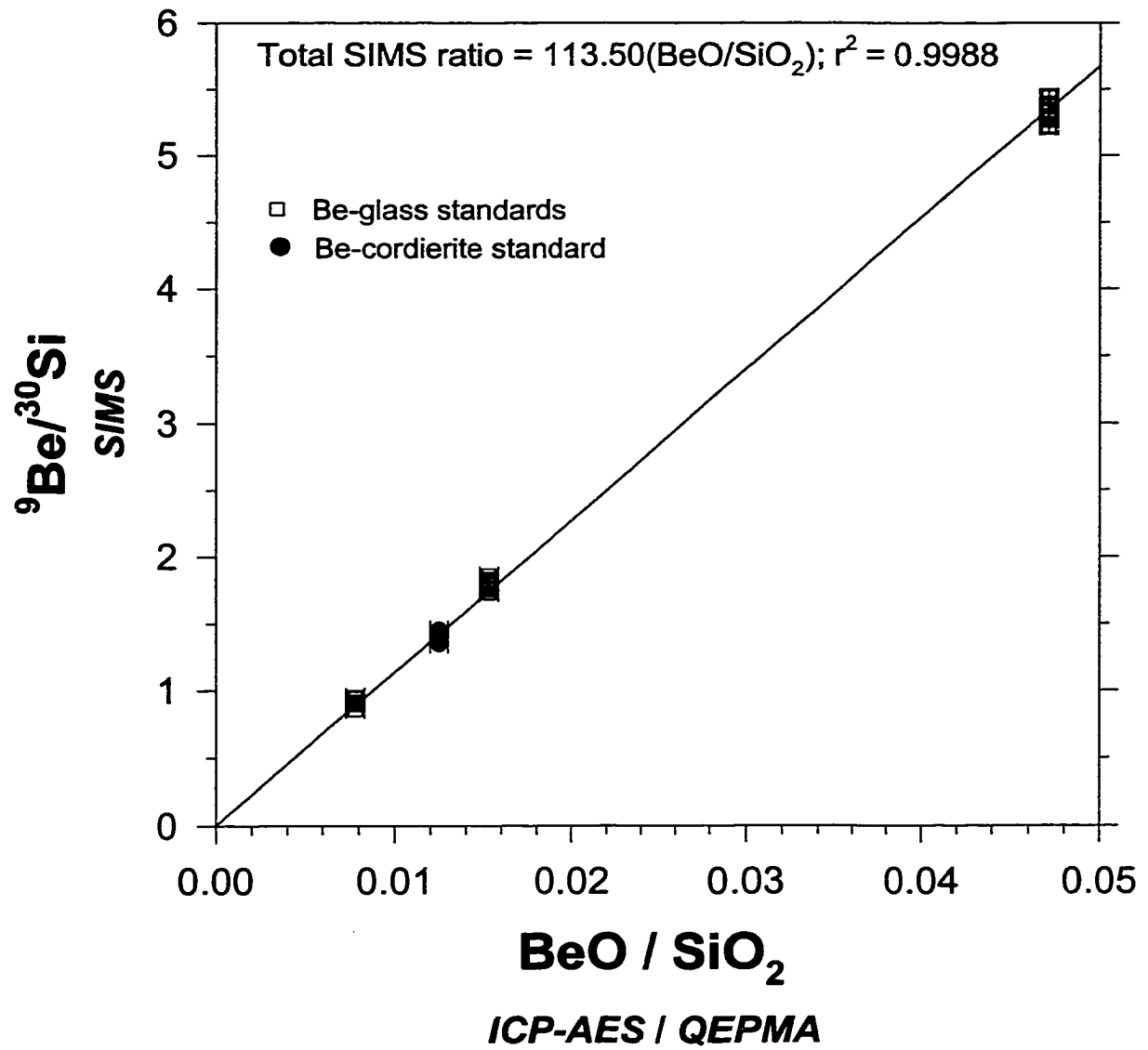


Figure 4-2a.

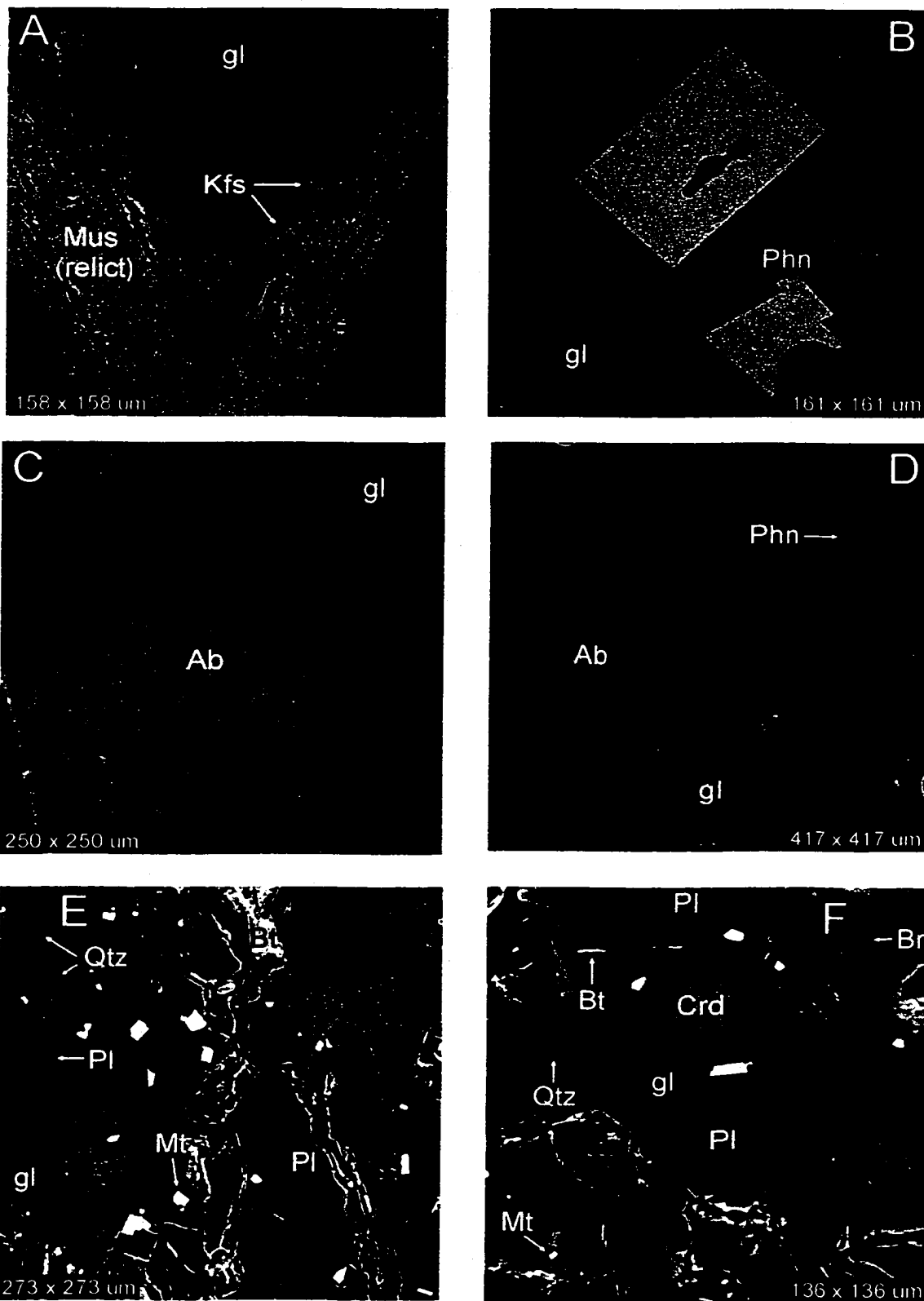


Figure 4-2b.

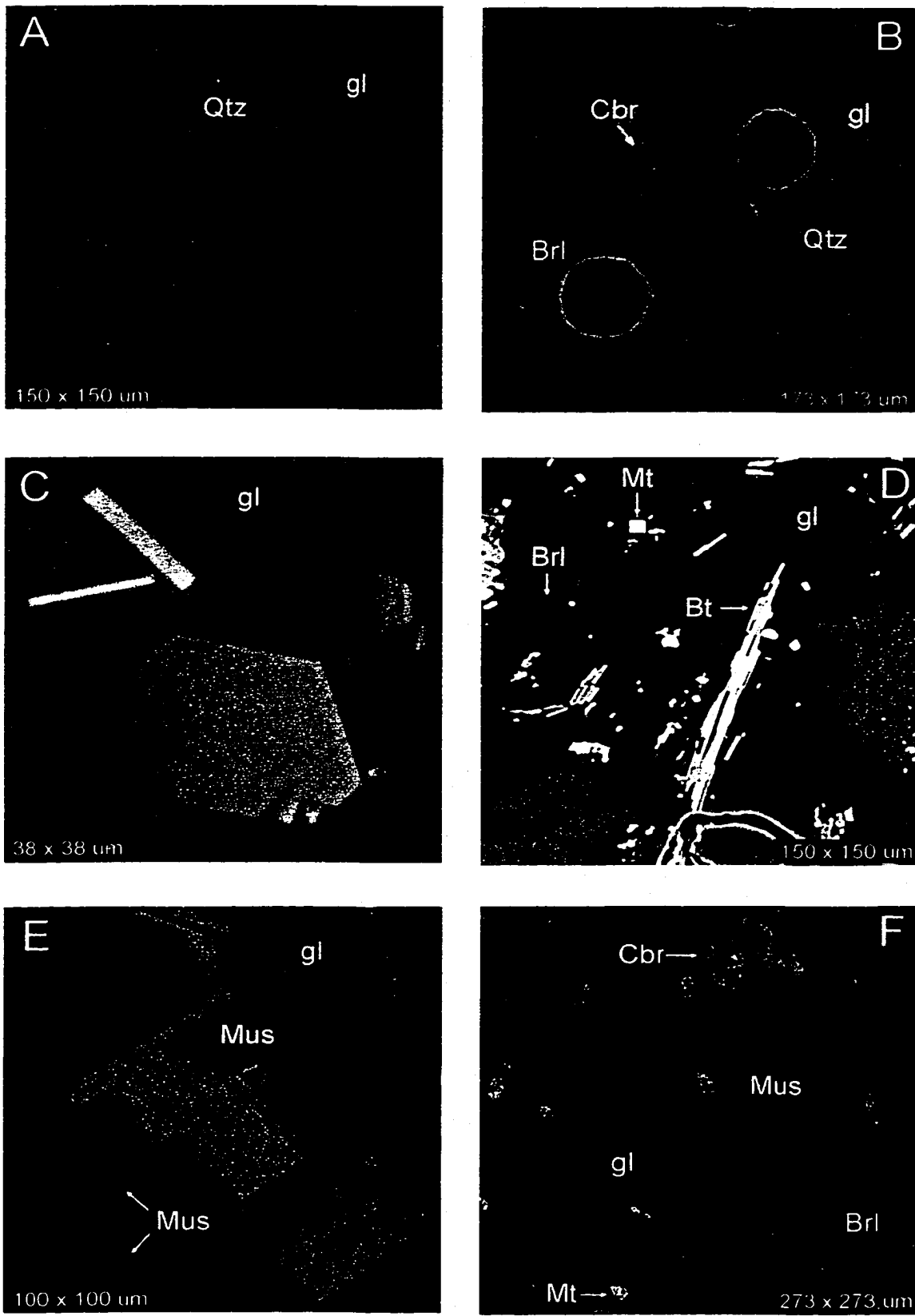


Figure 4-3.

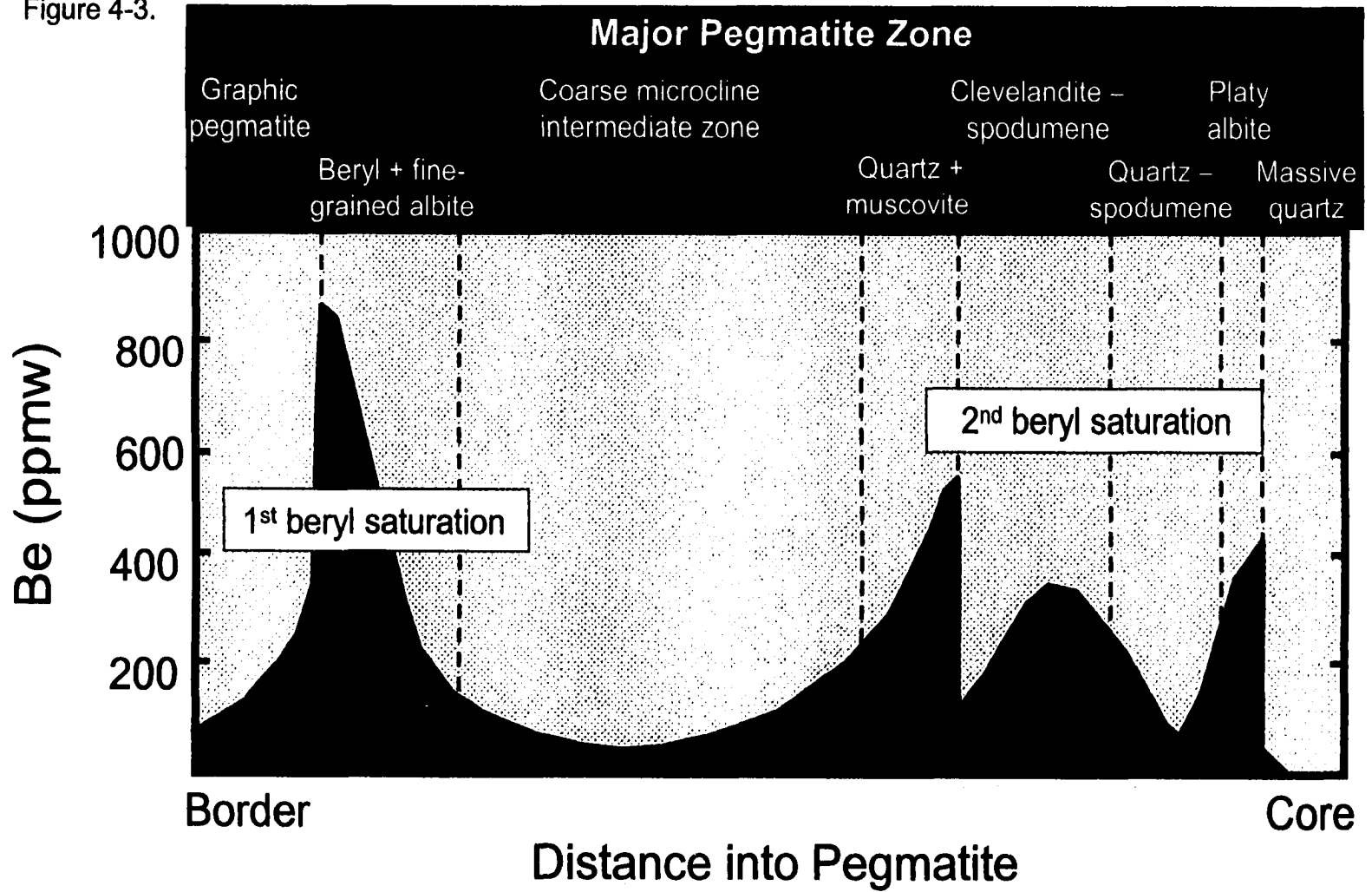


Figure 4-4.

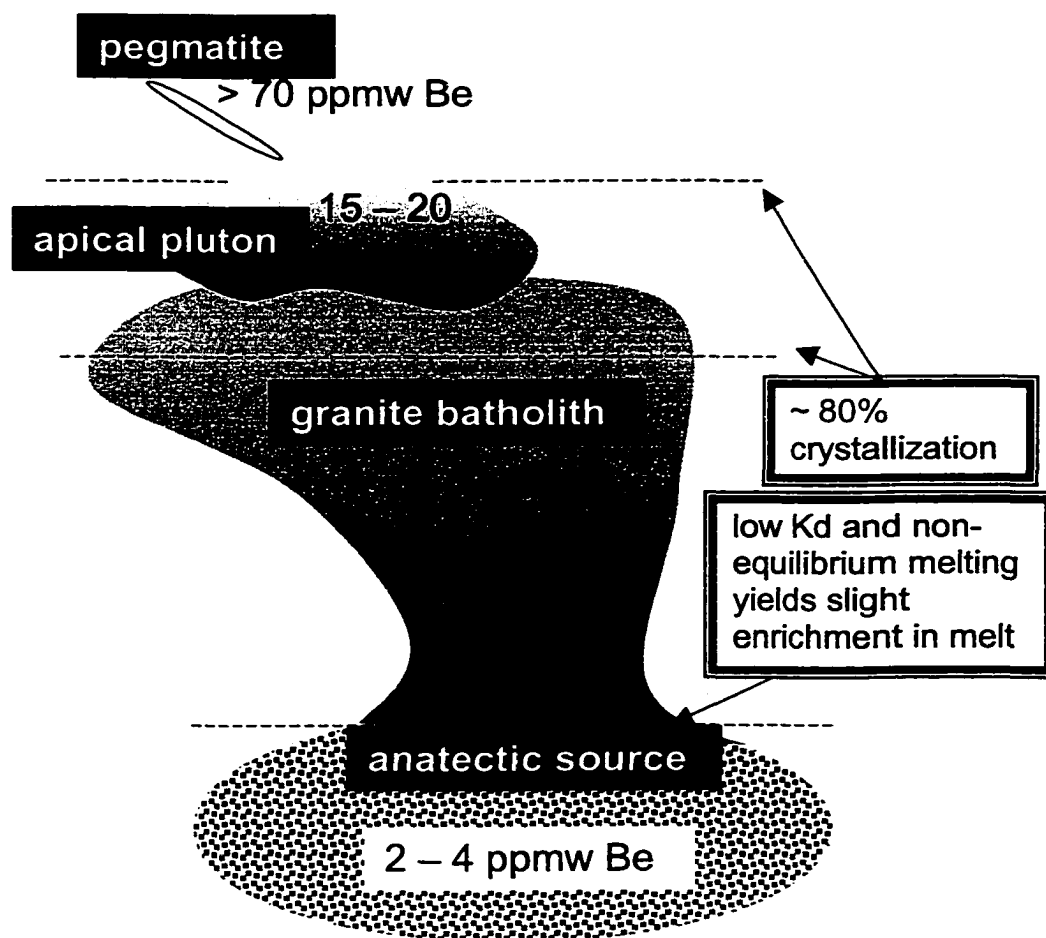


Figure 4-5a.

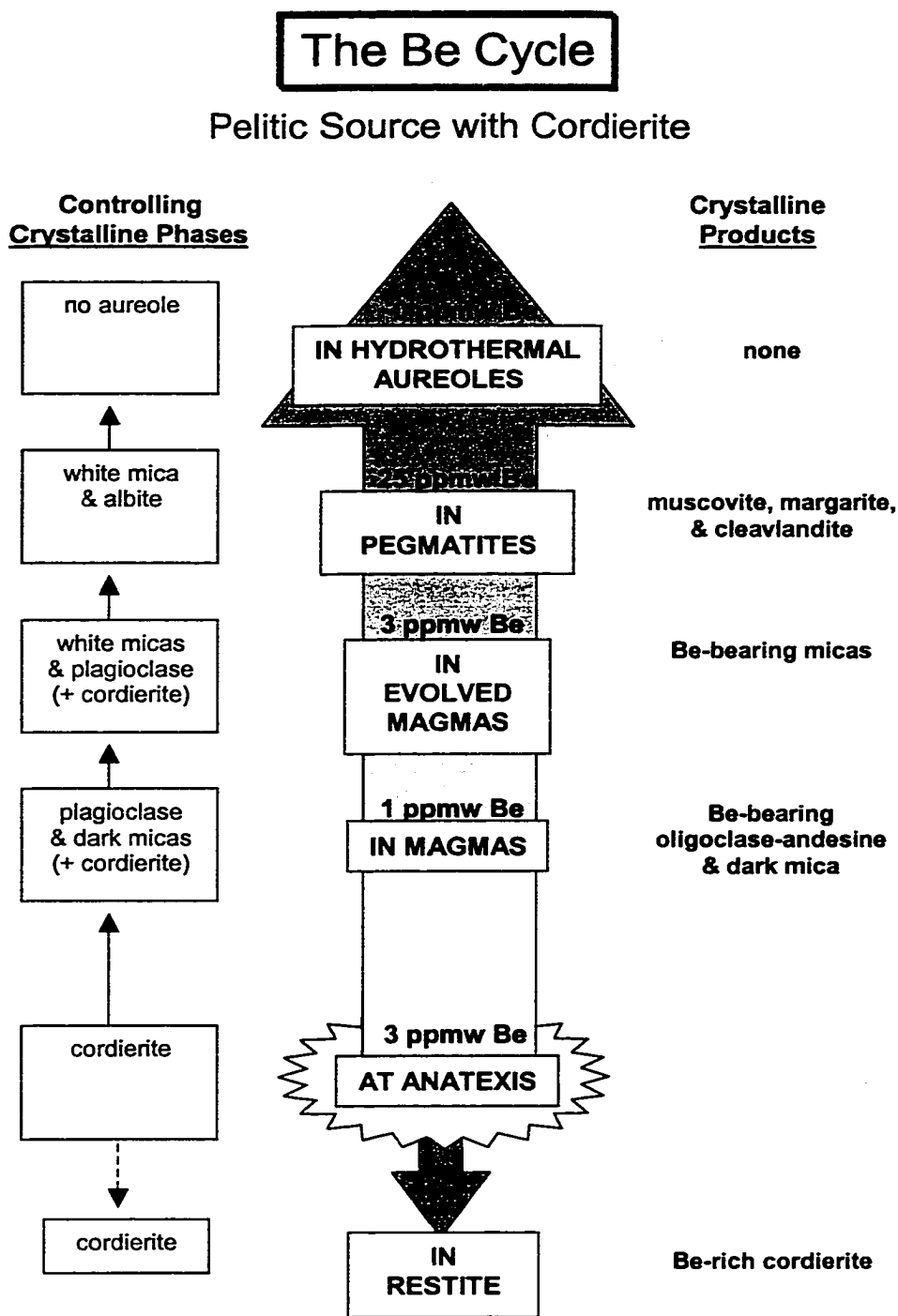


Figure 4-5b.

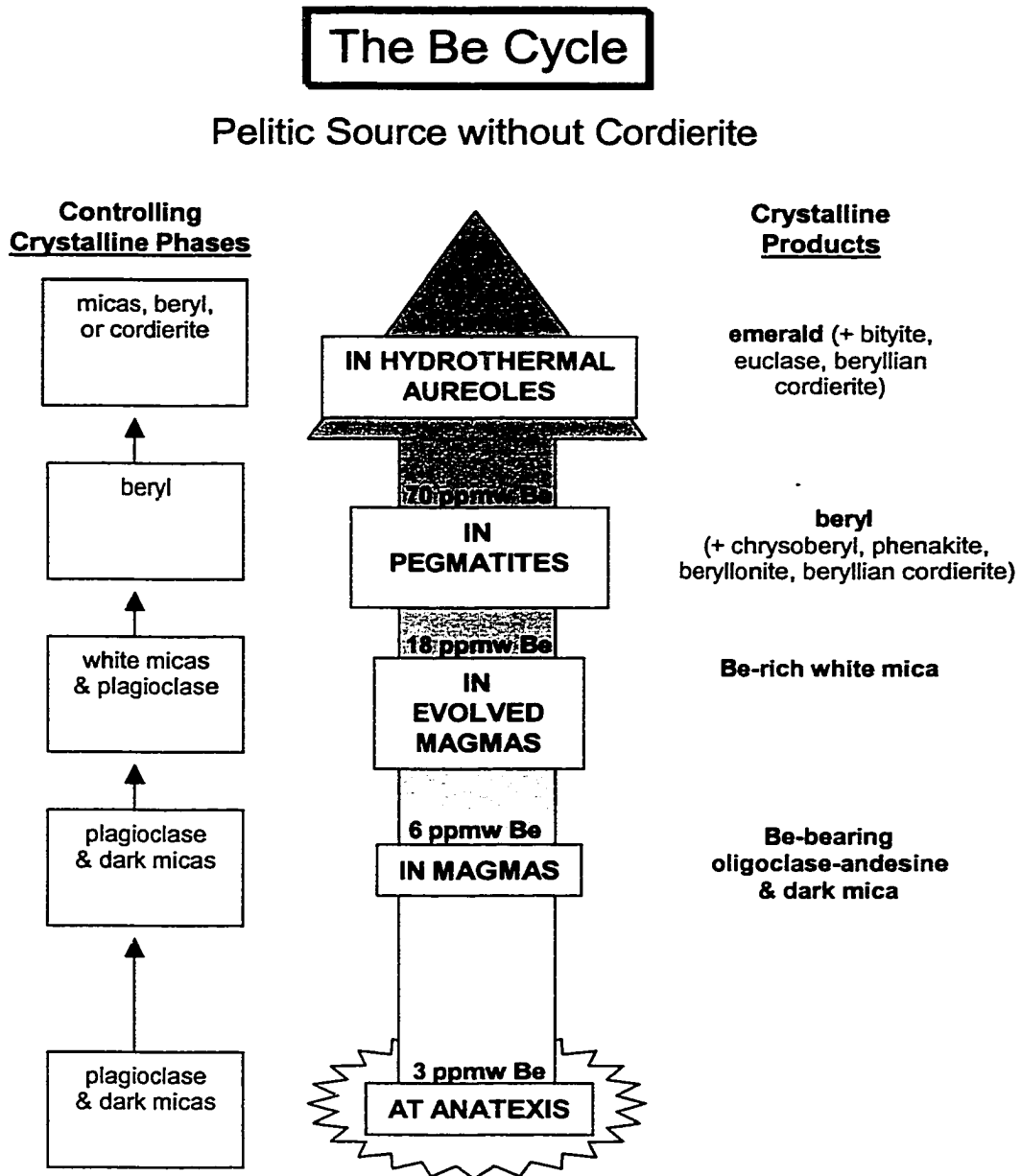
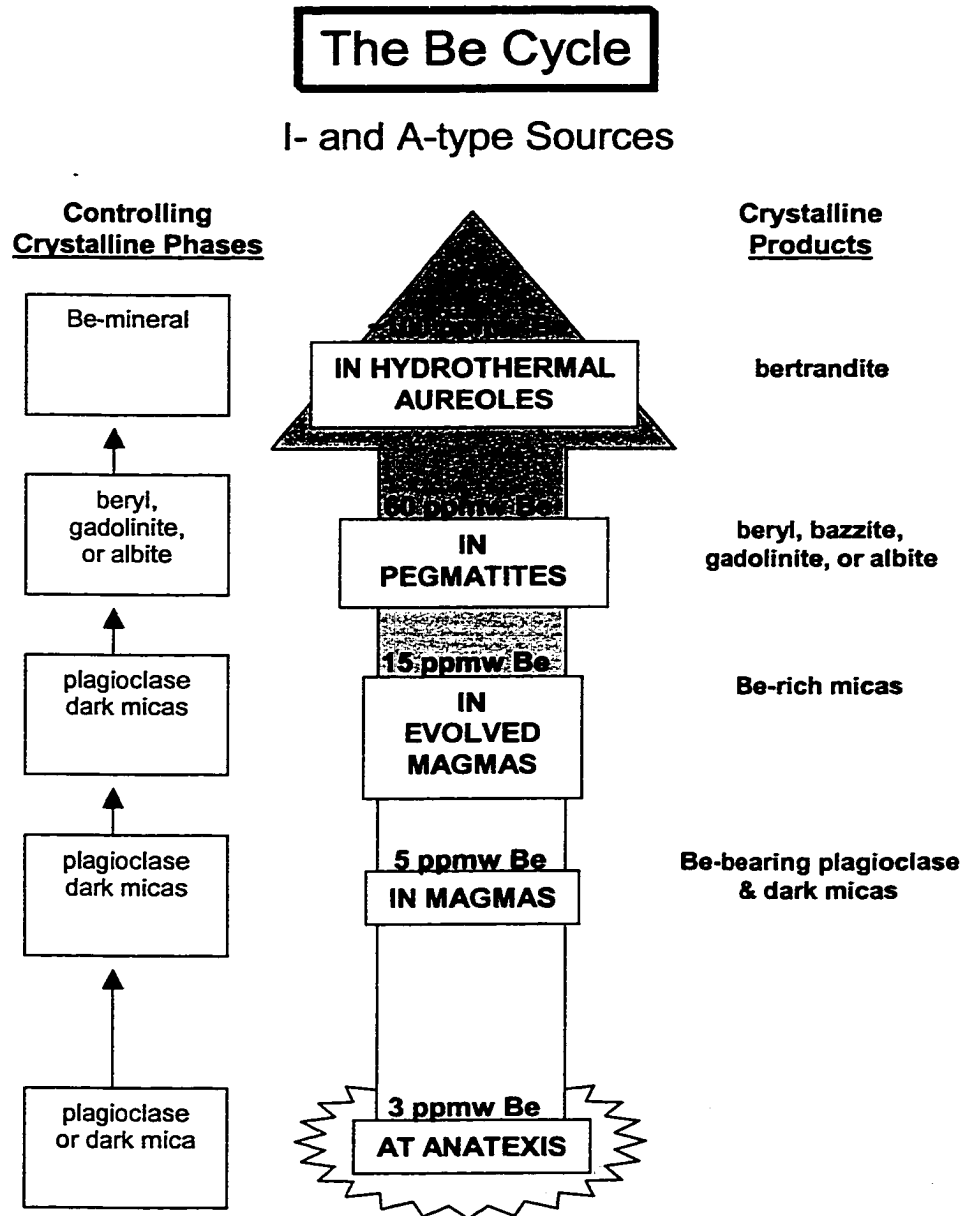


Figure 4-5c.



**CHAPTER 5. KINETICS OF CRYSTALLIZATION IN UNDERCOOLED
GRANITIC MELTS (Ab-Or-Qtz-H₂O): SUPERLIQUIDUS, SUBLIQUIDUS AND
STARTING MATERIAL EFFECTS**

INTRODUCTION

Unlike low-silica, basic or alkaline magmas that tend to track a condition of equilibrium between crystals and melt upon a liquidus line of descent, comparable crystal-melt reactions in silicic melts are sluggish and may not necessarily track the equilibrium liquidus closely. Such kinetic barriers are highly relevant to shallowly emplaced granitic liquids that cool rapidly. Petrologists have long recognized that metastable behavior is more prevalent in high silica magmatic systems (e.g., as reflected in the timescales required for experiments to equilibrate: e.g., Tuttle and Bowen 1958; Dingwell et al., 1996). Field studies (e.g., Bea 1996; Morgan and London 1999) and experimental assessments (e.g., Fenn 1986; Dingwell et al., 1996) increasingly point toward the need for a more comprehensive calibration of the response of silicic melt to cooling. While numerous aspects of the broad topic of crystallization relevant to undercooled granite melts have been investigated (e.g., melt speciation and structure: Mysen 1988, Hess 1995, McMillan and Wolf 1995, Stebbins 1995; melt viscosity: Dingwell 1993, Webb and Dingwell 1995; relaxation in melt/glass: Dingwell 1995, Moynihan 1995; diffusion: Chakraborty 1995), our purpose here is only to extract reaction rates as a function of thermal and structural histories relevant to silicic magmas.

Macroscopic Properties of Melt. While numerous studies have focused on microscopic properties of melts, the data base for macroscopic properties as a function of

P-T pathway is weak. Here we begin with a study of the effects of macroscopic properties of melt on crystallization, which fundamentally includes the presence of liquid, crystal and vapor phases. How these phases interact and the kinetic advantages or consequences for crystallization need to be delineated to fully characterize the crystallization of granitic magmas. The effects of variable degrees of vesicularity and crystallinity for crystallization must be evaluated as a function of thermal pathway to adequately represent magmatic analogues in nature.

Microscopic Properties of Melt & Nucleation Terminology. Diffusion, melt speciation and structural characteristics of melt/glass all fall within this category, but an investigation of crystallization fundamentally begins with focus on nucleation. A critical nuclei has been defined as a molecular cluster that achieves a size great enough to grow so that it is able to outweigh the odds that it will decay by random chance (e.g., Dowty 1980). Heterogeneous nucleation in melt is facilitated by a foreign substrate that reduces the activation energy barrier for nucleation, by reducing the surface free energy and allowing subcritical clusters or embryos (see Lofgren 1983 and references therein) to grow to critical radii. When nucleation occurs but is clearly separated from a foreign substrate like experimental capsule walls, it is termed *internal* nucleation. If nucleation clearly occurs along container walls as *sidewall* nucleation then crystal growth may proceed along container edges or inward into the melt. In this study the presence of unidirectional solidification textures (USTs), after Shannon et al (1982), are used to determine directions of crystal growth. Directional criteria include an asymmetry of crenulate, dendritic or intergrowth layering that shows crystal terminations in one

direction, and possibly hierarchical nucleation relationships that are manifested as overgrowths on such terminations.

Pertinent Variables

The control on crystallization not only results from process within the melting interval, but of that above the liquidus (e.g., Lofgren 1983, Marsh 1996) and, in rapidly cooled systems, below the solidus (e.g., Smith et al., 2001). Thus, the following parameters become pertinent to understanding crystallization in felsic melts.

Structural State of Melt

Starting Materials. Variation of structural state of the starting material (added reactants) is especially germane to experimental research aimed at equilibrium, although the effects of starting medium are rarely evaluated in experimental studies. This is particularly appropriate to silicic melts that often display sluggish responses to crystallization (e.g., Dingwell 1993). Starting materials that result in a particular nucleation state may have significant consequences for crystallization pathways in terms of available nuclei and vesicles in melt. While relationships between vesicles and nucleation and crystal growth, and potential consequences for crystallization have not been thoroughly assessed in silicate melts, the effects of the presence of nuclei are well known.

Studies relevant to basic liquids have emphasized that the availability of critical nuclei ultimately governs the development of crystalline texture in undercooled melts (e.g., Lofgren 1983), and thus, the dynamics of crystallization (e.g., Hort and Spohn 1991). In order to adequately assess magmatic responses to cooling in silicic systems, crystallization must be characterized in nuclei-bearing and nuclei-absent melts.

Recovery Time of Melt. The rate at which melt comes to equilibrium at a new set of P-T conditions, or its recovery time, may have potential kinetic effects upon subsequent cooling to subliquidus conditions. If structural equilibration of melt is important upon cooling, it represents an additional kinetic barrier for magmas prior to crystallization.

Recovery Time of Glass and The Glass Transition Temperature (T_G). Similarly, the rate at which glass comes to equilibrium with a new set of P-T conditions, or its fragility (e.g., Dingwell 1996, Toplis et al., 1997), is highly relevant. The advancement of crystallization below the glass transition temperature may be relevant for extremely undercooled granitic liquids (e.g., Webber et al., 1997; Morgan and London 1999). If so, characterizing the mechanisms and textural signature of devitrification could be important for delineating thermal histories of melt, as well as augment the recognition of igneous systems that may have crystallized under far from equilibrium conditions (e.g., Smith et al., 2001).

Undercooling (Supersaturation)

Liquidus undercooling ($-\Delta T \equiv T < T_{\text{liquidus}}$) relates the physical driving force for crystallization to the chemical saturation surface of a given mineral phase. As silicate liquids are cooled to subliquidus or subsolidus temperatures, changes occur in nucleation (e.g., Winkler 1949; Fenn 1977; Muncill and Lasaga 1987) and morphologies of crystal products (Swanson 1977; Lofgren 1980; Peterson and Lofgren 1986). Potential effects of undercooling on rates (e.g., Dingwell et al., 1996) and mechanisms of solidification are also likely to be important. These systematics have yet to be fully assessed in compositions relevant to silicate magmas, and particularly, granitic liquids.

Lag Times and Rate Changes during Crystallization

In order to effectively model crystallization scenarios for granitic liquids, a data base of nucleation delay times is fundamentally needed. How nucleation delay times vary as a function of starting material and thermal history may bear significant importance for the crystallization of silicic magmas.

Not only is the onset of crystallization critical (e.g., Dowty 1981), but possible mechanistic changes over the interval of crystallization—i.e., with time—could exert large effects on solidification (e.g., Hort and Spohn 1991). Field studies (e.g., McBirney 1987; Marsh 1995; Webber et al., 1997) have suggested that the kinetics of crystallization are an integral part of the solidification of melt, but these have neither been satisfactorily confirmed nor calibrated by experiment.

Metastable Fractionation of Melt. Evaluating fractionation as a function of crystallization may be accomplished by utilizing a minimum melt (eutectic) composition for experimental analysis. If fractionation from a eutectic melt occurs, it must be due to metastable reaction induced by crystallization.

Strategy

The Haplogranite Melting Minimum: A Reference Point

Should starting materials lie at the ternary minimum composition, the eutectic becomes the relevant reference point for superheating and undercooling pathways. From this bulk composition, both crystal crystalline and vitreous starting materials were derived (see Experimental Methods below) for the purposes of creating nuclei-bearing (feldspar or quartz) or nuclei-absent conditions upon cooling in experiments.

Freezing Point. Using a reactive fine-grained crystalline material, minimum melting for hydrous haplogranite was determined to lie between 680° and 685°C at 200MPa (Table 5-1a) and is thus taken to be 683°C. The composition of this minimum melt is $Ab_{36}Or_{27}Qtz_{37}$ (recalculated from QEPMA; Table 5-1b), which is slightly siliceous compared to previously reported values (e.g., Tuttle and Bowen 1958).

Congruency of Melting at Hydrous Conditions. Table 5-1c shows the glass compositions from melts that contained variable amounts of water, from undersaturated (~ 4 wt% H₂O) to significantly oversaturated (~ 50 wt% H₂O) conditions. Very rare vapor deposits of glassy spherules were found among charges which led to the assessment that melts derived from the Corning Glass at 200 MPa melt congruently.

Persistence of Crystal Phases Above the Liquidus. Few studies have appreciated how long silicate crystals persist at superliquidus temperatures in melts of silicic composition. Table 5-1d shows the results of a preliminary assessment of melting using the reactive crystalline mixture and proportions of melt : crystals with time. At 700 °C, crystals of both quartz and feldspar persist for at least 1 month (at which point relict crystal diameters ~ 3 um on average). When temperature was increased to 730 °C, complete melting (at the resolution of electron microscopy; i.e., > 0.5 um) occurred after a 24 hour run duration. Hence this preconditioning step became one reference point for study.

Single-Step Thermal Pathways

In experiments of variable cooling rate, the effects of the magnitude of thermal change for crystallization may not be independently assessed. Therefore, for reasons of extracting information from experiments, single-step thermal pathways were

implemented in these experiments. The approach allowed for the effects of thermal change on crystallization to be quantified. From the resultant data base, the effects of cooling rate may be ascertained.

This Study

In this study, undercooling is the means by which we get at chemical potential gradients during crystallization. Because conventions have been set this way, we define the change in temperature from the liquidus surface as ΔT . However, we include the modifiers + and - to indicate positive (“superheating”, $+\Delta T \equiv T > T_{\text{liquidus}}$) or negative (undercooling) thermal pathways from that point. The variables of interest become: superliquidus T step, subliquidus T step, and time (at each step). Characterization of the kinetics of crystallization in granite melts necessarily requires a (minimum) combination of these variables: (1) starting medium (containing variable nucleation state and vesicularity of melt), (2) superheating, (3) undercooling, and (4) time.

Here we examine the progression of crystallization in both nuclei-bearing and nuclei-absent haplogranite minimum melts at 200 MPa ($P_{\text{H}_2\text{O}}$) as a function of single-step superheating from 50 and 150 °C and subsequent single-step undercooling from ~ -13 to -310 °C with time ($+\Delta T = 1$ hr to 7 days; $-\Delta T = 1$ hr to 1 mo). During the solidification of hydrous haplogranite composition above and below T_G we report on controls for nucleation delays and characteristics (mechanisms), the sequence of appearance of crystalline phases, growth rates, mechanisms of solidification and consequences for the development of boundary layers.

EXPERIMENTAL APPROACH

Starting Materials

A single starting glass, with a composition of the hydrous haplogranite minimum at 200 MPa, was synthesized by Corning from heating a mixture of reagent oxides to 1800°C and 1 atm in a ZrO₂ crucible. The glass is homogeneous (by microprobe; Table 5-1b) though it contains rare traces of zirconia from the crucible wall; although, residual fragments of zirconia do not appear to react with silicate liquid during any stage of the crystallization process. Three different starting materials were derived from the initial glass (Figure 5-1a):

Glass Rods. Rods were cut with a precision saw, and rounded using an alumina grinding wheel. Each rod was briefly (~ 10 s) soaked in HF to minimize contamination by removing a thin layer of glass, then sonicated in ethanol and dried. The glass rods produced vesicle-free products whereas those of the powdered and crystalline materials contained vesicles.

Glass Powder. Powders were ground using an agate mill to a mean grain size of $\leq 10\mu\text{m}$. This step imparted similarity between the glass powder and crystalline mixture (derived from the glass powder). Grinding the glassy material had the following consequences: (a) the surface area of the mixtures was increased, (b) the decreased fragment size changed the way that water interacted with the mixture, (c) grinding strain may have been induced in the glass fragments, and (d) the mixture may have been marginally contaminated by agate.

Crystalline Mixture (Derived from the Glass Powder). The crystalline material is comprised of an aggregate of fine-grained Qtz (1-2 μm) and intermediate Afs (1-8 μm) produced by devitrification of glass powder plus ~ 10 wt% H_2O at 650°C for 4 days in a hydrothermal environment equivalent to water saturated conditions for haplogranite melt at 200 MPa. An assessment of crystallinity by XRD (Figure 5-1b) and EDXA shows that after the charge is completely crystalline after this treatment. At the same conditions, glass rods would not devitrify after 28 days. Because of this barrier, which was an effect of the surface area of the glass rods, only glass powders were used for the derivation of crystalline materials.

Gold capsules (3 x 20 mm) were cleaned by soaking overnight in bromopropane (25°C) then by boiling for several hours in nitric acid. Afterwards, a few capsules still contained remnants of the extrusion lubricants used in the fabrication of the tubing; these remnants were removed with polyurethane foam swabs. Water was loaded first, followed by powders or glass rods, into capsules (with additives confined to a central portion of the capsule), which were sealed by DC-plasma arc welding. Capsules were checked for leaks (optically and using weight changes) after welding, and again after storage in a drying oven (140°C). The heating step further allowed for homogenization of water contents throughout the powder prior to the experimental run. Care was taken to fashion all charges into slightly flattened cylindrical shapes, with an aspect ratio (\equiv length/width) of ~ 2 . This produced run products of similar shape and dimension.

Equipment

Experiments were pressurized cold in R-41® and NIMONIC-105® cold-seal reaction vessels using water plus trace Immunol® as the pressure medium. Pressure was measured with a factory-calibrated Heise bourdon tube gauge; fluctuations of < 3 MPa occurred over the course of experiments, with a total estimated uncertainty of ± 10 MPa. Total experiment durations varied from ~1 to 6 weeks. Temperature was monitored by internal Chromel-Alumel thermocouples with estimated maximum error of $\pm 5^\circ\text{C}$. Experiments were quenched isochorically using compressed air jet (5 to 15°C/s). The fugacity of oxygen within capsules was regulated by diffusion of H_2 across the metal capsule; the f_{O_2} of the pressure medium is estimated to be slightly below NNO (Huebner, 1971) at run conditions. Following quench, capsules were weighed to check for leaks, punctured, and the presence of free water was recorded. Capsules were heated in a drying oven, and then reweighed to verify loss of free water (~ 25% of initial water added) and saturation of glass (by difference). Vitreous and dimpled surfaces of charges that easily peeled away from the metal capsules were also used as criteria for water saturation. All capsules gain minor weight during experiments by diffusion of Ni-metal (from vessels and filler rods) into precious metal capsule walls; although, none of the experimental products reported here suffered detectable contamination by Ni.

Run Pathways

Multiple experiments were run together to eliminate temperature differences between charges where the determining variable is starting medium. The first series of experiments implemented isobaric superheating and undercooling cycles for all starting materials. These pathways entailed first heating runs to 730 or 830°C ($+\Delta T = 50$ or

150°C, respectively) for 1 day, which resulted in crystal-free melts, followed by a single-step undercooling. At the beginning ($t = 0$) of the undercooling step, the crystalline material resulted in nuclei-bearing melts, whereas the powdered glass and glass rod resulted in nuclei-free melts (but originating from different histories). It is this difference that allowed for the effects of starting medium to be assessed in the undercooling pathway. Final run (undercooling) temperatures were 670, 655, 630, 605, 580, 533, 450, and 375°C (i.e., from $-\Delta T = 13$ to $\sim 310^\circ\text{C}$). Durations at a given undercooling varied from ~ 1 hour, to 1, 3, 7, 14, 21, and 28 days. Figure 5-2 shows a schematic illustration of run pathways.

Another experimental series assessed the effects of longer preconditioning steps at both superheating temperatures. The last series evaluated the recovery behavior for liquids preconditioned at 830°C then lowered in T to 730°C for variable duration. By comparison of subsequent nucleation following undercooling, the equilibration rate for a change in superliquidus thermal conditions could be assessed.

Control products were obtained following each preconditioning step (Figure 5-2). In addition, several glasses which had been brought to the undercooling T for one hour (prior to quench), were analysed for homogeneity of water distribution. Several transects by quantitative electron probe microanalysis (QEPMA) from edges of charges into central regions (totaling ~ 75 analyses per charge), show that no variation exists within detection limits. Thus, all melts appear to be homogeneous upon arrival ($t = 0$) at undercooling conditions.

ANALYTICAL APPROACH

Extraction of Data from Run Products

Area for Sampling

In order to maximize the area of analysis, entire charges were mounted together in transparent epoxy or Beuhler Transoptic® thermal plastic. This allowed for optical characterization by transmitted light of the volumes of charges (minus the fraction lost to polishing) and data acquisition at the surface using BSEI. Many of the charges originating from glass powders or the crystalline mixture (~ 1.5 mm thick) broke upon opening capsules. Although fragments were mounted in their original orientations, differential thickness between them allowed for exposure of several different heights of the charges upon polishing. One-third to one-half of the bulk charge was removed during polishing. Therefore, this technique allows for successive sampling (e.g., vs. serial sectioning/ polishing) for representation of a given charge at once at 1/3 to 1/2 depth.

Textural Data

Approaches utilized backscattered electron imaging (BSEI) and image processing to quantify run products. Using the backscattered signal, images were acquired as 1024 X 1024 pixel arrays. Gray-level images were thresholded to binary images (black and white), and then several relevant shape descriptors were implemented (using software by Russ, 1999) for morphological statistics.

Centers of Nucleation. Because surface nucleation and sidewall crystallization clearly dominate the run products, measurements based on charge area (i.e., N/A in μm^2 where $N \equiv$ no. of nuclei) as well as perimeter (N/P), were made. Because of clear attachment relationships of new crystals on former crystals and spatial proximity of

crystals to one another in crystal clusters of like mineralogy, nucleation was measured in terms of *centers* of nuclei. Another reason to measure centers of nuclei stems from the nature of the skeletal crystal products: in a planar sample, connectivity between crystals lying in close proximity to one another is unknown—i.e., several apparent crystals stemming from a common center may indeed be a single crystal in three dimensions. Centers of nucleation data were then compared to total numbers of crystals (nuclei).

Crystal Densities and Morphologies. Crystal numbers were counted during imaging and from BSE micrographs. Morphological data were acquired, using the following descriptors:

- *Solidity*, the area measure of the filling density of a crystal [area/convex area].
- *Diameter Aspect Ratio*, the most accurate prediction of aspect ratio for unknown crystal shapes using a non-orthogonal function [max/min diameter]
- *Roundness*, an area/diameter calculation that relates 2-D projection of a crystal to sphericity [$4 \cdot \text{area} / (\pi \cdot (\text{max. diameter})^2)$]
- *Convexity*, a measure of convex perimeter/perimeter of a crystal. This tool is particularly powerful for identifying changes among spherulitic crystal clusters [provided that space (melt) exists between the radial arms or spokes of spherulites].
- *Crystal Length*, a linear measure of maximum, continuous length
- *Crystal Area*, the area density occupied by crystals

Different measures of shape were used in the calculation of crystal growth rates (area/time, length/time, and area/time corrected for crystalline solidity). For consistency,

all images were rotated so that the edge of the charge was flush with the right portion of the image.

Vesicularity of Melts. The vesicularity of run products varies with starting material. However, because of the intrinsic conditions of the experimental apparatus, the volume of run charges was not constrained; hence, the area occupied by vesicles should, once subtracted from the total, not affect area measurements of melt. Where vesicle heterogeneity was observed, morphological descriptors using some of the measures above were used to deduce size population characteristics. Spatial correlations between vesicles and crystals were tested to assess vesicle-crystal relations.

Compositions of Single and Multiply Intergrown Phases

Glass and single crystals were analysed using wavelength-dispersive spectroscopy on a Cameca SX-50 electron microprobe at the University of Oklahoma. QEPMA utilized crystalline and glass standards with TAP, PET, LIF, and a layered composite (PC1) diffraction crystals. Operating conditions for hydrous glass analyses used a two-beam condition (2 nA and 20 nA regulated currents method) with a 20 μm spot size, in which Na and Al were analyzed first (and concurrently) to inhibit beam-induced migration effects (Morgan & London, 1996). Analyses of minerals were conducted at 20 nA, 20 kV and a spot size of 3 to 5 μm . Counting times for all elements varied between 20 and 30 seconds. Data were reduced using the PAP (Pouchou & Pichoir, 1985) matrix correction program. Detection levels, taken at 3σ (precision within ± 3 standard deviations of the mean) above mean background, were < 500 ppmw for most elements.

For multiply intergrown crystals, broad-beam (a raster of 10x10 to 50x50 μm area) semi-quantitative analyses were accomplished using energy-dispersive X-ray

analysis (EDXA). These analyses were recalculated as mineralogical modes of quartz (Qtz), orthoclase (Or), and albite (Ab). This assignment allowed for characterization of microscopic intergrowths because these components represent the only end-member crystalline phases (at least at the higher T conditions in this system).

RESULTS AND DISCUSSION

Coverage of the time – temperature run matrix is shown for melts of each starting material in Figures 5-3a through 5-3c. Similar coverage of run pathways is seen for each starting material.

Nucleation Delays

Table 5-2 gives the minimum nucleation times following undercooling. Nucleation delays for melts derived from rod and powdered glass decrease with increasing undercooling, from ~ 7 days at $-\Delta T = -13^{\circ}\text{C}$ to ~ 4.5 days at $-\Delta T = -133^{\circ}\text{C}$. Melts originating from the crystalline material respond differently. Nucleation delays do not exist for melts of crystalline material at low undercoolings; these systems show significant crystallization after 1 hour at $-\Delta T = -13^{\circ}\text{C}$. With longer preconditioning times (2 to 3 days: Table 5-2), nucleation lag times appear to increase. I interpret decreased lag times to mean that some nuclei are not completely wiped out before undercooling. After the 24-hour preconditioning duration, remaining embryos of feldspar likely remain. At these conditions, the crystalline starting state effectively yields nuclei-bearing melts.

Nature of Nucleation

Nucleation invariably occurs along sidewalls of melt charges, either directly at the melt-vapor interface or 30 μm or more within the melt. Where nucleation occurred ≥ 300

μm inward from the edge of a charge, or approximately in the center of charges, and bearing no apparent spatial relation to crystal clusters associated with sidewalls, it was considered to be internal. Melts from glass rods and powders show almost exclusively sidewall nucleation, where crystals exhibit direct attachment relations or proximal locations to charge edges. At moderate to high undercoolings some internal nucleation may be observed (as much as 5% of total nucleation). For melts derived from the crystalline medium, most nucleation occurs at the sidewall, but far more (~ 27%) internal nucleation may be observed compared to melts origination from other materials.

Rate of Nucleation

Nucleation data in terms of total crystal numbers and total crystallization centers, are listed in Table 5-3. For melts originating from powdered glass (Figure 5-4a), total crystals increase with undercooling and time, though scatter is seen at $\Delta T = -103^\circ\text{C}$. Nucleation centers for the same melts (Figure 5-4b) show a rise in number followed by a constant values with increasing time under conditions of low undercooling. With increasing undercooling, nucleation centers increase in number. Data for melts originating from glass rods (Figures 5-4c and d) are fewer in number, though in general, a rise and eventual fall is seen with increasing undercooling.

For melts originating from the crystalline mixture, preliminary nucleation numbers show distinctly different character (Figure 5-4e and f). At low undercoolings, nucleation appears to rise (steeply) and then fall off (steeply), but only to rise again (shallow slope) with time. Hence, the probable existence of preexisting critical nuclei appear to only catalyze nucleation at short durations of undercooling. With greater

undercooling, significant increases in nucleation (total crystals and centers) are seen with time.

The Order of Crystallization

Despite the fact that the starting melts are eutectic in composition, they do not crystallize in eutectic proportions. K-feldspar is always the first crystalline phase to appear in these liquids upon undercooling. With increasing magnitude of undercooling, quartz also crystallizes early, near the sidewalls of charges (e.g., at -308°C). However, at low degrees of undercooling, quartz does not join the crystalline assemblage until long durations of time of ~ 14 to 21 days have passed—this is a full 7 to 14 days after the appearance of Kfs. Here, Qtz occurs in same fashion as Kfs, as crystal clusters along sidewalls. Individual crystals of Na-Afs are not seen until significant time has passed under higher degrees of undercoolings for moderate to long durations (e.g., 1 month at -103°C).

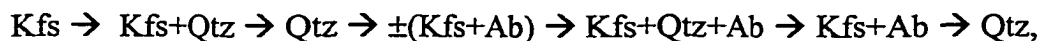
One working hypothesis to explain the sequence of crystallization stems from the proximity of the bulk composition to the metastable extensions of saturation surfaces with undercooling. This concept assumes that the free energy contours are roughly equivalent throughout this interval of chemographic space (e.g., Holland and Powell 2001). Because the metastable extension of the feldspar liquidus at subsolidus conditions is further away than that of quartz in these compositions, the driving energetics are comparably greater for the crystallization of feldspar. Therefore, feldspar is more stable than Qtz. The dominance of potassic over sodic compositions of alkali feldspar follow from the minimum melt composition lying closer to the potassic limb of the two-feldspar solvus (e.g., Luth and Tuttle 1966, Boettcher 1980).

For all melts except those at low degrees of undercooling, a sequential appearance of crystalline phases is observed with time. These sequences always contain at least one occurrence of two-phase intergrowths. Growing single or multiple phase aggregates seem to occur throughout a given charge. This suggests that the same kinetic response operates during crystallization throughout the entire charge.

Among the liquids originating from glass powders and crystalline mixtures, the regular sequence, with progressive undercooling and time, goes from Kfs-rich to Qtz-rich to Ab-rich products (where albite, Ab, is used to represent the sodic composition of the alkali feldspar). These are shown schematically in Figure 5-5a through 5-5c. For moderate undercoolings, the crystallization sequence initially includes, going into the charge from early-formed feldspar,



With increasing time the crystallization sequence becomes

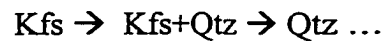


which contains at least two stepwise repetitions in crystalline phases during crystallization up to total solidification (which was found in only one experiment). Here, periodicity is evidenced by Qtz-rich products (layers). At higher $-\Delta T$ conditions in liquids from crystalline materials (Figure 5-5b) taken below the glass transition temperature (-233° and -308°C), the first appearance of monphase Kfs is absent. Instead, the order of crystallization with time appears to be



which is a similar, though more advanced version, of sequential products when compared to the low $-\Delta T$ data. The near-eutectic assemblage of Kfs+Qtz+Ab is seen early in this sequence, rather than later.

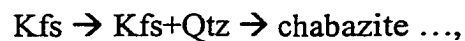
In glass rod experiments (Figure 5-5c), albitic zones are completely absent from the crystal products, despite more total solidification than seen for the liquids originating from the other starting media. Like above, low undercoolings of short duration are characterized by a sequence of



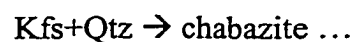
in run products. At high undercoolings below the glass transition temperature, longer duration runs contain the crystallization sequence,



Unlike the estimated repetitive cycles (with stepwise periodicity marked by Qtz) in the crystalline products above, this sequence is an exact oscillation showing 1.5 cycles of Kfs to Qtz products. Chabazite joins the assemblage here (see Boundary Layer section below). At high undercooling and duration, the sequence with time mimics the other melts in its pattern, with either,



or



Normative values of contributions from Kfs (Or), Qtz and Ab are calculated and presented using examples in Figure 5-6a through 5-6c. Among supercooled melts above T_G (Figure 5-6a,b), the modal values are strikingly regular per zone, showing the sequence,

Kfs (\sim Or₉₀) \rightarrow 3-phase Or-rich zone \rightarrow 3-phase Or-poor zone \rightarrow 3-phase zone
At \sim Ab₃₁Or₂₆Qtz₄₃, the latter zone (outermost zone in Figure 5-6a) lies very close to the hydrous eutectic haplogranite melt composition, Ab₃₆Or₂₇Qtz₃₇. Crystallization products from below T_G indicate a different sequence of zonation. Figure 5-6c shows that the Kfs (Or \sim 90) region is followed by two 3-phase (Qtz-Ab-Or) zones in which Or still occupies the majority of the mode but shows an increase in Or content (Or₄₉ to Or₆₈).

Summary. Overall, melts from both crystalline and glassy starting materials show some variation upon a regular sequence of zonation with undercooling and with duration. The sequences progresses from: Kfs to Qtz-rich intergrowths to finely intergrown alkali feldspars (i.e., graphic feldspars), and finally, to Qtz.

Banded Feldspars Layers and Single Quartz Crystals. In general, feldspar-rich zones, exclusive of single crystals of Kfs, show banding along layers that contain distinct UST character. Both at the early and late stages of solidification, quartz tends to form single, coarse and somewhat rounded crystals. Many of the solidified regions thus form single Kfs crystals at the margins of charges, and these are overgrown by banded layers of feldspar-rich zones. The feldspar-rich zones show progressive sequences as described above and these extend into the centers of charges where a few coarse crystals of late Qtz occur.

Apparent Crystal Growth Rates

Crystal sizes vary by at least 3 orders of magnitude within and between experimental products. Bulk crystal growth rates, Y, are given in Table 5-4 as a function of length (max. length/undercooling duration), area (max. area/undercooling duration), and area corrected for filling density using solidity (solidity*max. area/undercooling

duration). Rates are corrected for nucleation delays. Figure 5-7 shows the change of these rates as a function of undercooling. The area rate seems to give the highest values, and the length rates seem to be lowest; solidity measures fall in-between.

The highest value for Y for Kfs is $20 \mu\text{m/hr}$ ($5.6 \cdot 10^{-7} \text{ cm/s}$) for the crystalline experiment at 670°C , which presumably contained residual nuclei as discussed previously. At low degrees of undercooling, melts of the crystalline material fall steadily at first (Figure 5-7b). At greater $-\Delta T$ conditions, however, a consistent trend between experiments of all 3 starting media is a rise to a maximum near -103 to -133°C (Figure 5-7). At these conditions, and in both melts of powder and crystalline mixtures, Y values are better than $1 \mu\text{m/hr}$ in a linear rate (with area rates $\sim 3 \mu\text{m}^2/\text{hr}$ or solidity rates $\sim 2 \mu\text{m}^2/\text{hr}$).

Relative Crystal Growth Rates

Because of the experimental approach, a sequence of experiments was used to calculate growth rates for individual phases, thereby accounting for growth that may have occurred over narrow intervals of time. Unlike the approx. linear growth rates observed for Kfs only (Table 5-4) growth rates of intergrown crystal phases are non-linear (Table 5-5).

Potassic alkali feldspar always appears as the first crystalline phase. Normally it is followed by an intergrowth of two phases (Kfs + Qtz), then three phases (Kfs + Qtz + Ab) and eventually, produces one phase only (Qtz). Nonetheless, a consistent pattern is shown which matches visual observations of crystallization advancement fronts. Table 5-5 gives growth data using the intermediate measure of growth rate, the area growth rates corrected for solidity. At a given degree of undercooling, values of Y show an increase

on the order of ~ 8 to 50 times for intergrowths of Kfs+Qtz over Kfs alone. This behavior appears to be consistent in melts subjected to a considerable range of moderate to high degrees of undercooling. It suggests a fundamental relationship with diffusion: when two feldspars and quartz are co-precipitating, crystal growth becomes increasingly interface-controlled rather than diffusion-controlled. Diffusion away from the growth front, however, is still important for crystallization because all of the haplogranite mineral phases exclude water. In experiment K125-P, which was undercooled to -150°C for 21 days, Y increases among crystal products from 0.084 (Kfs only) to 0.490 (Kfs+Qtz) to $1.136 \mu\text{m}^2/\text{hr}$ (Kfs+Qtz+Ab). In this experiment, growth rates of Kfs+Qtz are ~ 6X greater than Kfs alone, while Kfs+Qtz+Ab rates are ~ 14X greater. It is clear that intergrowths of multiple crystal phases grow more rapidly than monomineralic crystals or crystal aggregates.

Total Solidification of Melt

Solidification patterns here support previous (e.g., Fenn 1986) and schematic (e.g., Dingwell et al., 1996) representations of the kinetics of crystallization of silicic melt. With the included dimensions of time and starting material, however, other effects may be elucidated by these data.

Some possible solutions for the depiction of solidified area in melts as a function of location in $-\Delta T - t$ space are shown in Figures 5-8a through 5-8c. In each plot, the 0% contour serves as the reference for crystallization (t_{nucl}) and the calculation of rates. For melts of glass powders, total crystallization data are sparse though still include the range from 0 to 100% solidification. The solidification trends of Figure 5-8a indicate a “nose” of crystallization at reasonably large undercoolings (~ -150°C) and after significant time

(~ 28 days), complete crystallization occurs. Contours on this plot reiterate the exponential behavior of the nucleation rate data with large durations between 0 and 1% crystallization followed by very short durations leading to complete solidification. The plot of liquids from glass rods contains far fewer data points, but shows a similar “nose” among the contours of solidification. Similarly, Figure 5-8c indicates curved iso-crystallization surfaces pointing toward shorter durations and centered at moderately high undercoolings.

Overall, the trends also suggests that crystallization is very similar between melts arising from glass rod and glass powder materials, once a given degree of undercooling and time are achieved. This may suggest an overall control by undercooling for crystallization in these supercooled liquids. Potential secondary controls, however, are noteworthy.

Between these melt types, glass rod systems exhibit the highest crystallinity, followed by those of powdered glass and finally, the crystalline starting mixture. The trend follows the inverse of the nucleation data, suggesting that perturbations which facilitate nucleation may decrease the efficiency of crystallization with time. A review of the starting materials indicates that the least physically disrupted glass network, vesicle-free solid glass rod, exhibits the highest nucleation lag times. Liquids from this material, however, are the first to reach 100% solidification at $-\Delta T = -150^{\circ}\text{C}$.

Residual critical nuclei in liquids from initially crystalline starting materials appear to facilitate short-term nucleation but not the rates of longer term crystallization, yielding the slowest solidification rates. The abundant surfaces inherent in the glass powder starting material appear to be manifested in derived melts, with nucleation

intermediate between the other two materials. With time, an intermediate solidification rate is observed for these melts.

Mechanisms for Advancement of Crystallization

Two- or three-dimensional crystallization is observed as a function of starting material. Crystallization advances as two-dimensional fronts, parallel to sidewalls in both glass rod and glass powder mixtures. As crystallization progresses, the growth component parallel to sidewalls is stronger than inward into the melt (Figure 5-9a). After the delay period in liquids of crystalline mixtures, crystallization centers commonly originate at the sidewalls, but crystallization most commonly advances inward as three-dimensional networks by semi-direct routes toward central regions of the charge (Figure 5-9b). Owing to a lack of random or homogeneous crystal distributions, it is interpreted that crystal networks utilize preexisting crystals for the advancement of crystallization. Some internal nucleation and growth centers are observed for melts of all three starting media, though in each case these are less numerous and thus subordinate (in total crystallization) to solidification from sidewalls inward.

Manifestations of Crossing the Glass Transition

Following the approximate “two-thirds rule” (e.g., Moynihan 1995), T_G for these melts ought to lie near the vicinity of $\sim 460^\circ\text{C}$. Between the melts undercooled by -150°C (run T = 533°C) and those undercooled by -233°C (run T = 450°C), several noticeable changes occur that likely confirm this transition. Below the apparent glass transition range, nucleation rates show mixed effects whereas growth rates decrease sharply. The abundance of thousands of nuclei have been noted in run products at these temperatures, showing a dramatic increase in nucleation rate. Crystallization mechanisms in these

charges differ from others by the order of appearances of crystalline phases with chabazite joining the assemblage.

The most convincing evidence for having passed a structural transition upon the undercooling pathway is the presence of very small vesicles in previously vesicle-free liquids. Figure 5-10a shows images from three experimental charges. Two of these result from glass powder and crystalline starting materials with run histories above the glass transition. The third image represents a glass rod experiment (normally vesicle-free) that was taken below the apparent glass transition T upon undercooling (to 375°C). The character of vesicles is noticeably different among runs from above or below T_G . Size and shape data are plotted from these experiments in Figure 5-10b. The graph shows vesicle length (= maximum diameter) plotted against vesicle perimeter for the experiments described above. It shows two things: (1) that the shape of the vesicles within representative experiments are quite circular (with a slope of $\sim 1/\pi$) thus excluding any type of differential deformation mechanism during vesiculation, and (2) that the vesicles formed above and below the glass transition T form discrete populations—with mean diameters of ~ 19 vs. 1.6 μm , respectively. A vesiculation event below T_G appears to create a new vesicle population. It is clear that melts taken below the glass transition temperature undergo a different response to crystallization than the melts above that temperature. Preliminary observations show that these also include, at a minimum, different crystalline phase stabilities and assemblages, altered nucleation growth behavior, and discrete morphological character of crystals.

Boundary Layer Effects

Boundary layers at the crystallization – melt interface have only been observed indirectly. Evidence for a boundary liquid of different composition than the bulk melt is seen in (1) cycling of crystal species (with a large absence of the Na component in some runs), and (2) probable evidence of water-rich fluid at the crystal – melt interface.

Zoned crystal products, or zoned aggregates of finely intergrown crystal products, must exclude components of melt during crystallization. Therefore, during an instantaneous moment of crystallization, a concentration gradient should be present. The small size and magnitude of such gradients have prevented resolution by EDXA.

Of the components in this system, Ab-Or-Qtz-H₂O (K₂O-Na₂O-Al₂O₃-SiO₂-H₂O), only water is incompatible among crystalline phases. Boundary layer processes are known to build-up incompatible elements at the crystallization front at rates that exceed diffusion into the bulk liquid. A distinct correlation between what appears to be evidence for boundary phase build-up and two-phase intergrowths of Kfs+Qtz exists. Recalling the increasing growth rates (~ 8 to 50X) associated with Kfs+Qtz over Kfs alone in Table 5-5, it seems likely that this is indeed a correlation between growth rate and the formation of a boundary phase. Charges that contained a boundary phase (as evidenced by the discussion below) are marked by filled squares in Figures 5-5a through 5-5c. In the case of products from crystalline and glass rod starting materials, boundary phase formation seems to overlap loosely with the maximum crystallization rate envelopes—i.e., the “nose” areas of Figure 5-8. No evidence for the occurrence of boundary phases to date have been observed for liquids from powdered glass.

Figure 5-11a shows the occurrence of non-random vesicles on the inward side of a crystallization front. Owing to deformation of vesicles between crystals, the vesicle population is interpreted to have arisen during quench from an excess component of water (i.e., at a level that exceeds solubility under these conditions, i.e., ≥ 5 to 6 wt%) that formed a fluid phase at the boundary. Note that the vesicles show a distinct spatial correlation to the presence of Kfs+Qtz, rather than Kfs alone, and that some Kfs crystals terminate within vesicles.

Figure 5-11b displays run products from experiments at high undercoolings which contain chabazite, bearing compositions equivalent to glass except that its low BSE signal indicates (in this system) the presence of significant water. The composition of haplogranite melt with an excess water component (15 %) was recalculated as a mineral formula to yield a Na-dominant chabazite. Like the vesicles in the previous example, these crystals only occur in regions adjacent to intergrowths of Kfs+Qtz. Formation upon quench for these phases is discarded due to well-formed crystal shapes, crystals terminating into vesicles, comparable grain sizes to other crystals, and nucleation relations of feldspar on chabazite which suggests the zeolite was present at undercooling conditions.

Close structural similarities between zeolites and feldspars (e.g., Smyth 1982) are known. Stability fields and natural occurrences of zeolites are well documented (e.g., assessed using glass reactants: Cheng 1985), particularly in geothermal systems owing to hydrothermal alteration of glassy products (e.g., Gianelli et al., 1998). It seems probable that chabazite stability is reached within a water-rich fluid in glass in which the molar ratios of water to network formers and modifiers approach its stoichiometry. Because the

undercooling temperature for charges containing these phases lies below the region of T_G , excess water in a hydrothermal environment likely stabilizes zeolite, and thus “traps” the boundary layer in progress—i.e., chabazite may potentially represent a boundary layer.

The Record of Thermal History in Crystal Morphology

A correlation matrix of morphological variables for K-rich alkali feldspar grown in melts of variable starting materials show that several crystal shape descriptors correlate with either undercooling, time, or the combined term, $-\Delta T \cdot t$. This combined term, which is an effective measure of the extent of reaction, shows that in many cases no correlation is observed for either ΔT or t , but significant correlation is seen with their product, $-\Delta T \cdot t$. A data set of thousands of crystals among 25 experiments shows that similar statistical relationships between mean measures of morphology and run conditions are seen for melts of all starting materials; liquids originating from the crystalline mixture, however, show more statistical scatter.

The highest values of the correlation coefficient, R , for undercooling magnitude are seen for diameter aspect ratio (0.94) and low degrees of roundness (-0.78). Undercooling duration correlates with crystal thickness or breadth (0.90), crystal area (0.80) and low aspect ratio (-0.89). The combined $-\Delta T \cdot t$ term shows correlation with overall increasing crystal length (0.83), low solidity (-0.92), and low convexity (-0.85). These values were obtained from typically means of hundreds of crystals per experiment (depending on numbers of crystals), and some of these are summarized in Table 5-6. Although general trends may obviously be tracked by mean crystal morphology, the entire data set for each run product contains what appears to be more information about the run history. For example, at low undercoolings from short to long duration, solid and

nearly equant crystals are seen; these are easily distinguished by their values of high solidity (~ 1.00), low diameter aspect ratio (~ 1.0 to 2.0), and moderate roundness (~ 0.65). High diameter aspect ratio and moderately low values of solidity are invariably observed in products from moderate to high undercooling temperatures of short duration. Solidity continues to decrease with undercooling to higher degrees of undercooling. Convexity increases at very high undercooling and very long durations. Crystal size drops radically at these conditions whereas the number of crystals (Table 5-3) increases with an equivalent magnitude. As a whole, data for two- and three-phase intergrowths match the statistical trends of Kfs above. Climbing values of roundness and area with a decrease in solidity is a characteristic signature of the intergrowth-rich region that corresponds to maximum growth rate (Figure 5-6).

Combining these observations with the total solidification could distinguish “morphological regimes” as a function of the variables, $-\Delta T$ and t . Figure 5-12 represents an attempt to do this by splitting the trends among descriptor statistics into 5 groups, plus a region of zero crystallization (nucleation delay). Whereas the validity of the “Fibrous (<<solidity)” region of Figure 5-12 is tenuous due to few available data, the other categories seem, at least schematically, to fit the observed experimental matrix. The proximity of the fibrous and aplitic morphological fields to T_G suggests a control by the glass transition on resultant textures. This type of methodology—that utilizes the spatial signatures of crystals as a record of their T-t history—may have quantitative potential for aiding the extraction of the histories that produced solidified products from silicic magmas.

A HIERARCHY OF CONTROLS FOR CRYSTALLIZATION IN HYDROUS HAPLOGRANITE MELTS

1. Intrinsic Subliquidus Controls

The data from the run matrix suggest that undercooling bears the greatest effect on crystallization in this system. Regardless of starting medium, solidification appears to be most rapid at moderately high degrees of undercooling, from about $-\Delta T = -103$ to -150°C . With the increase of the extent of reaction at subliquidus conditions, or the combination of undercooling and time ($\Delta T \cdot t$), the intrinsic properties of high silica hydrous melt at 200 MPa are shown.

Boundary Effects of Subliquidus Crystallization

The range of undercooling above appears to be most efficient at creating enrichments of crystal-incompatible components (water-rich, markedly sodic below T_G) at the crystallization front. Nucleation rates appear to increase as growth rates drop upon very high degrees of undercooling, below the glass transition temperature. Here chabazite may join the assemblage as a boundary layer product. However, cumulative effects on the kinetics of crystallization below T_G have yet to be resolved.

Diffusion and Crystal Growth

Growth rates increase, by at least one order of magnitude for intergrown crystalline phases compared to single crystals. Rates of advancement of intergrown phases among the melts of variable starting material all increase as new crystalline phases join the assemblage. This observation is suggestive of an intrinsic diffusion control: a build-up of (incompatible) components during crystallization is alleviated when an additional phase begins to grow.

2. Path-Dependent Superliquidus and Starting Material Controls

The starting structural and nucleation state of the melt as assessed by variable superheating and variable starting material, suggests secondary controls on crystallization. This is in contrast with less polymerized liquids (and nucleating phases) of basic composition where it is the availability of remaining nuclei that ultimately exerts the greatest control on textural development (Lofgren 1983).

For undercooled silicic melts, the starting medium influences the rate and mechanisms of crystallization in three ways: (1), *nucleation lag times are longest for the least physically disrupted nuclei-free melt (at the preconditioning step)*, (2), *total solidification is fastest for the least physically disrupted nuclei-free melt (at the preconditioning step)*, and (3), *the spatial advance of crystallization is different for melts that lacked critical nuclei upon undercooling (crystallization as 2-D fronts) versus those that contained silicate nuclei upon undercooling (crystallization as 3-D networks)*. Contrary to valid nucleation arguments, and a shared vitreous starting state with the powdered glass, these results indicate that crystallization is most rapid for melts of nuclei- and importantly, vesicle-free glass. Preexisting nuclei in undercooled melts actually inhibit total crystallization. Nucleation delays in nuclei-free melts are on the order of several days at very low undercoolings and these decrease with undercooling, though no data were reported for behavior at very high undercoolings. Nucleation and growth rates both follow conventional wisdom and rise to a maximum and then fall with undercooling.

Concluding Remarks

This study illustrates at a minimum what care is initially required in an experimental approach to characterize crystallization in silicic liquids. With a careful, multivariable approach, the effects of the intrinsic properties of melt may eventually be elucidated. In order to derive the data needed to satisfactorily separate pertinent variables of solidification in granitic melts, the type of starting material and thermal pathway is paramount.

References Cited

- Bea, F. (1996) Controls on the trace element composition of crustal melts. *Transactions of the Royal Society of Edinburgh, Earth Sciences*, 87, 33-42.
- Boettcher, A.L. (1980) The systems Albite-Orthoclase-Water and Albite-Orthoclase-Quartz-Water: Chemographic phase relationships. *Journal of Geophysical Research B* 85, 6955-6962.
- Cashman, K. (1990) Textural constraints on the kinetics of crystallization of igneous rocks. In *Modern Methods of Igneous Petrology* (Nicholls, J. & Russell, J., eds.). Mineralogical Society of America, *Reviews in Mineralogy* 24, 259.
- Chakraborty, S. (1995) Diffusion in silicate melts. In *Structure, Dynamics and Properties of Silicate Melts* (Stebbins, J.F., McMillan, P.F., and Dingwell, D.B., eds.). Mineralogical Society of America *Reviews in Mineralogy* 32, 411-497.
- Cheng, H. (1985) Study on thermal stability of lead-type clinoptilolite and its complex property. *Petrological Research* 6, 135-148.
- Dingwell, D.B. (1993) Experimental strategies for the determination of granitic melt properties at low temperature. *Chemical Geology* 108, 19-31.
- Dingwell, D.B. (1995) Relaxation in Silicate Melts: Some Applications. In *Structure, Dynamics and Properties of Silicate Melts* (Stebbins, J.F., McMillan, P.F., and Dingwell, D.B., eds.). Mineralogical Society of America *Reviews in Mineralogy* 32, 21-66.
- Dingwell, D.B., Hess, K.U., and Knoche, R. (1996) Granite and granite pegmatite melts: volumes and viscosities. *Transactions of the Royal Society of Edinburgh, Earth Sciences*, 87, 65-72.

- Dowty, E. (1980) Crystal growth and nucleation theory and the numerical simulation of igneous crystallization. In *Physics of Magmatic Process* (R.B. Hargraves, ed.). Princeton University Press, 419-485.
- Fenn, P.M. (1977) The nucleation and growth of alkali feldspars from hydrous melts. *Canadian Mineralogist* 15, 135-161.
- Fenn, P.M., (1986) On the origin of graphic granite. *American Mineralogist* 71, 325-330.
- Gianelli, G., Mekuria, N., Battaglia, S., Chersicla, A., Garofalo, P., Ruggieri, G., Manganelli, M., Gebregziabher, Z. (1998) Water-rock interaction and hydrothermal mineral equilibria in the Tendaho geothermal system. *Journal of Volcanology and Geothermal Research* 86, 253-276.
- Hess, P.C. (1995) Thermodynamic mixing properties and the structure of silicate melts. In *Structure, Dynamics and Properties of Silicate Melts* (Stebbins, J.F., McMillan, P.F., and Dingwell, D.B., eds.). *Mineralogical Society of America Reviews in Mineralogy* 32, 145-190.
- Holland, T., and Powell, R. (2001) Calculation of phase relations involving haplogranitic melts using an internally consistent thermodynamic dataset. *Journal of Petrology* 42, 673-683.
- Hort, M., and Spohn, T. (1991) Numerical simulation of the crystallization of multicomponent melts in thin dikes or sills. 2. Effects of heterocatalytic nucleation and composition. *Journal of Geophysical Research B* 96, 485-499.
- Lofgren, G.E. (1980) Experimental studies on the dynamic crystallization of silicate melts. In *Physics of Magmatic Process* (R.B. Hargraves, ed.). Princeton University Press, 487-544.

- Lofgren, G.E. (1983) Effect of heterogeneous nucleation on basaltic textures: A dynamic
- Luth, W.C., and Tuttle, O.F. (1966) The alkali feldspar solvus in the system $\text{Na}_2\text{O}-\text{K}_2\text{O}-\text{Al}_2\text{O}_3-\text{SiO}_2-\text{H}_2\text{O}$. *American Mineralogist* 51, 1359-1373.
- McBirney, A.R. (1987) Constitutional zone refining of layered intrusions. In: (Parsons, I., ed.) *Origins of Igneous Layering*. NATO ASI Series C, 196, 437-452.
- Marsh, B.D. (1996) Solidification fronts and magmatic evolution. *Mineralogical Magazine* 60, 5-40.
- McMillan, P.F., and Wolf, G.H. (1995) Vibrational spectroscopy of silicate liquids. In *Structure, Dynamics and Properties of Silicate Melts* (Stebbins, J.F., McMillan, P.F., and Dingwell, D.B., eds.). *Mineralogical Society of America Reviews in Mineralogy* 32, 247-316.
- Morgan, G.M., and London, D. (1999) Crystallization of the Little Three layered pegmatite-aplite dike, Ramona District, California. *Contributions to Mineralogy and Petrology* 136, 310-330.
- Moynihan, C.T. (1995) Structural relaxation and the glass transition. In *Structure, Dynamics and Properties of Silicate Melts* (Stebbins, J.F., McMillan, P.F., and Dingwell, D.B., eds.). *Mineralogical Society of America Reviews in Mineralogy* 32, 1-19.
- Muncill, G.E., and Lasaga, A.C. (1987) Crystal-growth kinetics of plagioclase in igneous systems: One-atmosphere experiments and application of a simplified growth model. *American Mineralogist* 72, 299-311.
- Peterson, J.S., and Lofgren, G.E. (1986) Lamellar and patchy intergrowths in feldspars: Experimental crystallization of eutectic silicates. *American Mineralogist* 343-355.

- Russ, J.C. (1999) *The Image Processing Handbook*, 3rd Ed. CRC Press, Boca Raton, Florida. 771p.
- Shannon, J.R., Walker, B.M., Carten, R.B., and Geraghty, E.P. (1982) Unidirectional solidification textures and their significance in determining the relative ages of intrusions at the Henderson Mine, Colorado. *Geology* 10, 293-297.
- Smith, R.K., Tremallo, R.L., and Lofgren, G.E. (2001) Growth of megaspherulites in a rhyolitic vitrophyre. *American Mineralogist* 86, 589-600.
- Smyth, J.R. (1982) Zeolite stability constraints on radioactive waste isolation in zeolite-bearing volcanic rocks. *Journal of Geology* 90, 195-201.
- Stebbins, J.F. (1995) Dynamics and structure of silicate and oxide melts: Nuclear and magnetic resonance studies. In *Structure, Dynamics and Properties of Silicate Melts* (Stebbins, J.F., McMillan, P.F., and Dingwell, D.B., eds.). *Mineralogical Society of America Reviews in Mineralogy* 32, 191-246.
- Swanson, S.E. (1977) Relation of nucleation and crystal-growth to the development of granitic textures. *American Mineralogist* 62, 966-978.
- Toplis, M.J., Dingwell, D.B., Hess, K.U., and Lenci, T. (1997) Viscosity, fragility, and configurational entropy of melts along the join $\text{SiO}_2\text{-NaAlSiO}_4$. *American Mineralogist* 82, 979-990.
- Tuttle, O.F., and Bowen, N.L. (1958) Origin of granite in light of experimental studies in the system $\text{NaAlSi}_3\text{O}_8\text{-KAlSi}_3\text{O}_8\text{-SiO}_2\text{-H}_2\text{O}$. *Geological Society of America Memoir* 74, 153 p.

- Webb, S.L., and Dingwell, D.B. (1995) Viscoelasticity. In *Structure, Dynamics and Properties of Silicate Melts* (Stebbins, J.F., McMillan, P.F., and Dingwell, D.B., eds.). Mineralogical Society of America *Reviews in Mineralogy* 32, 95-120.
- Webber, K.L., Faulster, A.U., Simmons, W.B., and Foord, E.E. (1997) The role of diffusion-controlled oscillatory nucleation in the formation of line rock in pegmatite-aplite dikes. *Journal of Petrology* 38, 1777-1791.
- Winkler, H.G.F. (1949) Crystallization of basaltic magma as recorded by the variation of crystal size in dikes. *Mineralogical Magazine* 28, 557-574.

Table 5-1a. Melting Experiments for Determination of the Freezing Point of Hydrous Haplogranite at 200 MPa.

RUN ID	Temperature (C)	Duration (hrs)	Phases present
K44-C	695	144.0	Afs+Qtz+glass
K45-C	690	144.0	Afs+Qtz+glass
K46-C	685	144.0	Afs+Qtz+glass
K41-C	680	144.0	Afs+Qtz
K42-C	675	144.0	Afs+Qtz
K43-C	670	144.0	Afs+Qtz

Table 5-1b. Composition of the Synthetic Haplogranite Anhydrous Starting Glass and a Representative Hydrous Run Product

RUN ID		K72-P
Preconditioning Step (days)		730C (1)
Undercooling Step (days)		580C (1)
Analysis of	Coming Glass	glass
No. analyses, QEPMA	29	50
No. fragments analysed	9	1
wt %	sd	sd
SiO ₂	77.69 (0.51)	72.02 (0.34)
TiO ₂	0.01 (0.01)	nd
Al ₂ O ₃	13.02 (0.16)	11.87 (0.15)
FeO	0.02 (0.01)	nd
MnO	0.00 (0.00)	nd
MgO	0.01 (0.00)	nd
CaO	0.01 (0.01)	0.01 (0.01)
BaO	0.01 (0.01)	nd
Na ₂ O	4.60 (0.11)	3.85 (0.13)
K ₂ O	4.78 (0.09)	4.44 (0.11)
F	0.03 (0.03)	nd
Cl	0.01 (0.01)	nd
O=F	-0.013	
total	100.18 (0.53)	92.19 (0.43)
water by difference		7.81
Anhydrous CIPW Norm	Ab ₃₉ Or ₂₈ Qtz ₃₃	
Hydrous CIPW Norm		Ab ₃₆ Or ₂₇ Qtz ₃₇

*nd = not determined

Table 5-1c. Composition of the Haplogranite Melt as a Function of Degree of Water Saturation

RUN ID	CGm-1	CGm-2	CGm-3	CGm-4
Forward Step (days)	830C (6)	830C (6)	830C (6)	830C (6)
Total Added Water (wt%)	4.7	10.0	25.4	45.7
No. analyses, QEPMA	10	15	15	15
No. fragments analysed	2	2	2	1
wt %	sd	sd	sd	sd
SiO ₂	73.08 (0.54)	72.52 (0.48)	72.72 (0.40)	73.01 (0.47)
TiO ₂	0.01	0.02 (0.02)	0.01 (0.01)	0.01 (0.01)
Al ₂ O ₃	11.78 (0.20)	11.77 (0.13)	11.84 (0.20)	11.71 (0.16)
FeO	0.01 (0.01)	0.03 (0.01)	0.03 (0.01)	0.08 (0.04)
MnO	0.01	0.00	0.01 (0.01)	0.00
MgO	0.01 (0.01)	0.01 (0.01)	0.01 (0.00)	0.01 (0.01)
CaO	0.02	0.08 (0.08)	0.05 (0.10)	0.08 (0.10)
Na ₂ O	4.03 (0.13)	3.87 (0.13)	4.00 (0.11)	4.05 (0.09)
K ₂ O	4.38 (0.08)	4.48 (0.11)	4.50 (0.10)	4.46 (0.13)
P ₂ O ₅	0.01	0.01 (0.01)	0.01 (0.01)	0.01 (0.01)
F	0.03 (0.03)	0.03 (0.02)	0.02 (0.03)	0.03 (0.04)
Cl	0.01 (0.01)	0.01 (0.01)	0.01 (0.01)	0.01 (0.00)
O=F	-0.01	-0.01	-0.01	-0.01
O=Cl	0.00	0.00	0.00	0.00
total	93.37 (0.68)	92.80 (0.52)	93.19 (0.48)	93.45 (0.60)
alumina saturation index	1.03 (0.02)	1.04 (0.02)	1.03 (0.03)	1.01 (0.04)
water by difference	6.63	7.20	6.81	6.55
CIPW Norm Ab	36.7	35.6	36.5	36.9
CIPW Norm Or	27.9	28.7	28.7	28.3
CIPW Norm Qtz	35.4	35.7	34.8	34.8

Table 5-1d. Superliquidus Melting Experiments at 700° and 730°C

RUN ID	Temperature (C)	Duration (hrs)	Apx. Modal % crystals : glass
K48-C	700	168.0	5 : 95
K47-C	700	336.0	3 : 97
K50-C	700	672.0	2 : 98
K49-C	730	24.0	0 : 100

Table 5-2. Preliminary Nucleation Lag Times

superheating T (C)	superheating duration (days)	undercooling T (C)	undercooling magnitude T (C)	nucleation delay (days)
MELTS FROM GLASS POWDER				
730	1.0	670	13	6 to 8
730	1.0	655	28	< 8
730	1.0	630	53	3 to 8
730	1.0	605	78	< 8
730	1.0	580	103	1 hour to 3
730	1.0	550	133	2 to 5
730	1.0	533	150	< 2 hours
730	1.0	450	233	< 21
830	1.0	670	13	> 1 hour
830	1.0	655	28	< 21
830	1.0	630	53	> 1 hour
830	1.0	580	103	> 1 hour
830	1.0	533	150	> 1 hour
MELTS FROM GLASS ROD				
730	1.0	655	28	< 7
730	1.0	630	53	< 7
730	1.0	605	78	< 7
730	1.0	580	103	< 7
730	1.0	533	150	< 8
730	1.0	450	233	< 21
730	1.0	375	308	< 21
830	1.0	655	28	> 7
830	1.0	630	53	< 7
830	1.0	605	78	> 7
830	1.0	580	103	> 7
MELTS FROM FINE-GRAINED CRYSTALLINE MATERIALS				
730	1.0	670	13	< 1 hour
730	1.0	655	28	< 7
730	1.0	630	53	1 hour to 7
730	1.0	605	78	< 7
730	1.0	580	103	< 1
730	1.0	533	150	< 14
730	1.0	450	233	< 3
730	1.0	375	308	< 21
830	1.0	670	13	> 7
830	1.0	630	53	< 7
830	1.0	580	103	> 7
730	2.0	670	13	> 3
730	7.0	655	28	> 3

Table 5-3. Preliminary Nucleation Data for all Crystalline Phases

RUN ID	superheating T (C)	duration (hrs)	run T (C)	undercooling magnitude T (C)	duration (hrs)	total crystals	total nucleation centers
GLASS POWDER							
70-P	730	24.0	670	13	1.5	0	0
79-P	730	24.0	670	13	23.0	0	0
96-P	730	24.0	670	13	74.0	0	0
78-P	730	24.0	670	13	132.0	0	0
33-P	730	24.0	670	13	185.5	1	2
99-P	730	24.0	670	13	346.0	7	2
101-P	730	24.0	670	13	581.0	2	2
34-P	730	24.0	655	28	185.5	1	3
71-P	730	24.0	630	53	1.5	0	0
80-P	730	24.0	630	53	23.0	0	0
97-P	730	24.0	630	53	74.0	0	0
35-P	730	24.0	630	53	185.5	52	9
36-P	730	24.0	605	78	185.5	57	18
72-P	730	24.0	580	103	1.5	0	0
98-P	730	24.0	580	103	74.0	1	3
37-P	730	24.0	580	103	186.5	49	22
102-P	730	24.0	580	103	346.0	195	13
124-P	730	24.0	580	103	672.0	0	0
2-P	730	24.0	550	133	48.0	0	0
3-P	730	24.0	550	133	120.0	0	0
1-P	730	24.0	550	133	288.0	0	0
4-P	730	24.0	550	133	672.0	0	0
77-P	730	24.0	533	150	2.0	2	2
125-P	730	24.0	533	150	504.0	1501	56
126-P	730	24.0	450	233	504.0	>1000	>5
128-P	730	24.0	450	233	672.0	>1000	>5
73-P	830	24.0	670	13	1.5	0	0
12-P	830	144.0	655	28	516.0	5	0
74-P	830	24.0	630	53	1.5	0	0
75-P	830	24.0	580	103	1.5	0	0
76-P	830	24.0	533	150	1.5	0	0
GLASS ROD							
24-R	730	24.0	655	28	168.0	21	14
25-R	730	24.0	630	53	168.0	32	37
26-R	730	24.0	605	78	168.0	22	3
152-R	730	24.0	580	103	168.0	538	8
28-R	730	24.0	580	103	168.0	112	8
154-R	730	24.0	533	150	187.5	1198	11
148-R	730	24.0	450	233	504.0	61300	8

RUN ID	superheating T (C)	duration (hrs)	run T (C)	undercooling magnitude T (C)		total crystals	total nucleation centers
					(hrs)		
147-R	730	24.0	375	308	504.0	1479	9
144-R	730	24.0	375	308	672.0	3260	14
29-R	830	24.0	655	28	168.0	0	0
30-R	830	24.0	630	53	168.0	2	1
31-R	830	24.0	605	78	168.0	0	0
32-R	830	24.0	580	103	168.0	0	0
FINE-GRAINED CRYSTALLINE							
58-C	730	24.0	670	13	1.5	64	8
54-C	730	24.0	670	13	23.0	104	27
119-C	730	168.0	670	13	72.0	0	0
162-C	730	48.0	670	13	72.0	0	0
57-C	730	24.0	670	13	69.5	28	5
56-C	730	24.0	670	13	167.0	1	1
95-C	730	24.0	670	13	337.0	43	8
89-C	730	24.0	670	13	529.5	71	6
91-C	730	24.0	670	13	780.0	10	5
59-C	730	24.0	655	28	167.0	5	2
86-C	730	24.0	630	53	1.2	0	0
88-C	730	24.0	630	53	24.5	0	0
60-C	730	24.0	630	53	167.0	827	22
87-C	730	24.0	630	53	337.0	11	7
61-C	730	24.0	605	78	167.0	329	15
85-C	730	24.0	580	103	24.5	24	7
62-C	730	24.0	580	103	167.0	34	3
82-C	730	24.0	580	103	337.0	33	9
108-C	730	24.0	580	103	689.0	2495	32
109-C	730	24.0	533	150	336.5	>100	>10
83-C	730	24.0	450	233	72.5	24	2
111-C	730	24.0	450	233	343.0	2990	5
113-C	730	24.0	450	233	689.0	0	59
81-C	730	24.0	375	308	200.0	>100	>5
114-C	730	24.0	375	308	504.0	>1000	>5
55-C	830	24.0	670	13	167.0	0	4
53-C	830	24.0	630	53	167.0	1	1
52-C	830	24.0	580	103	167.0	0	0

Table 5-4. Preliminary Crystal Growth Rates of K-alkali feldspar

RUN ID	superheating T (C)	duration (hrs)	undercooling T (C)	undercooling magnitude T (C)	duration (hrs)	dT*t (hrs-degC)	length growth rate (um/hr)	area growth rate (um ² /hr)	solidity	solidity growth rate (um ² /hr)	Kfs+Qtz area growth rate (um ² /hr)
MELTS FROM GLASS POWDER											
99-P	730	24.0	670	13	346.0	4498.0	0.041	0.119	0.66	0.079	
101-P	730	24.0	670	13	581.0	7553.0	0.040	0.282	0.92	0.260	
98-P	730	24.0	580	103	74.0	7622.0	0.290	0.497	0.78	0.388	
102-P	730	24.0	580	103	346.0	35638.0	0.344	2.623	0.33	0.866	51.624
77-P	730	24.0	533	150	2.0	300.0	3.515	3.690	0.92	3.395	
125-P	730	24.0	533	150	504.0	75600.0	0.085	0.323	0.26	0.084	
MELTS FROM GLASS ROD											
148-R	730	24.0	450	233	504.0	117432.0	0.231	0.231	0.40	0.093	
147-R	730	24.0	375	308	504.0	155232.0	0.079	0.084	0.32	0.027	
MELTS FROM FINE-GRAINED CRYSTALLINE MATERIALS											
58-C	730	24.0	670	13	1.5	19.5	4.667	20.027	0.69	13.818	0.000
54-C	730	24.0	670	13	23.0	299.0	0.826	5.978	0.94	5.619	0.000
57-C	730	24.0	670	13	69.5	903.5	0.393	2.740	0.51	1.397	0.000
56-C	730	24.0	670	13	167.0	2171.0	0.359	5.554	0.80	4.443	0.000
59-C	730	24.0	655	28	167.0	4676.0	0.042	0.134	0.94	0.126	0.000
60-C	730	24.0	630	53	167.0	8851.0	0.258	1.832	0.29	0.531	0.000
61-C	730	24.0	605	78	167.0	13026.0	0.362	3.539	0.39	1.380	0.000
85-C	730	24.0	580	103	25.4	2616.2	1.048	2.574	0.77	1.982	0.000
83-C	830	24.0	670	450	72.5	32625.0	0.081	0.161	0.85	0.136	0.000

Table 5-5. Preliminary Solidity Crystal Growth Rates of K-aikali feldspar and Graphic Intergrowths

RUN ID	superheating T (C)	duration (hrs)	undercooling T (C)	undercooling magnitude T (C)	duration (hrs)	Kfs SOL growth rate ($\mu\text{m}^2/\text{hr}$)	Kfs+Qtz SOL growth rate ($\mu\text{m}^2/\text{hr}$)	Kfs+Qtz+Ab SOL growth rate ($\mu\text{m}^2/\text{hr}$)
MELTS FROM GLASS POWDER								
102-P	730	24.0	580	103	346.0	0.866	47.494	
125-P	730	24.0	533	150	504.0	0.084	0.490	1.136
MELTS FROM FINE-GRAINED CRYSTALLINE MATERIALS								
83-C	830	24.0	670	450	72.5	0.136	1.064	

Table 5-6. A Selected Representation of Preliminary Crystal Morphology Measurements

RUN ID	superheating T (C)	duration (hrs)	undercooling T (C)	undercooling magnitude T (C)	duration (hrs)	Kfs length (um)	Kfs area (um ²)	Kfs diam. aspect ratio	Kfs solidity	Kfs roundness	Kfs convexity
MELTS FROM GLASS POWDER											
99-P	730	24.0	670	13	346.0	9.52	30.38	1.70	0.92	0.70	0.62
101-P	730	24.0	670	13	581.0	23.15	164.12	1.92	0.95	0.55	0.70
98-P	730	24.0	580	103	74.0	13.26	22.12	6.38	0.78	0.10	0.61
102-P	730	24.0	580	103	346.0	29.45	168.83	2.72	0.66	0.26	0.64
Kfs+Qtz						224.00	1786.00	0.45	0.92	0.45	0.70
77-P	730	24.0	533	150	2.0	7.03	7.38	4.36	0.92	0.19	0.89
125-P	730	24.0	533	150	504.0	5.34	9.99	2.05	0.69	0.27	0.80
Kfs+Qtz						12.09	321.81	1.99	0.85	0.33	0.64
MELTS FROM GLASS ROD											
148-R	730	24.0	450	233	504.0	11.69	131.22	2.20	0.74	0.31	0.70
147-R	730	24.0	375	308	504.0	7.98	8.37	2.95	0.75	0.31	0.85
MELTS FROM FINE-GRAINED CRYSTALLINE MATERIALS											
58-C	730	24.0	670	13	1.5	6.79	25.51	1.22	0.91	0.71	0.69
54-C	730	24.0	670	13	23.0	14.62	43.96	2.25	0.88	0.40	0.61
57-C	730	24.0	670	13	69.5	8.13	31.00	2.13	0.90	0.33	0.80
56-C	730	24.0	670	13	167.0	5.38	11.31	1.48	1.00	0.50	0.96
59-C	730	24.0	655	28	167.0	7.00	22.37	1.48	0.94	0.58	0.92
60-C	730	24.0	630	53	167.0	17.60	84.21	1.96	0.72	0.25	0.42
61-C	730	24.0	605	78	167.0	10.22	33.92	3.12	0.66	0.24	0.70
85-C	730	24.0	580	103	25.4	4.29	6.43	3.49	0.77	0.51	0.74
83-C	730	24.0	450	233	72.5	4.12	4.79	2.10	0.85	0.60	0.90

Figure Captions.

Figure 5-1 (a) Different starting conditions of the same material. Backscattered electron micrographs are shown of a melt derived from a glass rods (left), melt derived from glass powder (center), and the crystalline material prior to the preconditioning step (right). The crystalline mixture shows crystals of alkali feldspar (up to 10 μm in length) and quartz (up to 3 μm). Melts from the crystalline material produced vesicles similar to melts from the powdered glass. **(b)** Powdered X-ray diffraction spectra for crystalline products from starting powdered glass. After 4 days, the intensity of quartz and feldspar peaks reaches a maximum and does not increase in crystallinity with longer durations of heating. The spectra from run products were checked against a haplogranite mineral mixture (HGS4: Evensen et al., 1999) and show equivalent characteristics.

Figure 5-2. Schematic run pathways for different experimental series as a function of time and temperature.

Figure 5-3. Coverage of undercooling steps following a superheating of $\sim 50^\circ\text{C}$ ($T = 730^\circ\text{C}$) for 1 day, using **(a)** glass powder, **(b)** glass rod, or **(c)** crystalline materials as the starting medium.

Figure 5-4. Number of observed crystals and nucleation centers as a function of time of the undercooling step after superheating at 730°C for 1 day. Melts originating from the powdered glass are shown as **(a)** total number of crystals and **(b)** number of nucleation

centers. In plot (a), the $-\Delta T = -13^{\circ}\text{C}$ trend reaches a maximum at ~ 350 hours. Melts originating from glass rods, (c) and (d), and from the crystalline material, (e) and (f) are shown as total numbers of crystals or nucleation centers, respectively.

Figure 5-5. Examples of mineral growth sequences in run products. (a)

Backscattered electron micrograph of Experiment K125-P (field of view is $375 \times 375 \mu\text{m}$) that corresponds to the letter D in Figure 5-8a. Modal proportions of crystalline phases vary as 5 discrete zones in the crystal cluster at the lower center of the image. The arrow depicts the crystallization pathway, going sequentially from (1) $\text{Ab}_7\text{Or}_{93}\text{Qtz}_0$ to (2) $\text{Ab}_0\text{Or}_0\text{Qtz}_{100}$ to (3) $\text{Ab}_{16}\text{Or}_{61}\text{Qtz}_{23}$ to (4) $\text{Ab}_{44}\text{Or}_{14}\text{Qtz}_{42}$ and finally to (5) $\text{Ab}_{31}\text{Or}_{26}\text{Qtz}_{43}$.

(b) Backscattered electron micrograph of Experiment K108-C (field of view is $500 \times 500 \mu\text{m}$) that corresponds to the letter C in Figure 5-8b. Modal proportions of crystalline phases vary as 3 discrete zones from the nucleation center at right inward (shown by the arrow), going sequentially from (a) $\text{Ab}_8\text{Or}_{92}\text{Qtz}_0$ to (b) $\text{Ab}_{17}\text{Or}_{62}\text{Qtz}_{21}$ to spherulitic intergrowths of (c) $\text{Ab}_{44}\text{Or}_{16}\text{Qtz}_{40}$. Vapor-grown quartz is also shown at far right.

(c) Backscattered electron micrograph of Experiment K113-C (field of view is $150 \times 150 \mu\text{m}$) that corresponds to the letter E in Figure 5-8c. Modal proportions of crystalline phases vary as 3 discrete zones growing outward from the nucleation center at right (shown by the arrow), going sequentially from (a) $\text{Ab}_{12}\text{Or}_{88}\text{Qtz}_0$ to (b) $\text{Ab}_{10}\text{Or}_{49}\text{Qtz}_{41}$ to (c) $\text{Ab}_{16}\text{Or}_{68}\text{Qtz}_{16}$. Vapor-grown quartz is also shown at far right.

Figure 5-6. Mechanisms of crystallization in run products. (a) Backscattered electron micrograph of Experiment K52-R (field of view is $375 \times 375 \mu\text{m}$). Individual crystals of

K-feldspar and clusters of intergrown quartz + K-feldspar are present in glass. Sidewall nucleation is dominant showing growth both parallel and inward from the sidewall (black space at right). Note that crystals are not located at the melt-vapor-capsule interface, but proximal to it. (b) A mosaic of backscattered electron micrographs of Experiment K60-C showing crystals of Kfs (showing light values) in vesicular glass near the sidewall (field of view is 500 x 500 μm in each image). Though nucleation begins at the sidewall, the advancement of the crystallization front occurs from left to right (indicated by the arrow), as a network of crystals directed inward into melt. This is in contrast with planar fronts that crystallize parallel to the sidewall in other systems. No significant crystallization occurs in this region of the charge outside the area denoted by the dashed lines.

Figure 5-7. Maximum crystal length (of Kfs) as a function of time of the undercooling step after superheating at 730°C for 1 day. (a) Melts originating from the powdered glass; (b) melts originating from the glass rods; (c) melts originating from the crystalline material.

Figure 5-8. Total percent crystallization of undercooled melts as a function of time. (a) Melts originating from the powdered glass; (b) melts originating from the glass rods; (c) melts originating from the crystalline material.

Figure 5-9. Sequences of growth for single and intergrown minerals in undercooled melts originating from (a) glass powder, (b) glass rod, or (c) crystalline materials.

Figure 5-10 (a) Vesicle populations in run products above and below T_G . Backscattered electron micrographs of Experiments K147-R (left; 300 x 300 μm), K60-C (right; 1500 x 1500 μm) and K12-P (lower center; 750 x 750 μm). Different vesicle size populations are shown between the upper left image and the others. (b) Vesicle perimeter versus maximum vesicle diameter for vesicle populations above and below T_G .

Figure 5-11. Evidence for the formation of boundary layers at crystallization fronts. (a) Backscattered electron micrographs of Experiment K152-R showing anomalous vesicle occurrences near crystallization fronts of Kfs+Qtz. Two images are shown for adequate representation of the experiment (field of view of the upper image is 1500 x 1500 μm ; the lower image represents 375 x 375 μm). Single Kfs crystals are also shown. The vesicles at the upper left of the upper image represent typical vesicles that occur periodically in glasses from melts of the glass rod material. The smaller vesicles likely represent excess water at a boundary layer produced by rapid crystallization of intergrowths of Kfs+Qtz. (b) Backscattered electron micrographs of Experiment K144-R (at top; field of view is 94 x 94 μm) and K147-R (at bottom; field of view is 50 x 50 μm). The light phase is comprised of intergrowths of Kfs+Qtz, whereas the dark phase is the “zeolite”. The remaining region is glass containing unusually small vesicles. Charge edges (sidewalls) are shown at right in each image.

Figure 5-12. Preliminary “fields” of crystal morphology in granitic melt. Diagnostic spatial features of crystals are indicated in each grouping.

Figure 5-1a.

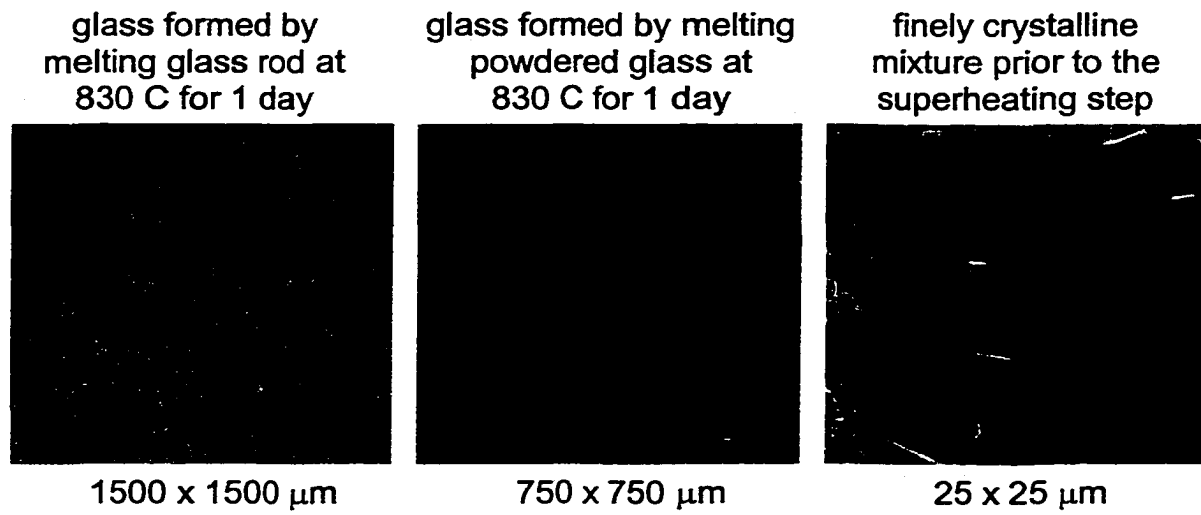


Figure 5-1b.

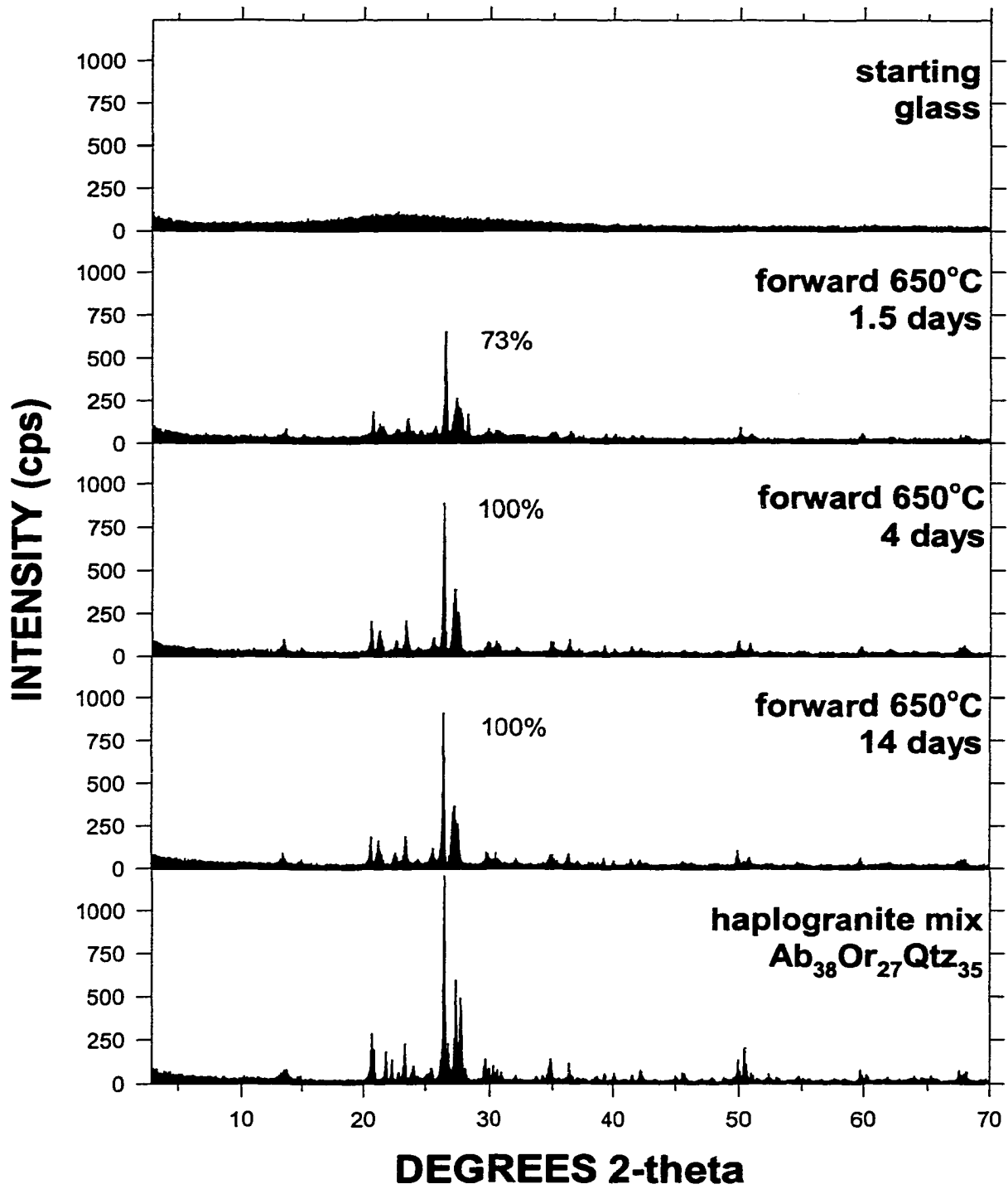


Figure 5-2.

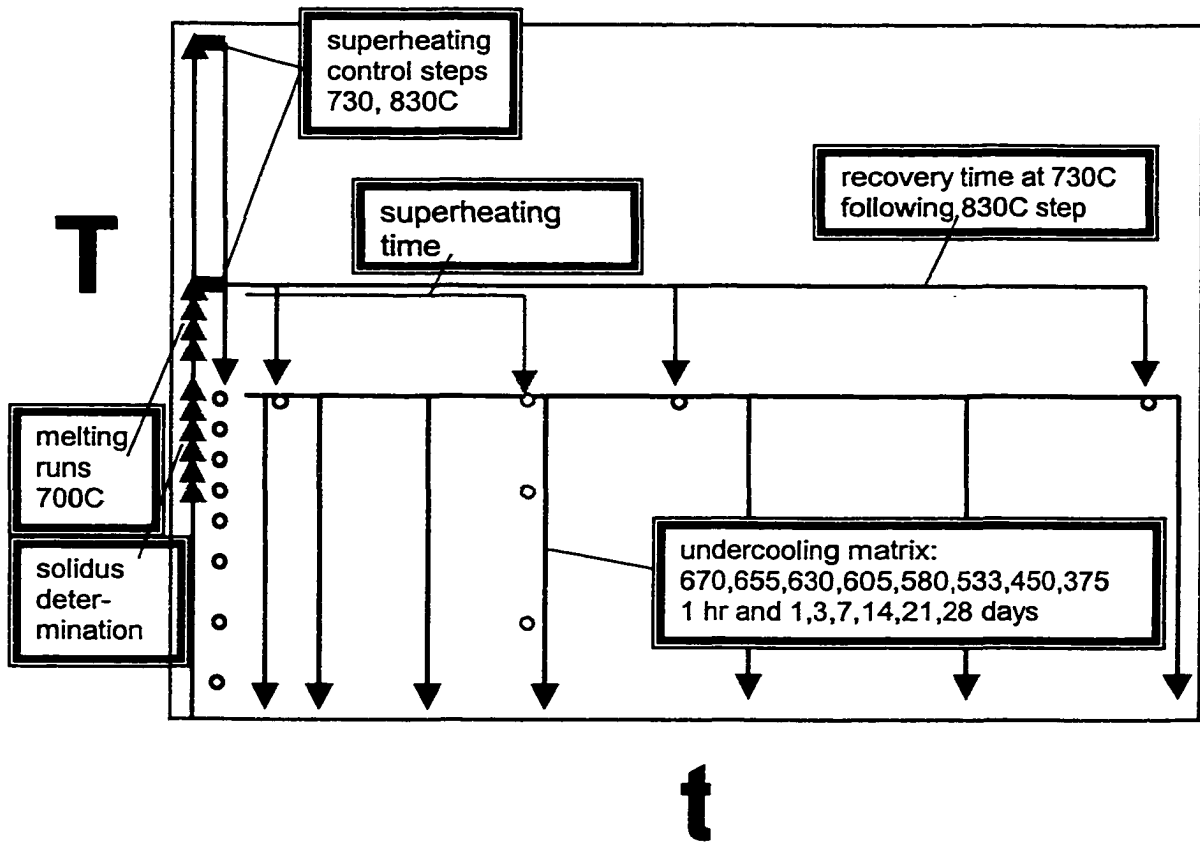


Figure 5-3a.

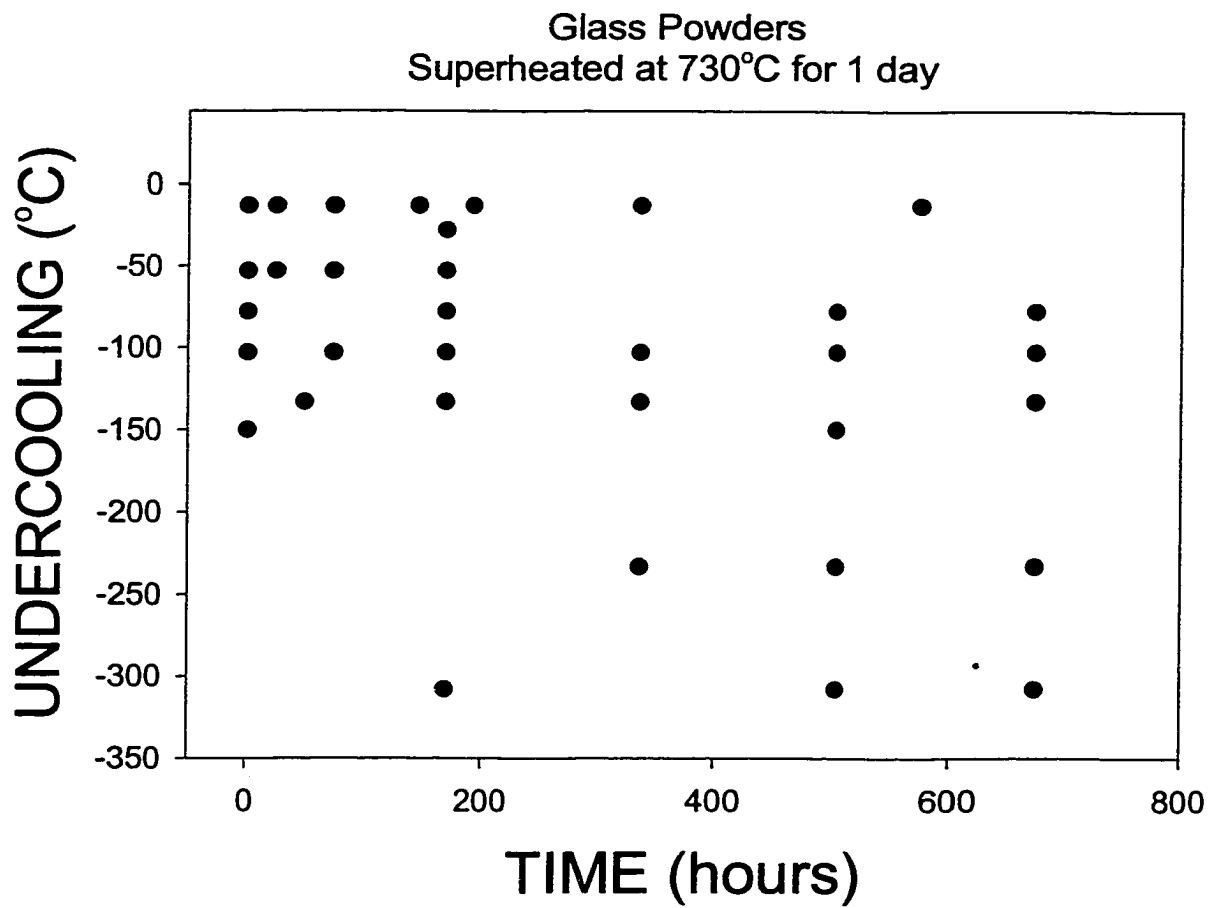


Figure 5-3b.

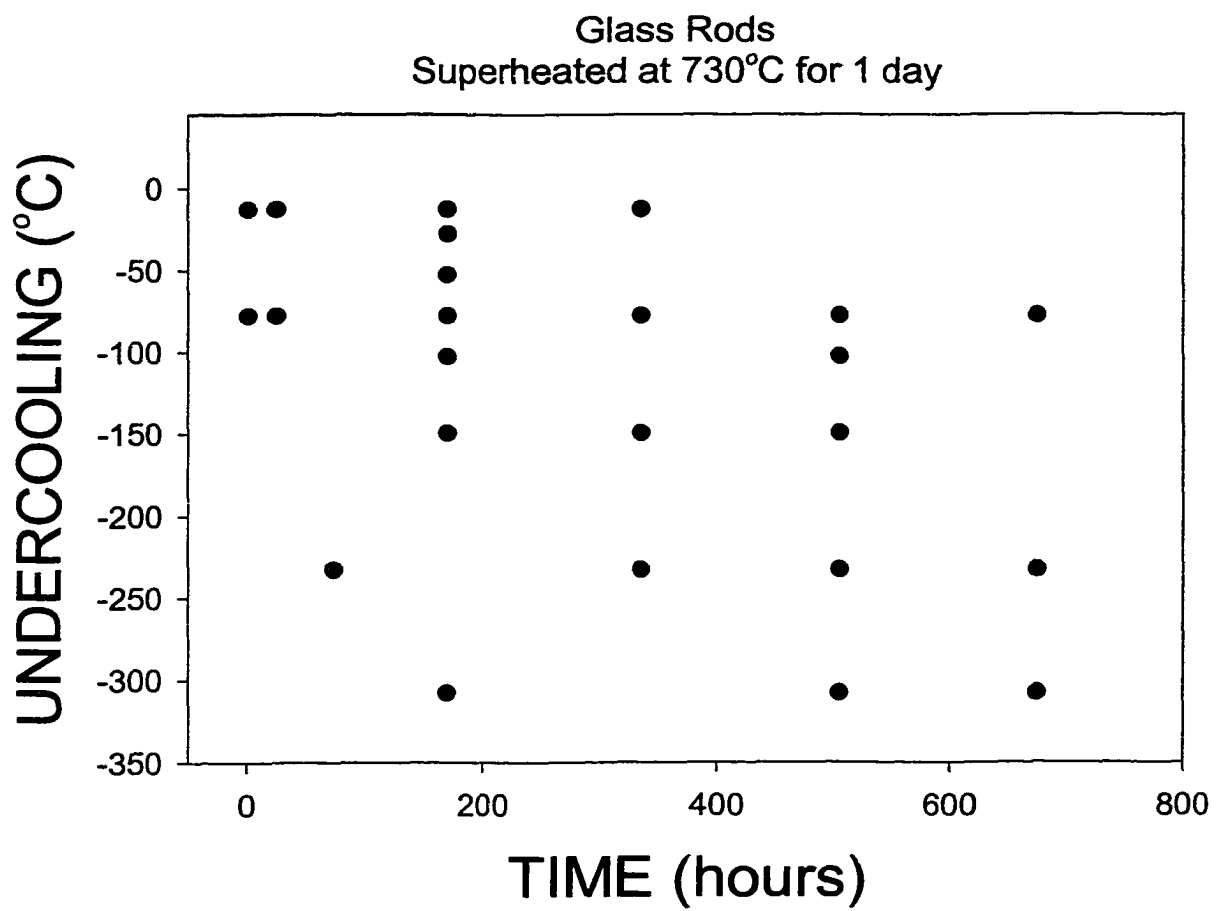


Figure 5-3c.

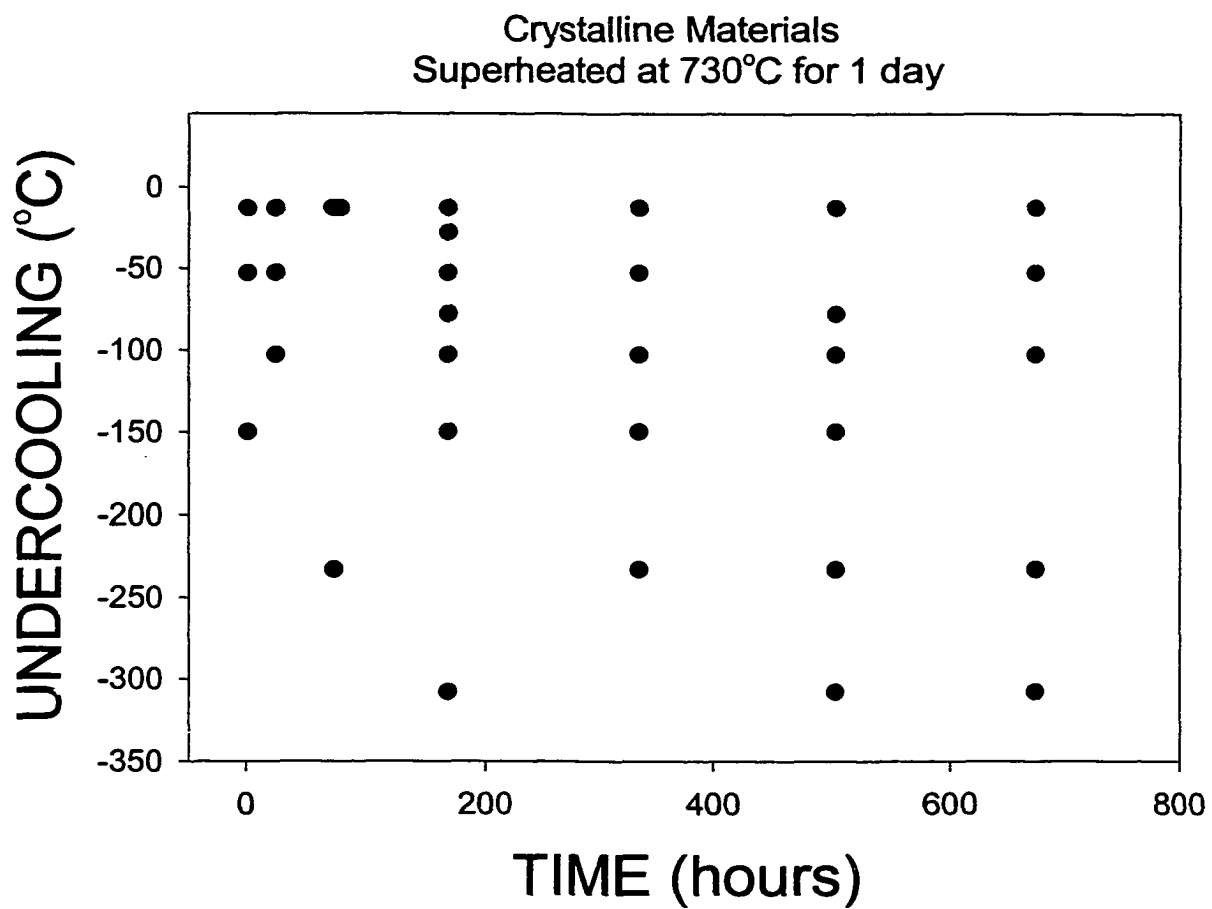


Figure 5-4a.

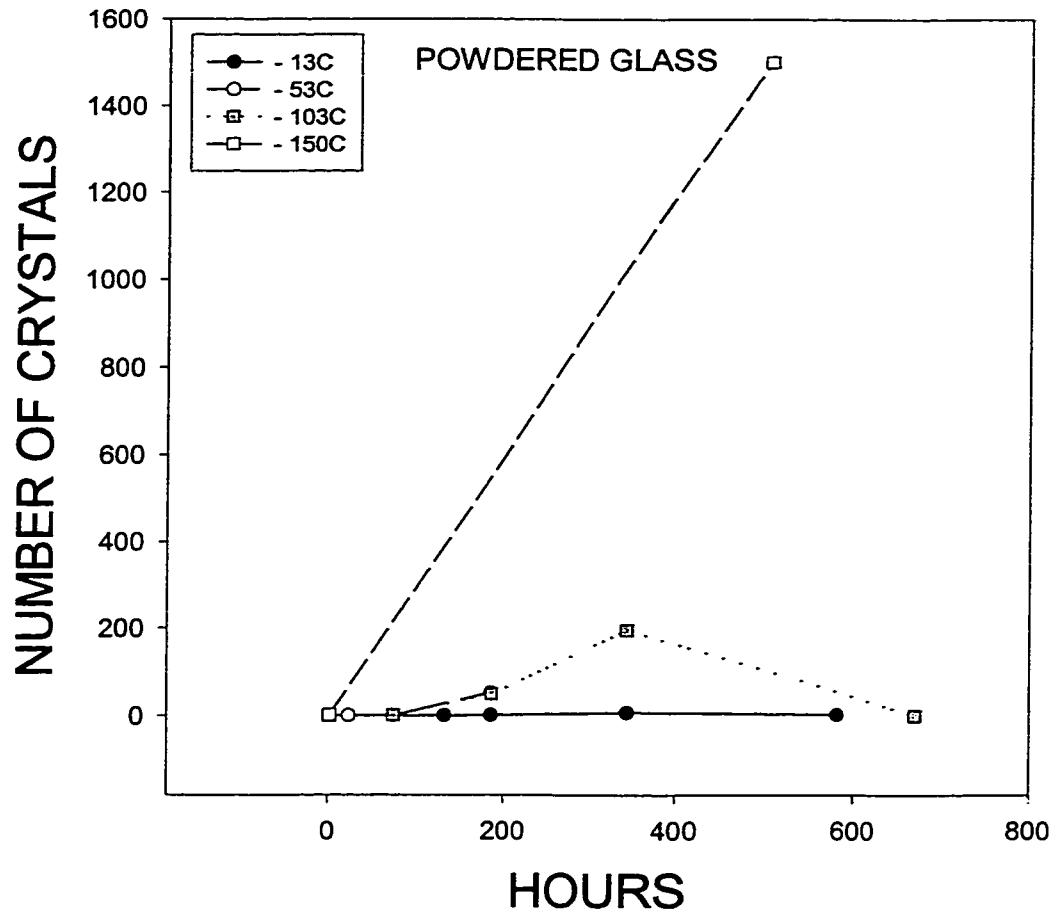


Figure 5-4b.

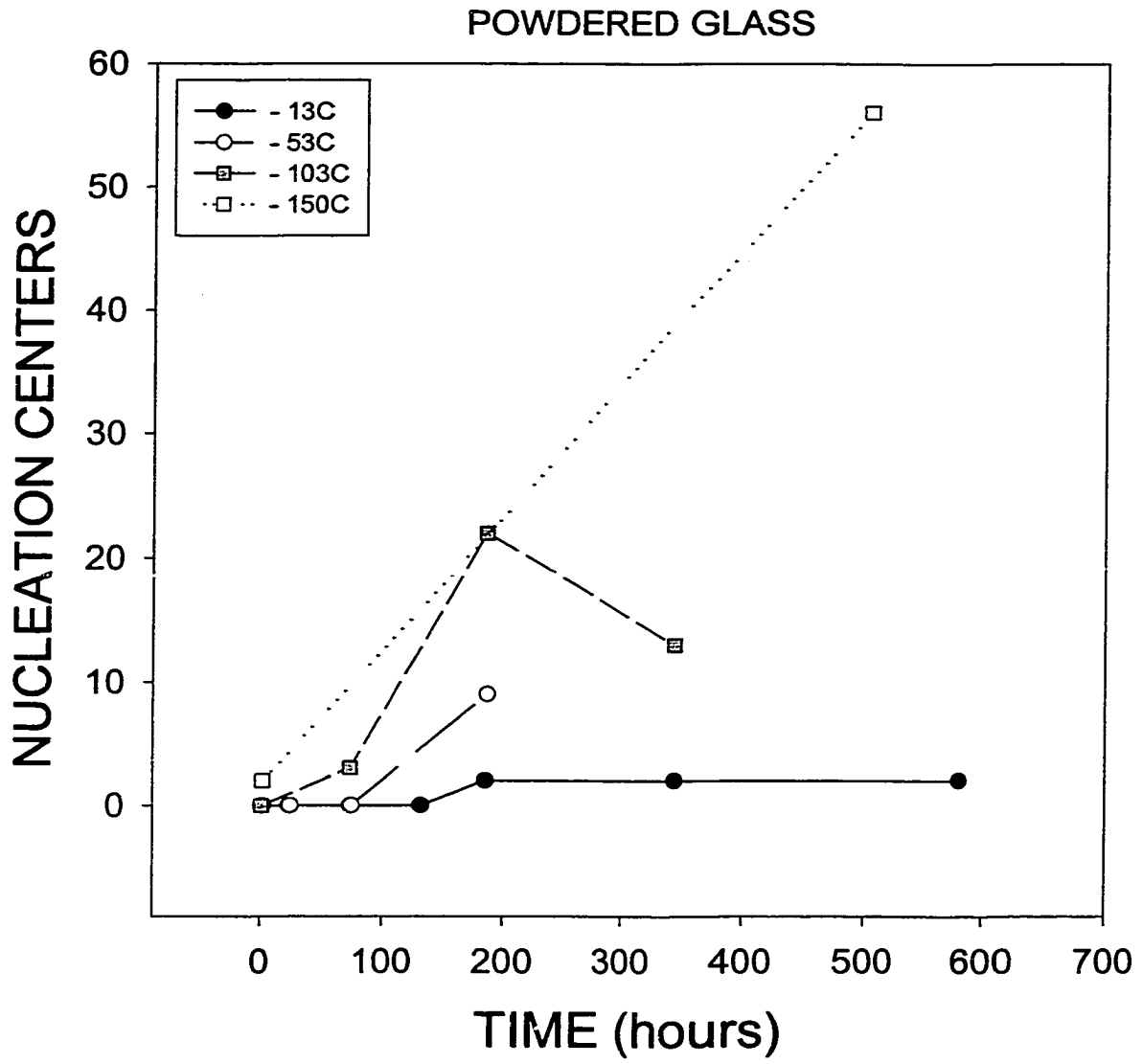


Figure 5-4c.

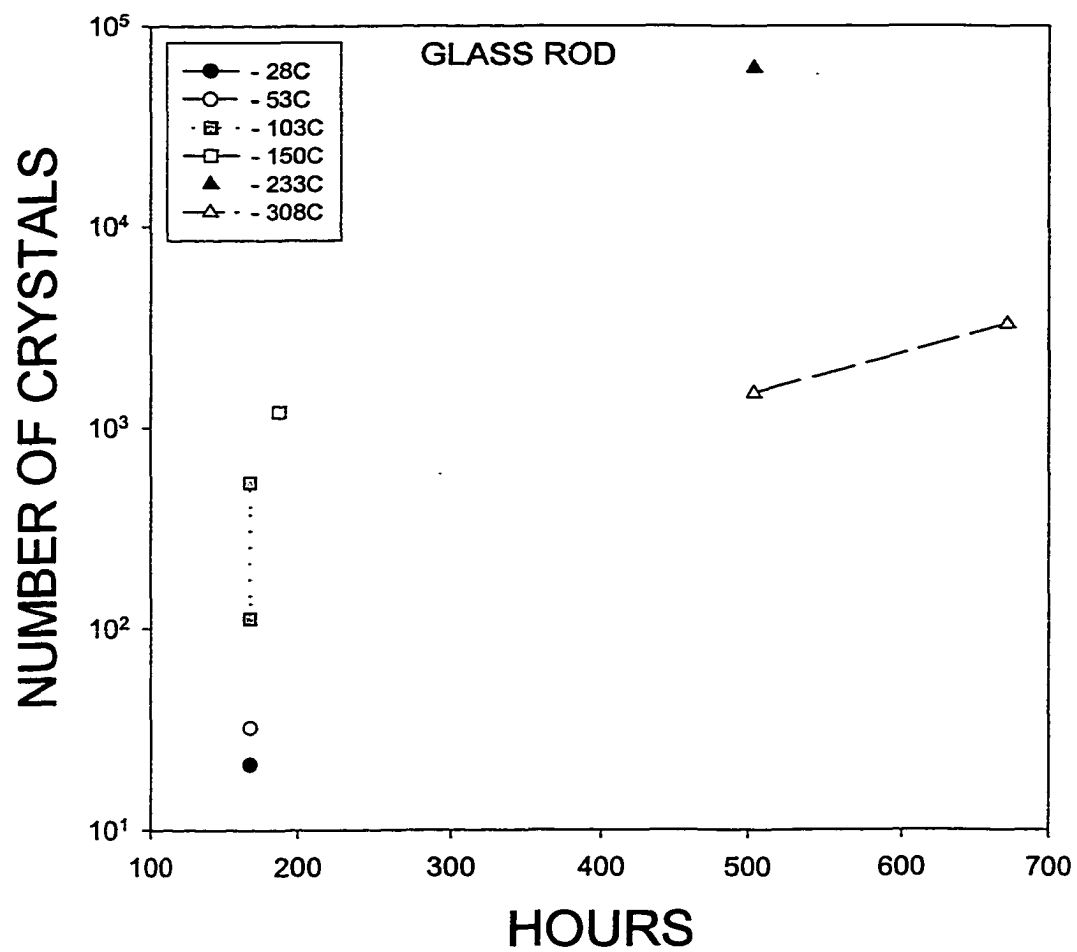


Figure 5-4d.

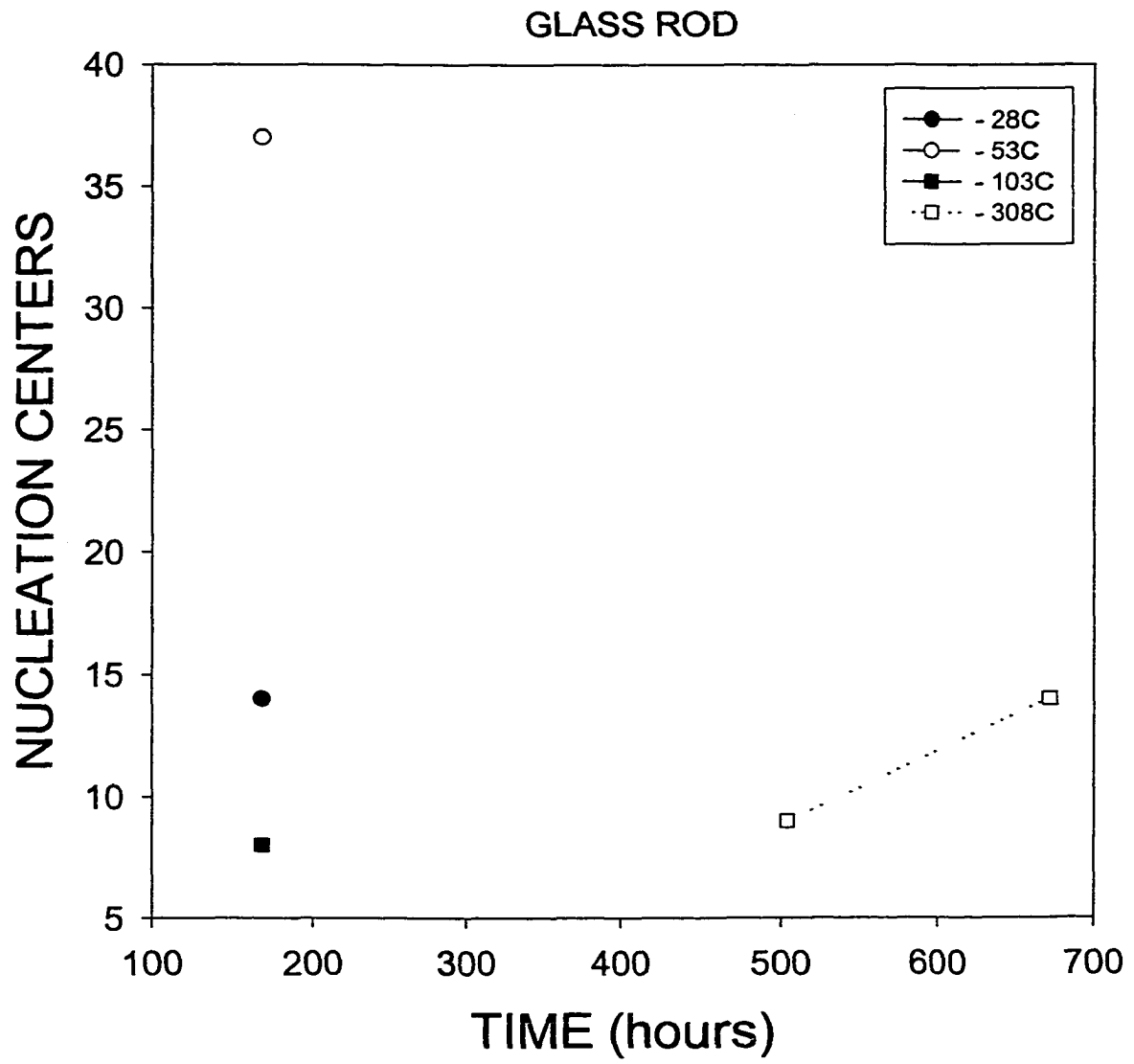


Figure 5-4e.

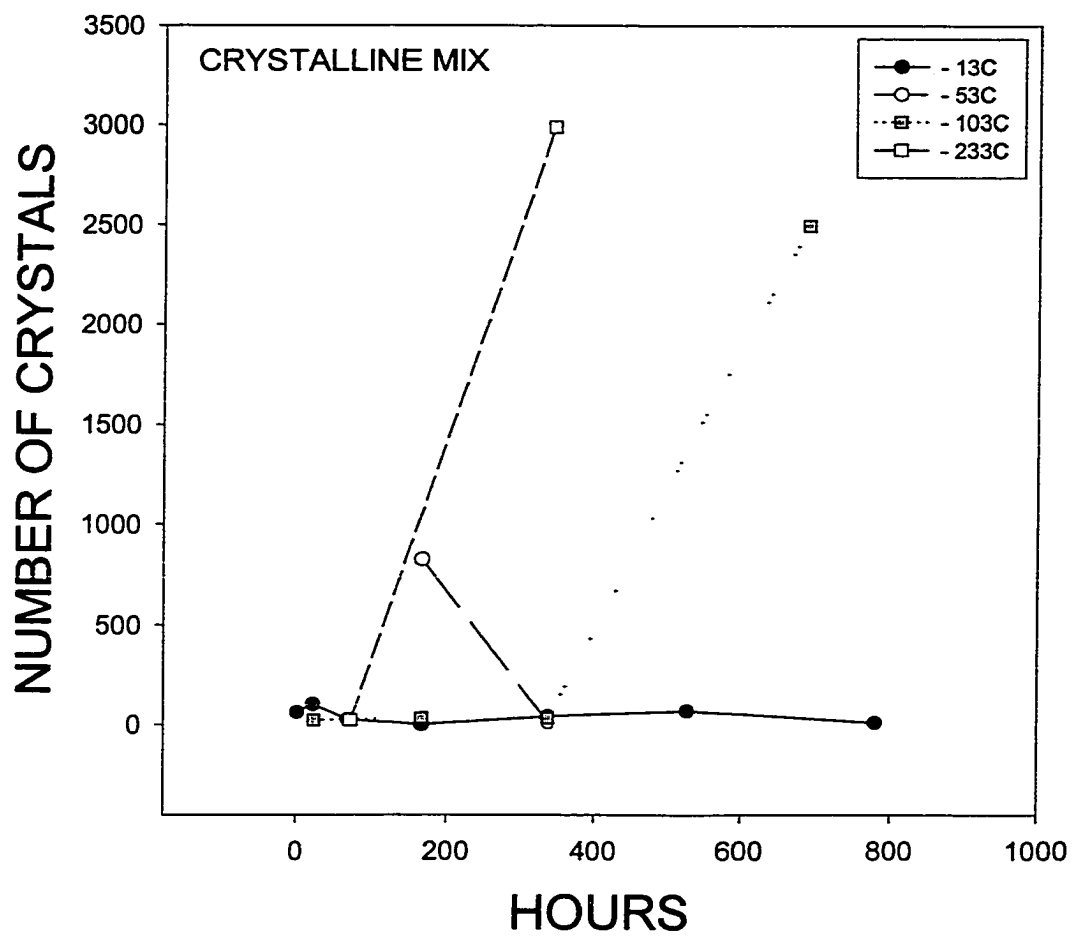


Figure 5-4f.

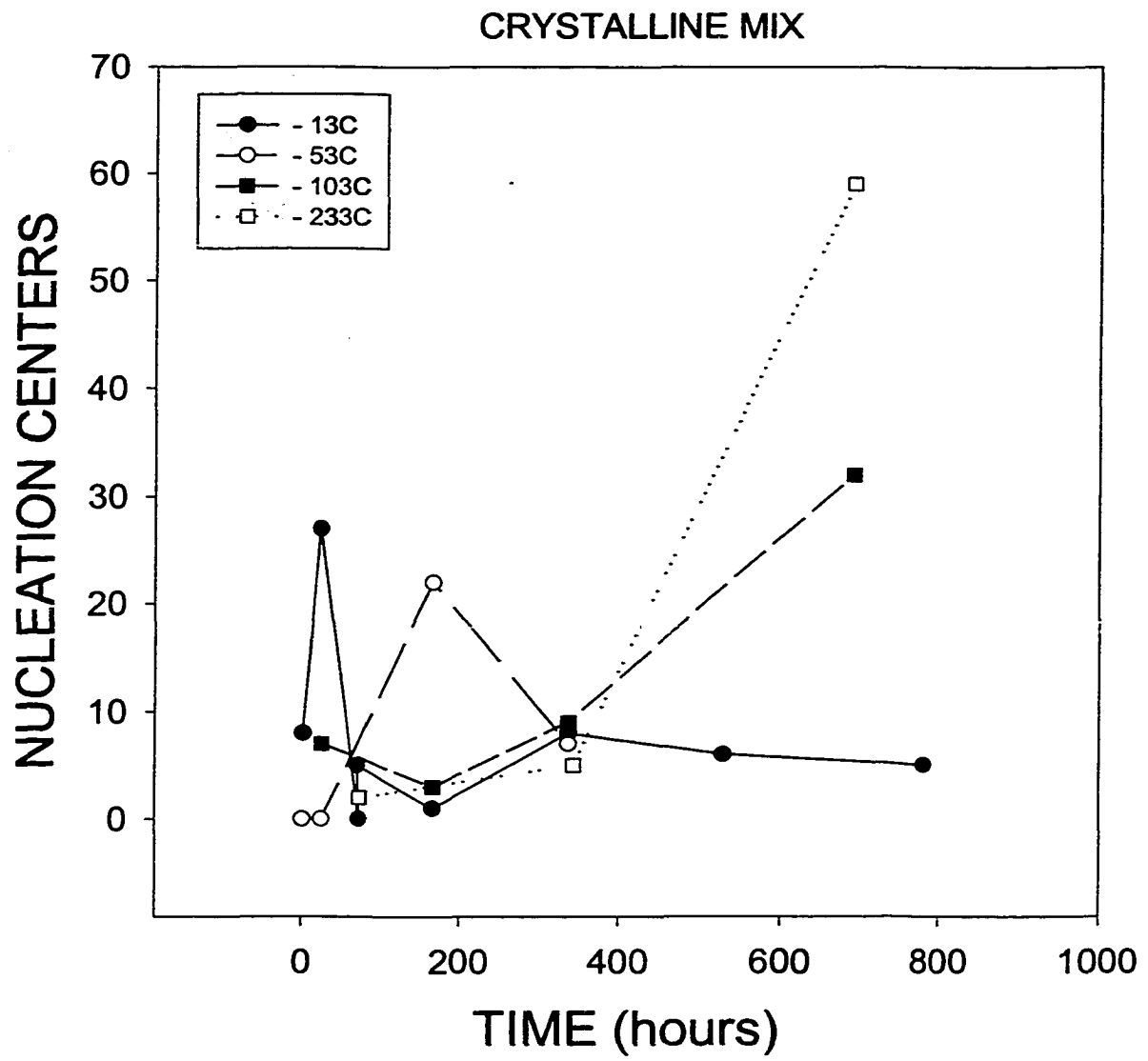
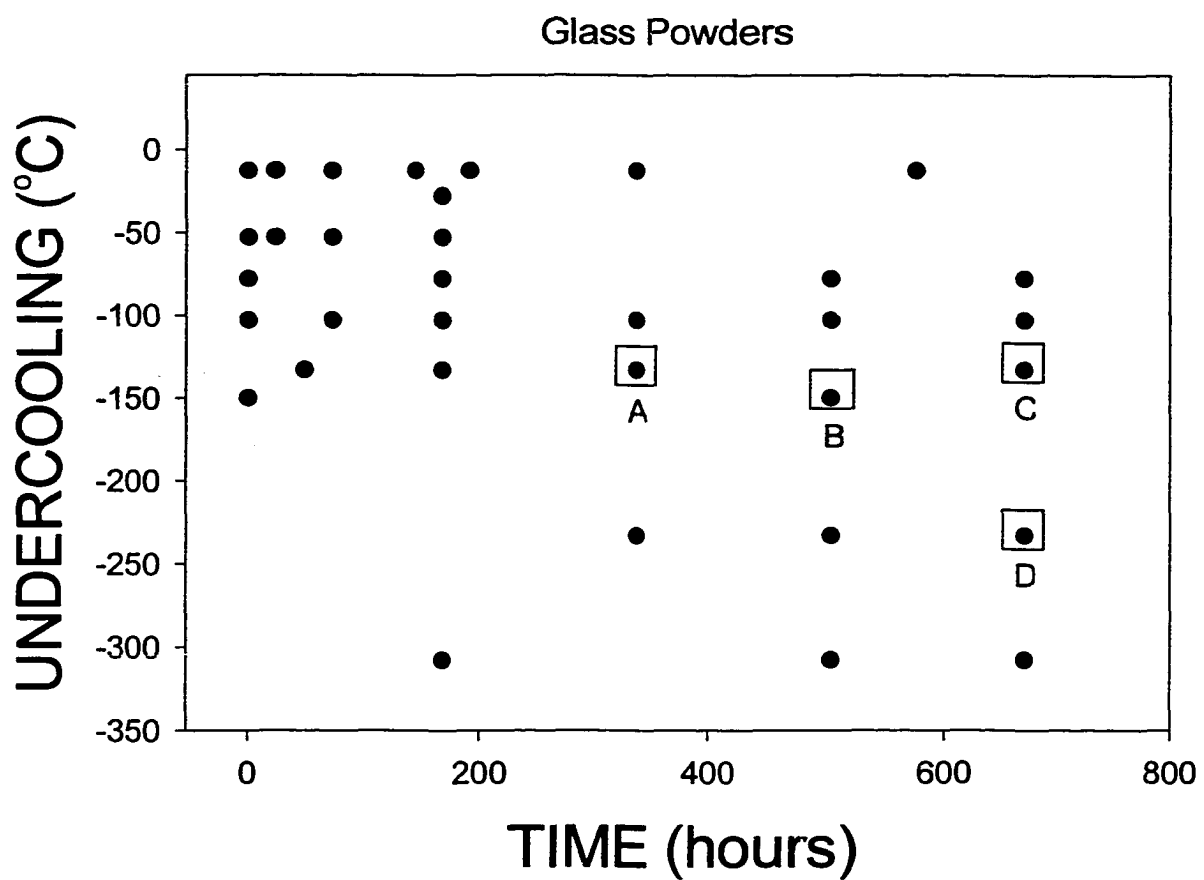
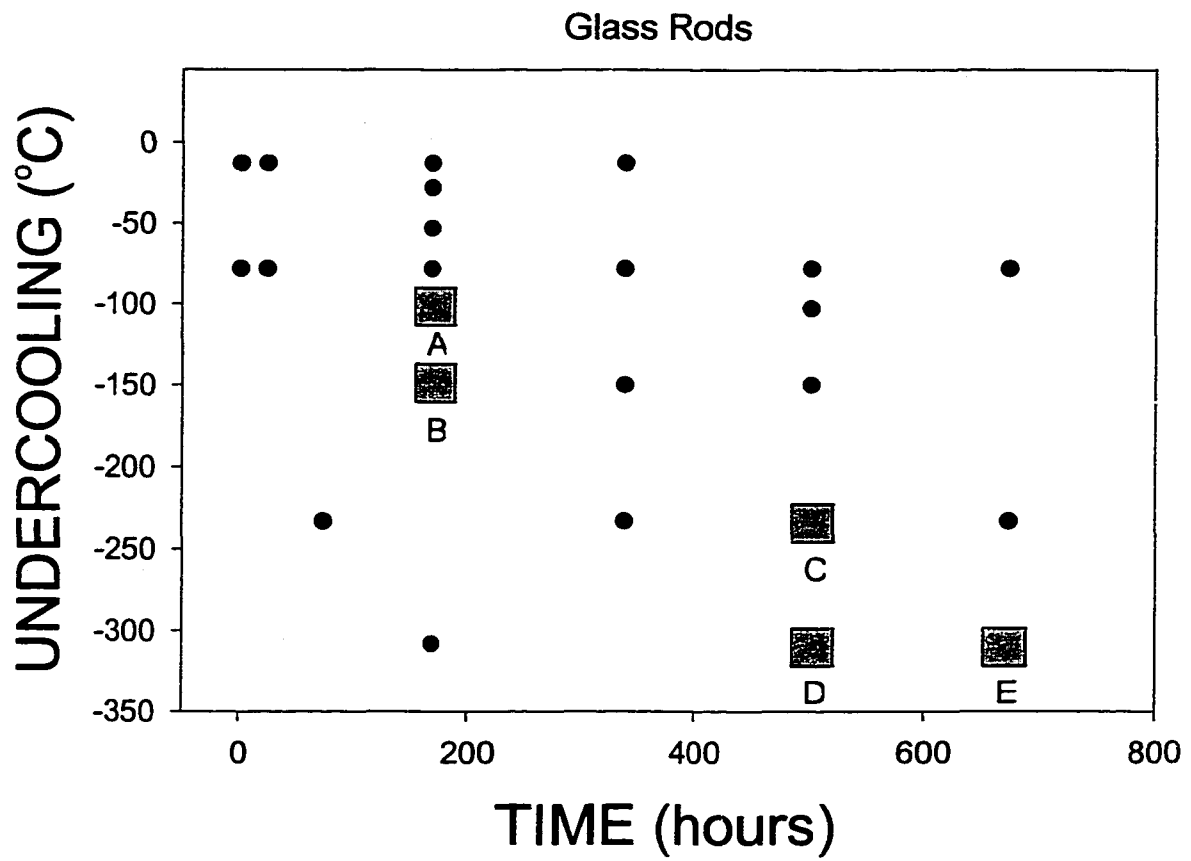


Figure 5-5a.



- A $K \rightarrow KQ$
- B $K \rightarrow KQ \rightarrow Q \rightarrow KA \rightarrow KAQ$
- C $K \rightarrow KQ \rightarrow KA \rightarrow K+A \rightarrow$
- D $K \rightarrow KAQ \rightarrow KQ$

Figure 5-5b.



- A K → KQ → Q
- B K → KQ → Q
- C K → KQ → Q → K →
- D K → KQ → ZEO
- E KQ → ZEO

Figure 5-6a.

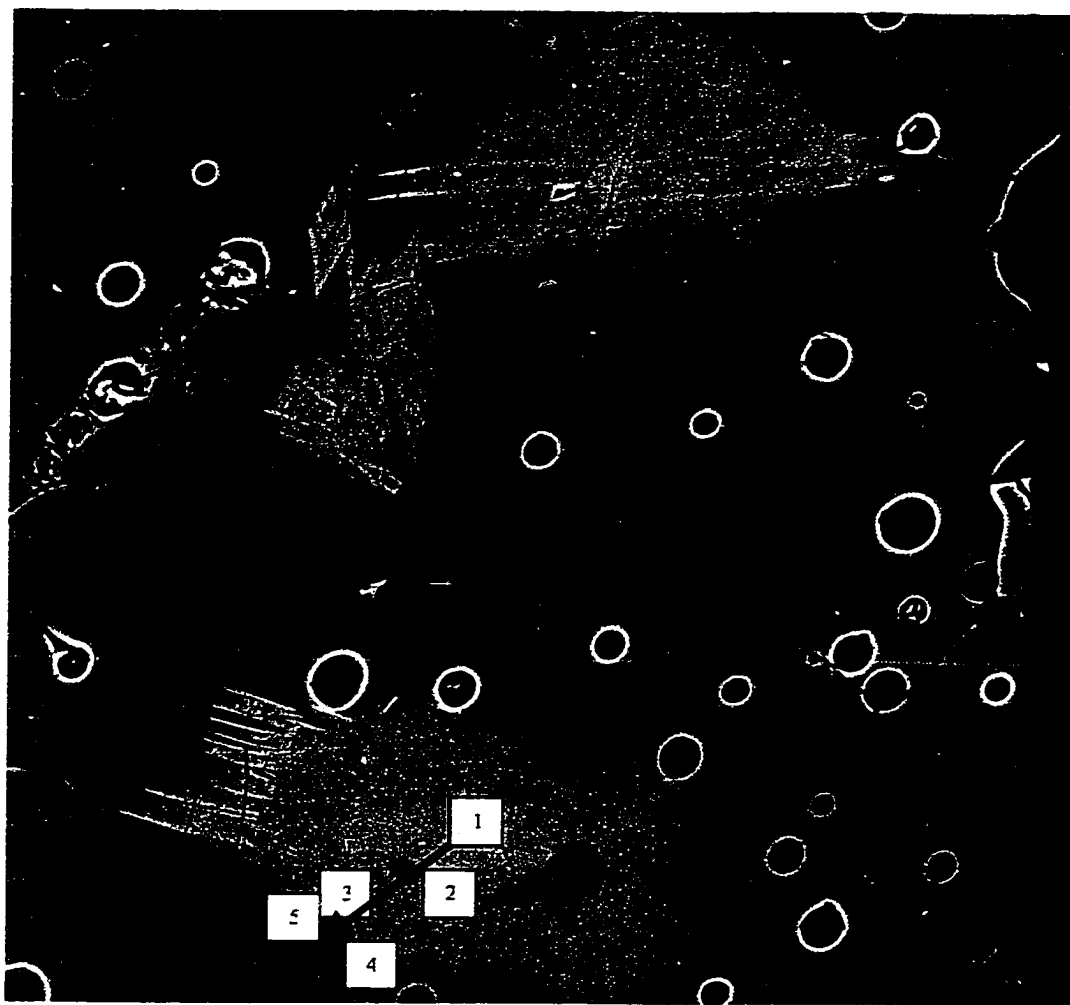


Figure 5-6b.

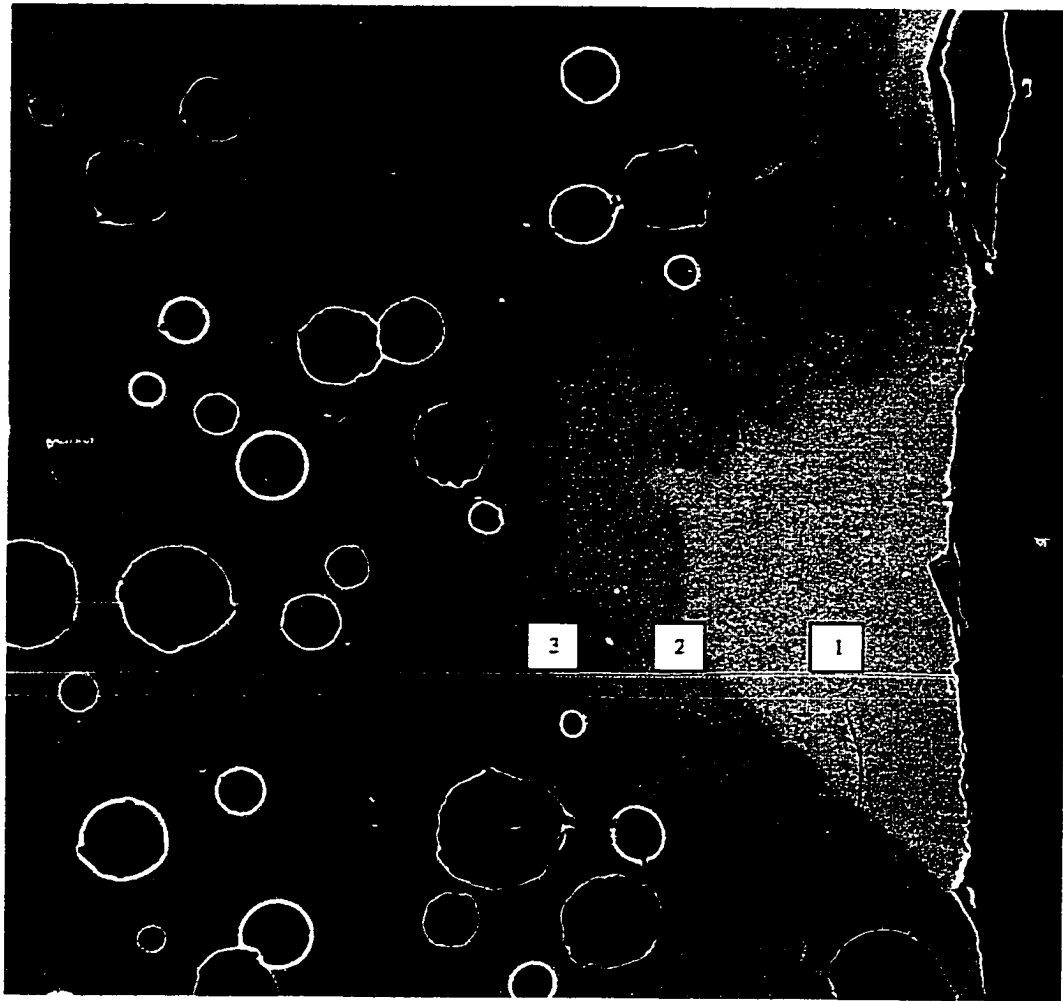


Figure 5-6c.

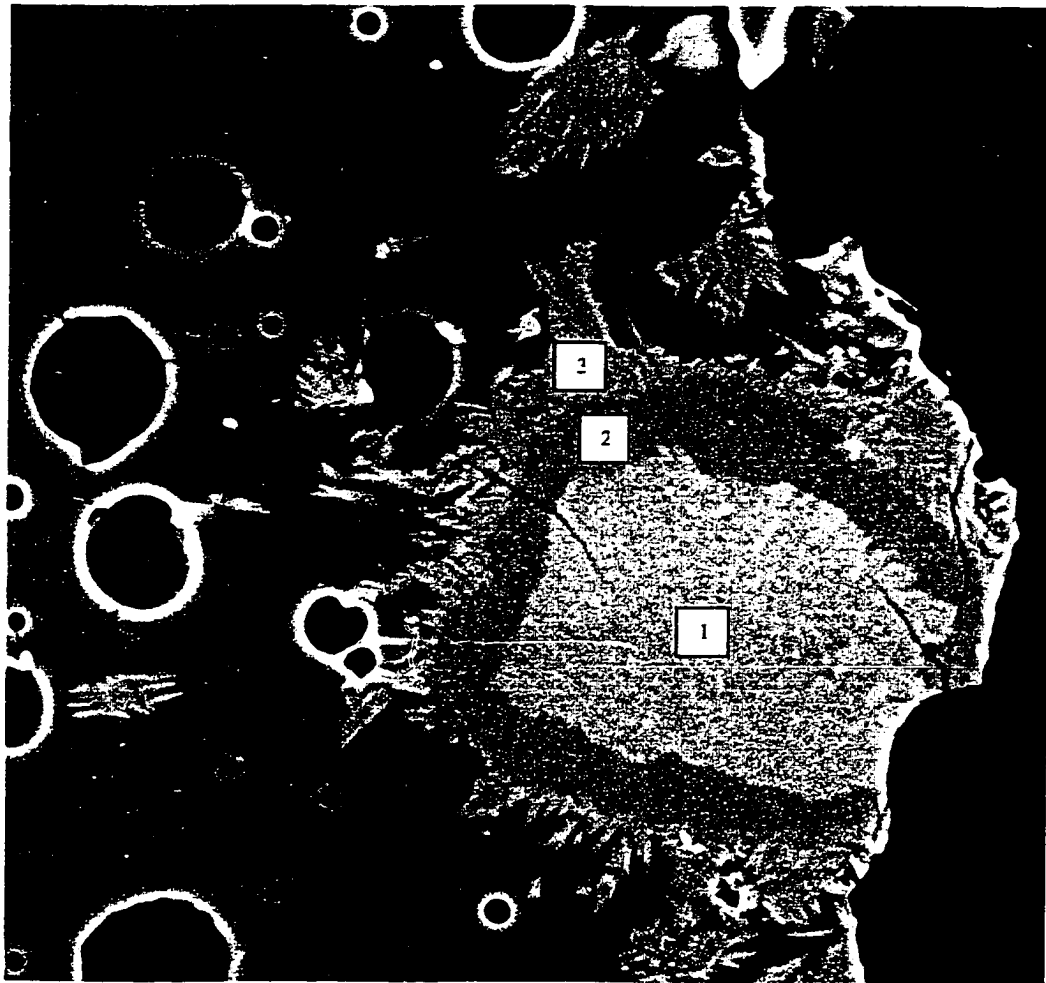


Figure 5-7a.

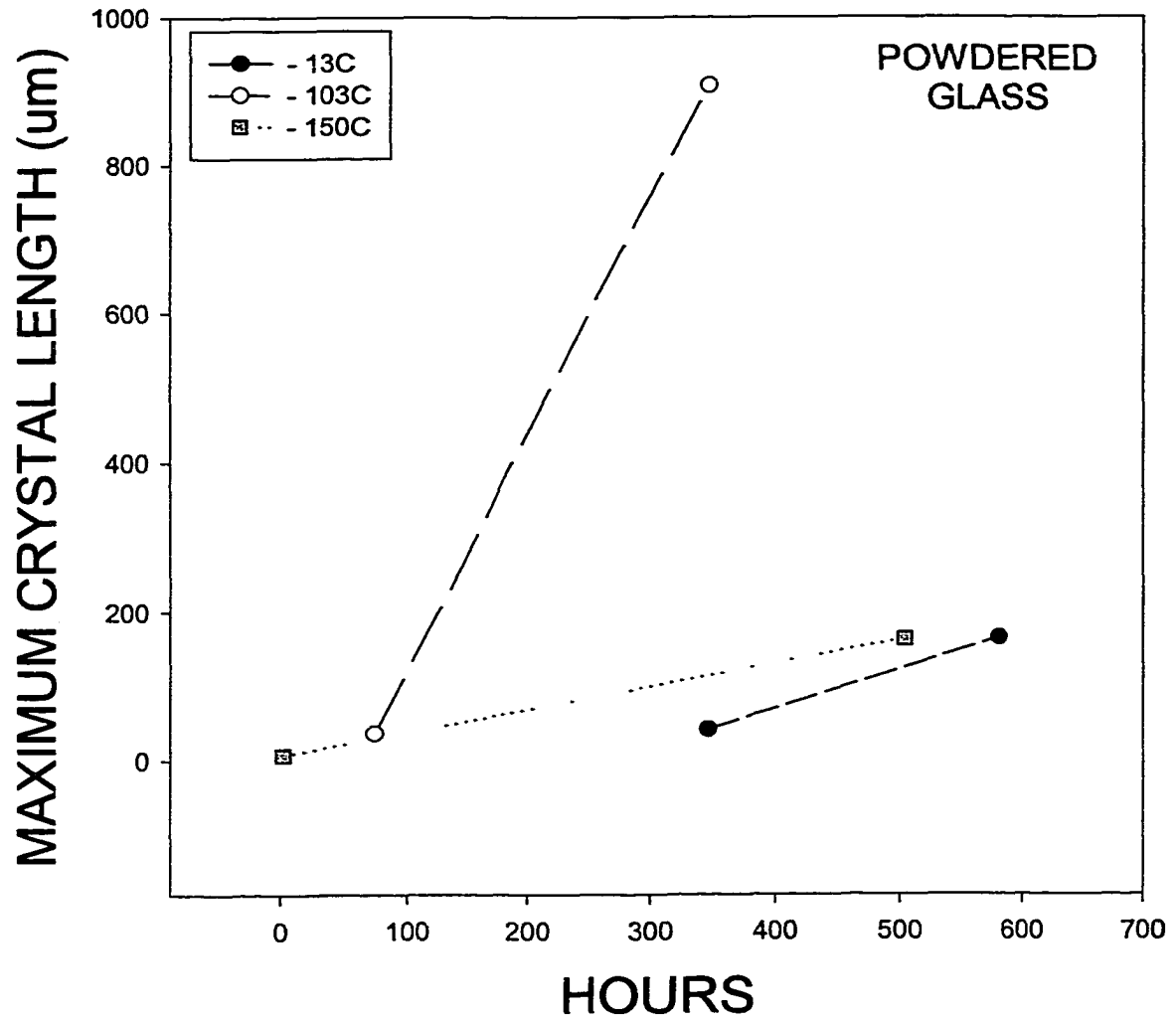


Figure 5-7b.

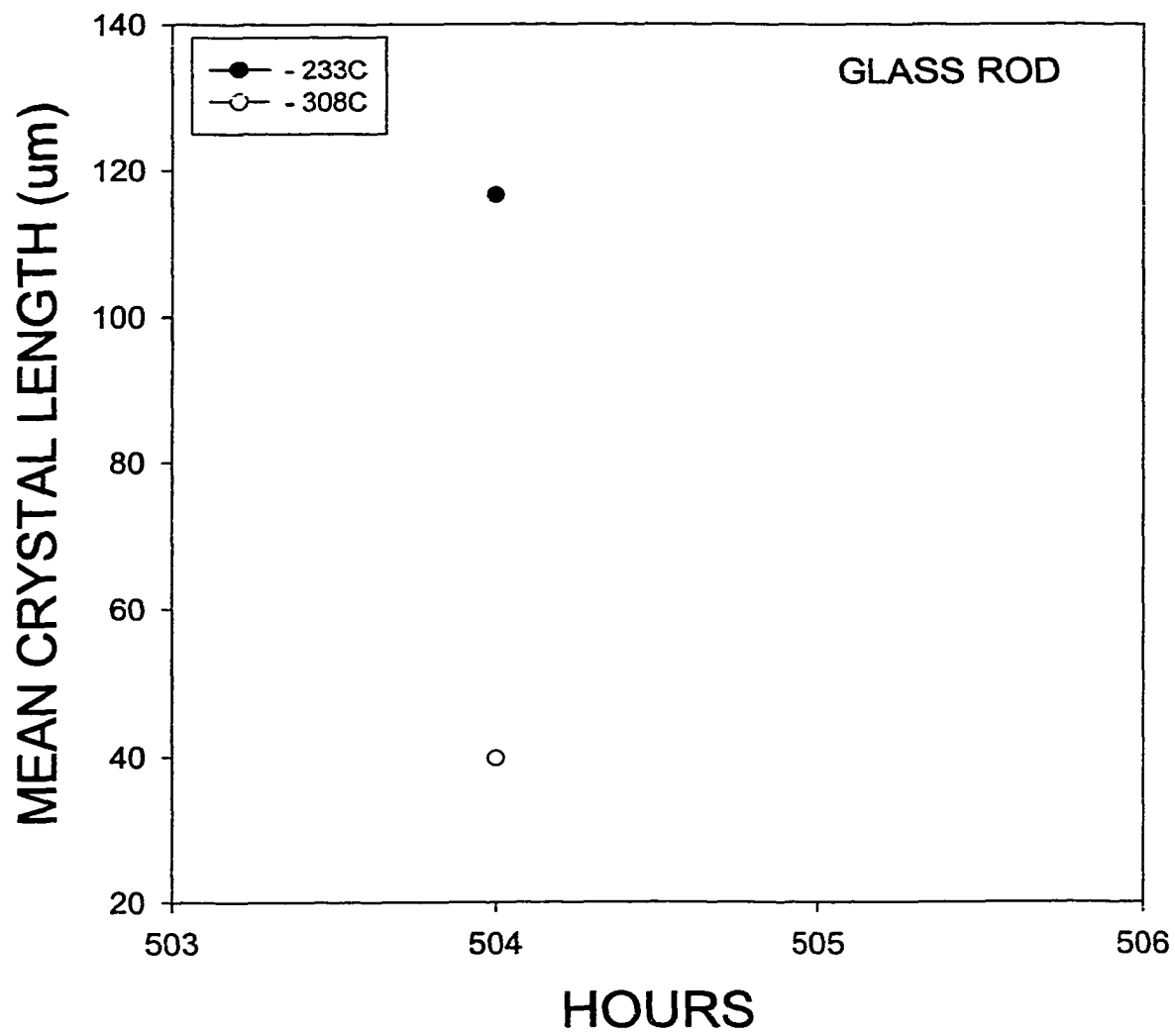


Figure 5-7c.

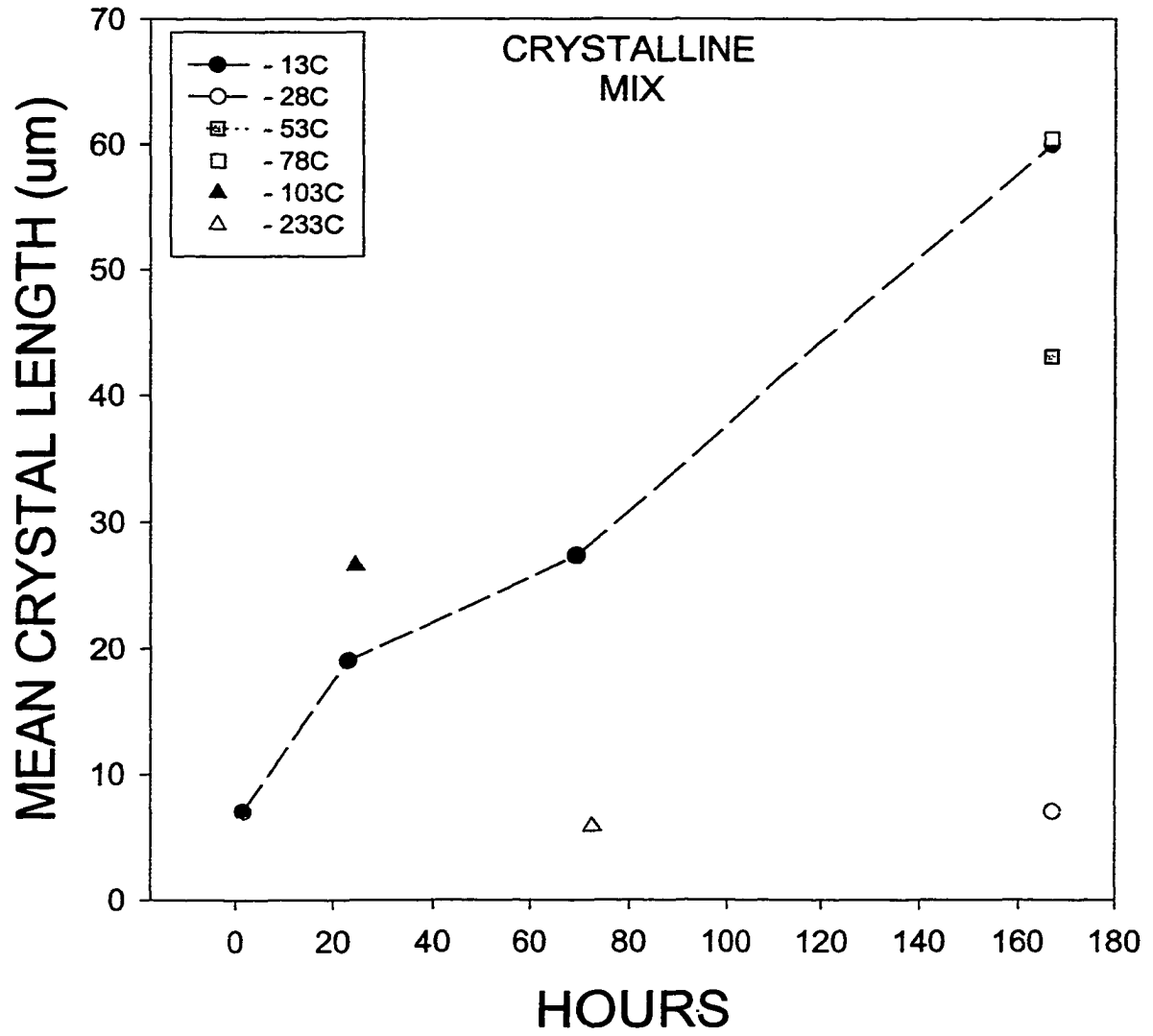


Figure 5-8a.

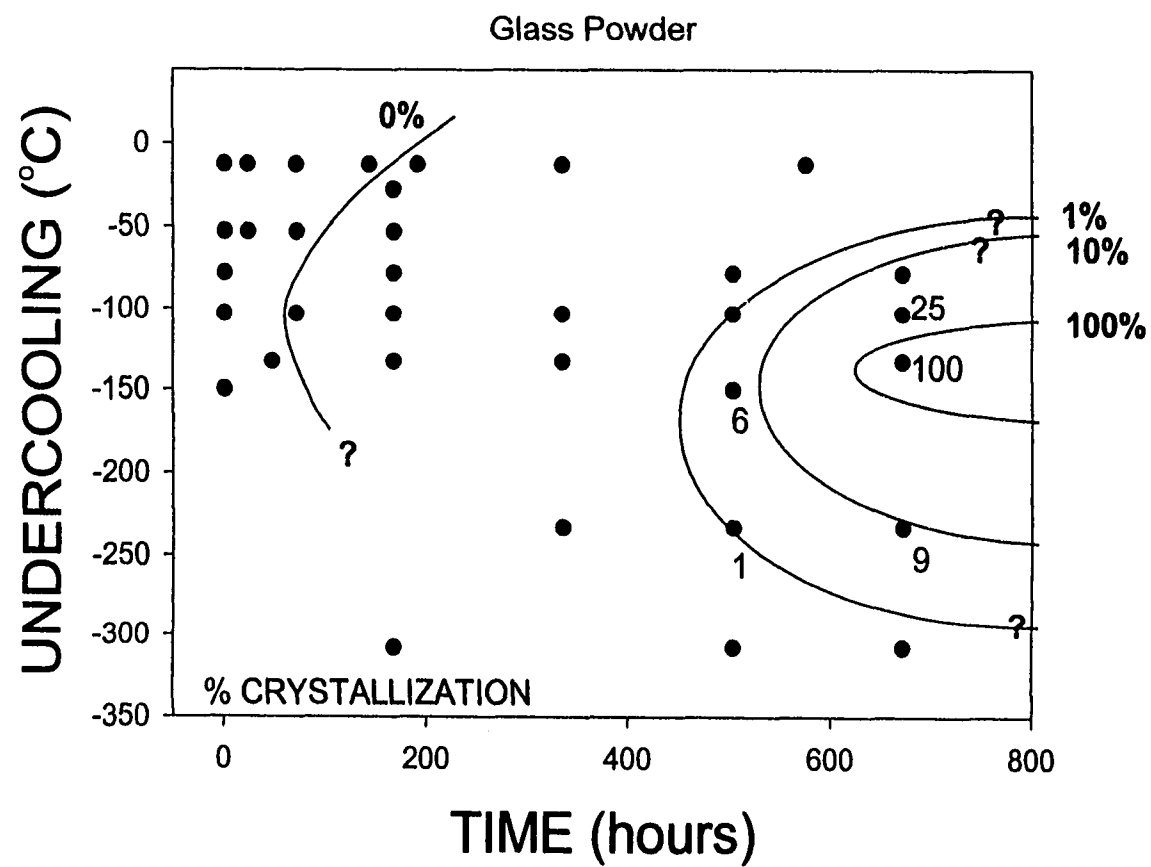


Figure 5-8b.

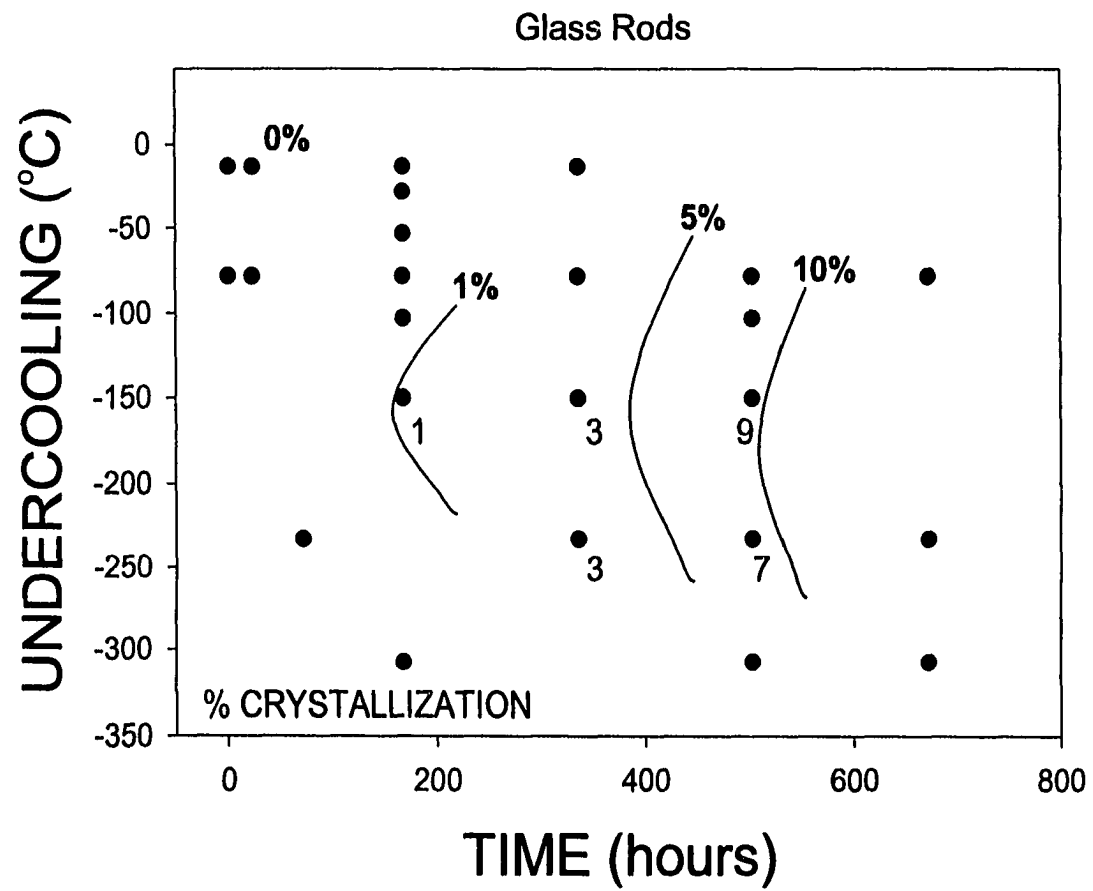


Figure 5-8c.

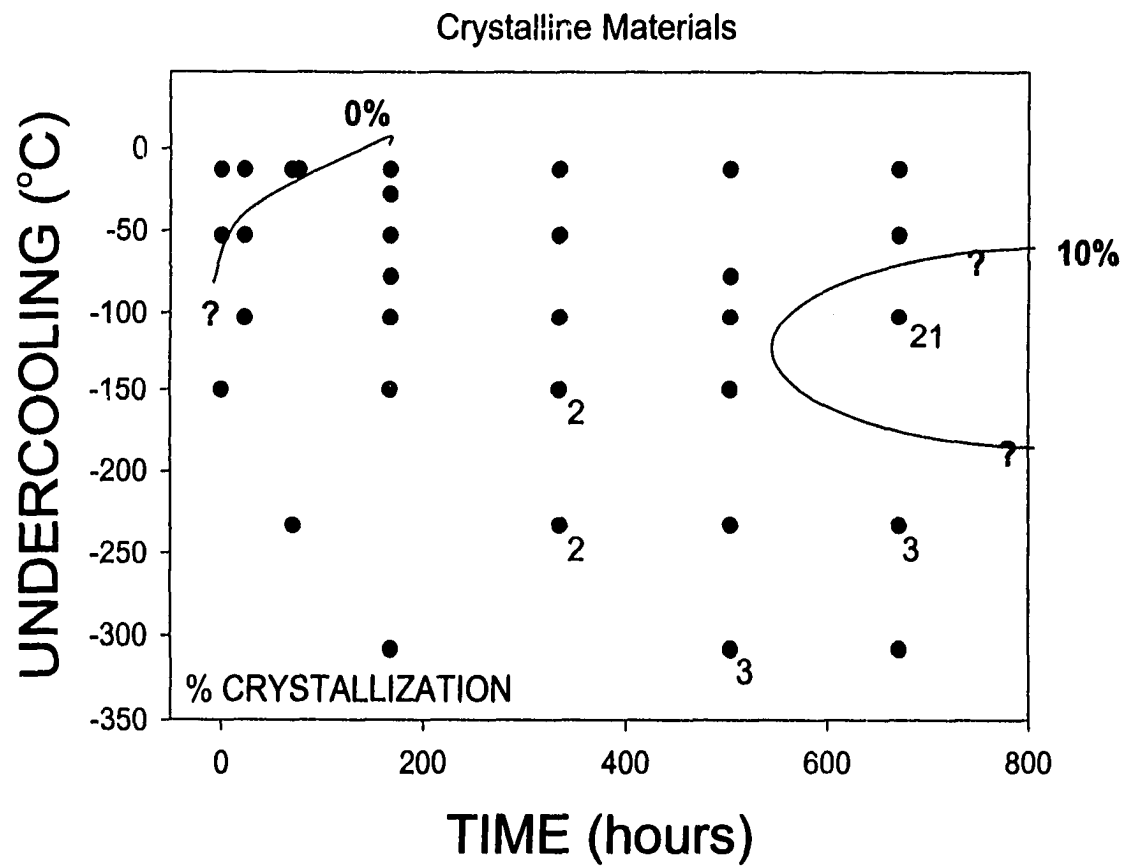


Figure 5-9a.

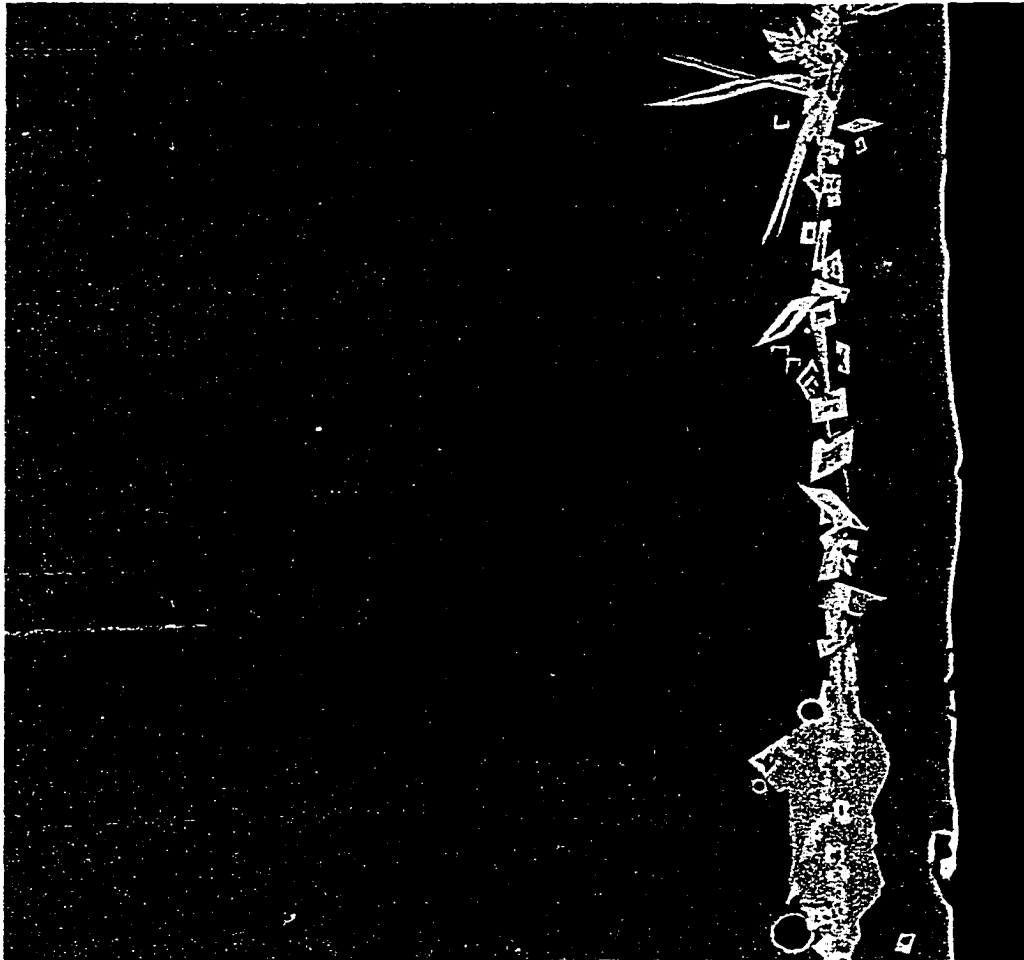


Figure 5-9b.

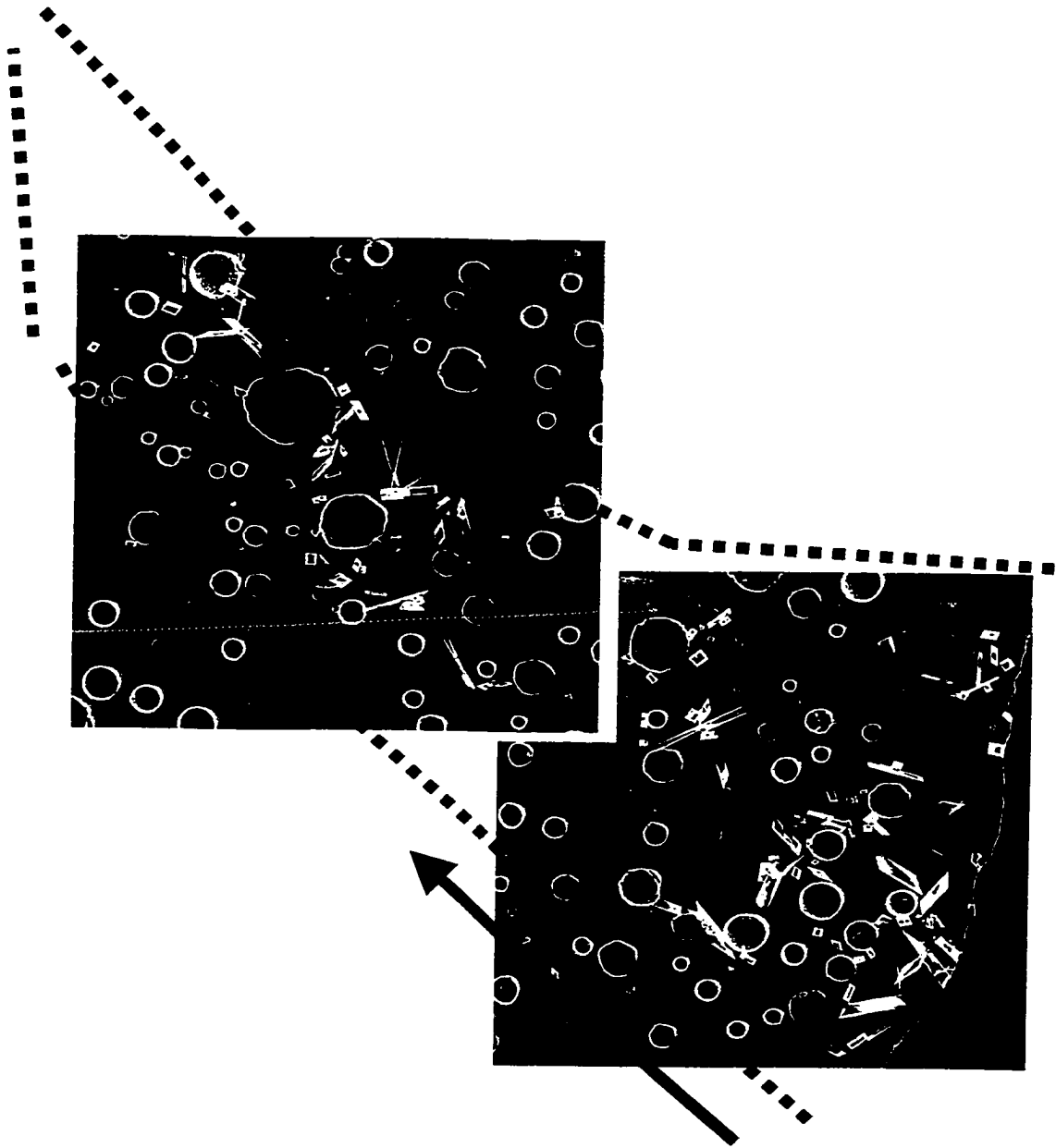


Figure 5-10a.

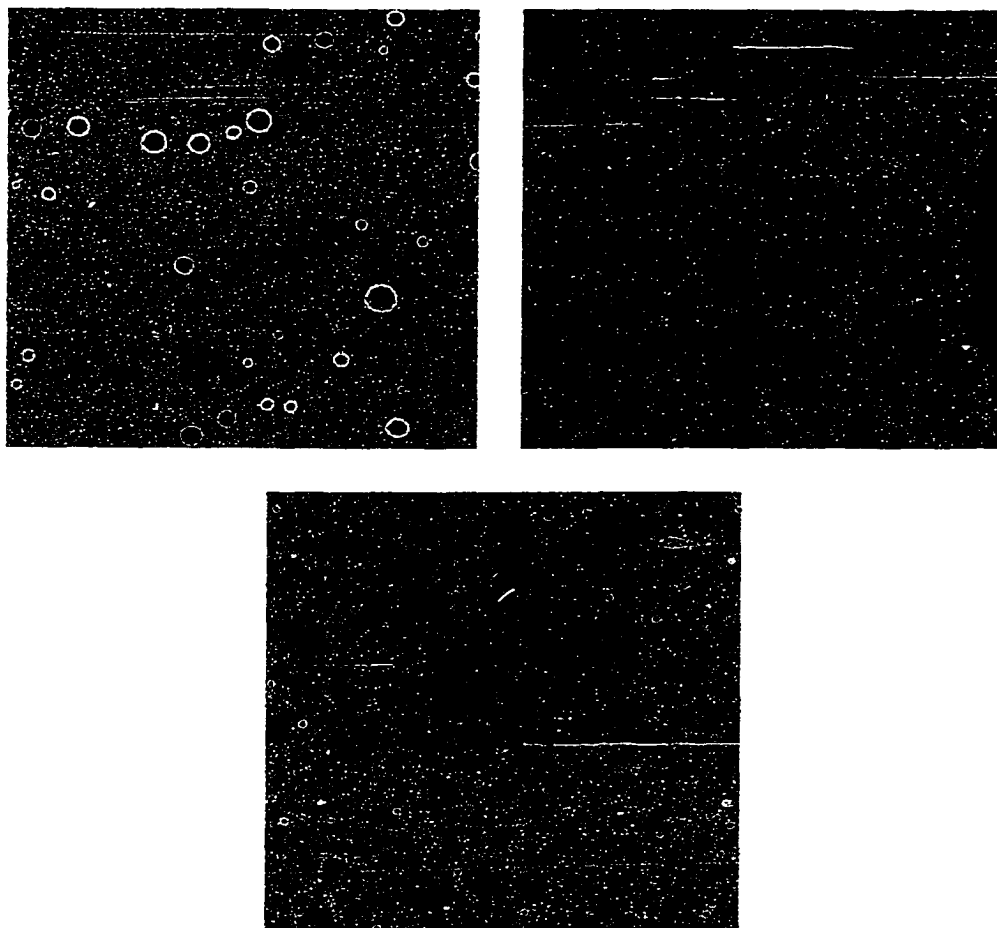


Figure 5-10b.

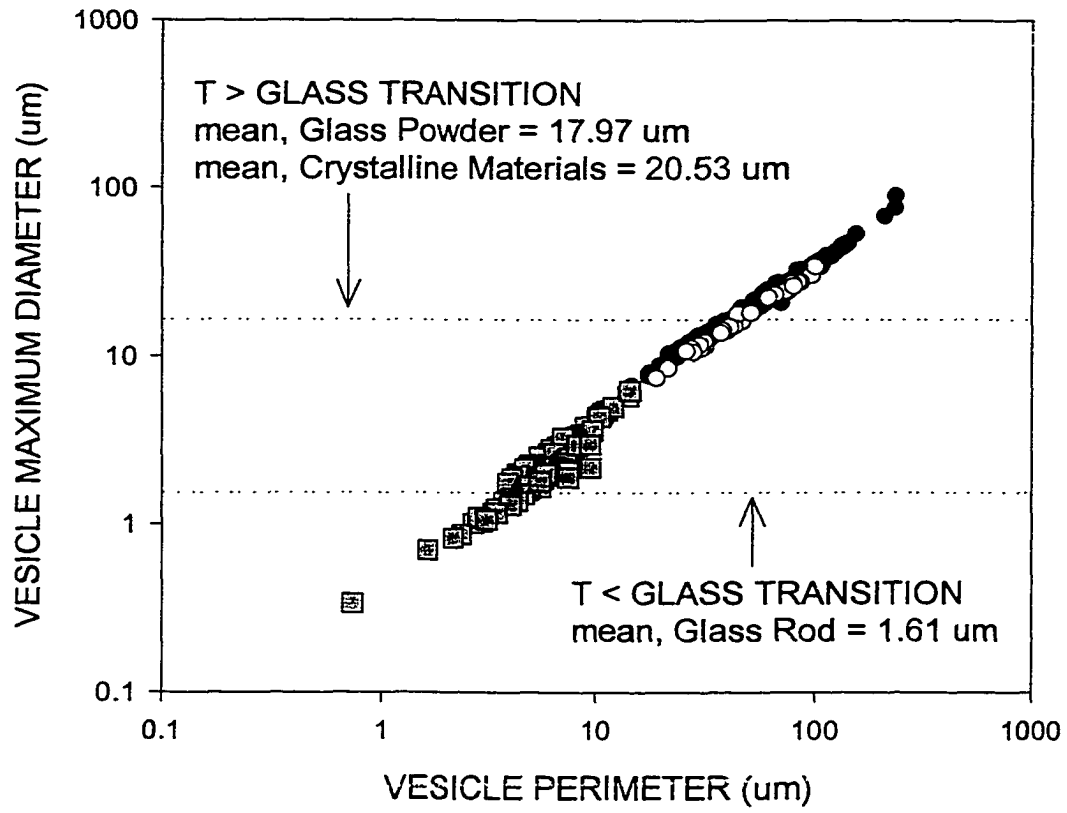


Figure 5-11a.

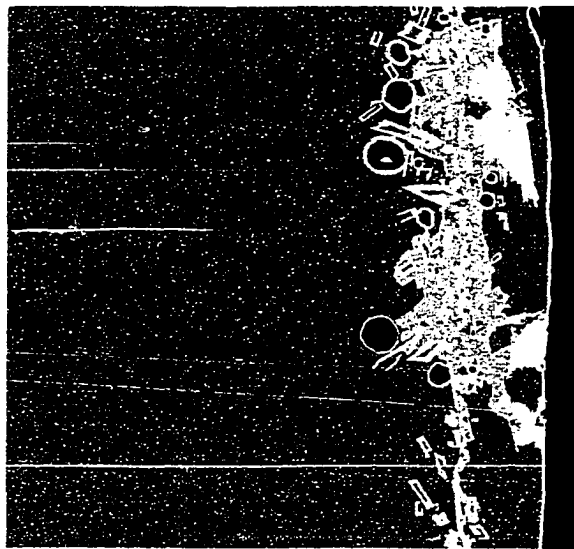
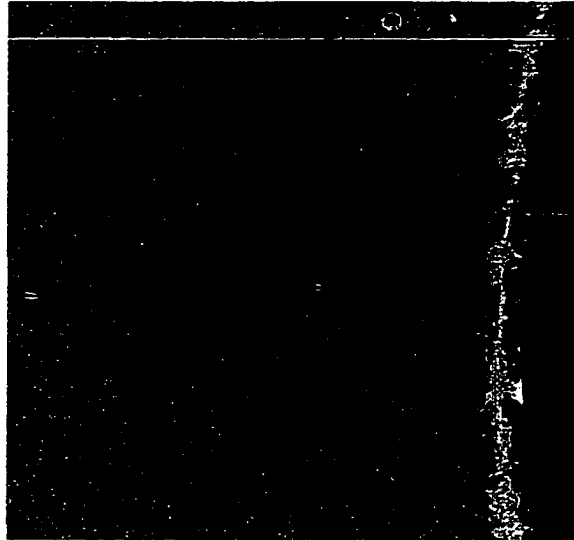


Figure 5-11b.

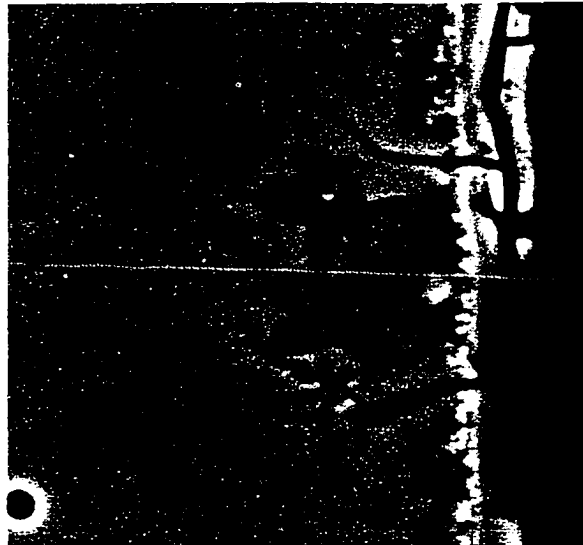
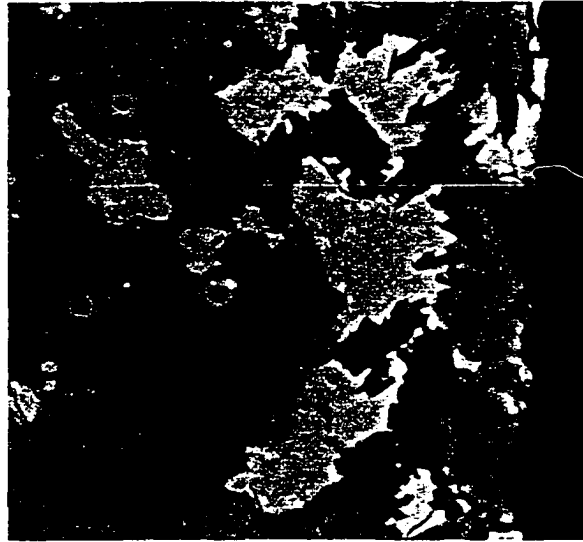


Figure 5-12.

